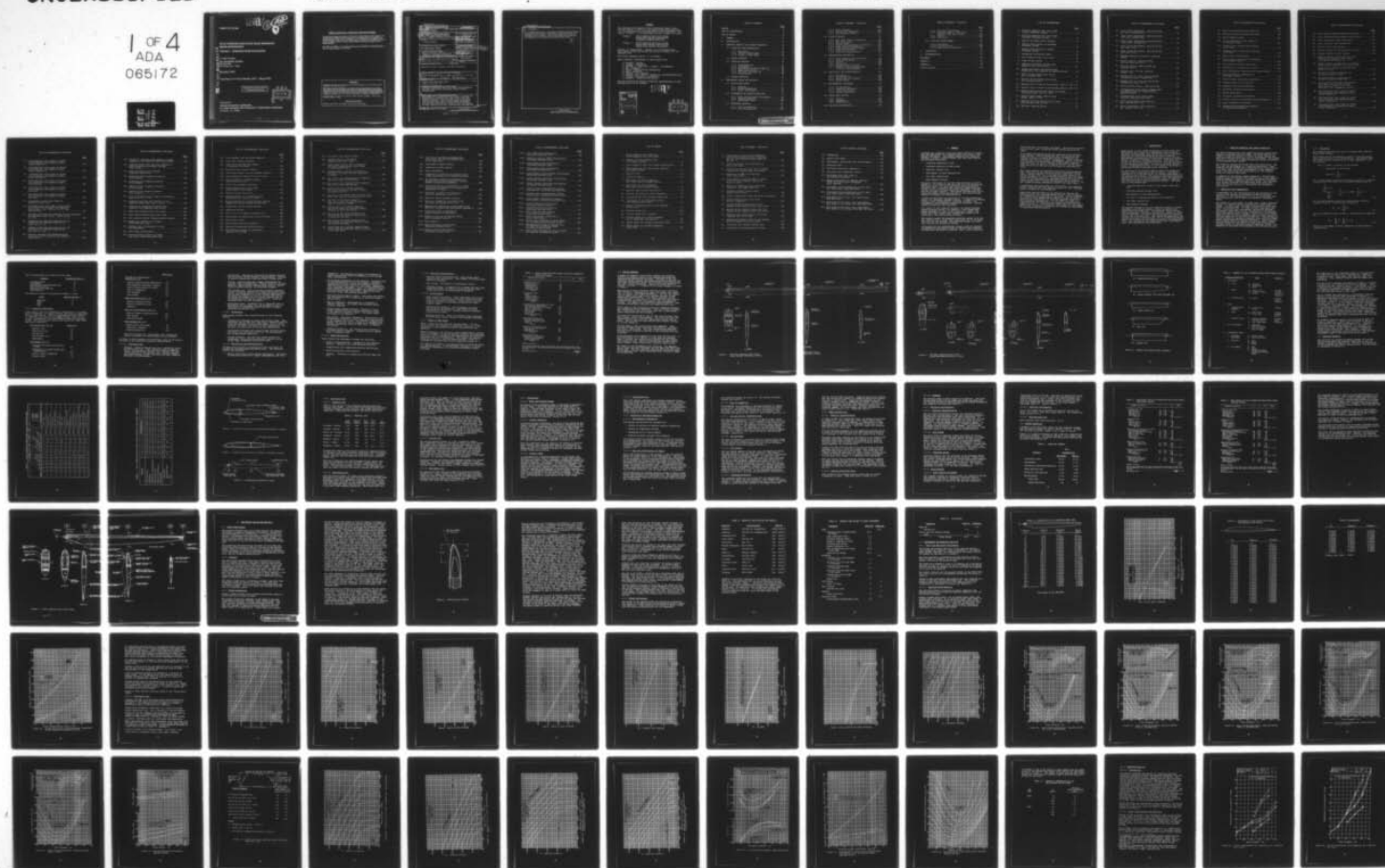


AD-A065 172

BELL HELICOPTER TEXTRON FORT WORTH TEX
OH-58 COMPOSITE MAIN ROTOR BLADE. PRELIMINARY DESIGN INVESTIGAT--ETC(U)
DEC 78 V H BROGDON, J BRASWELL, F FREEMAN DAAJ02-77-C-0073
699-099-086 USARTL-TR-78-38A NL

UNCLASSIFIED

1 OF 4
ADA
065172



USARTL-TR-78-38A

LEVEL II



**OH-58 COMPOSITE MAIN ROTOR BLADE PRELIMINARY
DESIGN INVESTIGATION**

VOLUME I - COMPOSITE BLADE EVALUATION

V. Hubert Brogdon

BELL HELICOPTER TEXTRON

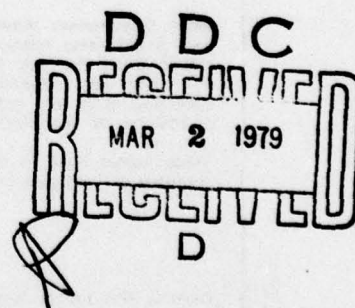
P.O. Box 482

Fort Worth, Tex. 76101

December 1978

Final Report for Period October 1977 - March 1978

Approved for public release;
distribution unlimited.



Prepared for

APPLIED TECHNOLOGY LABORATORY

U. S. ARMY RESEARCH AND TECHNOLOGY LABORATORIES (AVRADCOM)

Fort Eustis, Va. 23604

DDC FILE COPY AD A065172

79 02 27 082

APPLIED TECHNOLOGY LABORATORY POSITION STATEMENT

The preliminary design and analysis in this report provides insight into the feasibility and technical gains associated with the application of a composite main rotor blade to the OH-58 helicopter. Results from this program will be of benefit when establishing requirements and objectives for any follow-on blade Product Improvement Program for the OH-58 helicopter.

Mr. Harold K. Reddick, Jr., Structures Technical Area, Aeronautical Technology Division, served as project engineer for this effort.

DISCLAIMERS

The findings in this report are not to be construed as an official Department of the Army position unless so designated by other authorized documents.

When Government drawings, specifications, or other data are used for any purpose other than in connection with a definitely related Government procurement operation, the United States Government thereby incurs no responsibility nor any obligation whatsoever; and the fact that the Government may have formulated, furnished, or in any way supplied the said drawings, specifications, or other data is not to be regarded by implication or otherwise as in any manner licensing the holder or any other person or corporation, or conveying any rights or permission, to manufacture, use, or sell any patented invention that may in any way be related thereto.

Trade names cited in this report do not constitute an official endorsement or approval of the use of such commercial hardware or software.

DISPOSITION INSTRUCTIONS

Destroy this report when no longer needed. Do not return it to the originator.

Unclassified

SECURITY CLASSIFICATION OF THIS PAGE (When Data Entered)

REPORT DOCUMENTATION PAGE		READ INSTRUCTIONS BEFORE COMPLETING FORM
1. REPORT NUMBER USARTL TR-78-38A	2. GOVT ACCESSION NO.	3. RECIPIENT'S CATALOG NUMBER
4. TITLE (and Subtitle) OH-58 COMPOSITE MAIN ROTOR BLADE; PRELIMINARY DESIGN INVESTIGATION; Volume I of COMPOSITE BLADE EVALUATION.	5. TYPE OF REPORT & PERIOD COVERED Final-October 1977 to March 1978	6. PERFORMING ORG. REPORT NUMBER 699-099-086
7. AUTHOR(s) V. Hubert Brogdon	8. CONTRACT OR GRANT NUMBER(s) DAAJ02-77-C-0073	9. PROGRAM ELEMENT, PROJECT, TASK AREA & WORK UNIT NUMBERS 62209A 1L262209AH76 00 225 EK
10. PERFORMING ORGANIZATION NAME AND ADDRESS Bell Helicopter Textron Ft. Worth, Texas 76101	11. CONTROLLING OFFICE NAME AND ADDRESS Applied Technology Laboratory, U.S. Army Research & Technology Laboratories (AVRADCOM), Fort Eustis, Virginia 23604	12. REPORT DATE December 1978
13. MONITORING AGENCY NAME & ADDRESS (if different from Controlling Office)	14. SECURITY CLASS. (of this report) Unclassified	15. DECLASSIFICATION/DOWNGRADING SCHEDULE
16. DISTRIBUTION STATEMENT (of this Report) Approved for public release; distribution unlimited.		
17. DISTRIBUTION STATEMENT (of the abstract entered in Block 20, if different from Report) V. Hubert / Brogdon, J. / Braswell, E. / Freeman, J. / Yen T. / Muller		
18. SUPPLEMENTARY NOTES Volume I of a two-volume report. 335 p.		
19. KEY WORDS (Continue on reverse side if necessary and identify by block number) Composites, Helicopter, Main rotor blade, High performance, Low radar cross section, Survivable, Damage tolerant, Filament wound.		
20. ABSTRACT (Continue on reverse side if necessary and identify by block number) This program was a preliminary design study to evaluate the application of a composite main rotor blade to the Model OH-58C/A helicopter. The first phase of the study was a trade-off analysis in which a basic concept was selected that utilized a spar made of filament-wound glass/epoxy rovings looped around the main retention bolt hole bushing. The blade afterbody featured a machined Nomex honeycomb core		

DD FORM 1 JAN 73 1473 EDITION OF 1 NOV 65 IS OBSOLETE

Unclassified

SECURITY CLASSIFICATION OF THIS PAGE (When Data Entered)

054 200

19 02 27 087

Unclassified

SECURITY CLASSIFICATION OF THIS PAGE(When Data Entered)

20. Concluded

and filament-wound skins. The blade aerodynamic shape included a nonlinear chord length distribution, a high twist rate, and advanced airfoil contours. The second phase of the program consisted of a preliminary design of the selected concept and its comparison to the existing (standard) metal blade.

Unclassified

SECURITY CLASSIFICATION OF THIS PAGE(When Data Entered)

PREFACE

This document was prepared by Bell Helicopter Textron under Contract DAAJ02-77-C-0073 to the Applied Technology Laboratory, U.S. Army Research and Technology Laboratories (AVRADCOM), Fort Eustis, Virginia. It is subdivided into two volumes as follows:

Volume I OH-58 Composite Main Rotor Blade
Preliminary Design Investigation
(Composite Blade Evaluation)

Volume II OH-58 Composite Main Rotor Blade
Preliminary Design Investigation
(Radar Cross Section Evaluation)

Volume I is unclassified. Volume II is classified Secret. This report covers work during the period of October 1977 to February 1978.

The Project Engineer was Mr. V. H. Brogdon.

Major technical contributors to this program were:

J. Braswell - Design
F. Freeman - Structures
D. Kocurek, T. Trept and J. Tangler - Aerodynamics
J. Yen - Dynamics
T. Mullan - Manufacturing Engineering
S. Aker - Materials
N. Fischer - Cost Analysis
O. Hensley and F. Terrel - Reliability and Maintainability
J. Johnson - Ballistic Survivability
D. Hardesty - Stability and Control

The Army Contracting Officer's Technical Representative on this program was Mr. H. K. Reddick.

LEVEL II

ACCESSION for	
DTIC	White Section <input checked="" type="checkbox"/>
DDC	Grey Section <input type="checkbox"/>
UNANNOUNCED	<input type="checkbox"/>
JUSTIFICATION	
BY	
DISTRIBUTION/AVAILABILITY CODES	
ONE	AVAIL. ONE/Y SPECIAL
A	

DDC
RECEIVED
MAR 2 1979
D

TABLE OF CONTENTS

	<u>Page</u>
PREFACE	3
LIST OF ILLUSTRATIONS.	8
LIST OF TABLES	18
1. SUMMARY	21
2. INTRODUCTION.	23
3. TRADE-OFF ANALYSIS AND CONCEPT SELECTION.	24
3.1 TRADE-OFF STUDY METHODOLOGY.	24
3.1.1 Math Model.	25
3.1.2 Factors in Math Model	26
3.1.3 Inputs to Math Model.	30
3.2 DESIGN CONCEPTS.	32
3.3 TRADE-OFF ANALYSIS	39
3.3.1 Life-Cycle Cost	43
3.3.2 Performance	45
3.3.3 Reliability and Maintainability	46
3.3.4 Radar Reflectivity.	48
3.3.5 Ballistic Survivability	49
3.3.6 Miscellaneous	49
3.4 CONCEPT SELECTION.	50
4. PRELIMINARY DESIGN AND ANALYSIS	57
4.1 ROTOR BLADE DESIGN	57
4.1.1 Geometry.	57
4.1.2 Blade Construction.	57
4.1.3 Weight and Balance.	61
4.2 PERFORMANCE AND HANDLING QUALITIES	64
4.2.1 Rotor and Helicopter Performance.	64
4.2.2 Handling Qualities.	94
4.2.3 Aerodynamic Tests	105
4.3 STRUCTURAL ANALYSIS.	115
4.3.1 Section Properties.	115
4.3.2 Load Determination.	118

TABLE OF CONTENTS - Continued

	<u>Page</u>
4.3.3 Stress Analysis	123
4.3.4 Fatigue Life Estimation	130
4.3.5 Environmental Effects	137
4.4 DYNAMIC ANALYSIS	139
4.4.1 Main Rotor Natural Frequencies.	139
4.4.2 Main Rotor Loads.	140
4.4.3 Control Loads	151
4.4.4 Rotor Pylon Subharmonic Instability	167
4.4.5 Blade Flap-Lag Instability.	171
4.4.6 Blade Bending-Torsion Flutter	171
4.4.7 Blade Stall Flutter	171
4.4.8 Vibration Characteristics	179
4.5 MANUFACTURING METHODOLOGY.	179
4.5.1 Blade Manufacturing Background.	179
4.5.2 Blade Manufacturing	183
4.5.3 Tooling	184
4.5.4 Fabrication	185
4.5.5 Manufacturing Flow Chart.	197
4.5.6 Composite Blade Manufacturing Facilities and Equipment.	197
4.6 RELIABILITY AND MAINTAINABILITY.	205
4.6.1 Reliability	205
4.6.2 Maintainability	218
4.6.3 Maintainability Analysis.	222
4.6.4 System Safety	226
4.7 ENVIRONMENTAL SUBSYSTEMS	227
4.7.1 Ice Protection.	227
4.7.2 Lightning Protection.	229
4.7.3 Static Electricity.	229
4.7.4 Erosion Protection.	230
4.8 RADAR CROSS SECTION.	230
4.8.1 General	230
4.8.2 Discussion.	231
4.8.3 Compatibility	232
4.9 BALLISTIC SURVIVABILITY.	234

TABLE OF CONTENTS - Concluded

	<u>Page</u>
4.9.1 Analytical Methodology.	234
4.9.2 Ballistic Tests of the OH-58C Composite Main Rotor Blade.	251
4.9.3 Results	257
4.9.4 Conclusion.	263
4.10 COST AND EFFECTIVENESS.	263
4.10.1 Discussion.	263
4.10.2 Life-Cycle Cost	263
4.10.3 Effectiveness Comparison.	275
5. CONCLUSIONS	276
6. RECOMMENDATIONS	277
REFERENCES	278
APPENDIX A	281
APPENDIX B	324
LIST OF SYMBOLS.	334

LIST OF ILLUSTRATIONS

	<u>Page</u>
1. OH-58C/A composite main rotor blade tubular afterbody concept.	33
2. OH-58C/A composite main rotor blade honeycomb afterbody concept.	35
3. Typical tip shape design concepts.	37
4. Typical cross section of honeycomb afterbody concept.	42
5. Typical cross section of tubular afterbody concept.	42
6. Recommended aerodynamic shape.	42
7. OH-58 composite main rotor blade	55
8. Blade deicing system	59
9. Improved and baseline OH-58C blade geometric twist distribution	66
10. Design point hover and minimum power comparison of the improved and baseline OH-58C . . .	69
11. Hover ceiling versus gross weight, out of ground effect	71
12. Service ceiling versus gross weight, out of ground effect	72
13. Maximum rate of climb vs gross weight, 4000 ft, 95° F	73
14. Vertical rate of climb vs gross weight, 4000 ft, 95° F	74
15. Maximum speed versus gross weight at maximum continuous power, 4000 ft, 95°F.	75
16. Payload versus range, 3200-lb gross weight, 4000 ft, 95°F.	76
17. Nautical miles per pound of fuel versus gross weight, 4000 ft, 95°F.	77
18. Ceilings, improved OH-58C.	78

LIST OF ILLUSTRATIONS (Continued)

	<u>Page</u>
19. Level flight performance, improved OH-58C, sea level, standard day.	79
20. Level flight performance, improved OH-58C, 5000 feet, standard day.	80
21. Level flight performance, improved OH-58C 10,000 feet, standard day.	81
22. Level flight performance, improved OH-58C, sea level, 95°F.	82
23. Level flight performance, improved OH-58C, 4000 feet, 95°F.	83
24. Maximum endurance performance, improved OH-58C	84
25. Mission profile, improved OH-58C, 2000 and 4000 feet 95°F.	85
26. Vertical rate of climb, standard day, improved OH-58C.	86
27. Vertical rate of climb, improved OH-58C, 95°F	87
28. Maximum rate of climb, improved OH-58C, intermediate power, standard day	88
29. Maximum rate of climb, improved OH-58C, intermediate power, 95°F	89
30. Autorotational descent, improved OH-58C.	90
31. Nondimensional hover power, minimum power and advance ratio for minimum power, improved OH-58C.	91
32. Nondimensional level flight power required, improved OH-58 rotor	92
33. Static longitudinal trim stability, gw = 2500 lb, cg = 114.2	95
34. Static longitudinal trim stability, gw = 3200 lb, cg = 107	96

LIST OF ILLUSTRATIONS (Continued)

	<u>Page</u>
35. Static lateral-directional stability	98
36. RPM decay during autorotational entry.	100
37. Right sideward flight.	101
38. Static longitudinal trim stability in rearward flight	102
39. Standard rotor during stick reversal at 20 knots.	103
40. Composite rotor during stick reversal at 20 knots.	104
41. Model rotor configurations	106
42. Chord, twist, and airfoil distribution for the model rotors	108
43. Test stand in anechoic wind tunnel	109
44. Components of resultant rotor force.	109
45. Hover performance comparison for tapered blades. . . .	111
46. Hover performance comparison for rectangular blades	112
47. Forward flight performance comparison.	114
48. Blowback angle versus airspeed	116
49. Beamwise stiffness distribution.	119
50. Chordwise stiffness distribution	119
51. Weight distribution.	120
52. Torsional stiffness distribution	120
53. Center of gravity and neutral axis distribution. . . .	121
54. Axial stiffness distribution	121
55. Beamwise and chordwise mass moments of inertia distribution.	122

LIST OF ILLUSTRATIONS (Continued)

	<u>Page</u>
56. Limit beamwise bending moment distribution	124
57. Limit chordwise bending moment distribution.	125
58. Limit centrifugal force distribution	126
59. Limit torsional load distribution.	127
60. Main bolt hole cross section	128
61. Goodman diagram for unidirectional S-glass	134
62. Goodman diagram for $\pm 45^\circ$ S-glass	134
63. Spanwise moment distribution for a full autorotation landing at 2530 pounds gross weight and neutral cg.	136
64. Spanwise moment distribution for fore/aft cyclic control reversal at V_H , 2760 pounds gross weight, forward cg and 3000 feet density altitude	138
65. Calculated natural frequencies for OH-58C/A production rotor.	142
66. Calculated natural frequencies for OH-58C/A composite blade rotor	146
67. Correlation of calculated and measured main rotor loads for the OH-58A: gross weight = 3000 lb, cg = 112.2, 2100 feet, 75°F, airspeed = 102.5 kn	150
68. Calculated main rotor loads for OH-58C with production and composite blades: flight condition 1	153
69. Calculated main rotor loads for OH-58C with production and composite blades: flight condition 2	154
70. Calculated main rotor loads for OH-58C with production and composite blades: flight condition 3	155

LIST OF ILLUSTRATIONS (Continued)

	<u>Page</u>
71. Calculated main rotor loads for OH-58C with production and composite blades: flight condition 4	156
72. Calculated main rotor loads for OH-58C with production and composite blades: flight condition 5	157
73. Calculated main rotor loads for OH-58C with production and composite blades: flight condition 6	158
74. Calculated main rotor loads for OH-58C with production and composite blades: cyclic pullup.	159
75. Calculated main rotor loads for OH-58C with production and composite blades: right turn	160
76. Calculated main rotor loads for OH-58C with production and composite blades: left turn.	161
77. Correlation of pitch link loads for production blade rotor	162
78. Calculated pitch link loads in level flight for OH-58C with production and composite blade rotors: gw = 3200 lb, aft cg, 4000 feet and 95°F.	163
79. Computed pitch-link-load waveforms for the production and composite blade rotors: cyclic pullup at 1.5g.	164
80. Computed pitch-link-load waveforms for the production and composite blade rotors: right turn at 1.5g	165
81. Computed pitch-link-load waveforms for the production and composite blade rotors: left turn at 1.5g.	166
82. Stability boundary with swashplate/pylon coupling for both production and composite blade rotors	168

LIST OF ILLUSTRATIONS (Continued)

	<u>Page</u>
83. Production rotor and pylon response to pylon plucking at 100 knots, 354 RPM, level flight	169
84. Composite blade rotor and pylon response to pylon plucking at 100 knots, 354 RPM, level flight	170
85. Flap-lag stability for OH-58C/A production blade rotor	172
86. Production blade frequency variation with airspeed.	173
87. Production blade damping variation with airspeed.	174
88. Composite blade frequency variation with airspeed.	175
89. Composite blade damping variation with airspeed.	176
90. Plot for determination of onset of retreating blade stall at $\mu = .23$	177
91. Computed pitch-link-load waveform for the composite blade rotor: $C_T/\sigma = 0.109$, $\mu = .23$	178
92. Computed hub vibrations of OH-58C with production and composite blade rotors.	180
93. Model 649 fiberglass main rotor blade.	181
94. Model 206LM composite main rotor blade	182
95. High capacity orbital filament-winding machine	186
96. Compacting procedure for filament-wound blade spar caps.	187
97. Assembly tool and procedure for spar cap subassembly	189
98. Rotor blade bonding press.	190
99. Filament-winding machine and blade spar outer torque wrap application	191

LIST OF ILLUSTRATIONS (Continued)

	<u>Page</u>
100. Spar assembly tool and curing sequence.	192
101. Blade skin winding procedure.	193
102. Lower skin layup and warp bonding of honeycomb core blank	194
103. Honeycomb core contour carving.	195
104. Blade body bonding tool and assembly sequence	196
105. Electrohydraulic forming die for tip shoe	198
106. Vacuum forming of urethane leading edge protection strip	199
107. Blade final assembly operations	200
108. OH-58 composite main rotor blade manufacturing flow sequence	201
109. Composite blade lay-up area	202
110. McLean-Anderson W-2 filament-winding machine for $\pm 45^\circ$ winding of spars	203
111. McLean-Anderson W-2 filament-winding machine adapted for orbital winding of spar caps.	204
112. Goldsworthy orbital winding machine	206
113. Compacting machine.	207
114. K&T 5 ft x 32 ft numerical control mill	208
115. Distribution of removals due to all failures.	216
116. Blade repair areas.	221
117. Heat-pressure patching apparatus.	225
118. Replacing leading-edge abrasion strip	225
119. RCS reduction concept for the OH-58C/A composite rotor blade	233

LIST OF ILLUSTRATIONS (Continued)

	<u>Page</u>
120. Helicopter survivability model.	236
121. CALCOMP drawing of the OH-58C composite main rotor blade.	242
122. Damage model printer plot of damage to the OH-58C composite main rotor blade at blade Station 106.0.	246
123. Nondimensional torsional stiffness as a function of distance from the centerline of damage	248
124. Top view of the undamaged OH-58C composite main rotor blade test specimen.	252
125. End view of the undamaged OH-58C composite main rotor blade test specimen.	252
126. Bottom view of the OH-58C composite main rotor blade test specimen showing projectile entrance	254
127. Top view of the OH-58C composite main rotor blade test specimen showing projectile exit	254
128. End view of the OH-58C composite main rotor blade test specimen showing 23mm API projectile damage	255
129. Bottom view of the OH-58C composite main rotor blade test specimen showing entrance of shots one and two	256
130. Top view of the OH-58C composite main rotor blade test specimen showing exit of shots one and two.	258
131. End view of the OH-58C composite main rotor blade test specimen showing 12.7mm API projectile damage	259
132. Bottom view of the OH-58C composite main rotor blade test specimen showing entrance of all four shots	260

LIST OF ILLUSTRATIONS (Continued)

	<u>Page</u>
133. Top view of the OH-58C composite main rotor blade test specimen showing exit of all four shots.	260
134. Development program schedule	269
135. Production program schedule.	270
A-1. Hover performance.	283
A-2. Comparison of predicted and measured level flight performance of the OH-58A helicopter.	285
A-3. The optimum circulation distribution for minimum induced power compared to baseline OH-58C circulation distribution.	288
A-4. Chord distribution corresponding to optimum circulation distribution for a design lift coefficient of unity	289
A-5. Variation of airfoil lift-drag ratio with lift coefficient at $M = 0.5$	290
A-6. Effect of thrust weighted solidity	293
A-7. Variation of NACA 0012 lift-drag ratio with lift coefficient at $M = 0.5$	295
A-8. Maximum lift coefficient vs Mach number from NACA 0012 and FX69-H-098 data tables, Appendix B . .	296
A-9. Calculated effect of FX69-H-098 airfoil relative to NACA 0012.	298
A-10. Effect of tip loss on improved OH-58C shaft horsepower required.	299
A-11. Hover benefit.	303
A-12. Bound circulation distribution, calculated isolated rotor.	304
A-13. Induced velocity distribution, calculated isolated rotor.	305

LIST OF ILLUSTRATIONS (Concluded)

	<u>Page</u>
A-14. Lift coefficient distribution, calculated isolated rotor.	306
A-15. Effective angle of attack distribution, calculated isolated rotor.	307
A-16. Blade segment lift distribution, calculated isolated rotor.	308
A-17. Blade segment drag distribution, calculated isolated rotor.	309
A-18. Blade segment pitching moment distribution, calculated isolated rotor.	310
A-19. Thrust loading coefficient distribution, calculated isolated rotor.	311
A-20. Torque loading coefficient distribution, calculated isolated rotor.	312
A-21. Profile torque loading/thrust loading distribution, calculated isolated rotor.	313
A-22. Induced torque loading/thrust loading distribution, calculated isolated rotor.	314
A-23. Total torque loading/thrust loading distribution, calculated isolated rotor.	315
A-24. Profile drag/lift distribution, calculated isolated rotor.	316
A-25. Induced drag/lift distribution, calculated isolated rotor.	317
A-26. Total drag/lift distribution, calculated isolated rotor.	318
A-27. Rotor alone torque coefficient vs thrust coefficient	319
A-28. Engine shaft horsepower vs gross weight for the improved and baseline OH-58C	320
A-29. Nondimensional torque vs advance ratio for improved and baseline OH-58C helicopter without losses.	322
A-30. Engine shaft horsepower vs true airspeed for improved and baseline OH-58C	323

LIST OF TABLES

	<u>Page</u>
1. Design trade-off math model for OH-58 composite main rotor blade	31
2. Summary of OH-58 composite main rotor blade concepts	38
3. OH-58 composite main rotor blade configurations. . .	40
4. OH-58 composite main rotor blade trade-off math model summary	41
5. Material cost.	43
6. Trade-off summary.	50
7. Math model for OH-58 composite main rotor blade honeycomb concept	51
8. Math model for OH-58 composite main rotor blade tubular concept	52
9. Material specification and density	62
10. Material and weight of blade components.	63
11. Improved OH-58C blade planform shape data.	65
12. Coordinates of the FX69-H-098 airfoil with trailing edge reflex.	67
13. Effect of compressibility on the improved OH-58C rotor	93
14. Material properties.	117
15. Critical blade limit stresses.	131
16. Percent reduction in static strength due to temperature and moisture.	137
17. DN9100 inputs for OH-58C/A production rotor.	140
18. DN9100 inputs for OH-58C/A composite blade rotor.	144

LIST OF TABLES (Continued)

	<u>Page</u>
19. Comparison of production and composite blade OH-58C/A rotor natural frequencies for 16° root collective blade angle and 345 RPM	148
20. Flight conditions for calculations of main rotor loads.	152
21. Failure mode failure rates for the OH-58A standard and improved main rotor blade.	209
22. Comparison of MTBF of OH-58A main rotor blade design.	211
23. Significance of improved MTBF to a fleet of 100 OH-58A helicopters flying 300 hours per year.	211
24. Reason for removal of main rotor blade assemblies from RAMMIT MIRF data.	213
25. Estimate of blade foreign object damage failure rates.	219
26. Control limitations found from flight experience.	239
27. OH-58C composite main rotor blade material properties	243
28. Average stiffness properties of the damaged OH-58C composite main rotor blade	249
29. Results of the dynamic analysis for the damaged OH-58C composite main rotor blade	250
30. Ballistic test conditions for the OH-58C composite main rotor blade	253
31. Predicted stiffness values for the damaged OH-58C composite main rotor blade	262
32. Life-cycle cost analysis ground rules	265
33. Reliability and maintainability values.	266

LIST OF TABLES (Concluded)

	<u>Page</u>
34. Assumptions.	267
35. General cost model	267
36. Development, tooling, and unit cost estimates	271
37. Supporting data.	271
38. Life-cycle cost basic comparison	273
39. Life-cycle cost comparison variant	274
A-1. Conversion from rotor alone to the complete helicopter.	300
A-2. Sample calculations of complete improved OH-58C helicopter shaft horsepower (SHP) required	301
B-1. Government furnished NACA 0012 airfoil data, lift coefficient, NASA TMS-73990	324
B-2. Government furnished NACA 0012 airfoil data, drag coefficients, NASA TMS-73990.	326
B-3. FX69-H-098 airfoil data, lift coefficients, NASA TMS-73990	328
B-4. FX69-H-098 airfoil data, drag coefficients, Mach numbers 0.0 through 0.59, NASA TMS-73990. . . .	330
B-5. FX69-H-098 airfoil data, drag coefficients, Mach numbers 0.64 through 0.90, NASA TMS-73990 . . .	332

1. SUMMARY

A program was conducted at Bell Helicopter Textron to investigate the application of a composite main rotor blade to the OH-58C/A helicopter. The program commenced with trade-off analyses to select a design concept that would best satisfy the following objectives:

- 10-percent reduction in cost
- 6-percent reduction in hover power
- 3600-hour fatigue life
- High degree of field repairability
- Low radar reflectivity
- High damage tolerance

The major constraints for the new blade were that it be designed to: (1) attach to the rotor hub of the production OH-58C/A helicopter, (2) avoid high blade loads and aircraft vibration, and (3) maintain the functional capabilities and fatigue lives of existing interfacing components, including the hub and upper controls. The program concluded with an in-depth preliminary design and analysis of the selected blade concept to optimize its characteristics.

A trade-off math model was developed to evaluate design concepts in an unbiased, systematic manner. A number of different styles of spar configurations, afterbody concepts, root attachments, and aerodynamic shapes were evaluated. Several composite materials were considered.

As a result of the trade-off analysis, two design concepts (using S2-glass) proved to be superior. One concept used Nomex honeycomb as a core in the afterbody to support the skins; the other concept used filament-wound tubes in the afterbody as the load-carrying structure.

The analysis showed the honeycomb afterbody concept to be the best choice since it could more readily meet all of the goals set forth for the program. The honeycomb concept was therefore selected for preliminary design.

Concurrent with the configuration concept trade-off analysis, an aerodynamic performance trade-off analysis was conducted. Consideration was given to planform, twist, airfoil variation

with blade span, and various tip shapes. The planform selected has nonlinear taper, producing curved leading and trailing edges.

An in-depth preliminary design was conducted on the selected blade concept. Section properties were calculated and the structure refined to obtain blade natural frequencies well removed from the rotor harmonic frequencies. Static loads and stresses were also calculated, and adequate margins of safety were obtained. The OH-58 composite blade weight, spanwise effective center of gravity, flapping inertia, and the centrifugal force at the hub are close to those of the production rotor.

Main rotor beamwise and chordwise oscillatory bending moments were computed using the Rotorcraft Flight Simulation Program (C81). Fatigue analysis of the composite blade shows an unlimited fatigue life. No aeroelastic instabilities were found during the dynamic analysis. The manufacturing plan for fabrication of the composite blade developed during the program makes extensive use of mechanized processes and is based on the wet filament-winding technique to achieve the lowest cost.

A reliability and maintainability investigation was conducted. Results indicated that the composite blade will have increased safety, reliability, and durability.

Radar cross section reduction was obtained by treating the composite blade with radar-absorbing materials and by shaping the leading and trailing edges of the blade. The survivability of a ballistically damaged OH-58 composite blade was investigated and all indications are that the composite blade is a very survivable configuration. A life-cycle cost model was established for the selected blade concept and shows that the composite blade is a cost-effective replacement for the present metal blade, especially considering the significant improvement in operational characteristics.

2. INTRODUCTION

Advancements in rotor blade technology in recent years have demonstrated that significant improvements can be made by replacing existing metal rotor blades with ones of composite materials and associated advanced structural concepts. Improvements in operational characteristics can be obtained through increased performance, structural capability, survivability, reliability, and maintainability. Life-cycle cost reductions can also be expected to result from the application of this advanced technology. In order to estimate realistic levels of improvement for the A and C models of the OH-58, a preliminary design investigation was initiated.

The objective of this OH-58 composite main rotor blade preliminary design investigation was to conduct a systematic examination of an improved blade for possible replacement of the existing metal blade. The program investigated potential improvements in rotor blade performance, cost, and operational characteristics by the use of composite materials combined with advanced design and manufacturing concepts. The prime goals of the program were:

- 6-percent reduction in SHP at 3200 pounds, 4000 feet, 95°F
- 3600-hour minimum fatigue life
- High degree of field repairability
- At least a 10-percent production cost reduction
- Low radar reflectivity
- High damage tolerance

The program included an initial trade-off analysis to assess candidate blade design concepts iteratively against the design goals and objectives. The technical areas affected were aerodynamics, structures and materials, dynamics, safety and survivability, reliability and maintainability, manufacturing, and life-cycle cost. One concept was selected at the conclusion of the trade-off study, and an in-depth preliminary design and analysis was performed to optimize its characteristics. Also included in the investigation were complementary tests that substantiate key predictions.

3. TRADE-OFF ANALYSIS AND CONCEPT SELECTION

The OH-58 Composite Main Rotor Blade Preliminary Design Investigation was divided into two tasks. The first task was to conduct a trade-off analysis to select a design concept that would best meet the goals set forth in the program. The second task was to conduct an in-depth preliminary design and analysis of the selected blade concept.

The trade-off analysis was broken down into three parts. The first was the development of a trade-off math model. Next, candidate design concepts were established that could totally, or in part, meet the design requirements for the composite blade. The final task was the evaluation of the concepts using the trade-off math model.

In addition to the design concept trade-off, a detailed performance trade-off analysis was conducted over a wide range of blade parameters to define an improved aerodynamic configuration for the OH-58 composite main rotor blade. The rationale used, results obtained, and conclusions drawn during the trade-off analysis portion of the program are presented in this section.

3.1 TRADE-OFF STUDY METHODOLOGY

A requirement for the investigation was the evaluation of the various blade concepts by performing trade-off analyses. Therefore, it was a prerequisite to set up a math model such that evaluations could be made in an unbiased, systematic manner.

The concept of a math model can range from a simple "good-bad" system to a complex computer program with a large number of inputs. For this study, the model contained five prime categories of consideration. In order of their importance they were: Life-Cycle Cost, Performance, Reliability and Maintainability, Radar Reflectivity, and Ballistic Survivability. Many other factors such as weight, fatigue life, fail-safety, impact and FOD tolerance, dynamics, and vibrations were introduced as subfactors to the major categories. Each category of the math model was assigned a numerical value with the highest number representing the greatest importance. Subfactors were also assigned values of importance within the major category. Quality ratings for each aspect of each blade concept were assigned values by cognizant technical personnel at BHT. The mechanics of the model are discussed in the following section.

3.1.1 Math Model

The following math model was used to evaluate each composite blade design concept.

Each design concept represented an effort to meet the design goals and objectives of the investigation. The primary goals and objectives are categorized as to their importance. For any category:

Let n = number of factors in any category

k = importance of each factor

$$\text{such that } \sum_{i=1}^n k_i = 1 \quad (1)$$

If r is the quality rating for each factor, then for a specific configuration each factor has an average weighted value of:

$$\frac{\sum_{i=1}^n k_i \times r_i}{\sum_{i=1}^n k_i} = \sum_{i=1}^n k_i \times r_i \text{ since } \sum_{i=1}^n k_i = 1 \quad (2)$$

If R is the weighting factor for each category, then the weighted value of a configuration category is:

$$V_{C_j} = R_j \sum_{i=1}^n k_i r_i \quad (3)$$

The final numerical value on which a configuration is measured is:

$$V_f = \sum_{j=1}^m R_j \sum_{i=1}^n k_i \times r_i \quad (4)$$

where m is the number of major categories of prime areas of consideration.

The following numerical values of R were used:

<u>Category</u>	<u>Weighting Value, R</u>
Life-Cycle Cost	6
Performance	5
Reliability and Maintainability	4
Radar Reflectivity	3
Ballistic Survivability	2
Miscellaneous	2

The numerical values of the quality ratings, r, were:

<u>Value</u>	<u>Quality Rating, r</u>
Excellent	4
Good	3
Fair	2
Poor	1

3.1.2 Factors in Math Model

Within each of the five categories of objectives, it is necessary to subdivide into several factors and assign an importance value to each factor. These are represented by the values of k. They were arrived at on a judgement basis, which is the result of discussions held with cognizant technical personnel at BHT. The following are factors and values of k under their applicable categories:

<u>Life-Cycle Cost (R = 6)</u>	<u>Value of k</u>
Material cost	.15
Fabrication cost	.50
Tooling cost	.10
Safe fatigue life	.20
Maintenance	.05

<u>Performance (R = 5)</u>	
Optimized for hover and vertical climb	.50
Optimized for forward flight and autorotation	.25
Airfoil contour retention	.10
Control loads	.15

Value of k

Reliability and Maintainability (R = 4)

Quality control during fabrication	.20
Environmental resistance, erosion	.10
Ease of effectiveness of repair	.20
Ease of inspection	.15
FOD tolerance	.15
Fail-safety	.20

Radar Reflectivity (R = 3)

Material characteristics	.45
Erosion protection strip	.20
Geometry	.35

Ballistic Survivability (R = 2)

Material impact characteristics	.40
Spar design	.40
Afterbody design	.20

Miscellaneous (R = 2)

Blade inertia and weight	.50
Vibrations, dynamics	.30
Handling qualities	.20

Note that fatigue life, fail-safety, FOD, and environmental resistance are covered under earlier headings.

In order to avoid confusion in terminology, each of the factors and some of the evaluation guides are defined below.

3.1.2.1 Life-Cycle Cost

- Material. Material choices can have a significant effect on end-article cost. Basic materials such as graphite, Kevlar, and fiberglass can show cost benefits with judicious selection of the material form. Typical examples are unidirectional roving, unidirectional tape, preplied materials, and broad goods.

- Fabrication. Fabrication considerations address features such as joints, mating surfaces, and tolerances. Cocuring of details reduces part count and lowers tooling level.
- Tooling. Tooling trade-offs compare requirements for specific blade configurations. Typical areas are root-end geometry, tapered versus constant cross section, tapered versus straight planform, and afterbody concepts.
- Safe fatigue life. This is directly related to material fatigue allowables operating at steady and fatigue stress levels, and susceptibility of the unidirectional material and angle-ply laminates to elastic modulus degradation. The actual retirement life of a blade, however, may not be determined by fatigue but other factors. These are addressed under the next paragraphs.
- Maintenance costs. Susceptibility to repairable wear or degradation during normal use, and frequency as well as difficulty of recommended inspections and/or overhaul determine maintenance costs.

3.1.2.2 Performance

Blade design concepts were evaluated based on the following factors:

- Configuration designed for hover and vertical climb. This evaluation and the next were made after a detailed trade-off study that defined solidity, blade shape, twist, airfoil contours, thickness, and radial airfoil distribution, and how well the objectives are met by the configuration.
- Configuration designed for forward flight and autorotation. This factor was evaluated on how well the configuration met the performance objectives.
- Contour retention. How well the concept retains its aerodynamic contour during manufacture and also during flight under aerodynamic and inertial loads.

3.1.2.3 Reliability and Maintainability

Concepts were evaluated to determine how well each meets the reliability and maintainability design goals. The following factors were assessed:

- Quality and process control during fabrication. The degree of difficulty involved to inspect subassemblies and final

assemblies. The adequacy and degree of confidence in quality and process control procedures for the concept under consideration.

- Environmental degradation of the material. Susceptibility of the configuration to structural and/or functional degradation from such natural environmental factors as sand and rain erosion, moisture, salt spray, temperature, ozone, sunlight, and fungus. Also, its susceptibility to such induced environmental elements as vibration, transportation and storage constraints, temperature shock, aircraft fluids, and cleaning materials.
- Ease and effectiveness of repair. How easily and quickly the configuration can be repaired in the field without special tools.
- Ease of inspection. Detectability of incipient or inherent failures. How readily the structure may be visually inspected.
- Foreign object damage tolerance. Severity of local stress concentration due to discontinuities or holes in the material caused by impact. Low energy impact resistance of the material.
- Fail-safety. Structural redundancy. The ability of the flightworthy structure to carry loads after any one part of the assembly has failed. Fail-safety is measured by whether the aircraft can be brought to an immediate safe landing, immediately return to home base, or complete the mission.
- Lightning protection. How effective the structure is protected against lightning. Susceptibility to damage from a lightning strike.

3.1.2.4 Radar Reflectivity

Radar reflectivity assessment includes the following:

- Material characteristics. Impedance of the composite material. Necessity for using absorbing material.
- Compatibility with lightning protection and deicing.
- Erosion protection strip material.
- Geometry. Curvature of leading and trailing edges and tip.

3.1.2.5 Ballistic Survivability

- Material impact characteristics. High energy impact resistance of the material. Brittleness of fracture modes. Amount of unbalance.
- Spar design. Resistance to catastrophic failure.
- Afterbody design. Susceptibility to damage that may cause loads high enough to induce a low-cycle fatigue catastrophic failure or an uncontrollable condition.

3.1.2.6 Miscellaneous

- Blade inertia and weight. Blade centrifugal force (function of mass x radius) must stay below allowable values (this is a go/no-go decision). Blade inertia (function of mass x radius²) is evaluated by means of an auto-rotation index.
- Vibrations and dynamics. Blade frequency placement and the effect on vibrations. The effect of pitch-link loads on vibrations. Minimum torsional stiffness criteria must be met.
- Handling qualities. Check for expanded flight envelope with new blade, control margins, and rigging constraints.

3.1.3 Inputs to Math Model

Table 1 shows the form used for the math model. For each factor it was only necessary to establish a value of r , and the balance of the process was merely multiplication and addition.

Wherever possible, the values of r were established by calculation. For example, in the performance category, the percentage increase in hover performance over production OH-58 blades was calculated for each configuration. The highest increase was given an r value of 4 and the lowest increase a value of 1. Intermediate increases were given interpolated values of r .

For some of the factors it was not possible to establish values of r quantitatively. It was necessary, therefore, to obtain qualitative assessments from the most knowledgeable people available.

TABLE 1. DESIGN TRADE-OFF MATH MODEL FOR OH-58 COMPOSITE
MAIN ROTOR BLADE

Category and Factors	k	r	kr	RΣkr
Life-Cycle Costs (R=6)				
Material Cost	.15			
Fabrication Cost	.50			
Tooling Cost	.10			
Retirement Life	.20			
Maintenance Cost	.05			
Sum kr			-	-
Performance (R=5)				
Hover	.50			
Forward Flight	.25			
Contour retention	.10			
Control Loads	.10			
Flying Qualities	.05			
Sum kr			-	
Reliability and Maintainability (R=4)				
Environmental Degradation	.10			
Ease and Effectiveness of Repair	.20			
Ease of Inspection	.15			
Quality Control (Mfg)	.10			
FOD Tolerance	.15			
Fail-Safety	.20			
Lightning Protection	.10			
Sum kr			-	
Radar Reflectivity (R=3)				
Material Characteristics	.45			
Erosion Protection Strip	.20			
Geometry	.35			
Sum kr			-	
Ballistic Survivability (R=2)				
Material Characteristics	.40			
Spar Design	.40			
Afterbody Design	.20			
Sum kr			-	
Miscellaneous (R=2)				
Blade Inertia and Weight	.50			
Vibration and Dynamics	.30			
Handling Qualities	.20			
Sum kr			-	-
Total R x sum kr				
The maximum theoretical score would result from an excellent rating (r=4) in all categories. For this case, the Σ(RΣkr) would be equal to 88; hence; we have:				
Normalized total				$\frac{\text{(Total)}}{88}$

3.2 DESIGN CONCEPTS

A number of composite rotor blade concepts were proposed during brainstorming sessions with Engineering Design and Manufacturing Engineering personnel. Sketches of the most promising design concepts were prepared and distributed to the applicable engineering groups and to Manufacturing Engineering for their initial evaluation. Typical are those shown in Figures 1 through 3. A summary of the blade concepts is listed in Table 2.

Many styles of blade afterbody construction were considered. They included a honeycomb panel type, full-depth core, multi-cell or tubular, and ribbed afterbodies. All but the tubular and full-depth core types were eliminated because of some undesirable characteristic. The tubular approach looked viable because it could build in a one-shot cure cycle and it eliminated the expensive core material and core machining process. Two types of core materials looked promising. They included carved Nomex honeycomb and foamed in-place core.

Three types of skin construction and four composite materials were considered viable candidates. They are listed in Table 2. The filament-wound and cloth skins were felt to have better impact resistance and FOD tolerance.

The materials considered for use for the trailing-edge strip were S-glass, Kevlar, and graphite. The latter two were considered because they would be lighter than a strip made of glass. This is good for blade section mass balance; however, it is more expensive.

Various types of spar construction were suggested. They included filament wound, pultruded, multitubular, pultruded half shell, and braided. Only the filament-wound approach survived early elimination because of its efficient root end attachment.

Glass and Kevlar were suggested for the spar torsion wrap. It was questionable as to whether an inner wrap was required. Steel, titanium, and urethane were proposed for the leading-edge abrasion strip. Metal offered the best abrasion resistance, however, radar reflectivity reduction would suffer.

Two types of root attachments were conceived. One approach used a single vertical attachment pin and upper and lower wrap-around lugs. The other approach required two horizontal pins, four wraparound lugs, and an additional metal fitting to adapt to the OH-58 hub.

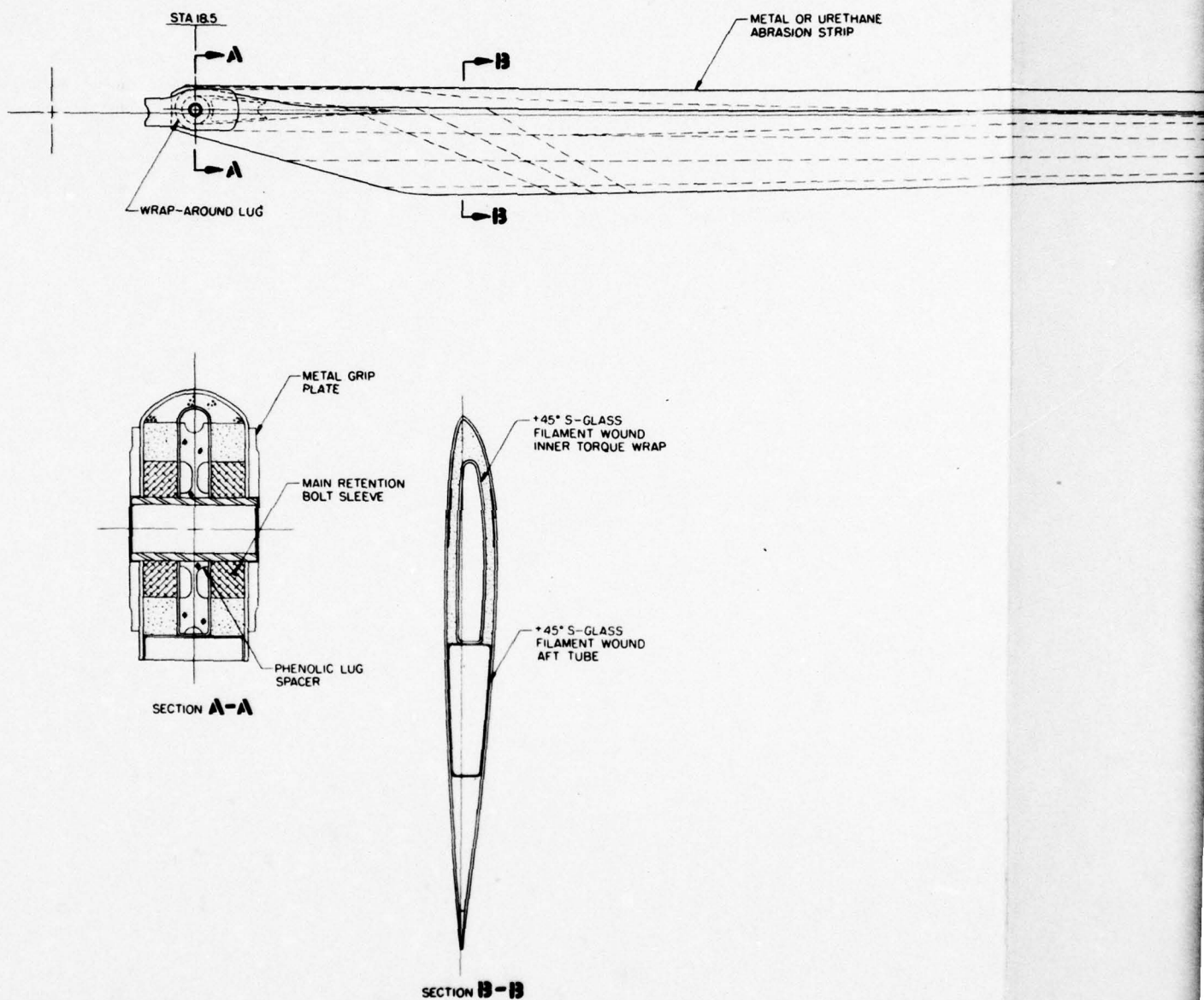
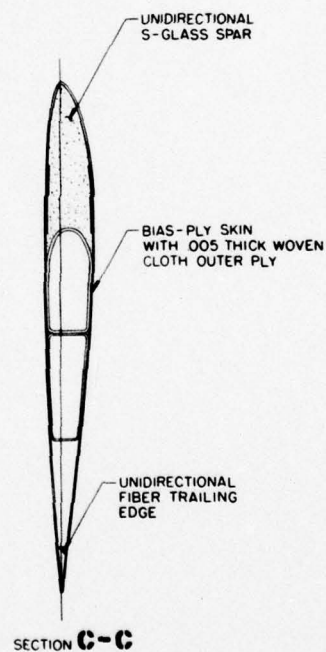
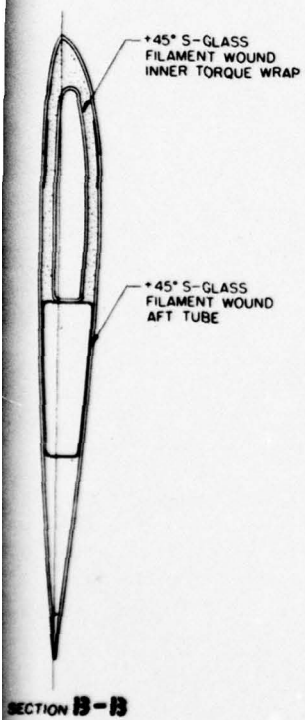
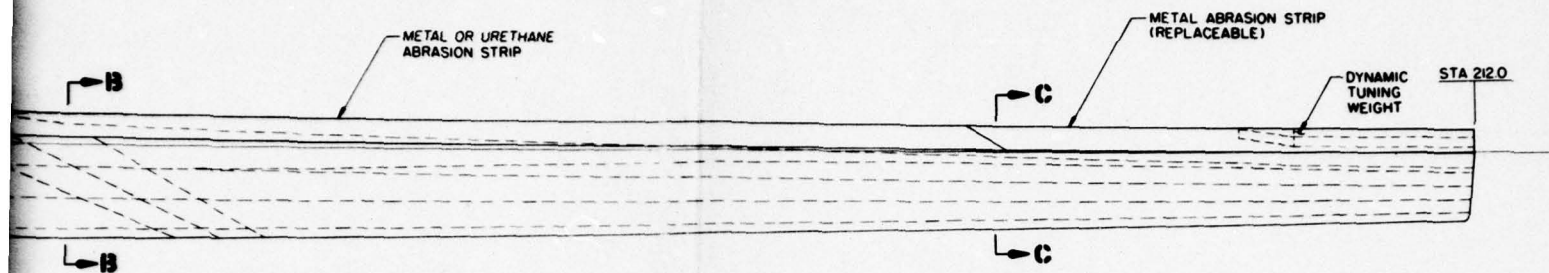
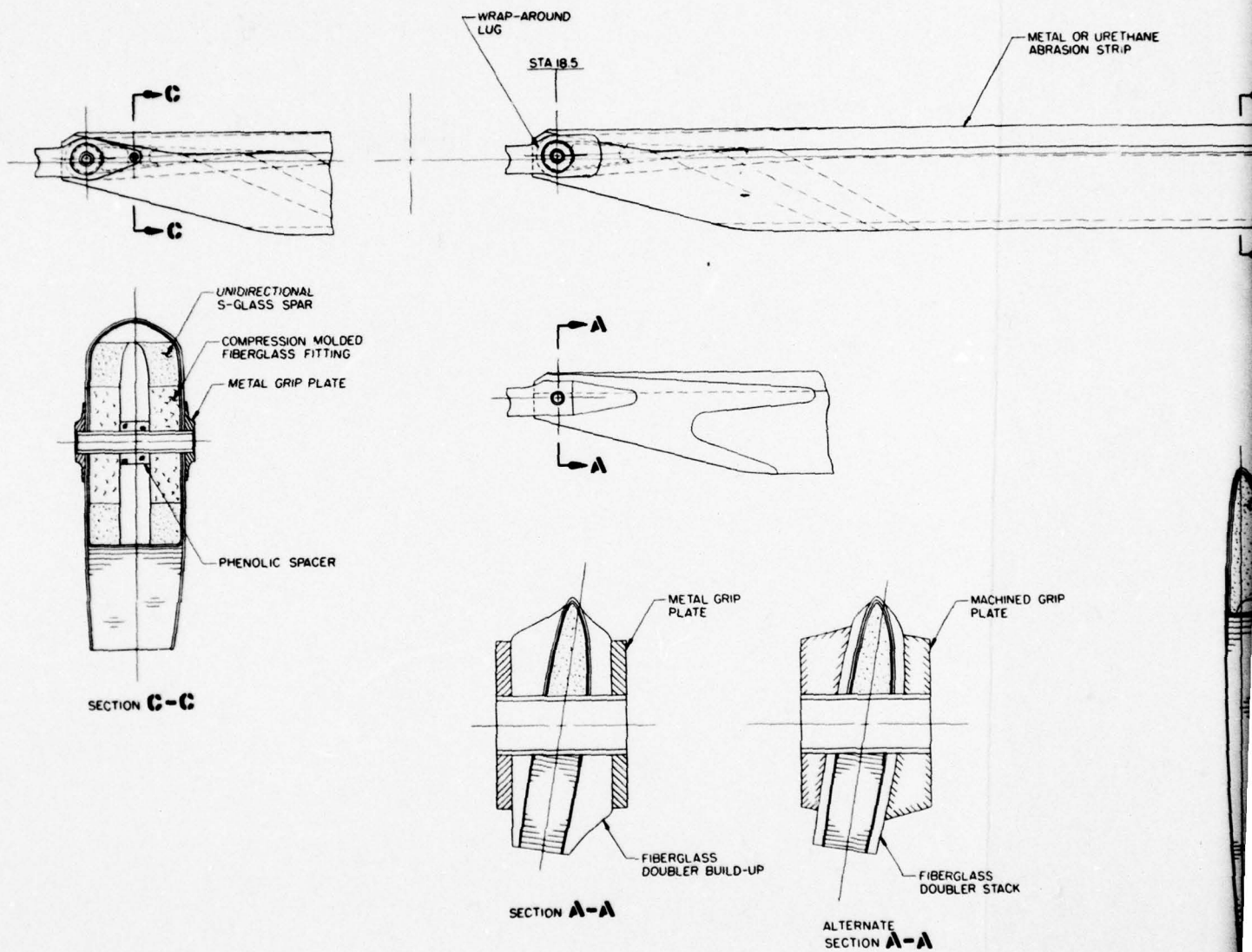
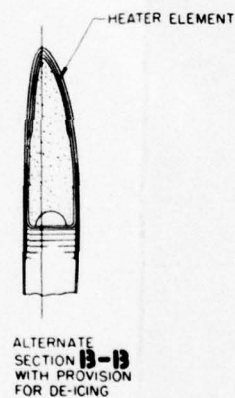
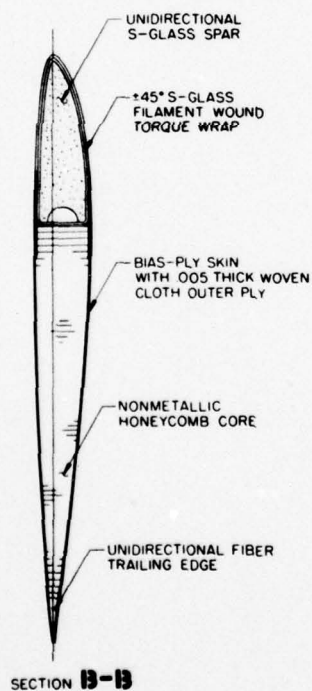
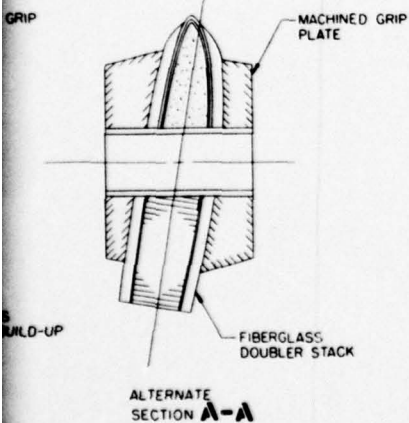
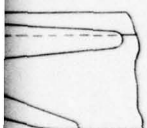
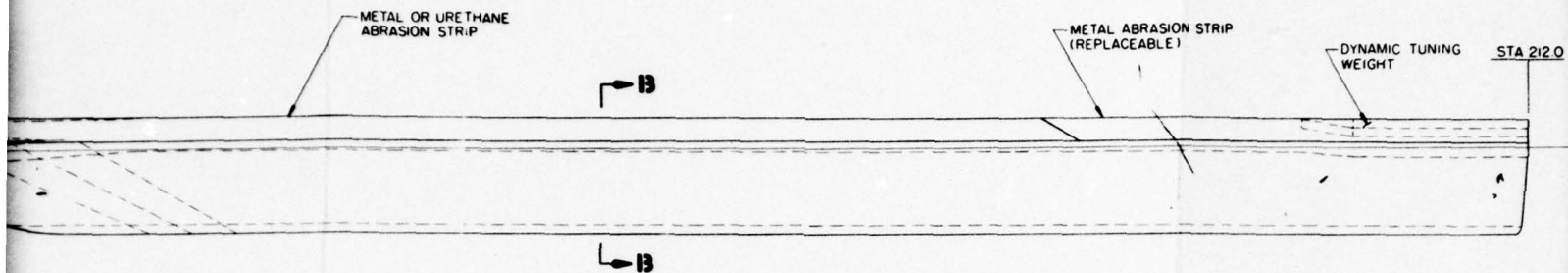


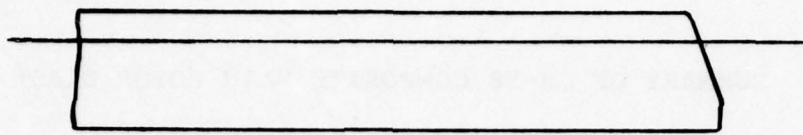
Figure 1. OH-58C/A composite main rotor blade tubular afterbody concept.



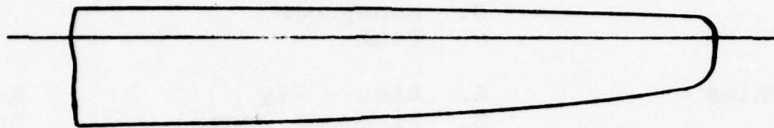
site main rotor
afterbody concept.



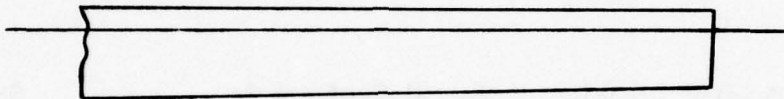




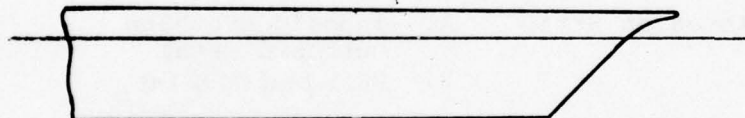
(a) Production OH-58 tip



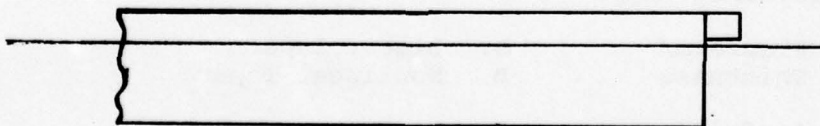
(b) Curved leading- and trailing-edge tip



(c) Linear taper tip



(d) Ogee tip



(e) Subwing tip

Figure 3. Typical tip shape design concepts.

TABLE 2. SUMMARY OF OH-58 COMPOSITE MAIN ROTOR BLADE CONCEPTS

<u>Component/Subsystem</u>	<u>Style</u>	<u>Material</u>
1. Afterbody		
a. Core	A. Tubular B. Honeycomb C. Foam	
b. Skins	A. Bias - Ply B. Filament Wound C. Cloth	S-Glass E-Glass Kevlar 49 Graphite
c. Trailing Edge	A. Solid	S-Glass Kevlar Graphite
2. Spar		
a. Unidirectional Material	A. C-Section to Solid	S-Glass
b. Wrap	A. Outer Wrap B. Inner Wrap	S-Glass E-Glass Kevlar
c. Abrasion Strip	A. Inboard Urethane Outboard Metal B. Full Length Metal	Urethane Steel Titanium
3. Root Attachment	A. Wraparound Lugs (Vertical) B. Two Horizontal Pins (4 Lugs)	
4. Aerodynamic Shape		
a. Planform/ Thickness	A. Linear Taper B. Nonlinear Taper	
b. Airfoils	A. VR-7 B. FX098 C. FX080	
c. Tip Shapes	A. Ogee B. Square C. Elliptical (Curved Leading and Trailing Edges)	

The complexity of the aerodynamic shape of the blade would be traded off with the cost of construction. Therefore, constant section, linear taper, and nonlinear taper were considered. Also, advanced airfoils and tip shapes were considered.

From the list of concepts and materials of Table 2, 10 blade configurations were selected as the most promising. These configurations are listed in Table 3. The letters A, B, and C represent the component/subsystem style listed in Table 2. The composite materials are coded A through D as listed in the top right-hand corner of this table.

The 10 concepts were subjected to a preliminary trade-off analysis using the math model described in Section 3.2. Appropriate personnel rated the concepts in their area of expertise. The results, after multiple ratings were averaged, are shown in Table 4. This exercise produced two different concepts superior to all the others. They were configuration number 2, the honeycomb afterbody concept, and number 9, the tubular afterbody concept. Configuration 6, although it ranks higher than 9, is very similar to configuration 2 except for planform shape and was therefore not considered a unique concept. Both blade designs were almost identical except for the afterbody portion of the blade. Both had the optimum aerodynamic shape and a wraparound vertical lug root attachment.

An in-depth trade-off analysis was performed on these two finalist candidates. Typical cross sections of the two blade concepts are shown in Figures 4 and 5. Included in the figures are the improvements made to the blades to obtain the highest scores possible. For instance, the abrasion strip was changed from titanium to urethane to reduce radar reflectivity. This, however, lowered the environmental resistance and erosion rating. The selected aerodynamic shape of the blade is shown in Figure 6.

3.3 TRADE-OFF ANALYSIS

The rationale for rating the design concepts will be presented by reviewing the trade-off math model of the two primary candidate configurations. They will be referred to as the honeycomb and tubular configurations. The math model is presented in Section 3.1.

TABLE 3. OH-58 COMPOSITE MAIN ROTOR BLADE CONFIGURATIONS

CONFIG		1. AFTERBODY				2. SPAR		3. ROOT		4. AERO		5. MATERIALS	BRIEF DESCRIPTION
		CORE	SKINS	TRAILING EDGE	UNI MATERIAL	WRAP	ABRASION STRIP	ATTACHMENT	PLANFORM/THICKNESS	AIRFOIL	TIP SHAPE		
1	A	A	A	A	A	A	A	A	A/C	A	Material	Tubular Concept All Glass, Ogee Tip	
2	B	B	A	A	A	A	A	A	A/B/C	C	Material	Honeycomb Concept Kevlar T. E., "H" Tip	
3	B	A	A	A	A	A	A	A	A	B	Material	Least Expensive Const. Section Square Tip	
4	C	B	A	A	A	A	A	B	A/C	A	Material	Foam Core, 4 Lug Attachment Kevlar T.E.	
5	A	B	A	A	A	B	A	B	A/B/C	C	Material	Tubular, 4 Lug Elliptical Tip	
6	B	A	A	A	A	A	A	A	B	B	Material	Honeycomb Core, All Glass Square Tip	
7	C	C	A	A	A	A	A	A	A/B/C	A	Material	Foam Core, Kevlar Cloth Skins, Kevlar T.E.	
8	A	B	A	A	A	A	A	B	A/C	C	Material	Tubular, Wound Skins Kevlar T.E., In- and-Out Star Web	
9	A	B	A	A	A	A	A	A	A/B/C	C	Material	Tubular, All Glass Vertical Lug, Curved Tip	
10	A	A	A	A	A	B	A	A	A/B/C	C	Material	Tubular, Vertical Lug Kevlar T.E., E-Glass Skins	

TABLE 4. OH-58 COMPOSITE MAIN ROTOR BLADE TRADE-OFF MATH MODEL SUMMARY

CATEGORY	CONFIGURATION NO.									
	1	2	3	4	5	6	7	8	9	10
Life-Cycle Costs	17.22	15.54	20.82	15.42	15.60	20.28	14.70	12.54	16.44	14.34
Performance	7.75	19.25	8.00	6.25	19.00	11.75	6.25	14.25	18.00	18.50
Reliability & Maintainability	10.32	12.68	12.40	10.36	10.40	12.28	10.20	10.40	10.88	10.44
Radar Reflectivity	5.82	9.32	7.08	6.57	6.57	8.57	7.41	5.97	6.27	6.72
Ballistic Survivability	4.72	5.68	5.48	6.52	4.84	5.48	6.24	6.20	6.36	4.40
Miscellaneous	6.40	6.74	6.74	4.74	6.06	6.74	4.74	6.40	6.06	6.40
Total R\$kr	52.59	68.69	60.52	49.86	62.47	65.10	49.54	55.76	64.01	60.35
Normalized Total	.60	.78	.69	.57	.71	.74	.56	.63	.73	.69
Rank	8	1	5	9	4	2	10	7	3	6

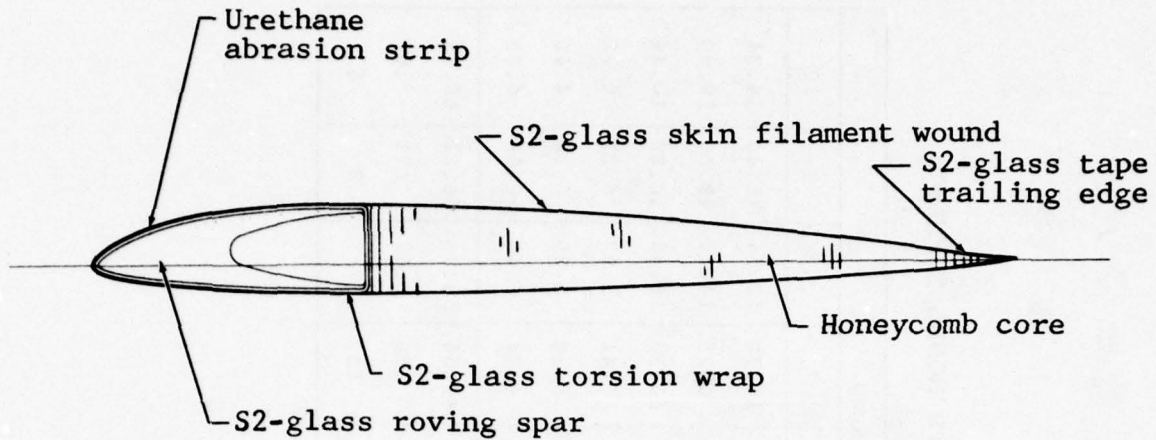


Figure 4. Typical cross section of honeycomb afterbody concept.

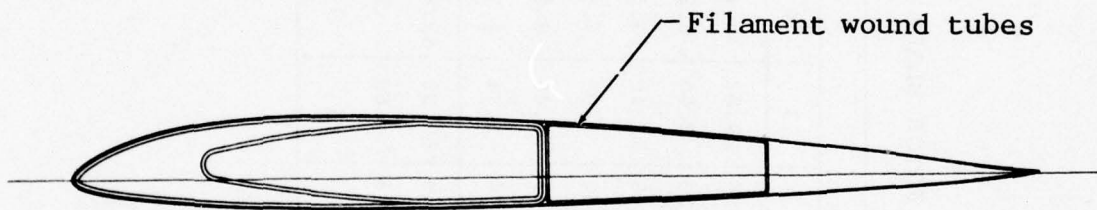


Figure 5. Typical cross section of tubular afterbody concept.

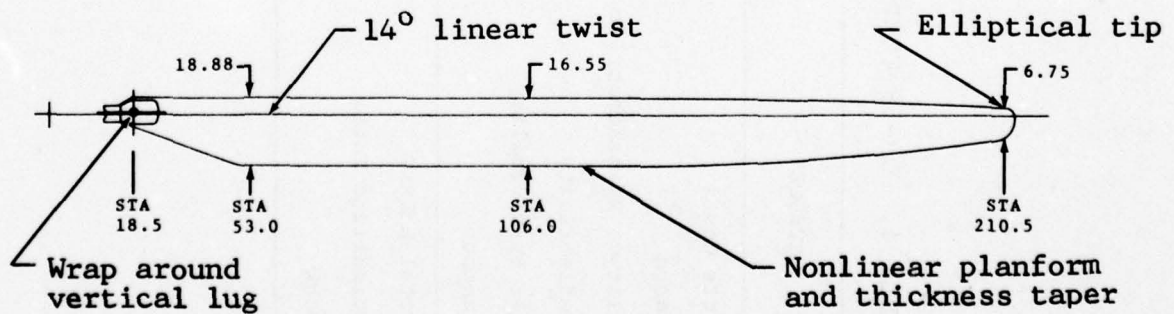


Figure 6. Recommended aerodynamic shape.

3.3.1 Life-Cycle Cost

3.3.1.1 Material Cost

Table 5 lists prices of the candidate composite materials used for this study. It also lists their respective densities, ultimate strength, fatigue strength, and tension modulus for comparison. Honeycomb was priced at \$67.08 per cubic foot.

TABLE 5. MATERIAL COST

	<u>Cost</u> <u>(\$/lb)</u>	<u>Density</u> <u>(pci)</u>	<u>F_{ult}</u> <u>(ksi)</u>	<u>F_{el}</u> <u>(ksi)</u>	<u>E</u> <u>(msi)</u>
S2-glass - Roving	9.64	.069	215	14.0	6.6
E-glass - Roving	7.45	.069	160	10.0	5.7
Kevlar 49 - Roving	29.00	.050	200	17.0	11.0
Graphite - Roving	51.80	.055	168	45.0	19.5
E-glass - Fabric	5.53	.069	45	5.0	3.1
Kevlar - Fabric	34.96	.050	60		3.3
Graphite - Fabric	58.18	.055	80	4.5	9.5

S2-glass was chosen as the primary structural composite material because of its good structural properties, and also because of its cost effectiveness over the other materials. Strength, moduli, density, and environmental resistance were evaluated versus cost.

The cost of materials for the honeycomb and the tubular concepts was estimated to be \$902 and \$812, respectively. Material costs for the 10 final concepts ranged from \$776 to \$1106. Interpolating between 4.0 and 1.0, the honeycomb concept was rated 2.85 while the tubular concept was rated 3.67.

3.3.1.2 Fabrication Cost

With the tubular blade, all blade curing operations could be performed in a single step since the pressurized afterbody tubes provide a reaction for pressure in the spar section. In the honeycomb blade, the edge of the honeycomb core would not provide sufficient reaction for the pressure in the spar. Therefore the honeycomb blade requires that the spar be cured prior to the main blade assembly operations. This single-step cure

procedure reduces the number of curing operations, thus providing minimum assembly costs. In the honeycomb blade another additional cure cycle is required to bond the core blanks to the lower skin. The cost of the core blank material and the cost of machining the core to contour increases the relative cost of the honeycomb blade concept when compared to the tubular concept. While there is some cost associated with the winding of the tubular components of the afterbody, these cost do not bring the tubular blade concept up to that of the honeycomb blade.

Fabrication labor costs were estimated to be \$530 more per blade for the honeycomb concept than for the tubular concept. However, it was Manufacturing Engineering's opinion that the cost objective of \$3400 per blade could be met, even with the additional labor cost of fabricating the honeycomb blade. The \$530 is a 16-percent difference in cost. It was rationalized that if the tubular concept is given a rating of 4.0, the honeycomb concept should be given a rating of 16 percent less, or $.84 \times 4 = 3.36$. It should be noted that it was also Manufacturing Engineering's opinion that there is considerably more technical risk involved in successfully manufacturing an acceptable blade using the tubular approach.

3.3.1.3 Tooling Cost

The tooling approach chosen is a full closed-die concept. This closed-die concept is required to obtain the close control over blade contour necessary to achieve the benefits of the advanced airfoils proposed for these blades. Another benefit of the closed die with internal pressure is the high quality of the laminate resulting from uniform pressure on the parts undergoing cure. The material chosen for the tools is steel. Steel tools provide stability and durability over aluminum tools and are a closer thermal match for the glass in the blade structure. No alternate concepts were considered.

Tooling costs for the tubular and honeycomb concepts are almost identical. Although the honeycomb concept requires an additional bond fixture, the tubular concept requires an additional winding fixture. Tooling costs for both concepts were rated 2.5.

3.3.1.4 Retirement Life

All indications show that the blades will have an unlimited fatigue life. This is based on the assumption that the blade loads will not change drastically and the stiffness distributions are similar. Thus, retirement life will depend on other factors such as susceptibility to damage and wear. Both concepts were given the same rating of 2.75.

3.3.2 Performance

3.3.2.1 Hover and Forward Flight

The choice of the aerodynamic shape is discussed in Appendix A of this report. The study resulted in the shape shown in Figure 6. The nonlinear planform is more costly than a rectangular or linear taper planform, but in order to meet the performance goals it is required. It also allows the use of a linear twist distribution except possibly near the tip. Both the honeycomb and tubular concepts, having the same optimum shapes, were given an excellent rating of 4.0.

3.3.2.2 Contour Retention

To maintain proper performance, the skins on the afterbody must support aerodynamic loads without excessive deformation of the airfoil contour. Honeycomb provides a nearly rigid backup for the skins. The tubular afterbody thickens the skins effectively in the forward cell and provides a shear tie at its rear to carry the loads with little deformation. The aft cell has lower airloads, and proper skin thickness should preclude excessive deflections. However, it is apparent that the honeycomb approach will retain the contour better at less weight than the tubular approach. Honeycomb was given a rating of 3.5, and the tubular concept received a rating of 2.0.

Foam was considered for core material and ideally it would be best; however, the technical data base is not presently at hand. It should be considered an alternate material for the honeycomb and, if it becomes available at reasonably low densities, substituted directly.

3.3.2.3 Control Loads

In the absence of a detailed description of the blade, the analysis of control loads is difficult. Proper mass balance, low torsional inertia, and a reasonable frequency placement are desirable features. The heavier afterbody concepts rate lower because of section cg placement. It also will increase torsional inertia, giving rise to higher propeller moments. The effects of torsional rigidity are also difficult to evaluate at this time because of differences in opinion-based separate studies. The honeycomb afterbody will be lighter, but possibly less stiff torsionally than the tubular afterbody. It was given a good rating of 3.0 and the tubular concept a rating of 2.0. The difference is based mainly on the lower weight aspect.

3.3.2.4 Flying Qualities

Both final design candidates will exhibit excellent flying qualities during hover and forward flight; however, the honeycomb blade with its lower weight afterbody will allow more weight to be placed at the tip of the blade. In this manner, a higher rotational inertia can be obtained at the same centrifugal force at the hub. This higher inertia will provide better autorotation characteristics for the honeycomb concept. It was rated 4.0 and the tubular concept 3.0.

3.3.3 Reliability and Maintainability

3.3.3.1 Environmental Degradation

Each design configuration was designed for:

- Effects of moisture on material physical properties
- Effects of temperature extreme
- Susceptibility to erosion damage
- Relative residual strength after exposure

The primary structural material chosen for the two finalists is S2-glass/epoxy. One reason for this choice was its good environmental resistance characteristics. E-glass/epoxy was considered to have less resistance to the environment. Both finalist concepts, being of the same material, were given a rating of 3.5.

3.3.3.2 Ease and Effectiveness of Repair

One of the prime goals of this program is that the selected blade have a high degree of field repairability. The possibility of using a foam core in the afterbody was rated highly in the evaluation since no preformed plugs would be required. Only preformed skin patches would be needed in repair kits. The Nomex core afterbody, easily repairable using preformed plugs, was rated only slightly lower. Configurations with the tubular afterbody construction were rated poor not only because of the lesser possibility of repair, but also because repair would be more difficult, even in cases where it is possible.

The incorporation of urethane abrasion strips in lieu of metal strips also enhances field repairability. The urethane strips can be easily replaced in the field on an "on-condition" basis and should exhibit good wear qualities except under prolonged use in heavy rain.

The honeycomb concept was rated 3.0. The tubular afterbody concept was rated 2.0.

3.3.3.3 Ease of Inspection

The honeycomb core afterbody is considered easiest to inspect in the field. Disbonds between the core and skin are easily detectable. The tubular afterbody has a structural bond in the shear web, which cannot be seen from the outside. The honeycomb configuration was rated 3.7, the tubular approach, 2.0.

3.3.3.4 Quality Control (Manufacturing)

The tubular configuration was given a slightly higher rating than the honeycomb design. It is inspected only once after its "one-shot" cure cycle, and there is access to the inside of the blade after removal of the mandrels allowing a more thorough inspection. However, the advantage of the honeycomb design is that subassemblies can be inspected for quality and weighed before final assembly, possibly avoiding entire blade scrappage. Ratings of 3.0 and 2.5 were given the tubular and honeycomb concepts, respectively.

3.3.3.5 FOD Tolerance

The major difference in susceptibility to foreign object damage for the two final concepts is in effective skin thickness. The tubular design has thicker skins over most of the afterbody. It was rated 3.4 and the honeycomb design 3.1.

3.3.3.6 Fail-Safety

The fail-safety aspects of the two final candidates are nearly the same except for the afterbody structure. The tubular approach has more redundant load paths for torsional and bending loads than does the honeycomb design. In event of a skin puncture or structural failure, the tubes will carry the loads and act as crack stoppers, suppressing further deterioration. The tubular and honeycomb concepts were rated 3.3 and 3.1, respectively. The two horizontal pin (four lugs) root attachment concept at first glance would appear to be more fail-safe than the two-lug arrangement. However, this design requires an additional metal adapter fitting that would release the entire blade in the event of failure. It was therefore eliminated because of this poor fail-safe and nonredundant characteristic.

3.3.3.7 Lightning Protection

The candidate blades will be covered with an aluminum mesh screen on the upper and lower surfaces. This screen has a dual purpose. It reduces radar signature and also allows a lightning strike to travel along the surface of the blade to the hub

and into the airframe structure. Lightning potentials flashing over the surface will prevent the composite matrix from vaporizing due to intense heat. Comparing the honeycomb and the tubular concepts, both are adequately protected. However, if lightning did enter the blade, the tubes would allow the flash to travel internally down the blade, possibly causing considerable damage. For this reason, the tube configuration was rated slightly lower at 3.0. Honeycomb rated 4.0.

3.3.4 Radar Reflectivity

3.3.4.1 Material Characteristics

In order to meet the reduced RCS goals, the abrasion strip must be nonmetallic. Also, additional radar cross section (RCS) reduction treatment must be applied. A formed sheet of radar absorbing material (RAM) will be embedded in the nose of the spar beneath the torsion wrap. This will reduce the signature from the front of the blade.

The trailing edge signature will be reduced by treating the aft 2 inches of the honeycomb core with radar absorptive material. This treatment is not possible with the tubular blade concept.

The upper and lower surfaces of the blades will be covered with aluminum screen mesh overlapping the treated areas slightly. This will allow radar energy to be reflected at an angle of incidence away from the source instead of entering the blade, being dispersed, and reflected back.

Looking into the trailing edge of the tubular blade, the best treatment would be to cover the surfaces with aluminum screen mesh and wrap around the trailing edge. This would give the composite blade the appearance of a metal blade. Without using a strip of treated core, this is probably the best procedure for utilizing this concept at a reasonable cost and weight.

Both the tubular and the honeycomb concepts require treatment to reduce the RCS and meet the goals of the program. However, the Nomex honeycomb material can be treated very easily at an acceptable weight at the trailing edge. The honeycomb concept was given an excellent rating of 4.0, the tubular a poor rating of 1.0.

3.3.4.2 Erosion Protection Strip

Both concepts have urethane erosion strips that are nearly transparent to radar. They were given a rating of 4.0.

3.3.4.3 Geometry

The external shape of both concepts are identical. They have curved leading and trailing edges and curved tip shape that will benefit the RCS by reducing peak return energy intensities. The candidate finalists were rated 3.5.

3.3.5 Ballistic Survivability

3.3.5.1 Material Characteristics

The two blade configurations chosen for detailed trade-off analysis use S2-glass/epoxy as the basic structural material. This material has relatively good impact resistance. To enhance this characteristic even more, the skin will be filament wound. The interwoven filaments will serve as crack stoppers to localize damage caused by ballistic impact. In addition, the unidirectional spar is filament wound with a +45-degree wrap minimizing impact damage. Since both the honeycomb and the tubular designs use the same material, they were both rated 3.1 for their material characteristics.

3.3.5.2 Spar Design

Ballistic tests of composite blades with spars of similar construction have shown very good damage tolerance to 7.62mm and 12.7mm projectiles. Aligned hits in the spar normally punch a small hole through the spar doing minimal damage. Fully tumbled projectiles are the most damaging hits, but in no case is it expected that failure will result. Aligned 23mm AP hits from some aspects could possibly cause failure, but tests of blade specimens will be required. The spars of both finalist configurations are similar and are rated 3.1.

3.3.5.3 Afterbody Design

Ballistic impacts into the afterbody of the honeycomb design will create holes that can be easily repaired. Impacts into the tubular afterbody design will cause slightly more apparent damage, be more difficult to repair, but less severe structurally because of its redundant attributes. The tubular afterbody was rated slightly more survivable, 3.5, than the honeycomb afterbody, 3.0, for that consideration.

3.3.6 Miscellaneous

3.3.6.1 Blade Inertia and Weight

The lightest concept (no tuning weight) will generally provide the greatest latitude in increasing rotational inertia. Nonstructural mass may be added near the tip to give the greatest increase in inertia for the smallest increase in

centrifugal force at the hub. This must be tempered by tuning considerations, but for this study the lightest blades will receive the highest score. Again, since the honeycomb afterbody is lightest and the remainder of the structure for the two final candidates are the same, it was rated highest. Honeycomb rated 3.3. Tubular rated 2.7.

3.3.6.2 Vibration and Dynamics

All of the blades can be designed to have very similar fan plots; as a result, they were ranked equally. All blades were given a score of 3.0.

3.3.6.3 Handling Qualities

Both finalists were rated excellent, or 4.0.

3.4 CONCEPT SELECTION

A summary of the math model inputs for the honeycomb concept and the tubular concept is shown in Tables 7 and 8. It shows the honeycomb afterbody concept to be a superior design.

Table 6 is a numerical summary of the trade-off, comparing the results by category. The tubular design is rated higher than the honeycomb design in material and fabrication costs but not as good in maintenance cost.

TABLE 6. TRADE-OFF SUMMARY

<u>Category</u>	<u>R_{ikr}</u>	
	<u>Configuration</u>	
	<u>Honeycomb</u>	<u>Tubular</u>
Life-Cycle Costs	18.24	20.70
Performance	19.25	17.75
Reliability and Maintainability	13.00	11.29
Radar Reflectivity	11.49	7.44
Ballistic Survivability	6.16	6.28
Miscellaneous	6.70	6.10
Total R _{ikr}	74.84	69.55
Normalized Total	.85	.79

TABLE 7. MATH MODEL FOR OH-58 COMPOSITE MAIN ROTOR BLADE
HONEYCOMB CONCEPT

Category and Factors	k	r	kr	REkr
Life-Cycle Cost (R=6)				
Material Cost	.15	2.85	.43	
Fabrication Cost	.50	3.36	1.68	
Tooling Cost	.10	2.50	.25	
Retirement Life	.20	2.75	.55	
Maintenance Cost	.05	2.50	.13	
Sum kr				3.04 x 6 = 18.24
Performance (R=5)				
Hover	.50	4.00	2.00	
Forward Flight	.25	4.00	1.00	
Contour Retention	.10	3.50	.35	
Control Loads	.10	3.00	.30	
Flying Qualities	.05	4.00	.20	
Sum kr				3.85 x 5 = 19.25
Reliability and Maintainability (R=4)				
Environmental Degradation	.10	3.50	.35	
Ease and Effectiveness of Repair	.20	3.00	.60	
Ease of Inspection	.15	3.70	.56	
Quality Control (Mfg)	.10	2.50	.25	
FOD Tolerance	.15	3.10	.47	
Fail-Safety	.20	3.10	.62	
Lightning Protection	.10	4.00	.40	
Sum kr				3.25 x 4 = 13.00
Radar Reflectivity (R=3)				
Material Characteristics	.45	4.00	1.80	
Erosion Protection Strip	.20	4.00	.80	
Geometry	.35	3.50	1.23	
Sum kr				3.83 x 3 = 11.49
Ballistic Survivability (R=2)				
Material Characteristics	.40	3.10	1.24	
Spar Design	.40	3.10	1.24	
Afterbody Design	.20	3.00	.60	
Sum kr				3.08 x 2 = 6.16
Miscellaneous (R=2)				
Blade Inertia and Weight	.5	3.30	1.65	
Vibration and Dynamics	.3	3.00	.90	
Handling Qualities	.2	4.00	.80	
Sum kr				3.35 x 2 = 6.70
Total R x sum kr				74.84
The maximum theoretical score would result from an excellent rating (r=4) in all categories. For this case, the $\Sigma(REkr)$ would be equal to 88; hence, we have:				
Normalized total				$\frac{(Total)}{88} = .85$

TABLE 8. MATH MODEL FOR OH-58 COMPOSITE MAIN ROTOR BLADE
TUBULAR CONCEPT

Category and Factors	k	r	kr	RΣkr
Life-Cycle Cost (R=6)				
Material Cost	.15	3.67	.55	
Fabrication Cost	.50	4.00	2.00	
Tooling Cost	.10	2.50	.25	
Retirement Life	.20	2.75	.55	
Maintenance Cost	.05	2.00	.10	
Sum kr				3.45 x 6 = 20.70
Performance (R=5)				
Hover	.50	4.00	2.00	
Forward Flight	.25	4.00	1.00	
Contour Retention	.10	2.00	.20	
Control Loads	.10	2.00	.20	
Flying Qualities	.05	3.00	.15	
Sum kr				3.55 x 5 = 17.75
Reliability and Maintainability (R=4)				
Environmental Degradation	.10	3.50	.35	
Ease and Effectiveness of Repair	.20	2.00	.40	
Ease of Inspection	.15	2.00	.30	
Quality Control (Mfg)	.10	3.00	.30	
FOD Tolerance	.15	3.40	.51	
Fail-Safety	.20	3.30	.66	
Lightning Protection	.10	3.00	.30	
Sum kr				2.82 x 4 = 11.29
Radar Reflectivity (R=3)				
Material Characteristics	.45	1.00	.45	
Erosion Protection Strip	.20	4.00	.80	
Geometry	.35	3.50	1.23	
Sum kr				2.48 x 3 = 7.44
Ballistic Survivability (R=2)				
Material Characteristics	.40	3.1	1.24	
Spar Design	.40	3.1	1.24	
Afterbody Design	.20	3.5	.70	
Sum kr				3.14 x 2 = 6.28
Miscellaneous (R=2)				
Blade Inertia and Weight	.5	2.70	1.35	
Vibration and Dynamics	.3	3.00	.90	
Handling Qualities	.2	4.00	.80	
Sum kr				3.05 x 2 = 6.10
Total R x sum kr				69.55
The maximum theoretical score would result from an excellent rating (r=4) in all categories. For this case, the Σ(RΣkr) would be equal to 88; hence, we have:				
Normalized total				$\frac{(Total)}{88} = .79$

The honeycomb concept is better in performance because of its good contour retention, lower control loads, and better autorotational characteristics. It also rated higher for reliability and maintainability considerations because of its ease and effectiveness of repair, ease of inspection in the field, and better lightning protection. However, the tubular design had slightly better quality control aspects, FOD tolerance, and fail-safety characteristics.

The largest difference in rating is shown for radar reflectivity. The honeycomb concept can more easily be treated to meet the RCS reduction goals. The tubular concept is more difficult to treat in the trailing-edge area.

The tubular afterbody design is considered more survivable from ballistic impact; however, the afterbody with the Nomex honeycomb core is easier to repair.

The honeycomb blade concept with its lighter afterbody allows maximum rotational inertia for improved autorotational characteristics, minimizing height-velocity restrictions.

Both final design candidates have significant attributes and neither is an overwhelming winner. However, the honeycomb concept can more easily meet all of the goals set forth for this program and was chosen to be pursued further during Task II, Preliminary Design and Analysis.

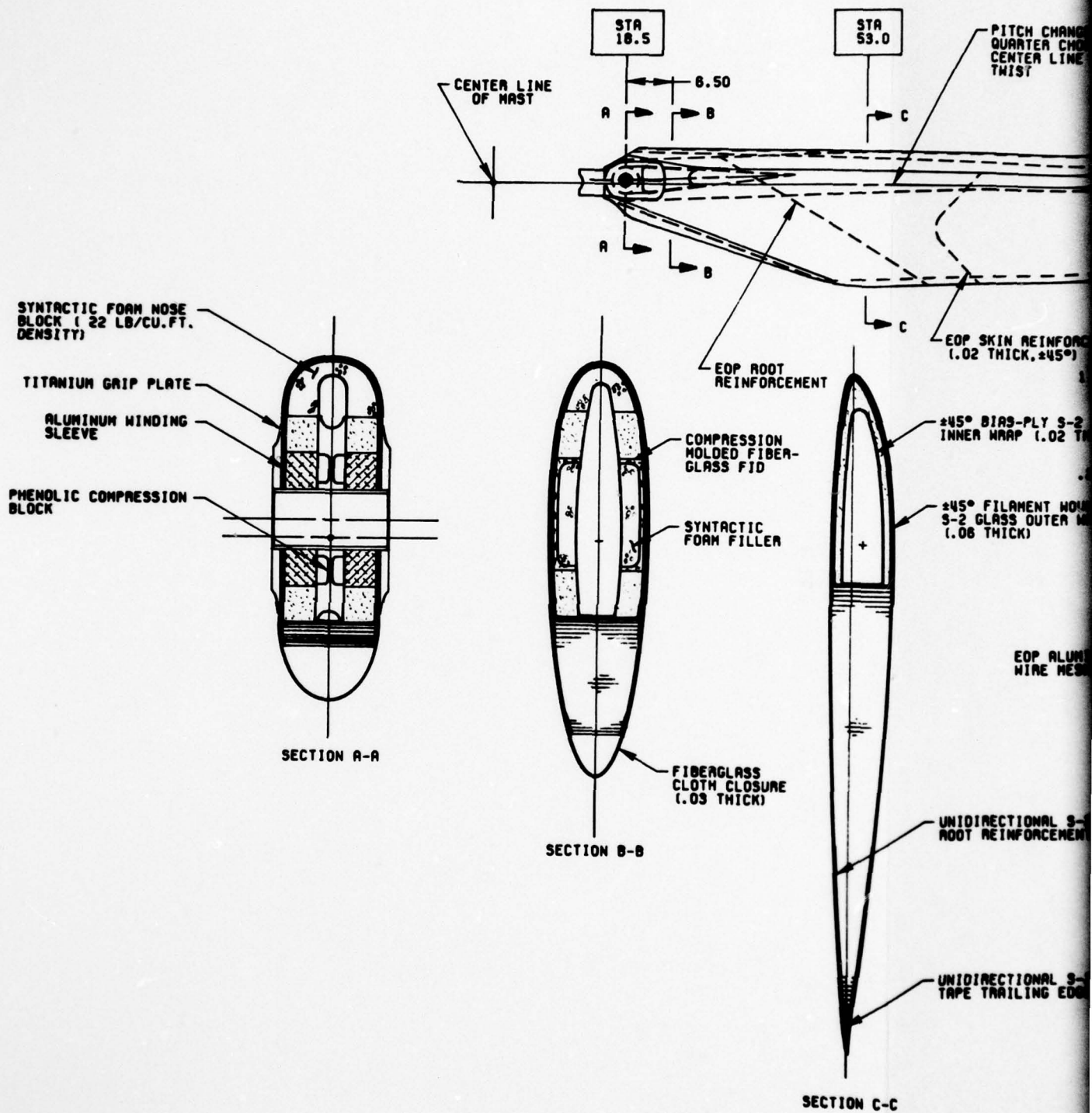
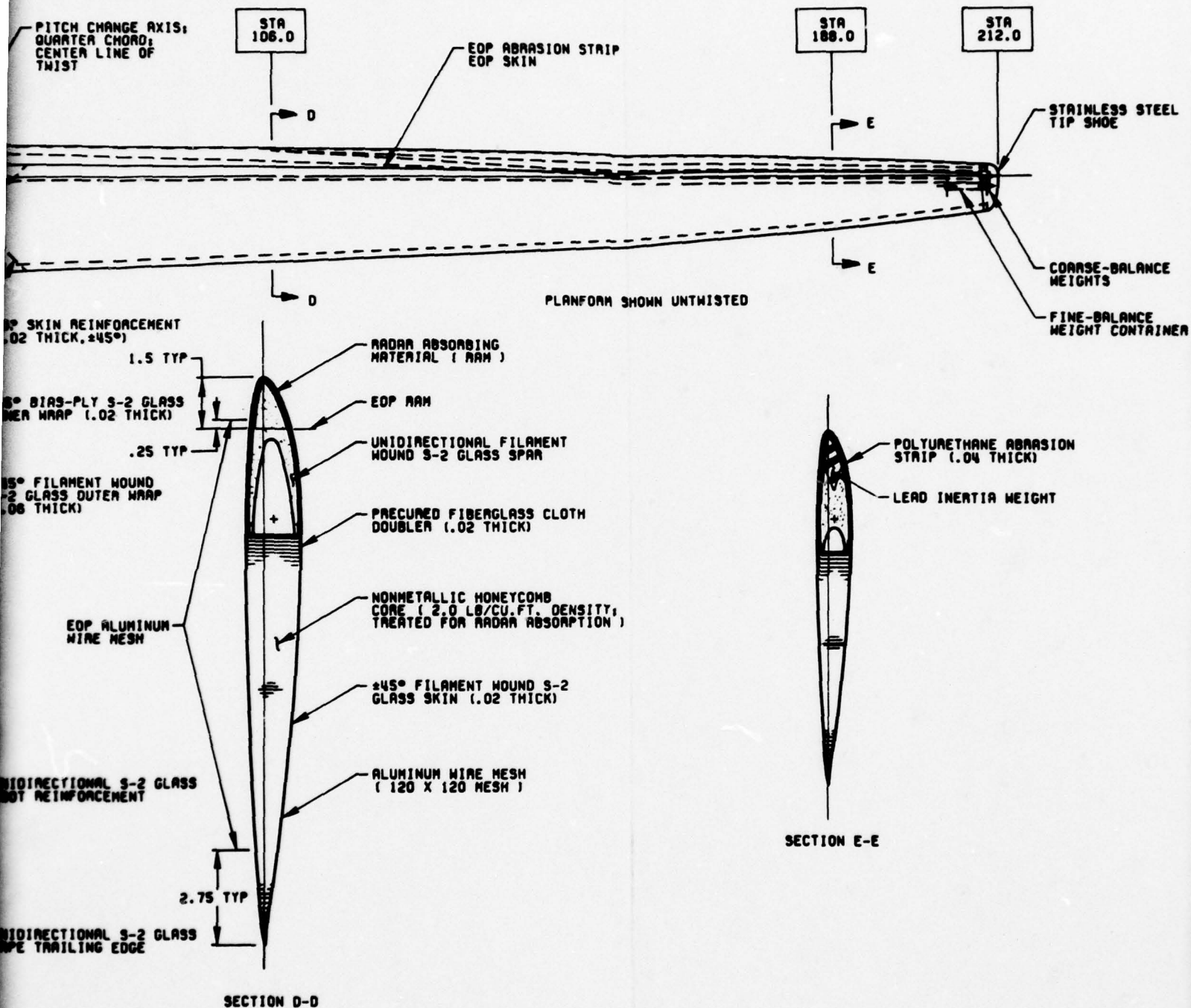


Figure 7. OH-58 composite main rotor blade.



4. PRELIMINARY DESIGN AND ANALYSIS

4.1 ROTOR BLADE DESIGN

The proposed OH-58A/C main rotor blade achieves the required objectives of improved aerodynamic performance, reliability, and maintainability at minimum cost. It is constructed primarily of fiberglass and is inherently tolerant of ballistic strikes, tree strikes, and other foreign object damage. It has a nonlinear twist distribution and a nonlinear chordwise taper from root to tip for more efficient aerodynamic performance.

The technology developed during the Model 214 and Model 654 fiberglass blade program at BHT will be used in the OH-58C/A blade. Many of its composite parts will be made by machine, thereby achieving low cost and repeatable physical characteristics. The blade can be fabricated from preimpregnated rovings or by the wet filament-winding process.

4.1.1 Geometry

The rotor blade designed during this investigation is 35.33 feet in diameter and has a nonlinearly tapered chord width. The root end of the blade is shaped so that the entire blade structure is contained within the airfoil shape. Flats are incorporated into the basic root airfoil shape to make the blade compatible with the existing hub grip. The root section transitions smoothly at the 25-percent radius into a 9.8-percent-thick FX69-H-098 airfoil, which is held constant to the tip. The tip planform is a semielliptical shape with the leading edge tangent to the basic blade leading and trailing edges at Station 210.4 ($r/R = 0.9925$).

The overall blade twist is nonlinear; however, the twist from 25-percent radius to the tip is linear. Root flats are oriented for correct pitch rigging on the existing OH-58 hub and control system. The twist transitions smoothly from the root to 25-percent radius.

4.1.2 Blade Construction

Figure 7 shows a layout of the blades with sections taken at significant points along the span.

The primary structural component in the blade is the spar, consisting of spar caps, sleeves, fids, torque wraps, nose block, inertia weights, and radar-absorbing material. The spar caps are the primary structural elements of the spar. They are composed of spanwise-oriented unidirectional S-2 glass fibers in an epoxy matrix. These fibers are wrapped

around the main bolt sleeve to form an integral attachment to the hub. Stress concentrations require the spar to have more material around the main bolt than in the basic blade. This additional material is built up during the filament-winding operation by interleaving reinforcement packs in the lug area of each spar cap. Fids made of compression-molded fiberglass/epoxy and syntactic foam fill the open areas in the inboard end of the spar caps where the fibers divide to wrap around the sleeve. These fids carry the compression loads that occur in the straps when the rotor is in static droop. The inner torque wrap is a ply of E-glass cloth that overlaps itself at the spar web. The outer wrap is a filament-wound tube of ± 45 -degree S-2 glass/epoxy. These wraps provide torsional stiffness and shear continuity and create a ballistically tolerant box structure. A structural nose block made of syntactic foam fills the forward part of the spar cavity from Station 53.0 to the root. This block maintains airfoil contour definition during the spar curing operation. Rotational inertia and blade natural frequency placement is achieved with a 24-pound lead weight in the tip area. The weight is made in several pieces and bonded in place during the spar cure operation to form an integral unit. Film-type adhesive is used between the weight and the fiberglass. Sufficient bond area is provided to retain the weight under all operating conditions. Redundant retention is achieved by the taper in the weight, which is larger in the middle than at the tip. The taper serves as a mechanical means of retention if the bond should fail. The inboard end of the weight is tapered to a thin section for blade tuning and also to gradually distribute its centrifugal load into the unidirectional fiberglass.

Low radar signature is achieved by treating both the spar and the afterbody with radar-absorbing material (RAM). The spar treatment consists of imbedding a strip of ferrite/epoxy material in the spar between the outer torque wrap and the inertia weight and spar caps. The strip wraps around the nose and extends 1.5 inches chordwise. This effectively hides the inertia weight and spar structure aft of the weight from oncoming radar.

Blade deicing is provided by an electrothermal deicing system. The heater element or deicing blanket is a thin strip .015 inch thick. It consists of an etched circuit bonded to a single ply of fiberglass cloth. The blanket is installed between the abrasion strip and the outer torque wrap as shown in Figure 8. The blanket, being an excellent conductor, gives a high radar signature, thereby negating the effect of the radar-absorbing material inside the spar. The RAM is therefore left out of the spar assembly during manufacture to provide space for the deicing blanket.

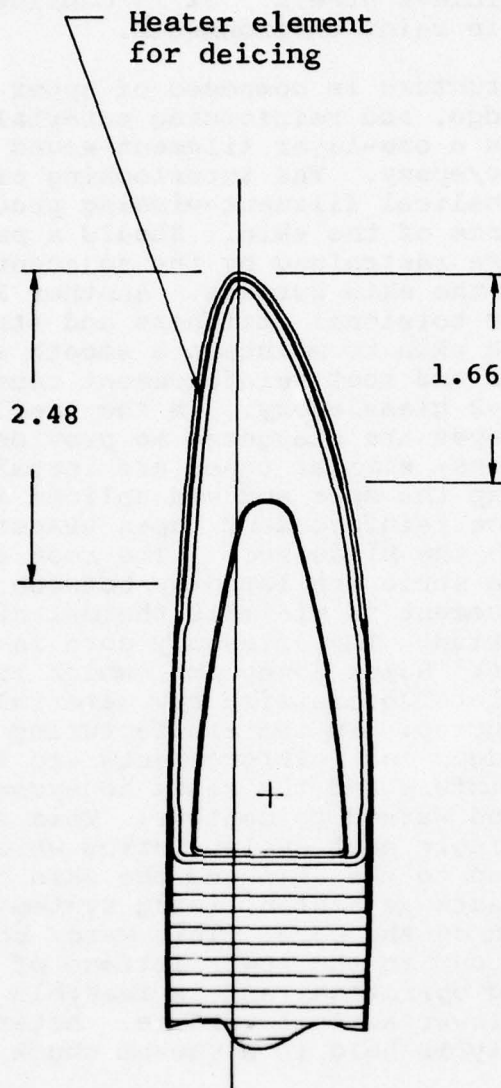


Figure 8. Blade deicing system.

Erosion protection for the blade is provided by a full-length urethane abrasion strip. Urethane was chosen because of the low radar reflectivity objectives. It is a low-cost, easily formed material and its erosion protection in sand is better than that of stainless steels. It is considered to be adequate for limited use in rainy environments.

The afterbody structure is composed of upper and lower skins, core, trailing edge, and reinforcing material where needed. The basic skin is a one-layer filament-wound part of ± 45 degrees S-2 glass/epoxy. The interlocking of fibers, characteristic of the helical filament-winding process, increases the ballistic tolerance of the skin. Should a puncture occur, the damaged fibers are restrained by the adjacent fibers from stripping out of the skin surface. Another layer of skin is added inboard for torsional stiffness and strength. It lies beneath the basic skin to maintain a smooth airfoil surface. The trailing edge and root reinforcement consist of tapes of unidirectional S-2 glass/epoxy. In the trailing edge, the lengths of the tapes are staggered to provide the required chordwise stiffness; similar tapes are installed in the root end. They overlap the spar and are spliced into the trailing edge strip. These reinforcement tapes transfer the chordwise bonding load into the blade root. The root reinforcement and the trailing-edge strip are layed-up between the basic skin and the skin reinforcement to minimize thermal distortion due to the curing operation. The afterbody core is made from 3/16-inch cell, 2-lb/ft³ Nomex honeycomb, which is procured in wedge-shaped billets to minimize raw material requirements through reduced scrap. In the manufacturing process, the lower skin, trailing edge, and reinforcements are layed-up, uncured, in a contoured fixture and the Nomex honeycomb material is placed over it and warped to contour. This assembly is then subjected to a single heat cycle, during which the wedge-shaped billets are bonded to the skin and the skin cured at the same time. The skin acts as a stabilizing system for the subsequent carving operation on the core. This warp/ bonding operation produces the contour in the lower surface of the core, avoiding a machine carving operation, and is feasible because of the relatively flat lower airfoil surface. After curing, the skin/core assembly is held in a vacuum chuck to carve the upper surface.

Bridges composed of two plies of E-glass cloth are installed between the skin and core at the leading edge of the core. They bridge the gap between the core and the spar and increase the shear continuity from the afterbody to the spar. The bridges are precured detail parts. The lower bridge is installed in the layup of the lower skin and core assembly. The upper bridge is installed during final blade assembly.

Radar considerations for the afterbody include treatment of the core and the skins prior to bonding. The core billets are dipped in a solution that deposits a film of radar-absorbing material on the cell walls. The treatment extends from the trailing edge forward 3 inches. The RAM is compatible with the resin system in the blade and does not cause weakened bond lines. Treatment for the skins consists of applying a 120-mesh aluminum screen to the outer surfaces of the airfoil. The screen overlaps the RAM in the spar and the treatment in the core. The screen wire provides lightning protection for the conductive RAM, reflects radar, and makes the skins more resistant to handling damage.

Titanium grip plates are bonded to the upper and lower surfaces of the blade root to transfer chord bending moments into the hub. Titanium was chosen because of its excellent fatigue characteristics, and because it is more strain compatible with fiberglass than steel.

After the blade has been trimmed to length at the root, a phenolic compression block is installed between the upper and lower fiberglass lugs to carry the compression due to blade-bolt torque.

Trimming the root structure to achieve the proper planform exposes the spar cavity and afterbody. To protect these elements, a precured fiberglass/epoxy closure is installed. This part is contoured to provide an aerodynamic fairing in the root and transition areas.

The tip of the blade is protected by a stainless steel cap to prevent local erosion at the tip and to house the tip balance package. The tip cap has curved surfaces for noise reduction, low drag, and radar reflectivity. It is produced by stamping and welding with the final contour achieved by a high-energy electrohydraulic-forming operation.

Balance weights are added to the blade in two places at the tip. Weights are attached to studs imbedded in the spar and the hollow aluminum casting, which is attached to the aft wall of the spar. The casting houses steel shot, which is used for final balance of the blades after a tip cap installation. The coarse balance weights are attached prior to installing the tip cap.

4.1.3 Weight and Balance

The weight of the improved blade was derived by calculating the volume of the detail parts and multiplying by their respective densities. These densities are listed in Table 9 along with the material specifications for the components.

TABLE 9. MATERIAL SPECIFICATION AND DENSITY

<u>Material</u>	<u>Specification</u>	<u>Density</u>
Adhesive	299-947-121 (Supported)	.00042 lb/in. ²
Adhesive	299-947-121 (Unsupported)	.00021 lb/in. ²
Aluminum Alloy	356	.100 lb/in. ³
Glass Fabric	299-947-076	.058 lb/in. ³
Lead Alloy	AMS 7721	.390 lb/in. ³
Molded Fiberglass	MIL-P-46069	.072 lb/in. ³
Nomex	299-947-103	2.0 lb/ft ³
Phenolic	General Purpose	.050 lb/in. ³
Polyurethane	Tuftane TF310	.043 lb/in. ³
S2-Glass	299-947-134C1	.069 lb/in. ³
Stainless Steel	CRES 321	.282 lb/in. ³
Steel	Alloy 4140	.283 lb/in. ³
Syntactic Foam	Dapcocast 3050	22.0 lb/ft ³
Titanium	MIL-T-9046	.160 lb/in. ³

Weights by functional component of the blade are listed in Table 10. The dimensions used in the calculations are from the layout drawing, Figure 7. The total calculated minimum weight of one blade assembly (without balance weights) is 68.8 pounds. With the average balance weights, the blade weight is 94.3 pounds. By comparison, the current metal master blade weight is 94.8 ± 1.0 pound. It is therefore anticipated that the improved blade will have the same weight as the standard blade.

TABLE 10. MATERIAL AND WEIGHT OF BLADE COMPONENTS

<u>Component</u>	<u>Material</u>	<u>Component</u>
SPAR		75.3
Unidirectional filament-wound S2-Glass	32.5	
Foam (Dapcocast 3050)	1.5	
Aluminum winding sleeve	1.6	
Phenolic compression block	.5	
Titanium grip plates	3.3	
Molded fiberglass fid	.9	
±45° filament-wound S2-Glass outer wrap	10.0	
Lead-inertia weight	25.0	
Afterbody		13.3
S2-Glass root reinforcement (.02 thick)	.9	
S2-Glass root trailing edge (.04 thick)	3.7	
S2-Glass trailing edge (0.2 thick)	5.2	
S2-Glass trailing edge strip (.01 thick)	.2	
299-947-076 cloth bridge (.02 thick)	.6	
Nomex Core	2.7	
Tip Closure		.2
Steel tip shoe	.2	
Root Closure		.3
299-947-076 cloth	.3	
Sleeves		.4
Steel blade bolt	.4	
Abrasion Strip		1.8
Polyurethane leading-edge strip	1.8	

TABLE 10. (Concluded)

<u>Component</u>	<u>Material</u>	<u>Component</u>
Adhesive		2.5
299-947-121	2.5	
Coarse and Fine Balance Weights		.5
Steel	.5	
TOTAL WEIGHT		94.3
	94.3	

4.2 PERFORMANCE AND HANDLING QUALITIES

4.2.1 Rotor and Helicopter Performance

The primary performance objective of the improved OH-58C/A rotor program was achieved. Hover performance at 3200 pounds gross weight, 4000 feet, 95°F design point and using a T63-A-720 engine was improved by 6.3 percent.

The final planform is unchanged from that defined in Task I. Table 11 shows a schematic of the planform and lists the coordinates that define the planform taper.

The blade has a geometric twist of 14 degrees and is faired to the grip in order to utilize the control rigging of the OH-58A. Figure 9 defines the geometric pitch of the blade and compares it to that of the baseline.

The airfoil selected for the improved OH-58C is the FX69-H-098; an airfoil profile and corresponding coordinates are shown in Table 12.

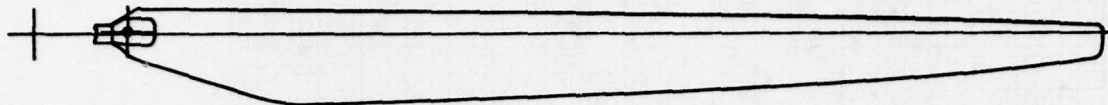
Forward flight performance improvements were also achieved as a result of the basic design philosophy used. The predicted forward flight characteristics of the improved rotor are conservative as discussed in Section A-4, Appendix A.

4.2.1.1 Improved OH-58C Benefits

The following figures illustrate by detail comparison the benefits derived by utilizing the improved composite rotor for the OH-58C helicopter.

Figure 10 shows hover power, out of ground effect (OGE), and minimum power required. At an operating weight empty (OWE) of 2400 pounds and a design point of 3200 pounds, hover performance improvements of 4.5 and 6.3 percent, respectively, were demonstrated (see Figure A-11). Also, growth potential is evident with a 7.3-percent improvement in hover performance indicated at 3600 pounds gross weight.

TABLE 11. IMPROVED OH-58 A/C PLANFORM SHAPE DATA



% Radius (-)	Station (-)	.25 Chord (in.)	Chord (in.)
0	0.0	5.250	21.0
5	10.6	5.14724	20.5889
10	21.2	5.04389	20.1755
15	31.8	4.93947	19.7579
20	42.4	4.83353	19.3341
25	53.0	4.72562	18.9025
30	63.6	4.61526	18.4610
35	74.2	4.50201	18.0080
40	84.8	4.38550	17.5420
45	95.4	4.26535	17.0614
50	106.0	4.14050	16.5620
52.5	111.3	4.07556	16.3023
55	116.6	4.00830	16.0332
57.5	121.9	3.93826	15.75303
60	127.2	3.86500	15.45999
62.5	132.5	3.78804	15.15215
65	137.8	3.70679	14.82716
67.5	143.1	3.62064	14.48256
70	148.4	3.52898	14.11595
72.5	153.7	3.43125	13.72499
75	159.0	3.32658	13.30635
77.5	164.3	3.21400	12.85603
80	169.6	3.09220	12.36899
82.5	174.9	2.96009	11.84035
85	180.2	2.81631	11.26524
87.5	185.5	2.65955	10.63823
90	190.8	2.48808	9.95232
92.5	196.1	2.30000	9.20000
95	201.4	2.09300	8.37199
97.5	206.7	1.86475	7.45899
100	212.0	1.61301	6.45204

Tip Starts at Sta 210.3875

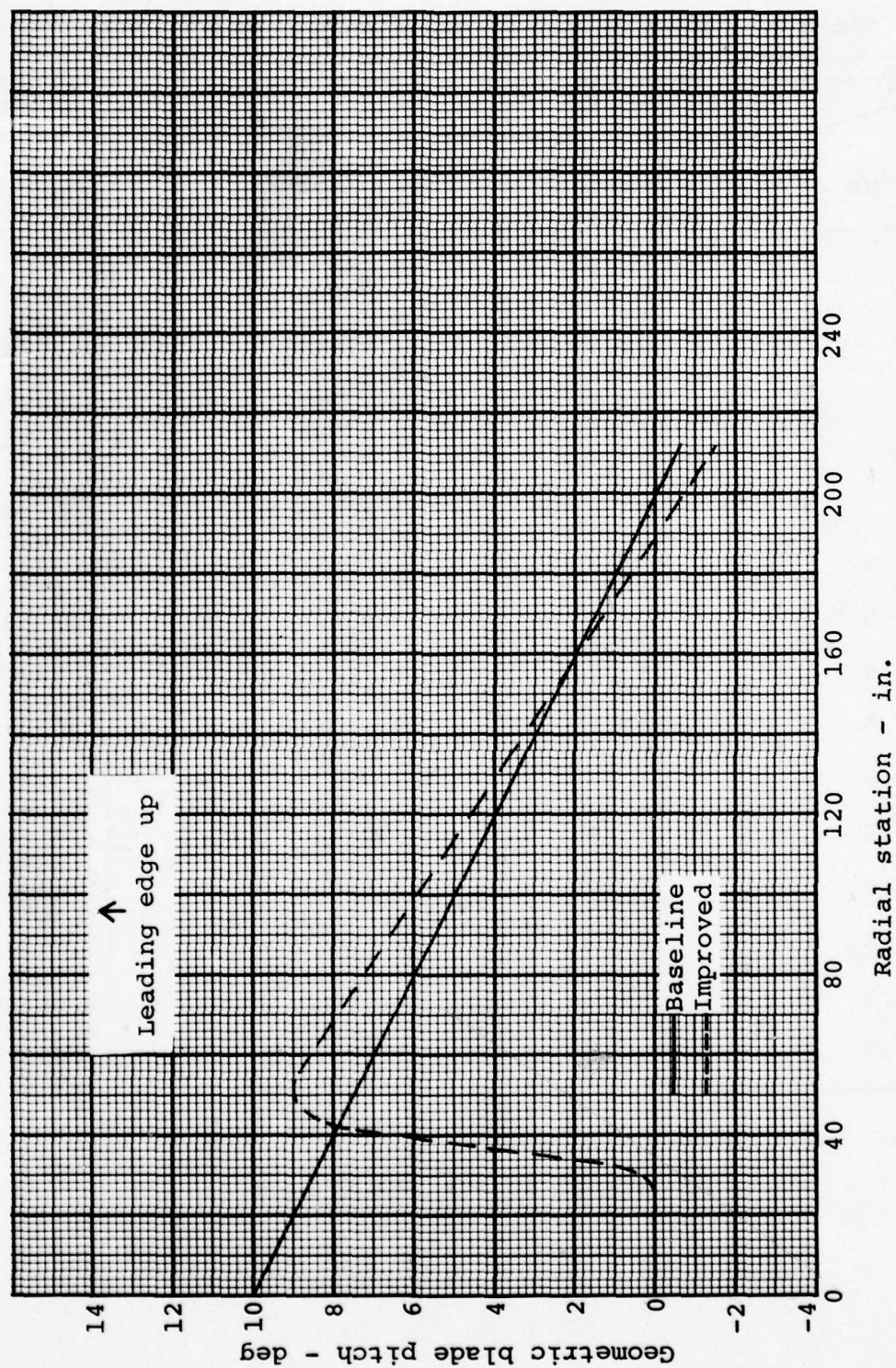
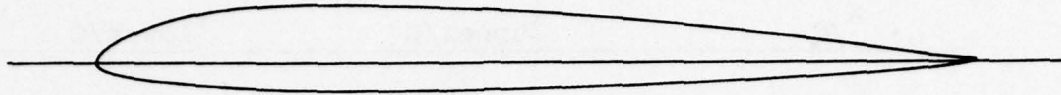


Figure 9. Improved and baseline OH-58C geometric twist distribution.

TABLE 12. COORDINATES OF THE FX69-H-098 AIRFOIL
WITH TRAILING EDGE REFLEX



x/c	y_{upper}/c	y_{lower}/c
0.0	0.0	0.0
0.00107	0.00458	-0.00332
0.00428	0.00948	-0.00645
0.00961	0.01468	-0.00938
0.01704	0.02016	-0.01210
0.02654	0.02585	-0.01460
0.03806	0.03165	-0.01690
0.05156	0.03743	-0.01902
0.06699	0.04300	-0.02097
0.08427	0.04818	-0.02280
0.10332	0.05281	-0.02452
0.12408	0.05676	-0.02614
0.14645	0.05997	-0.02763
0.17033	0.06244	-0.02896
0.19562	0.06422	-0.03010
0.22222	0.06539	-0.03099
0.25000	0.06598	-0.03163
0.27886	0.06599	-0.03201
0.30866	0.06557	-0.03215
0.33928	0.06480	-0.03206
0.37059	0.06374	-0.03179
0.40246	0.06244	-0.03138
0.43474	0.06090	-0.03086
0.46730	0.05913	-0.03021
0.50000	0.05712	-0.02946
0.53270	0.05487	-0.02858
0.56526	0.05238	-0.02758
0.59755	0.04966	-0.02648
0.62941	0.04675	-0.02527
0.66072	0.04369	-0.02399
0.69134	0.04055	-0.02265
0.72114	0.03735	-0.02127
0.75000	0.03414	-0.01985
0.77779	0.03097	-0.01838
0.80438	0.02781	-0.01690
0.82967	0.02462	-0.01541

TABLE 12. (Concluded)

x/c	y_{upper}/c	y_{lower}/c
0.85355	0.02143	-0.01393
0.87592	0.01826	-0.01246
0.89668	0.01520	-0.01100
0.91573	0.01233	-0.00954
0.93301	0.00973	-0.00808
0.94844	0.00763	-0.00661
0.96194	0.00605	-0.00509
0.97346	0.00489	-0.00358
0.98296	0.00407	-0.00212
0.99039	0.00351	-0.00083
0.99572	0.00316	0.00020
0.99893	0.00296	0.00086
1.00000	0.00291	0.00109

Leading edge radius - .0055c

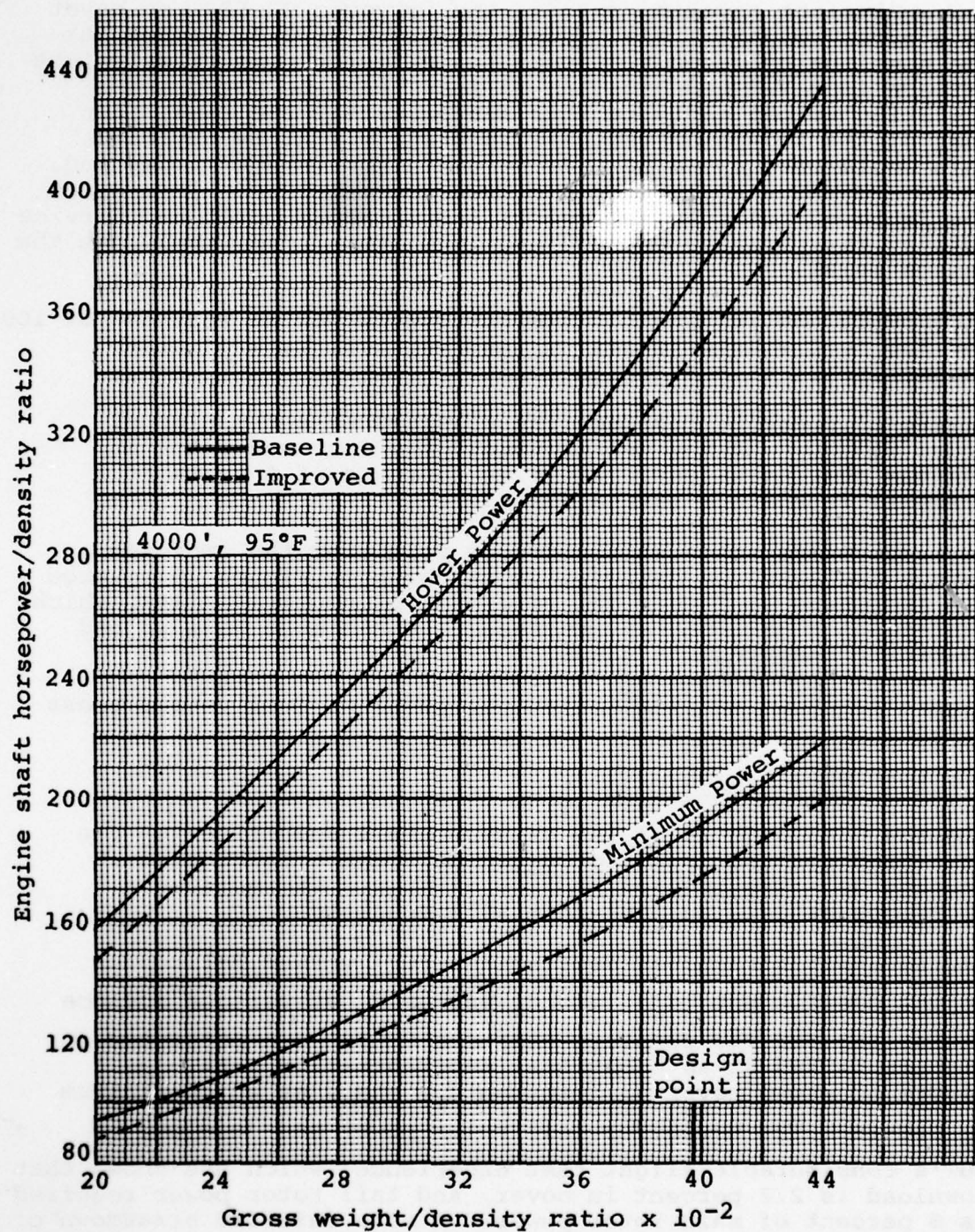


Figure 10. Design point hover and minimum power comparison of the improved and baseline OH-58C.

For equivalent hovering rotors, the improved OH-58C can hover at a gross weight of 3390 pounds compared to 3200 pounds for the baseline helicopter. Since the difference in blade weight between improved and baseline is less than one pound and operating weight empty remains approximately the same, then most of the 190-pound increase in gross weight is payload. This would correspond to a 24 percent improvement in payload.

The improved rotor in Figures 11 and 12 shows hover and service ceiling improvements of 1300 and 1600 feet respectively, at the design point.

Figures 13 and 14 show for the improved rotor an increase of 100 and 300 feet/minute in maximum and vertical rate of climb respectively, at the design point.

Figure 15 presents maximum true airspeed as a function of gross weight. At the design point, the improved rotor at maximum continuous power shows an increase of 4 knots (4.2 percent) in maximum true airspeed.

Payload versus range at the design point for the improved versus the baseline helicopters is shown in Figure 16. Range was increased by 7 nautical miles to 202 nautical miles, which represents a 35.1-percent increase. A 2-minute warm-up and 30-minute reserve were assumed.

Figure 17 shows nautical miles per pound of fuel versus gross weight.

4.2.1.2 Performance Data

Figures 6 through 18 of the OH-58C Detail Specification are presented for the improved OH-58C helicopter in Figures 18 through 30. The mission profile of Figure 25 includes a 4000-foot as well as 2000-foot 95°F condition.

Engine shaft horsepower coefficient (C_p) versus helicopter weight coefficient (C_w), and C_p versus C_w at various advance ratios (μ) for the complete improved OH-58C are presented in Figures 31 and 32 as additional substantiation data. Figure 31 shows hover C_p , minimum C_p , and μ at which minimum C_p occurs. The basis for tail rotor power and download is BHT's considerable flight test experience, which has shown that download is 2.8 percent in hover, and tail rotor power required is 8 percent of main rotor power. A more detailed breakdown of losses may be found in Table A-1, Appendix A.

Figure 32 shows C_p for forward flight. As in hover, tail rotor power is 8 percent of main rotor power required.

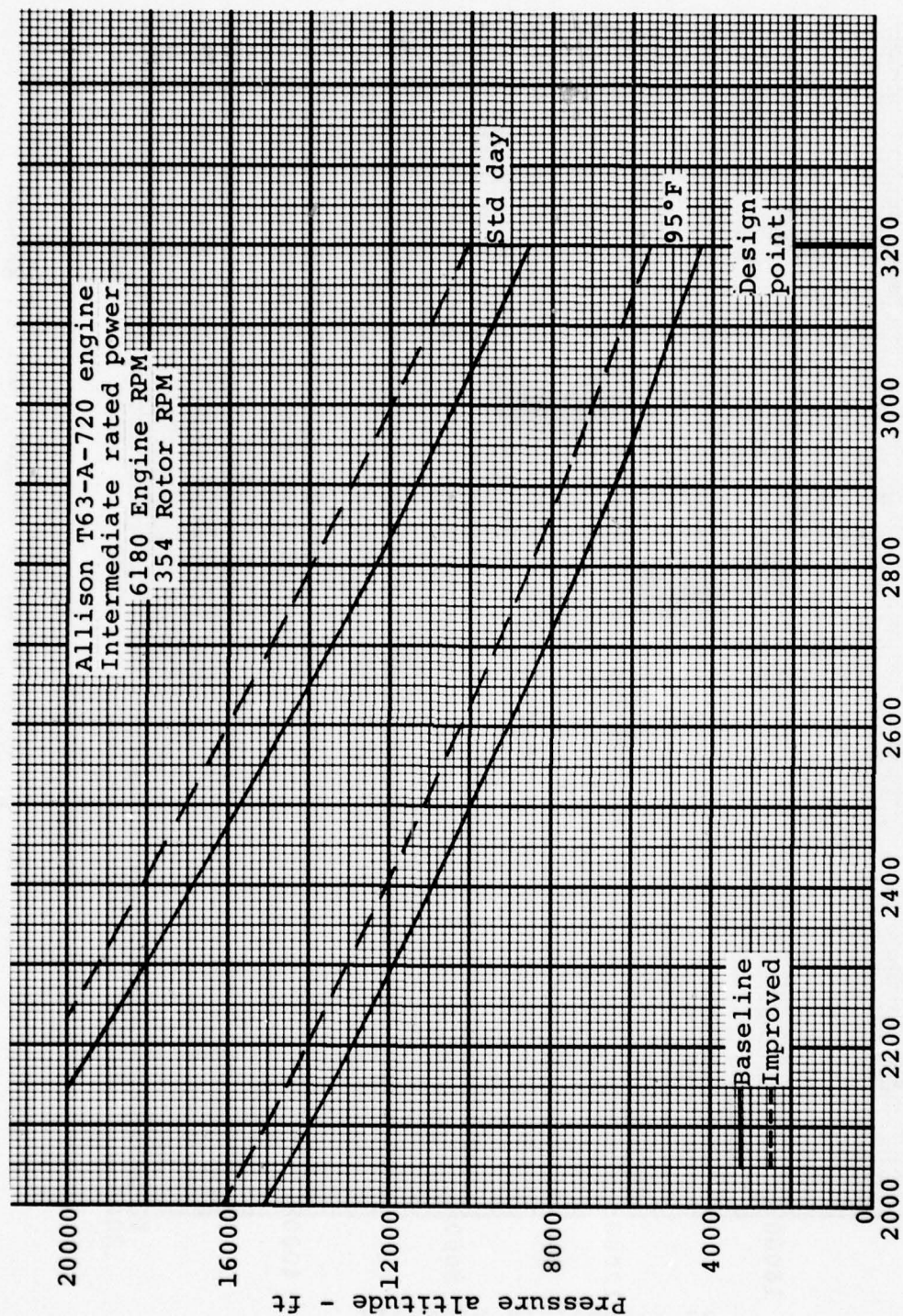


Figure 11. Hover ceilings vs gross weight, out of ground effect (OGE).

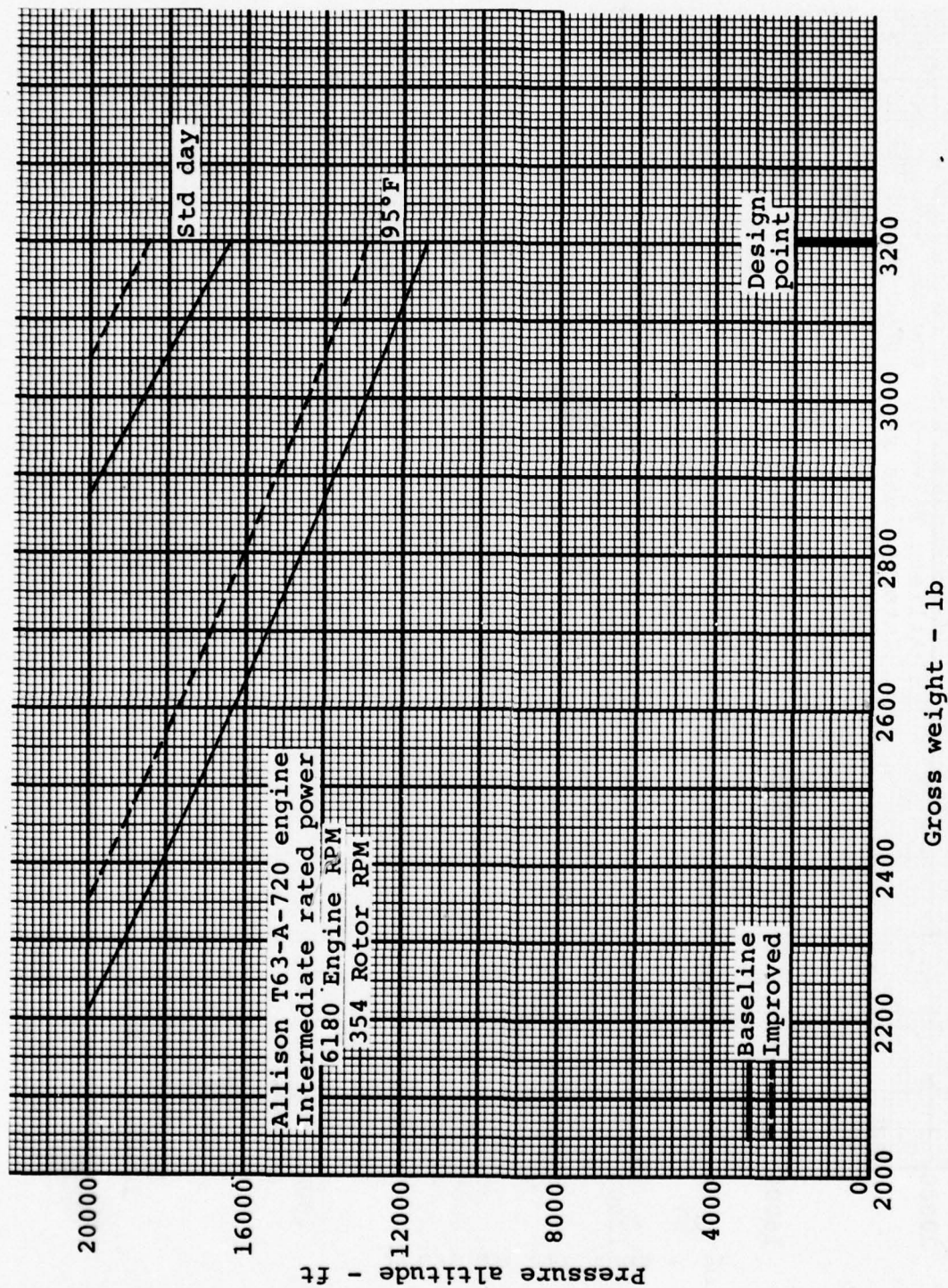


Figure 12. Service ceilings vs gross weight, out of ground effect (OGE).

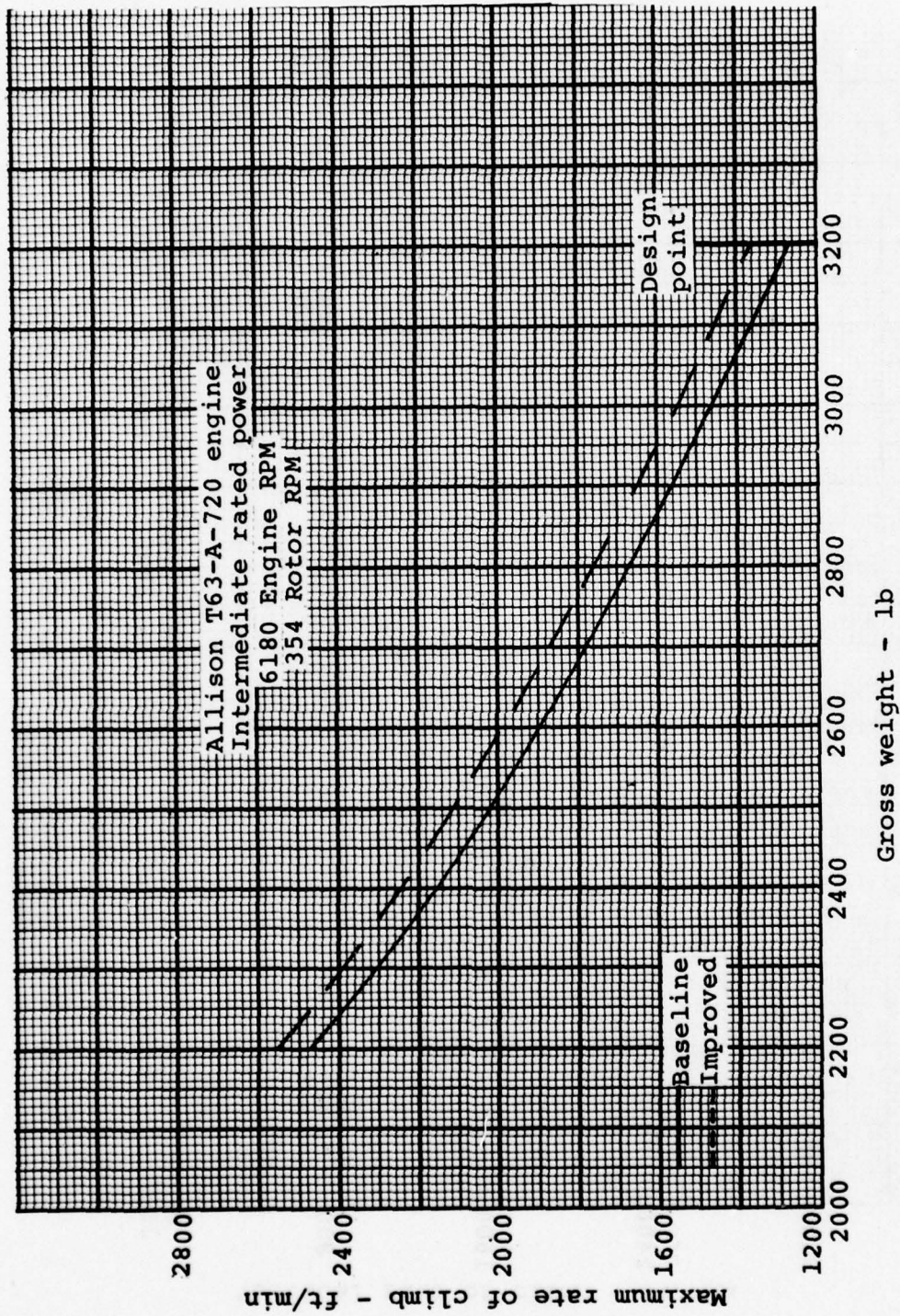


Figure 13. Maximum rate of climb vs gross weight, 4000 ft, 95°F.

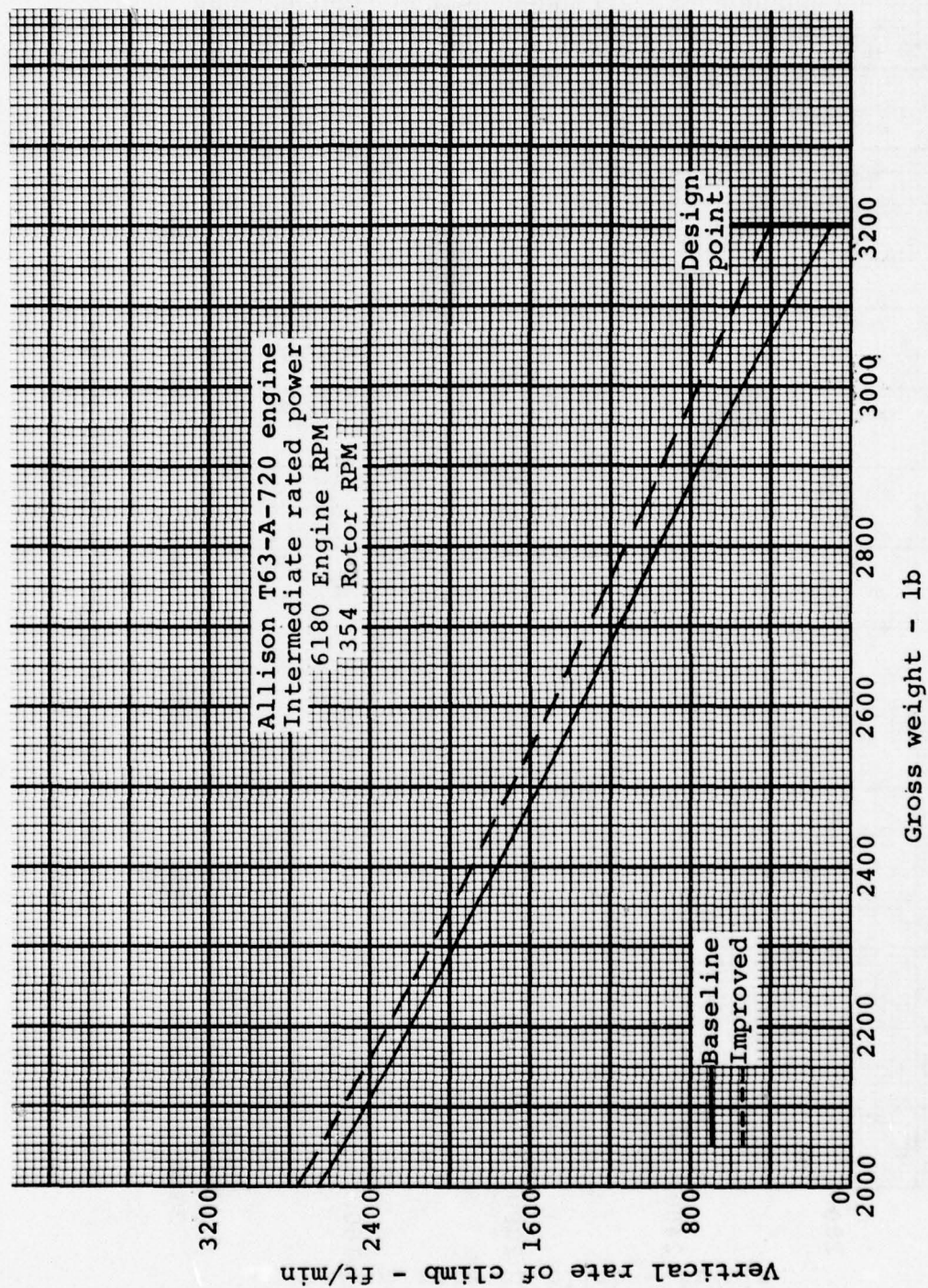


Figure 14. Vertical rate of climb vs gross weight, 4000 ft, 95°F.

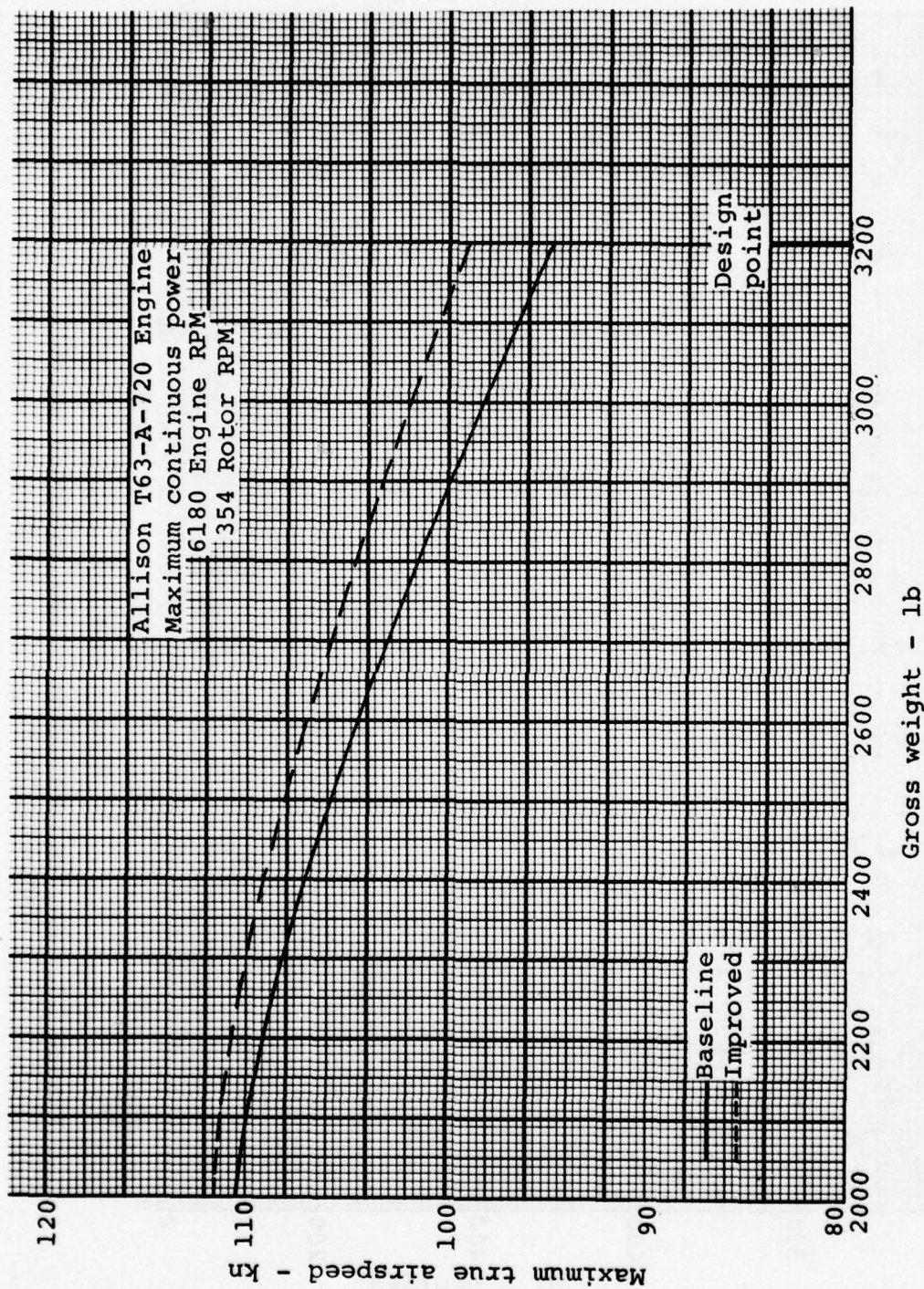


Figure 15. Maximum speed vs gross weight at maximum continuous power, 4000 ft, 95°F.

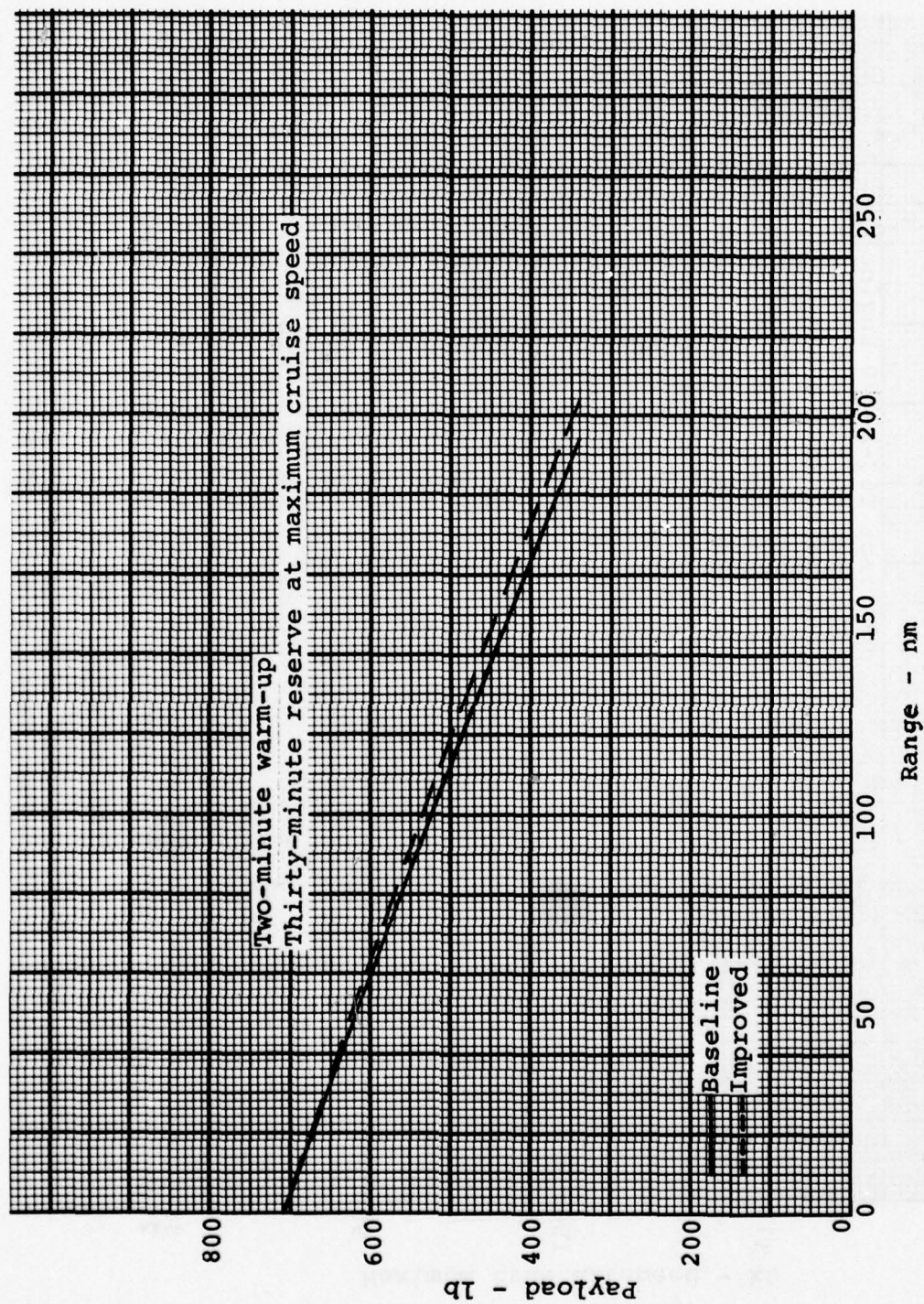


Figure 16. Payload vs range, 3200 lb gross weight, 4000 ft, 95°F.

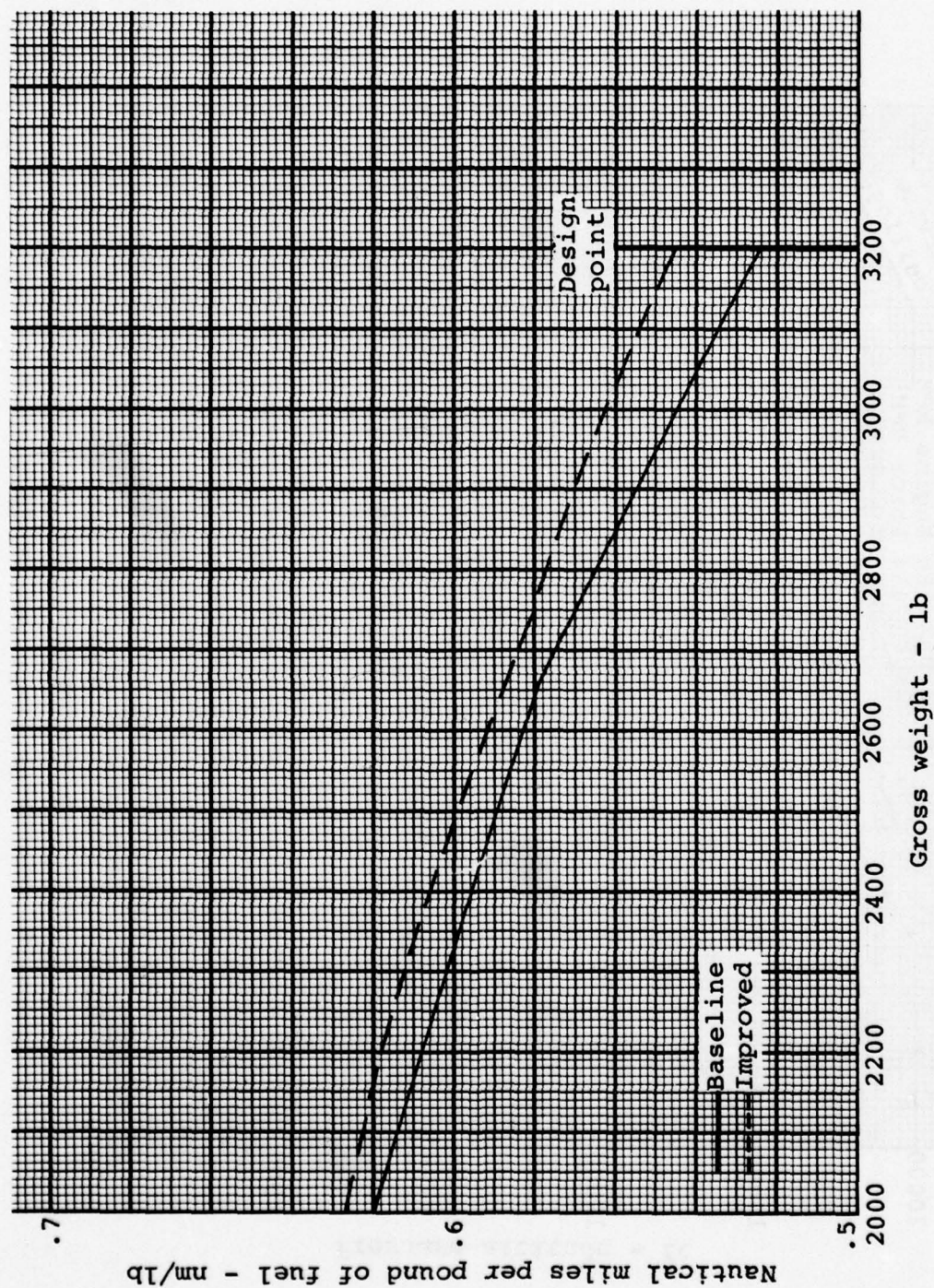


Figure 17. Nautical miles per pound of fuel vs gross weight, 4000 ft, 95°F.

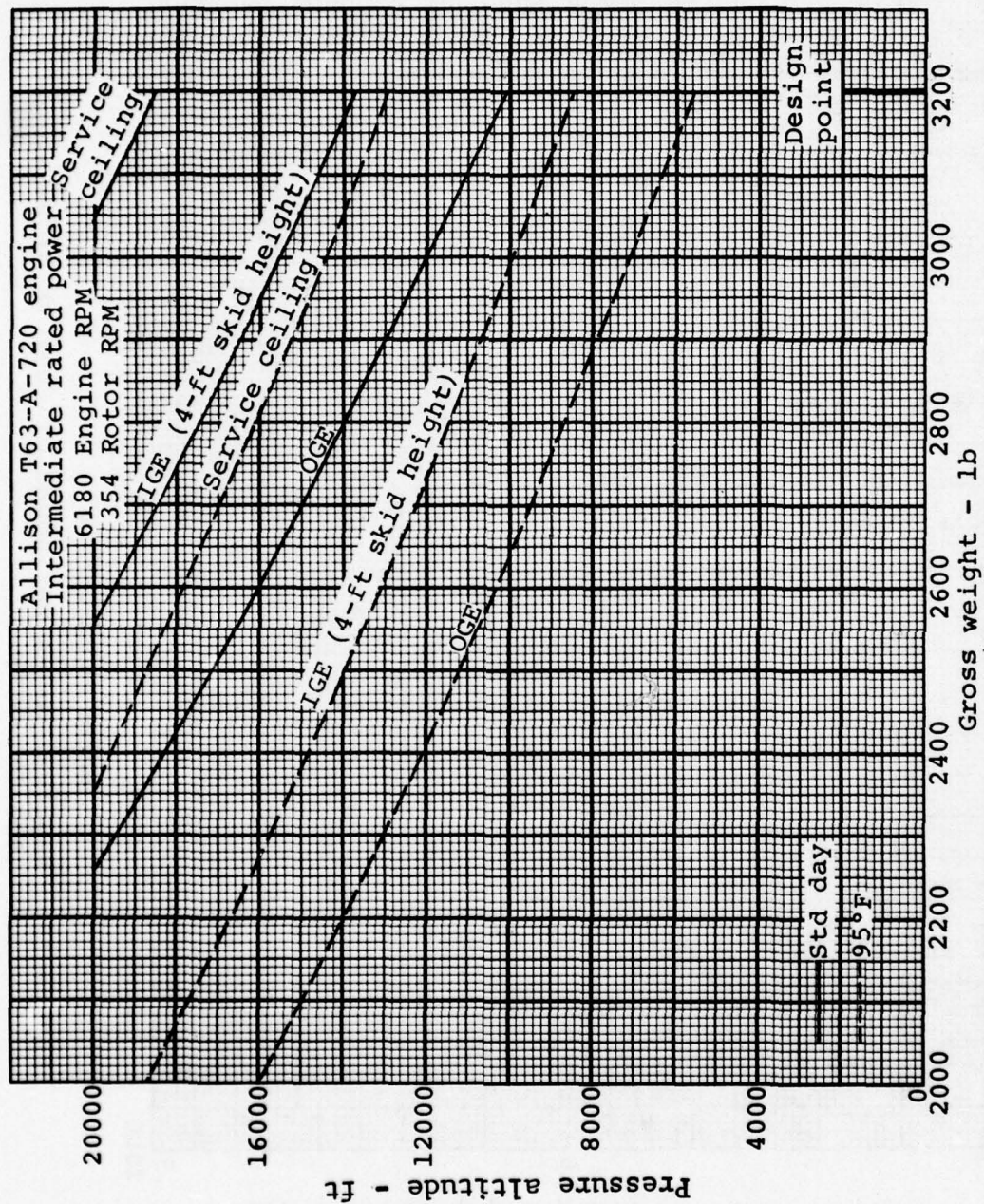


Figure 18. Ceilings, improved OH-58C.

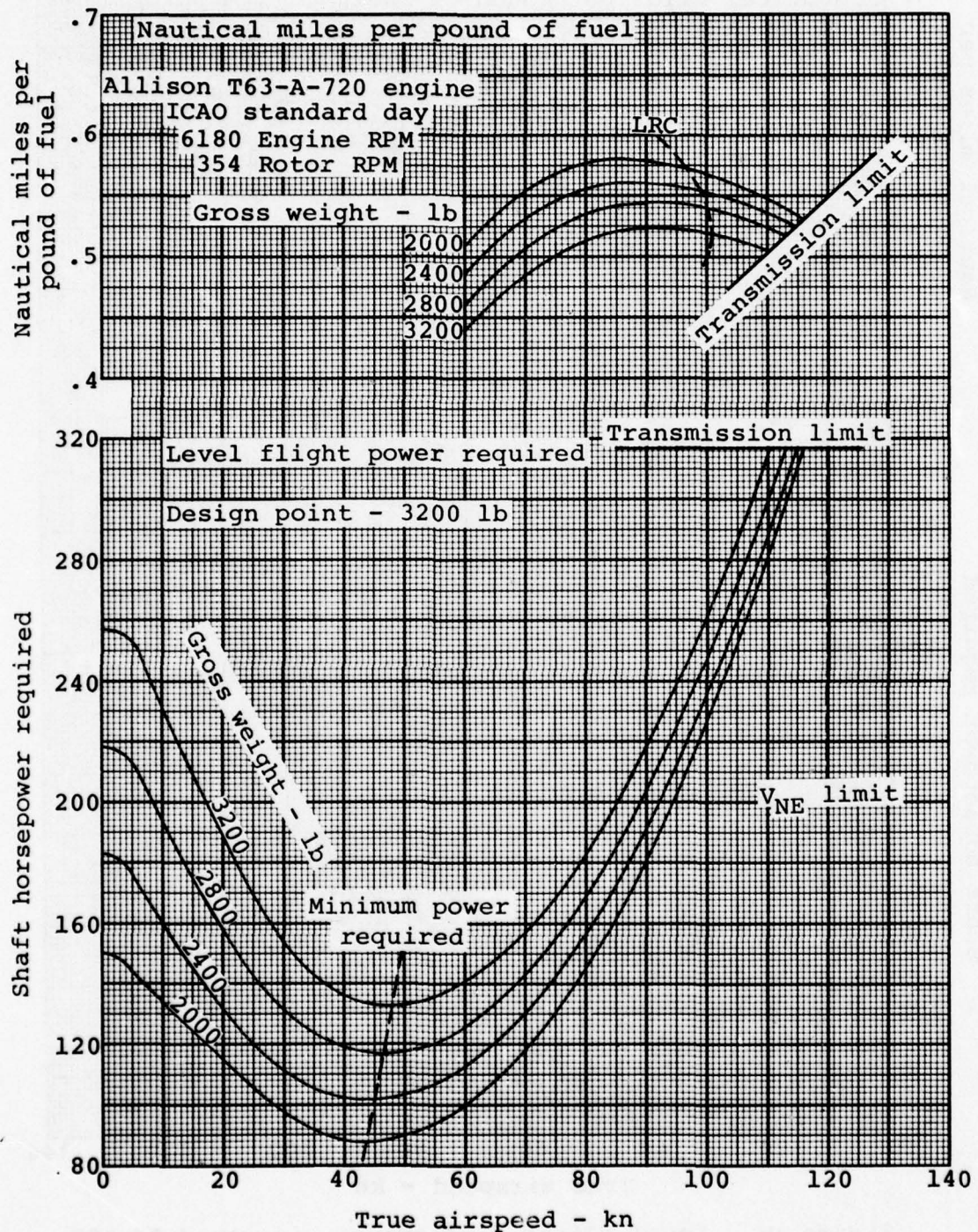


Figure 19. Level flight performance, improved OH-58C, sea level, standard day.

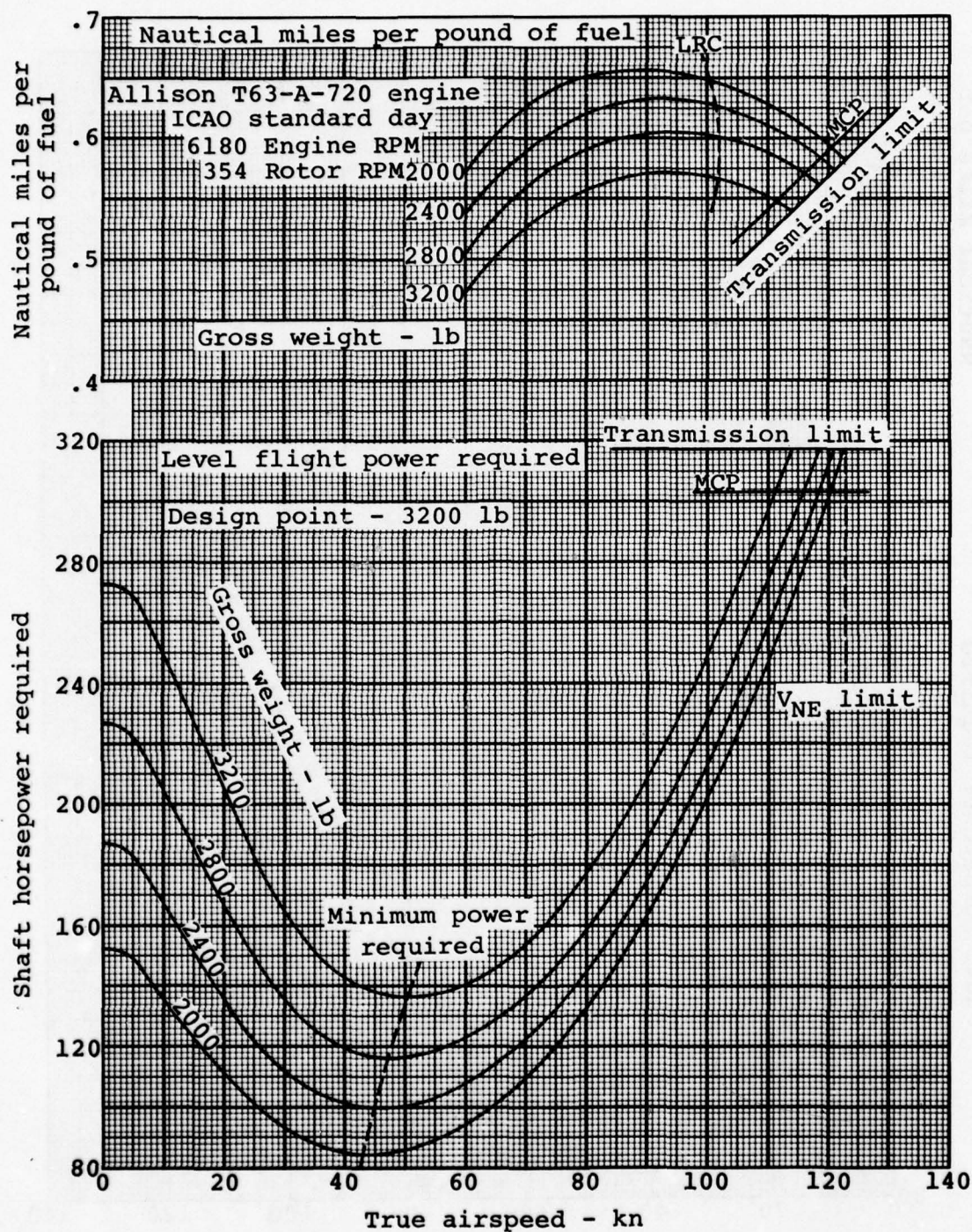


Figure 20. Level flight performance, improved OH-58C, 5000 ft, standard day.

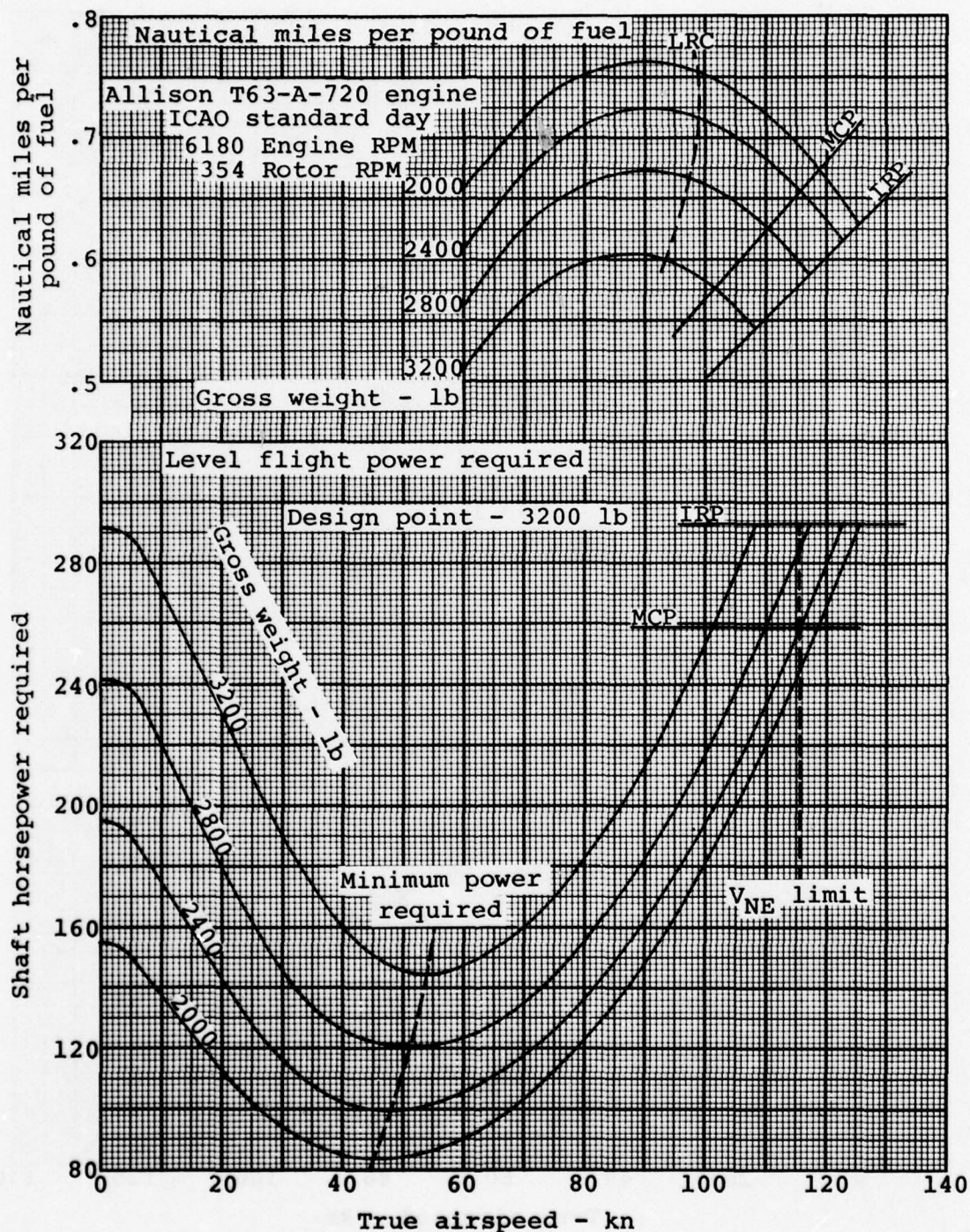


Figure 21. Level flight performance, improved OH-58C, 10000 ft, standard day.

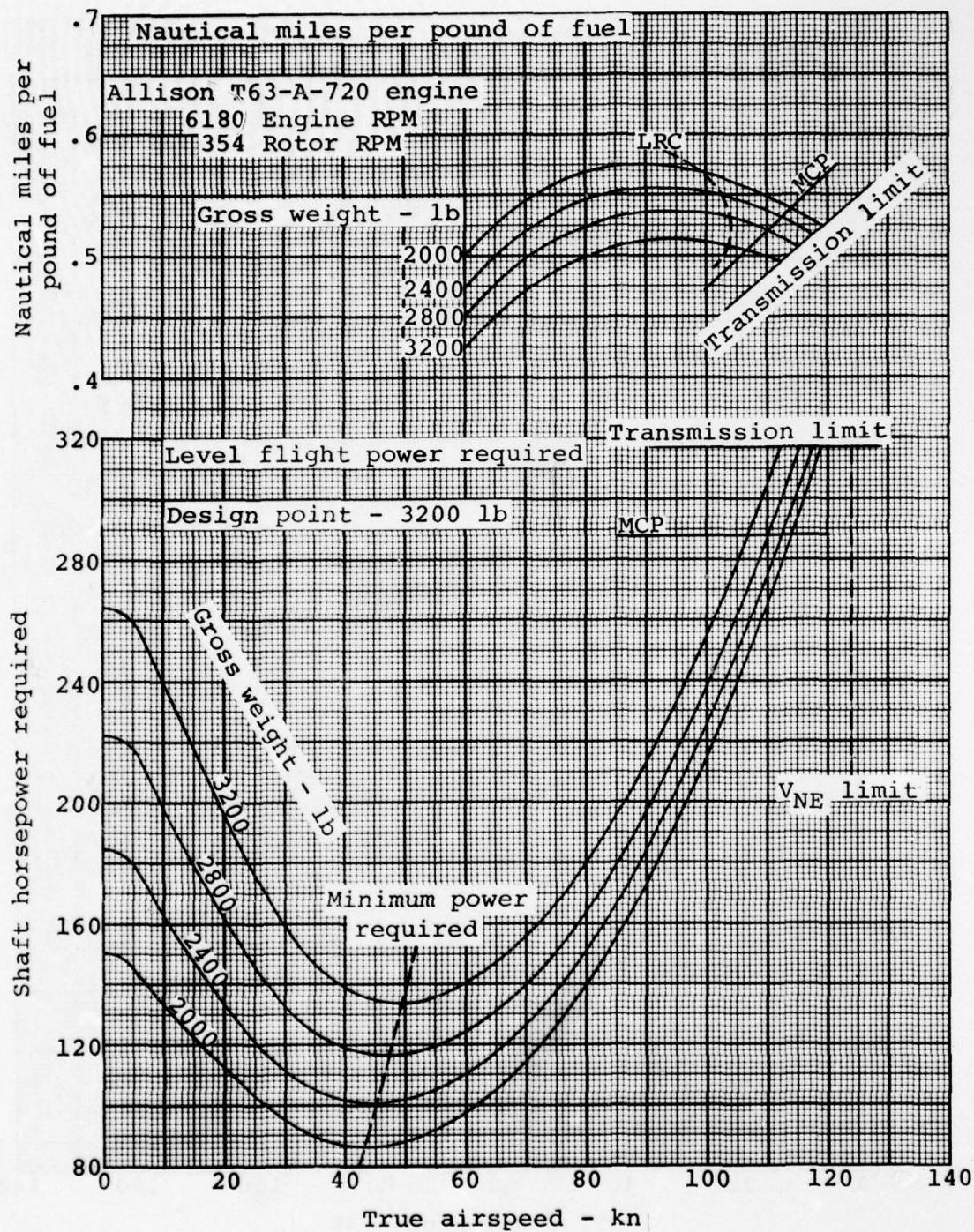


Figure 22. Level flight performance, improved OH-58C, sea level, 95°F.

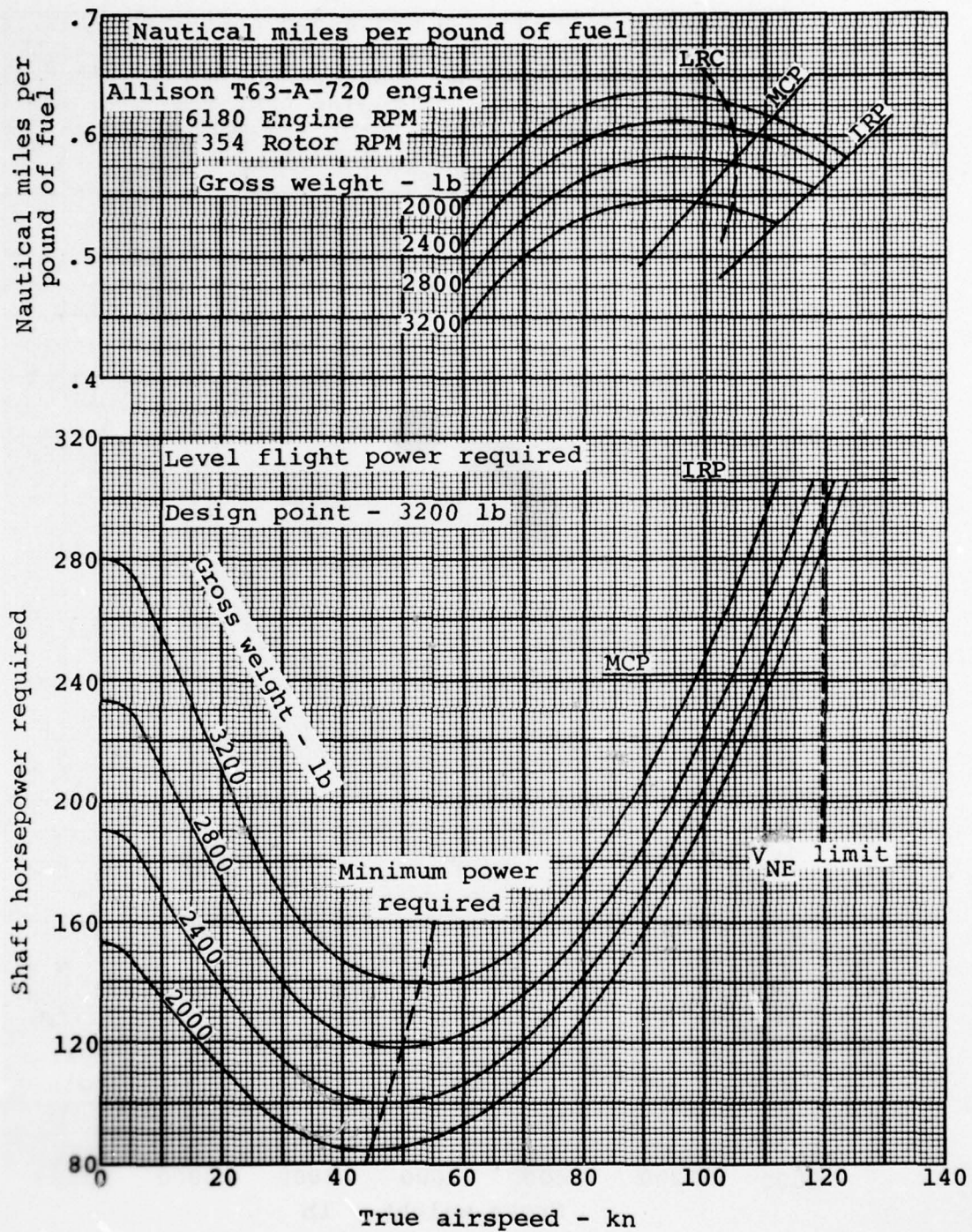


Figure 23. Level flight performance, improved OH-58C, 4000 ft, 95°F.

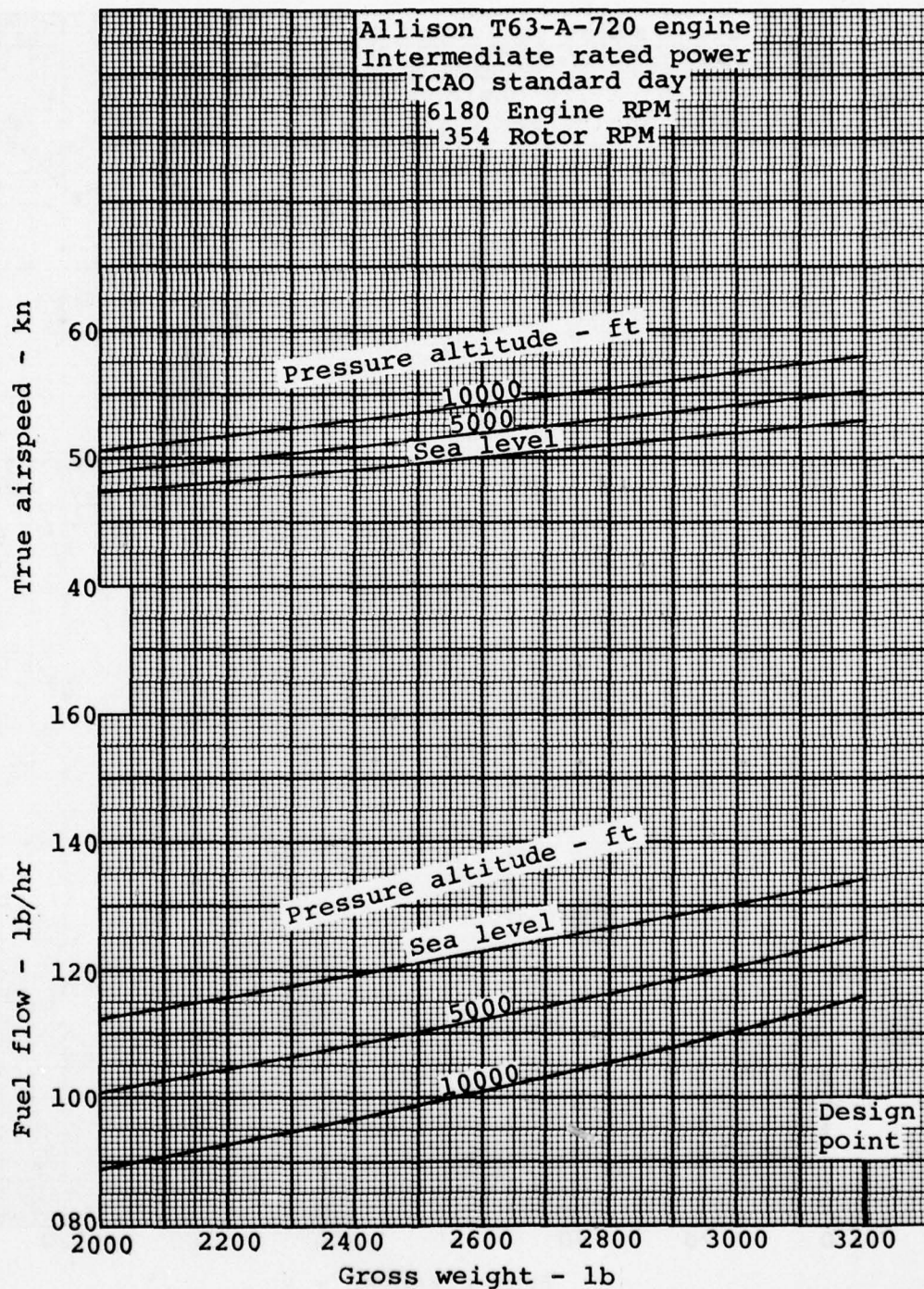
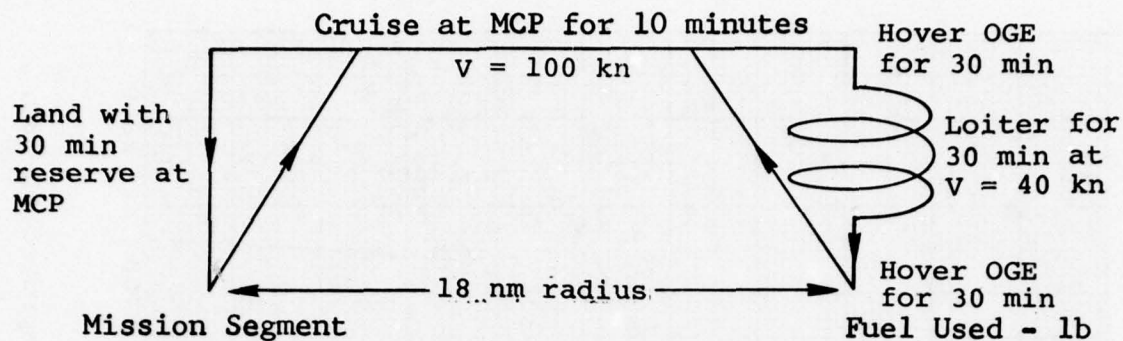


Figure 24. Maximum endurance performance, improved OH-58C.



	<u>Fuel Used - lb</u>	
	2000 FT	4000 FT
8 minutes at ground idle	14	13
Cruise out at MCP for 10 min	33	30
Hover for 30 min at OGE	100	100
Loiter for 30 min at V = 40 kn	69	69
Hover for 30 min at OGE	100	100
Cruise in at MCP for 10 min	33	30
Land with 30 min reserve at MCP	97	91
Total fuel for mission	446	433

Notes:

1. Takeoff gross weight = 3200 lb
2. Usable fuel = 457 lb
3. All mission segments calculated at 3200 lb

Figure 25. Mission profile, improved OH-58C, 2000 and 4000 feet, 95°F.

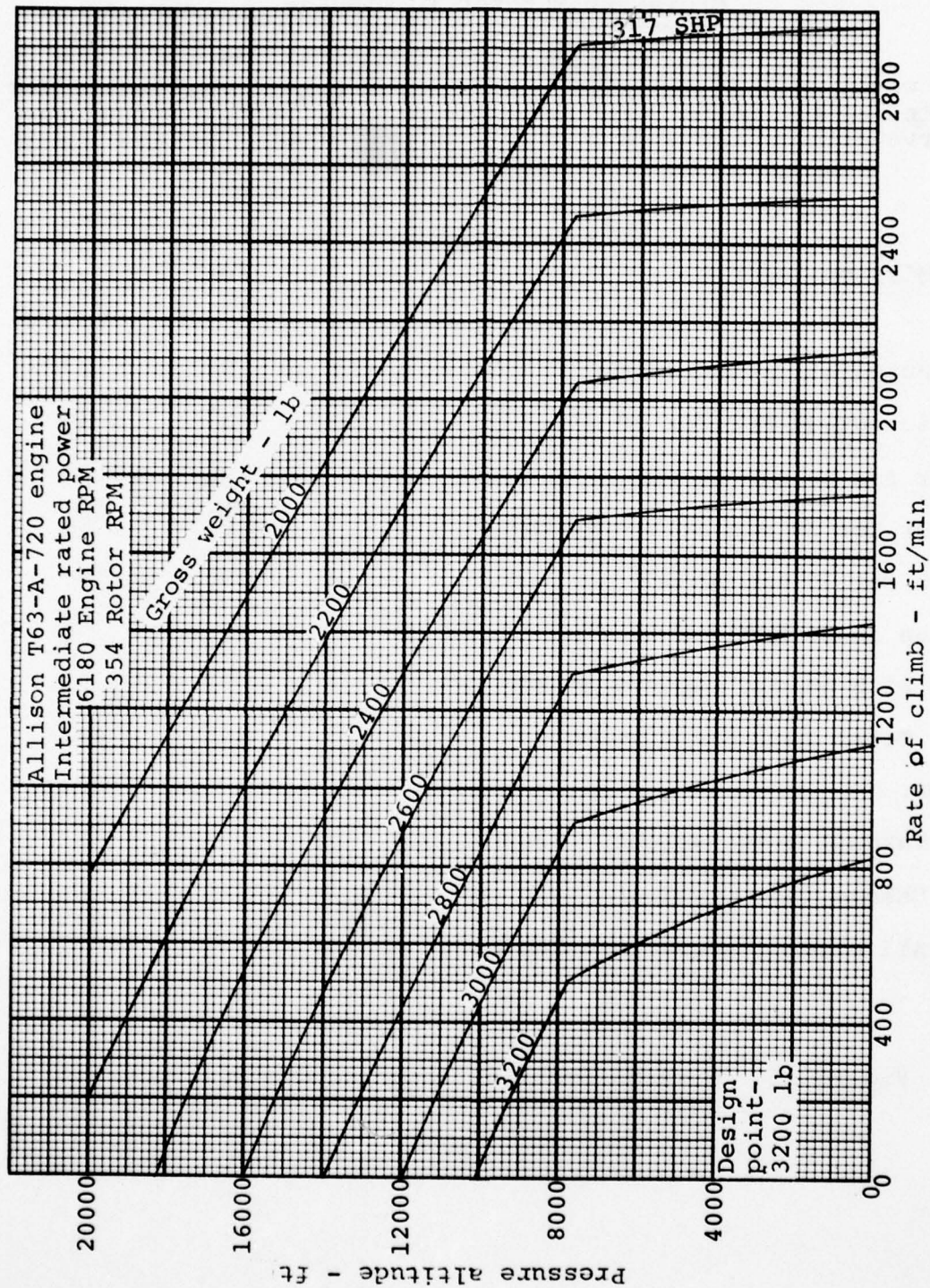


Figure 26. Vertical rate of climb, standard day, improved OH-58C.

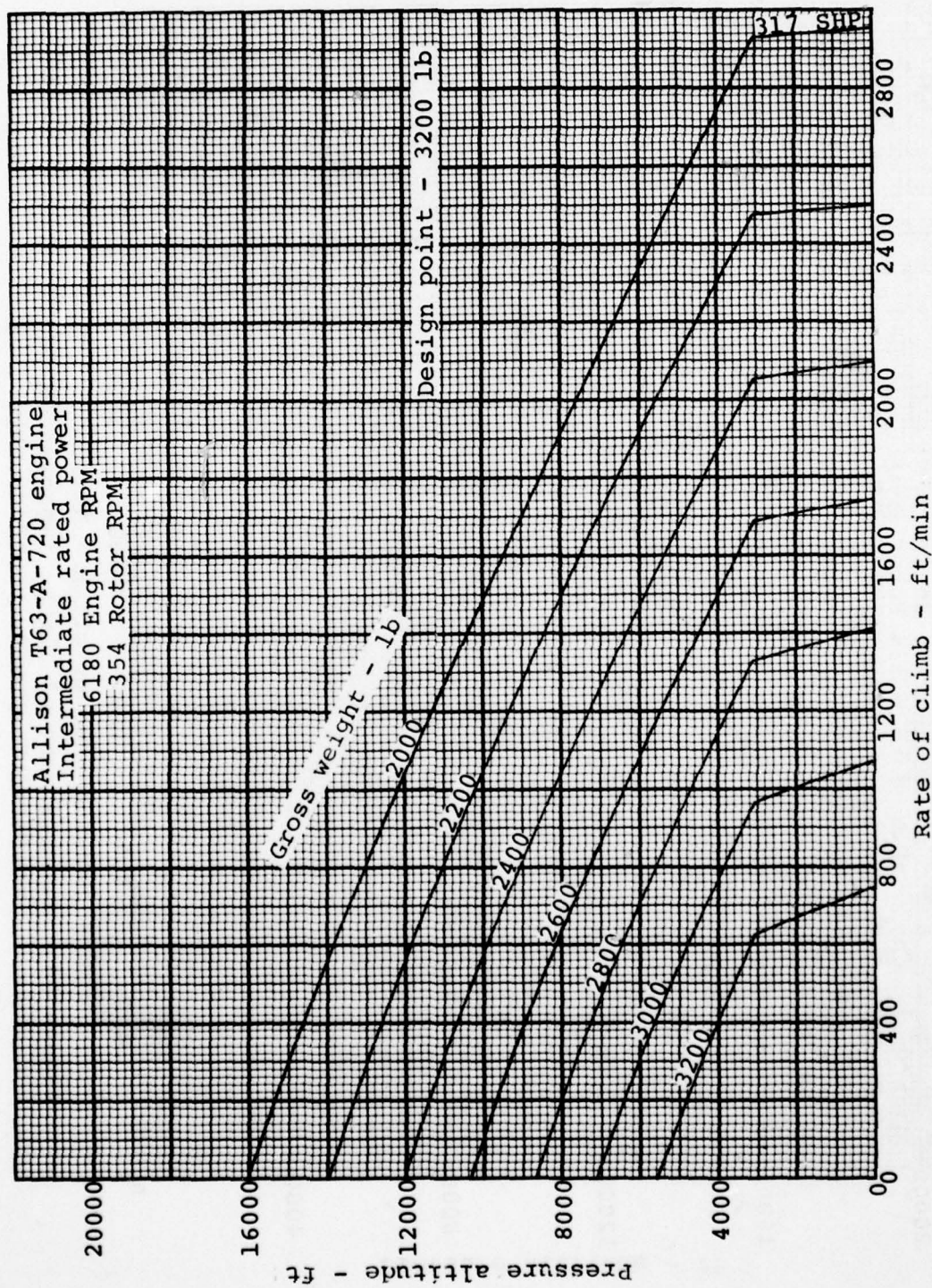


Figure 27. Vertical rate of climb, improved OH-58C, 95°F.

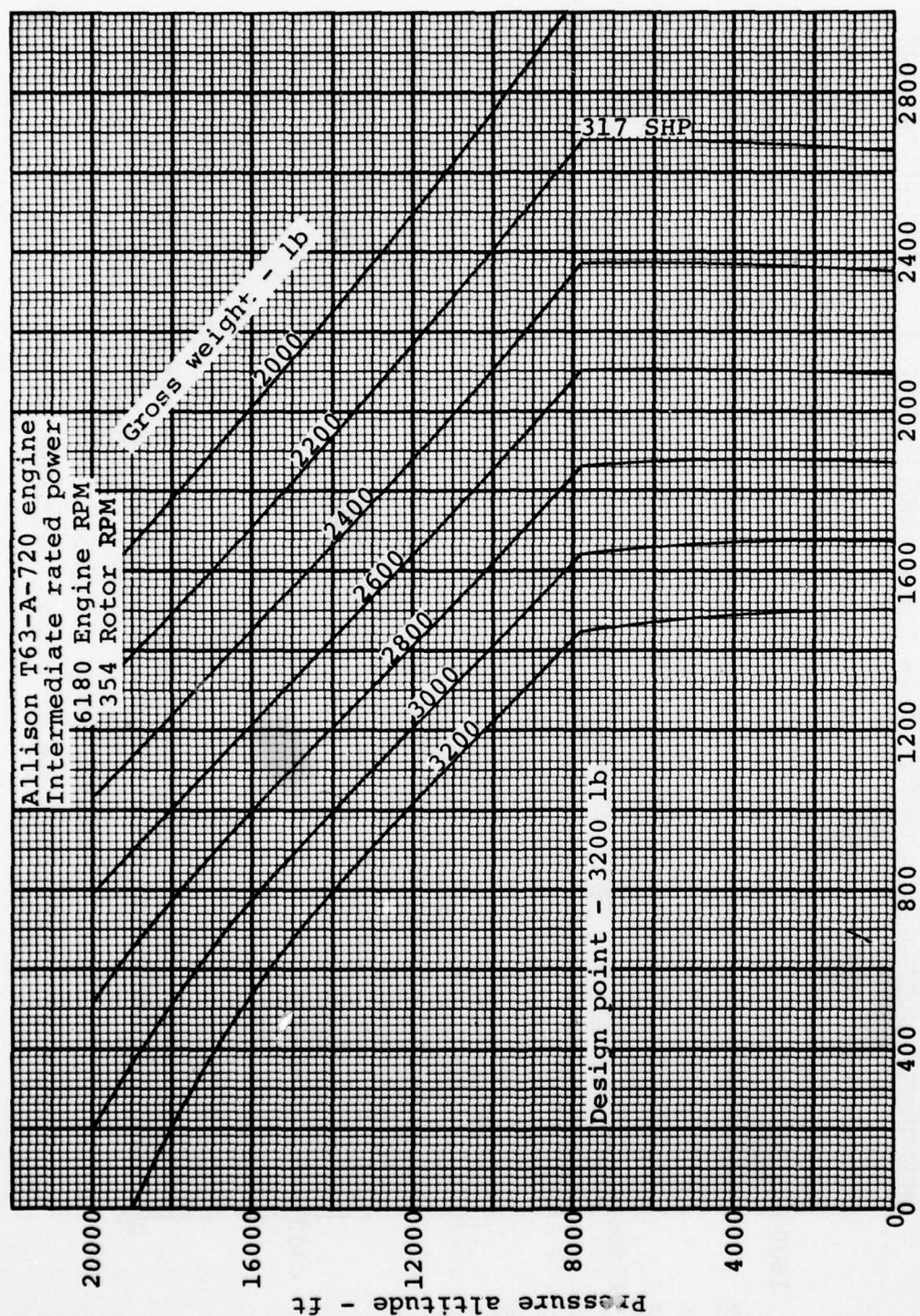


Figure 28. Maximum rate of climb, improved OH-58C, intermediate power, standard day.

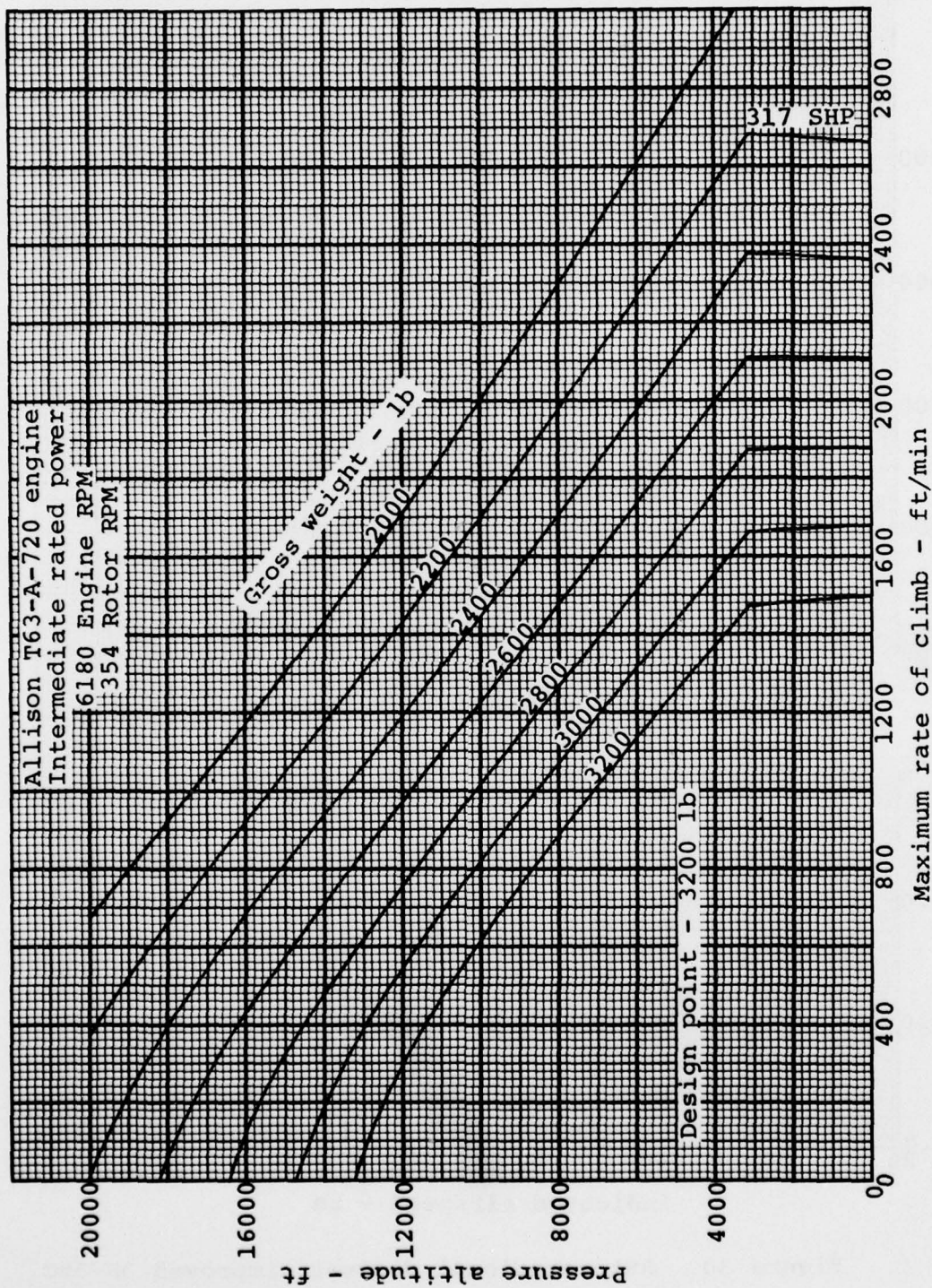


Figure 29. Maximum rate of climb, improved OH-58C, intermediate power, 95°F.

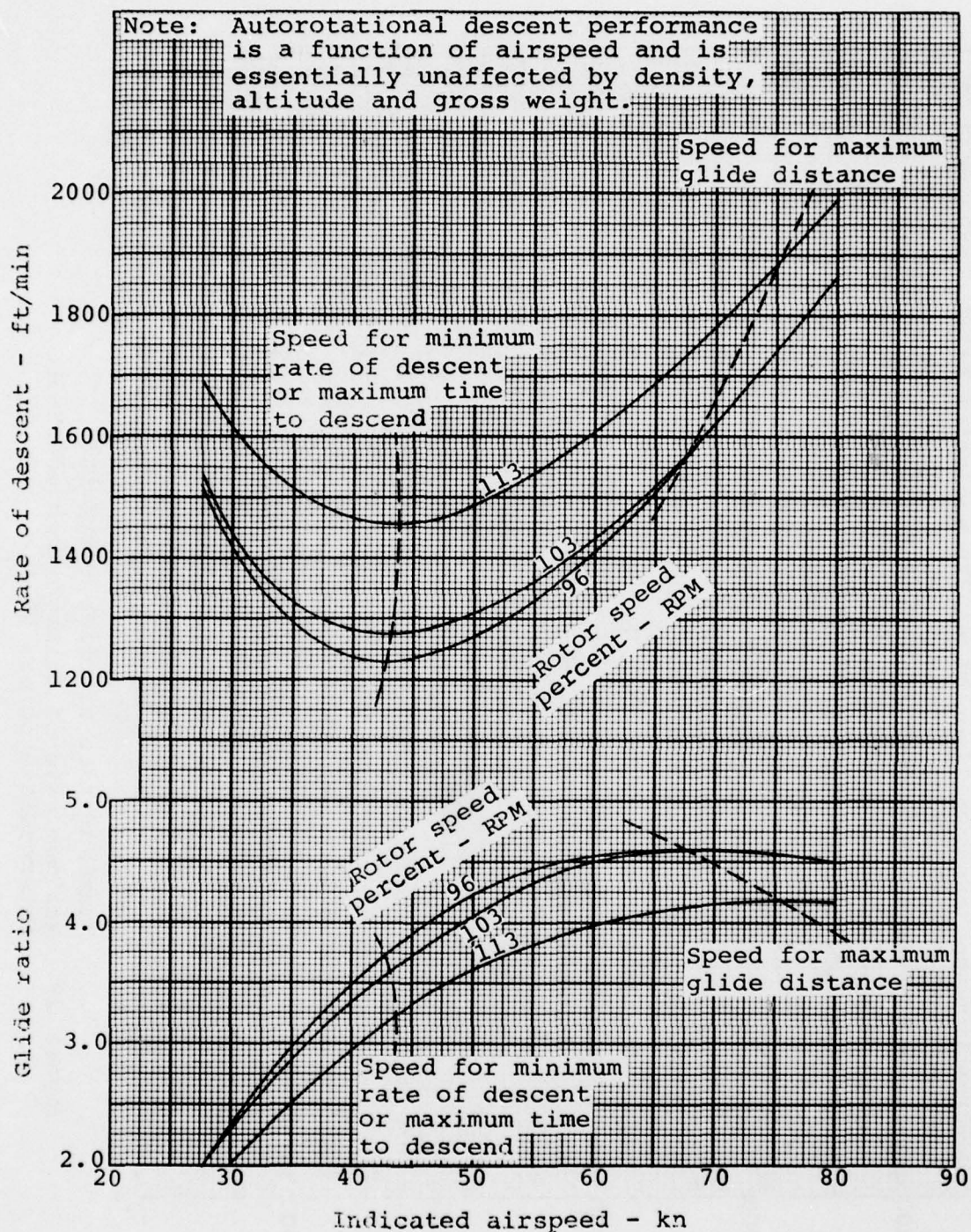


Figure 30. Autorotational descent, improved OH-58C.

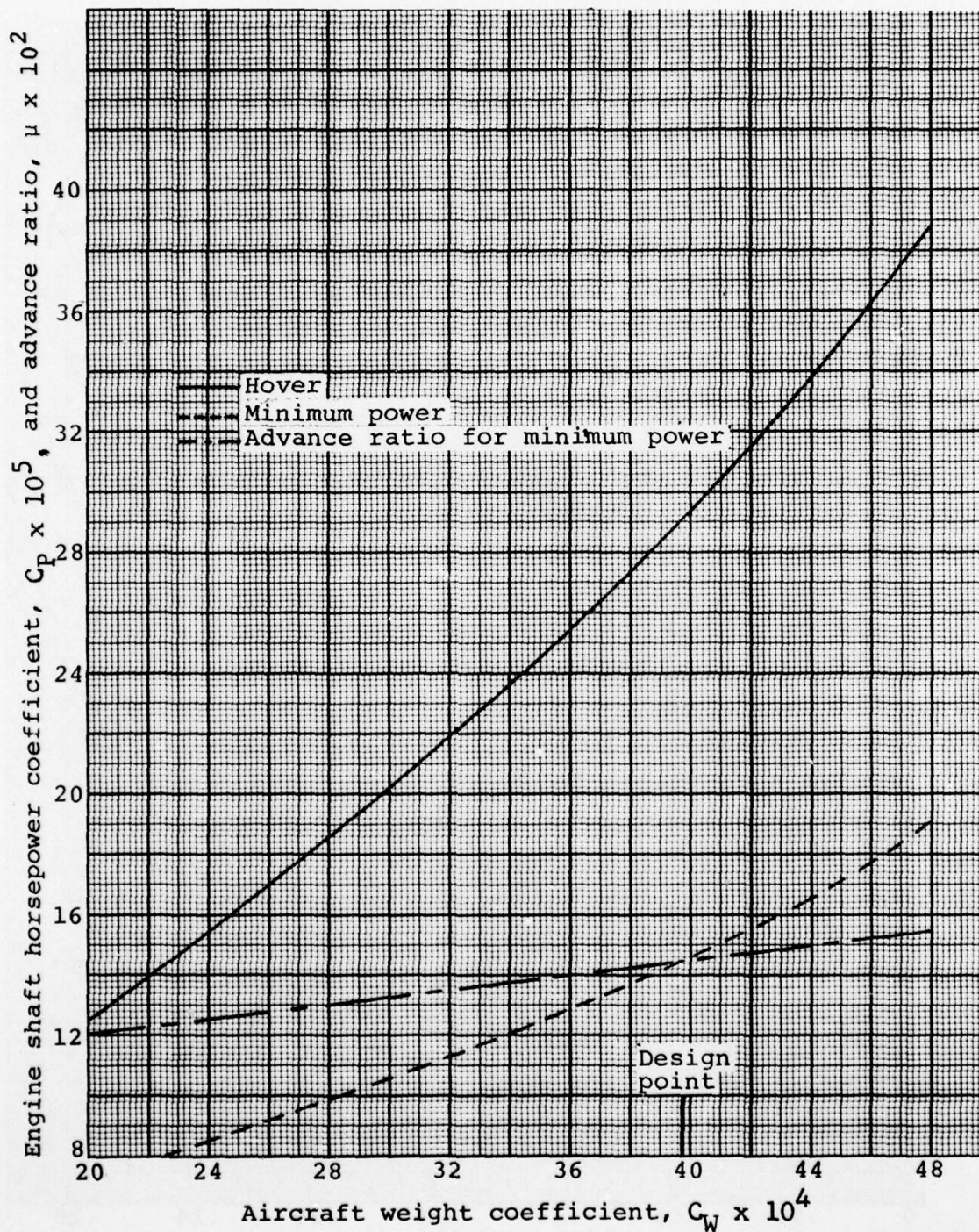


Figure 31. Nondimensional hover power, minimum power, and advance ratio for minimum power, improved OH-58C.

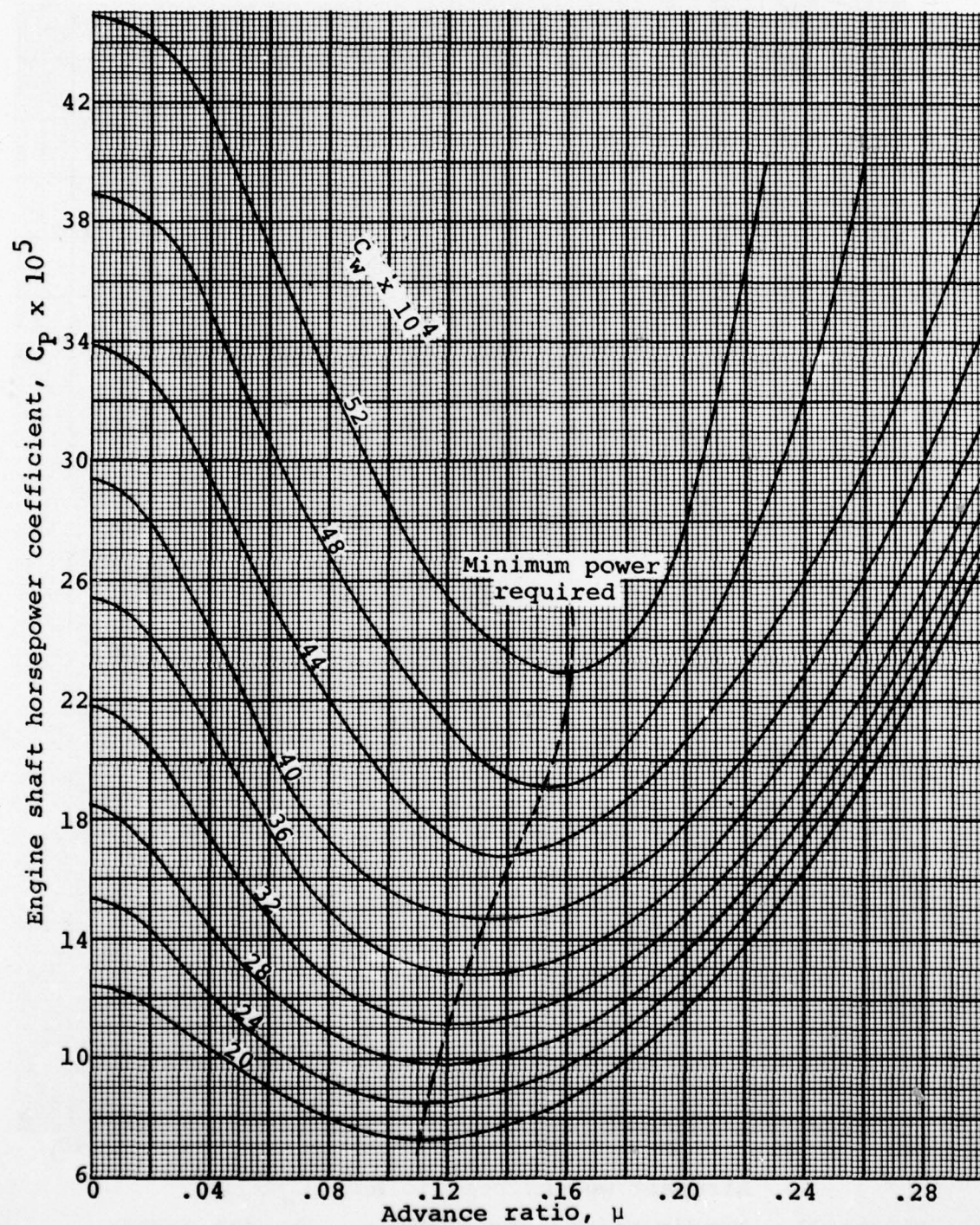


Figure 32. Nondimensional level flight power required, improved OH-58C.

In Figures 31 and 32 the effects of Mach number were not shown, since for the improved helicopter these effects are negligible as shown in Table 13. The change in power required due to Mach number was established by varying flight conditions from 59°F to 95°F at sea level.

TABLE 13. EFFECT OF COMPRESSIBILITY ON
THE IMPROVED OH-58C ROTOR

<u>GW (lb)</u>	<u>V (kn)</u>	<u>Absolute Power Difference (hp)</u>
2400	50	.2
	75	.3
	100	.4
	125	1.0
3200	50	.2
	75	.2
	100	.2
	125	1.0

4.2.2 Handling Qualities

4.2.2.1 Introduction

This section presents the results of a handling qualities analytical comparison between the proposed composite rotor and the existing production rotor installed on the OH-58C. The stability and control analysis method used for this evaluation was the Rotorcraft Digital Flight Simulation Computer Program (C8176) described in Reference 1. The handling qualities investigated for each rotor system include static longitudinal trim stability, static lateral/directional stability, dynamic stability, autorotational entry characteristics, low-speed translational flight and a rotor-tailboom clearance study. The latter analysis, described in Reference 2, was conducted with a specialized hybrid version of the C81 program described in Reference 3. All of the characteristics for each configuration were evaluated at ambient conditions of 4000 feet pressure altitude and 95°F. The aircraft loading conditions investigated were those judged as the most critical during recent OH-58C flight tests for each handling qualities category.

Within the scope and limitations of this evaluation, the flying qualities of the OH-58C with the improved composite blade rotor system are found to be similar to those of the OH-58C with the current rotor design.

4.2.2.2 Static Longitudinal Trim Stability

Figures 33 and 34 present the longitudinal speed stability data for the light weight/aft center of gravity (cg) and the heavy weight/forward cg loading conditions respectively. In each case, data are shown for level flight, takeoff power climb, and autorotation. For each of these flight conditions, the longitudinal control positions are plotted for both blade configurations.

In all cases, control gradients are identical or slightly more positive with the proposed design, which is a desirable feature if, in addition, sufficient longitudinal control margin remains

¹Van Gaasbeek, J. R., C8176 ROTORCRAFT FLIGHT SIMULATION WITH COUPLED ROTOR AEROELASTIC STABILITY ANALYSIS, Report 599-326-900, Bell Helicopter Textron, Fort Worth, Texas, May 1977.

²Popelka, D., MAIN ROTOR FLAPPING CLEARANCE ANALYSIS, Report 299-099-873, Bell Helicopter Textron, Fort Worth, Texas, February 1977.

³Schramm, M., DEVELOPMENT, CAPABILITIES, AND LIMITATIONS OF REAL TIME HYBRID C81, Report 299-099-535, Bell Helicopter Textron, Fort Worth, Texas, February 1972.

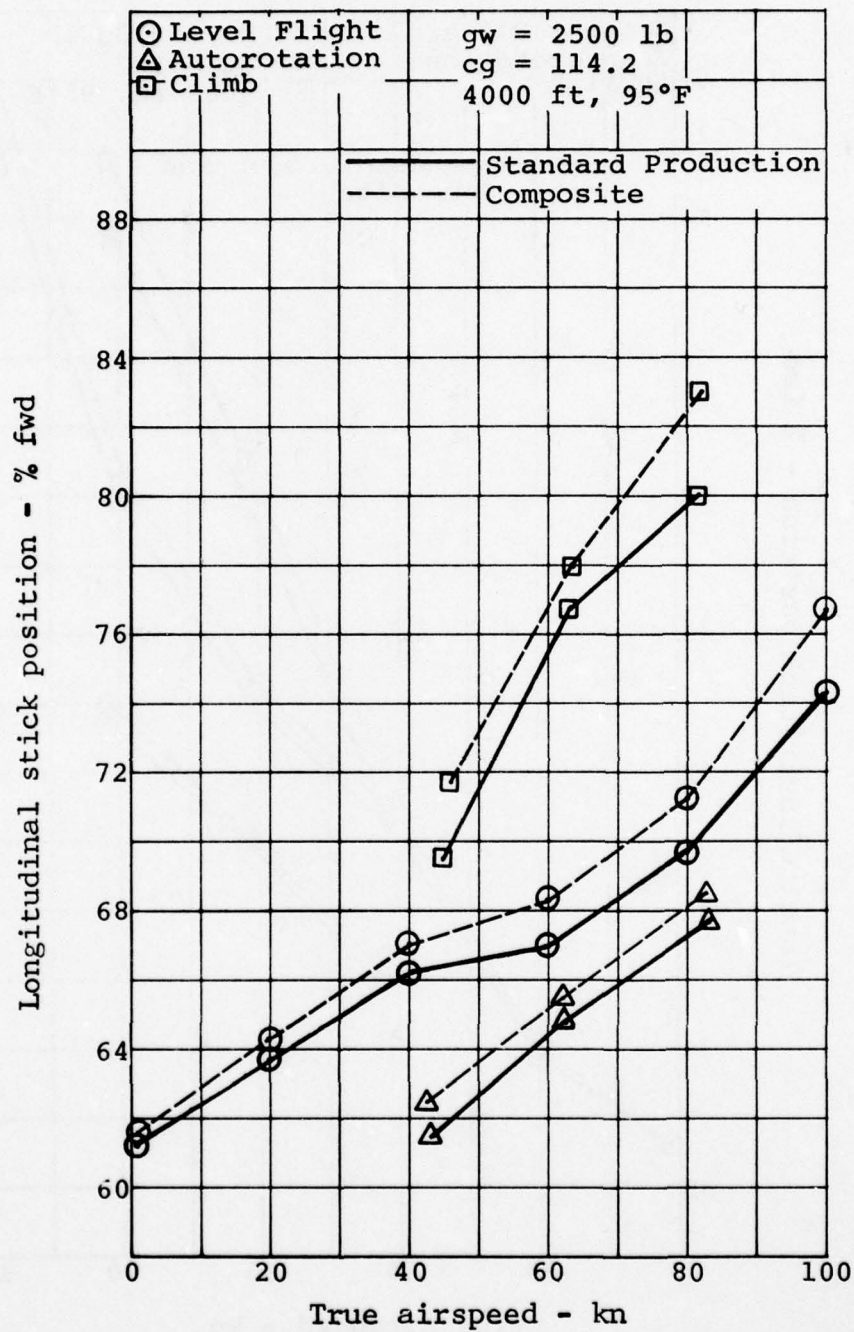


Figure 33. Static longitudinal trim stability, gw = 2500 lb, cg = 114.2.

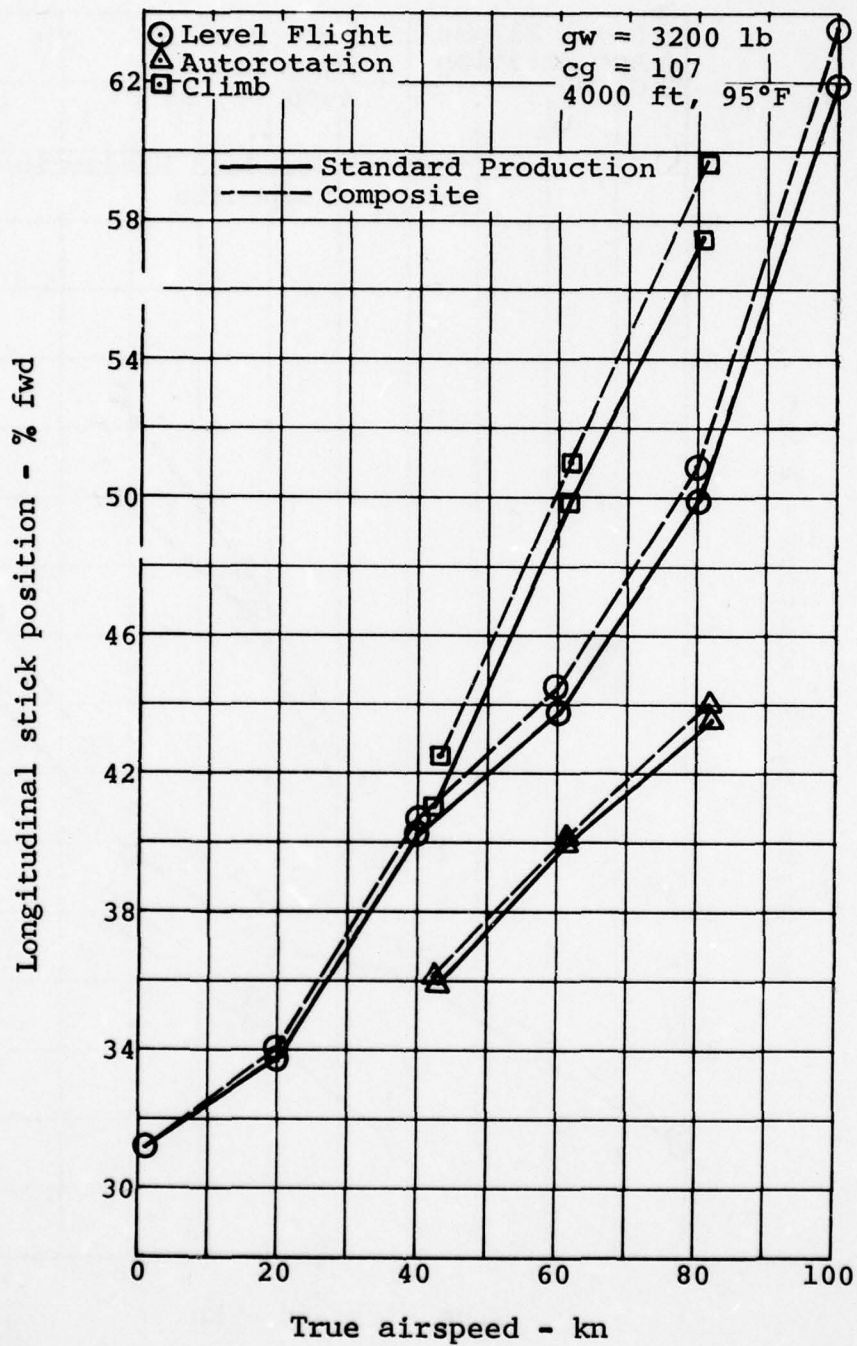


Figure 34. Static longitudinal trim stability, gw = 3200 lb, cg = 107.

AD-A065 172

BELL HELICOPTER TEXTRON FORT WORTH TEX
OH-58 COMPOSITE MAIN ROTOR BLADE. PRELIMINARY DESIGN INVESTIGAT--ETC(U)
DEC 78 V H BROGDON, J BRASWELL, F FREEMAN DAAJ02-77-C-0073
699-099-086 USARTL-TR-78-38A NL

UNCLASSIFIED

2 OF 4
ADA
065/72



at the most critical condition. This situation occurs during a light weight/80-knot climb where the F/A cyclic margin is slightly reduced from 20 percent with the present design to 17 percent. However, this margin will still allow adequate control power for pitch response.

Trim change following power reduction is not significantly increased at constant airspeed when comparing the improved design with the existing configuration.

4.2.2.3 Static Lateral/Directional Stability

The influence of the composite blade on the lateral/directional characteristics is minimal, as indicated in Figure 35. The directional stability (gradient of pedal position with slideslip angle), effective dihedral (gradient of lateral cyclic with sideslip), and side force characteristics (gradient of roll angle with sideslip angle) at 100 knots, light weight/aft cg, remain virtually unaffected by the incorporation of the improved design.

4.2.2.4 Dynamic Stability

The effect of the proposed blade on the dynamic flight mode stability was investigated in level flight from hover to 100 knots airspeed at the heavy weight (3200 lb)/most forward cg (107) loading condition. The following conclusions are drawn from the results of the 6 by 5 coupled analysis. The Dutch-roll mode period and damping are not influenced by the composite rotor. The improved design provides slightly less damping of the spiral mode from 40 to 100 knots while providing slightly more damping of the roll-subsidence mode throughout the speed range from hover to 100 knots. Damping of the longitudinal short-period mode is slightly improved during transition from hover to 60 knots with no change in damping occurring from 80 to 100 knots. No change in period is discernible between the two configurations for this longitudinal short mode. The composite blade does not influence the phugoid damping; however, a mild reduction in phugoid period is noted. In no event did the improved rotor fail to meet the VFR requirements of Reference 4 when compared to the current design.

4.2.2.5 Autorotational Entry Characteristics

The main rotor RPM decay rate of each rotor configuration was analyzed using the maneuver phase of Reference 1. Throttle chops were performed at identical 100 knot/heavy weight/forward cg conditions, and the RPM was observed for 2 seconds without

⁴Military Specification MIL-H-8501A(1), GENERAL REQUIREMENTS FOR HELICOPTER FLYING AND GROUND HANDLING QUALITIES, Department of Defense, Washington, D.C., 3 April 1963.

gw = 2500 lb
 cg = 114.2
 4000 ft, 95°F
 V = 100 KTAS

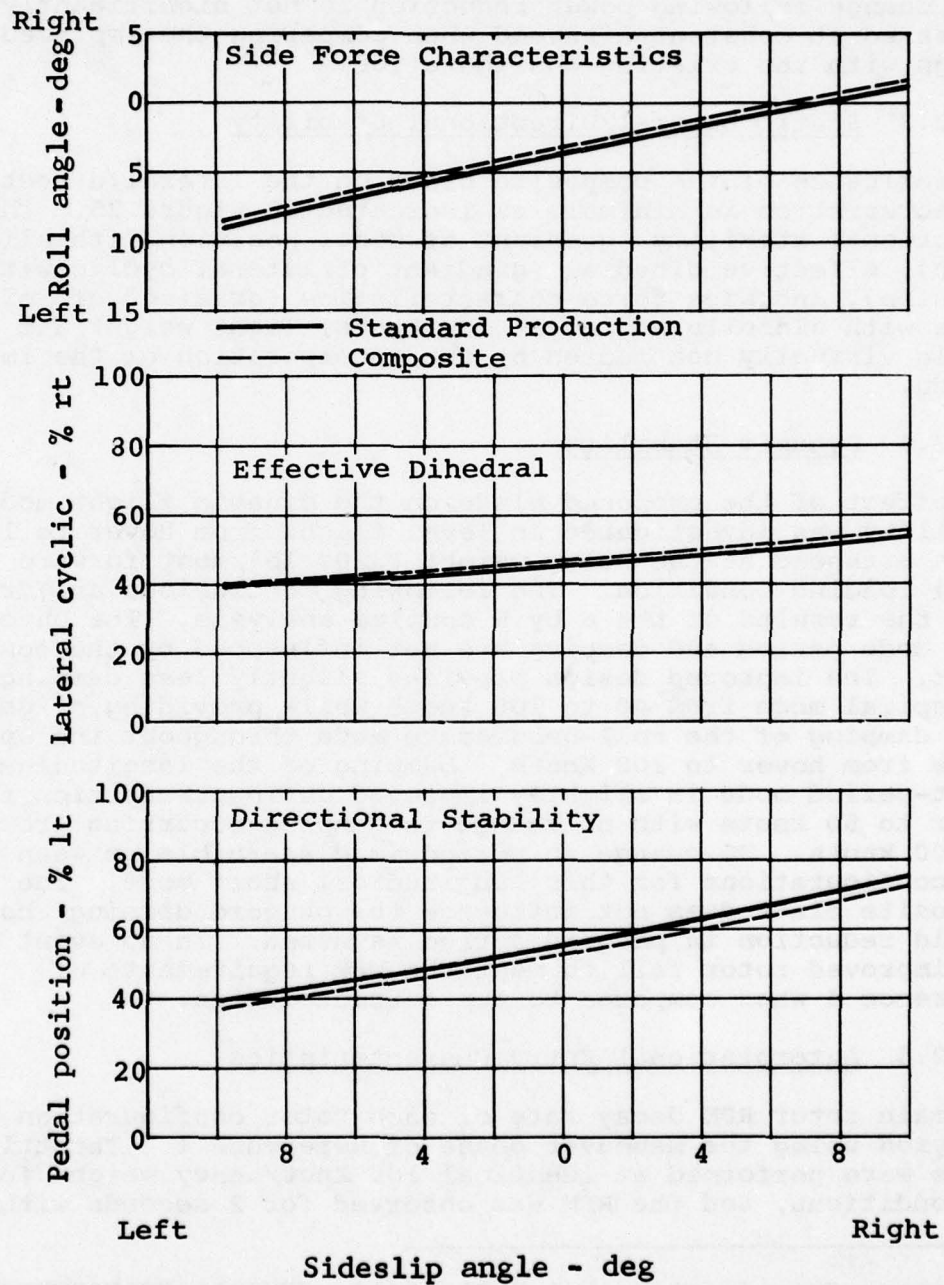


Figure 35. Static lateral/directional stability.

any control movements during the maneuver. The results (shown in the Figure 36 time history) indicate that due to the reduced level flight power required for an equivalent flight condition, the composite rotor exhibits a noticeable improvement in RPM decay rate over that of the standard rotor.

4.2.2.6 Low-Speed Translational Characteristics

During low-speed translational flight, control characteristics again are virtually unaltered from the baseline aircraft with the installation of the composite configuration. Effects on pedal and lateral cyclic control positions in the most critical lateral condition, right sideward flight, are shown in Figure 37 for both rotors at the light weight/forward cg loading. At the maximum allowable speed of 35 knots, the pedal margin increases about 2 percent with the composite rotor. Yaw control sensitivity remains unchanged; therefore, the yaw displacement following a pedal input to the stop will increase with the improved design. Lateral cyclic control position and margin remains essentially identical for both rotor configurations at 35 knots.

Rearward flight to the maximum limit of 30 knots was evaluated at the light weight/most forward cg loading as shown in Figure 38. The remaining aft control position margin is the most critical at this light weight condition, where the standard rotor value of 9.2 percent is reduced to 8.2 percent with the composite rotor installed. However, adequate control power remains at this condition for correcting external disturbances. The available pitch-control moment is still greater than 10 percent of that available in hover as required by paragraph 3.2.1 of Reference 4.

4.2.2.7 Rotor-Tailboom Clearance

Computation of the clearance between the main rotor blade and the tail rotor driveshaft cover was made for both the existing production blade and the composite blade as briefly described in paragraph 4.2.2.1. By combining aircraft geometry with the detailed time-variant rotor-motion analysis of the digital simulation, these inputs can be utilized on the modified hybrid simulation to compute this clearance continuously during trim and maneuvering flight. Previous studies indicated the most critical flight maneuver, in terms of minimum blade/tailboom clearance, is a stick reversal at 20 knots forward speed. Time-history results for such a maneuver are shown in Figure 39 and 40 for the standard and composite rotors, respectively. The longitudinal cyclic input amplitudes and rates are identical for each case. It is evident from the tailboom clearance trace that the minimum value has not decreased with the installation of the composite rotor. In addition, values of maximum flapping angle, pitch attitude, and pitch rate are virtually identical for both rotors.

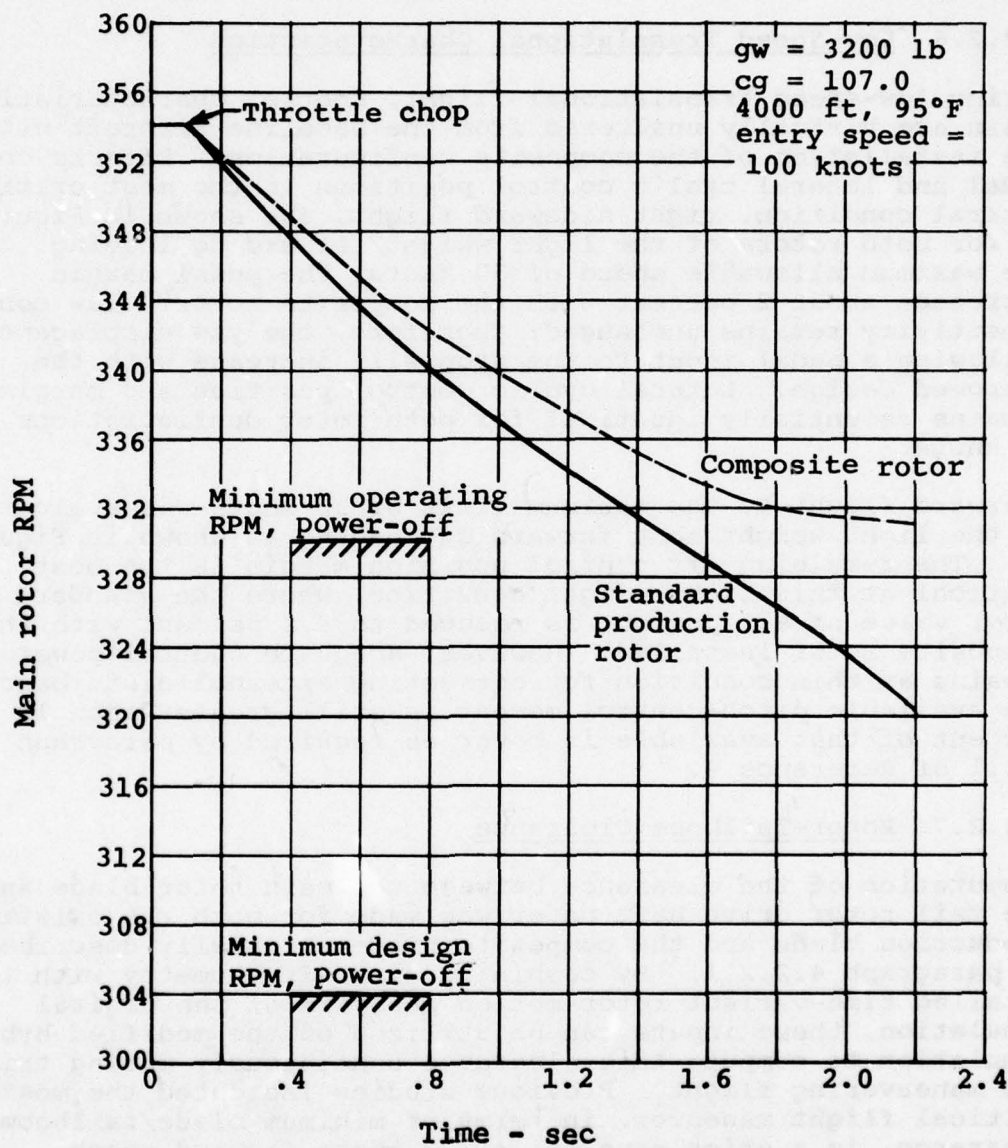


Figure 36. RPM decay during autorotational entry.

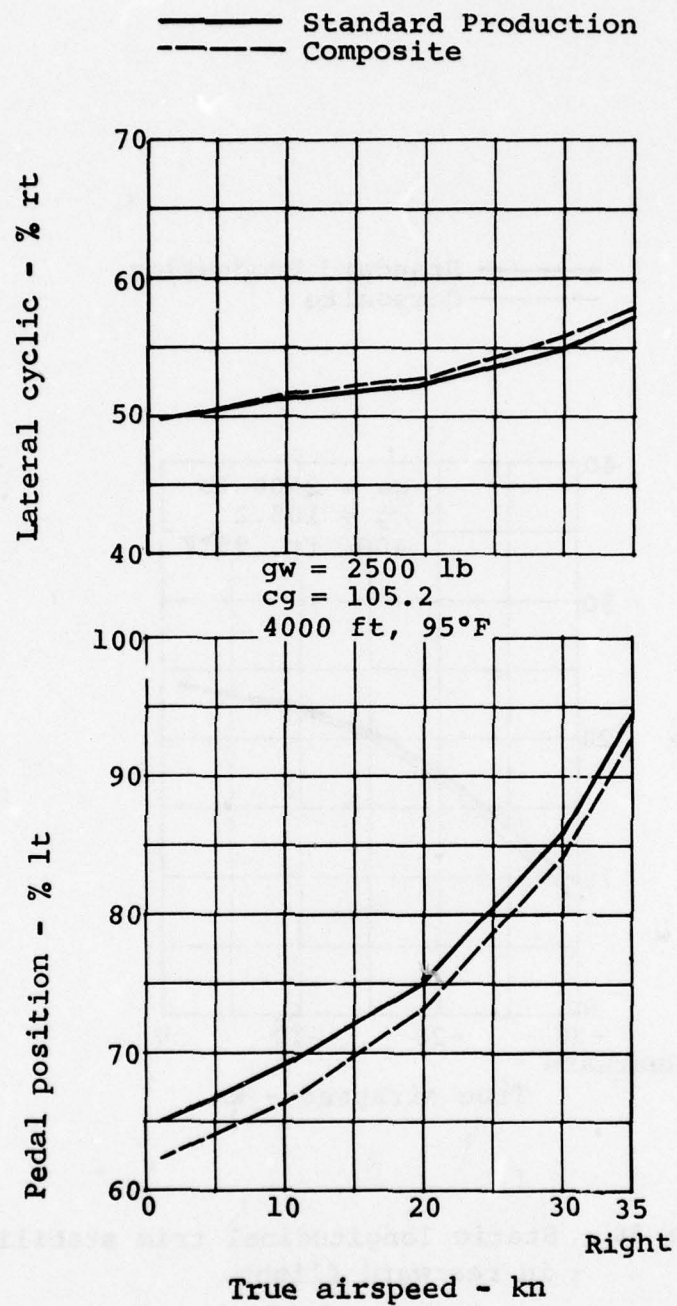


Figure 37. Right sideward flight.

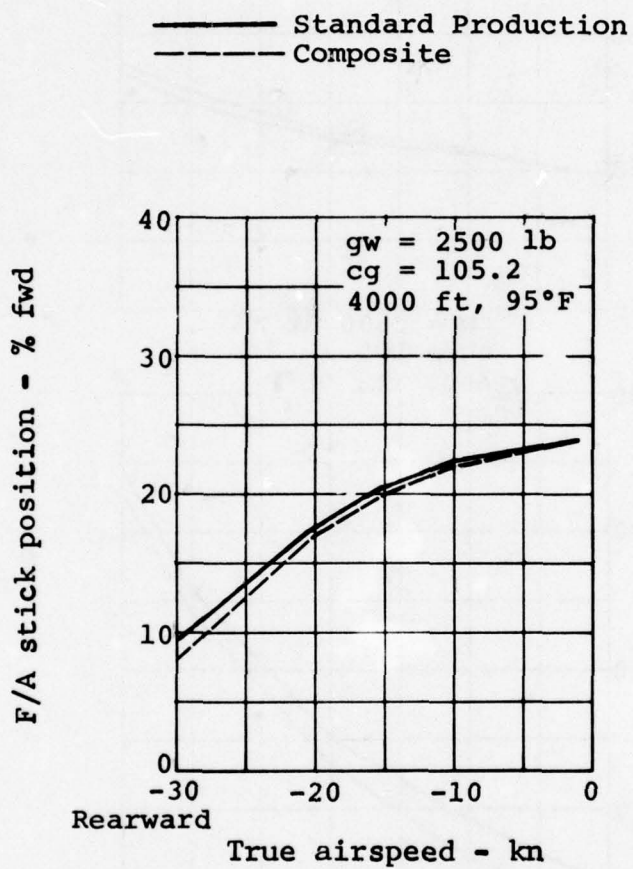


Figure 38. Static longitudinal trim stability in rearward flight.

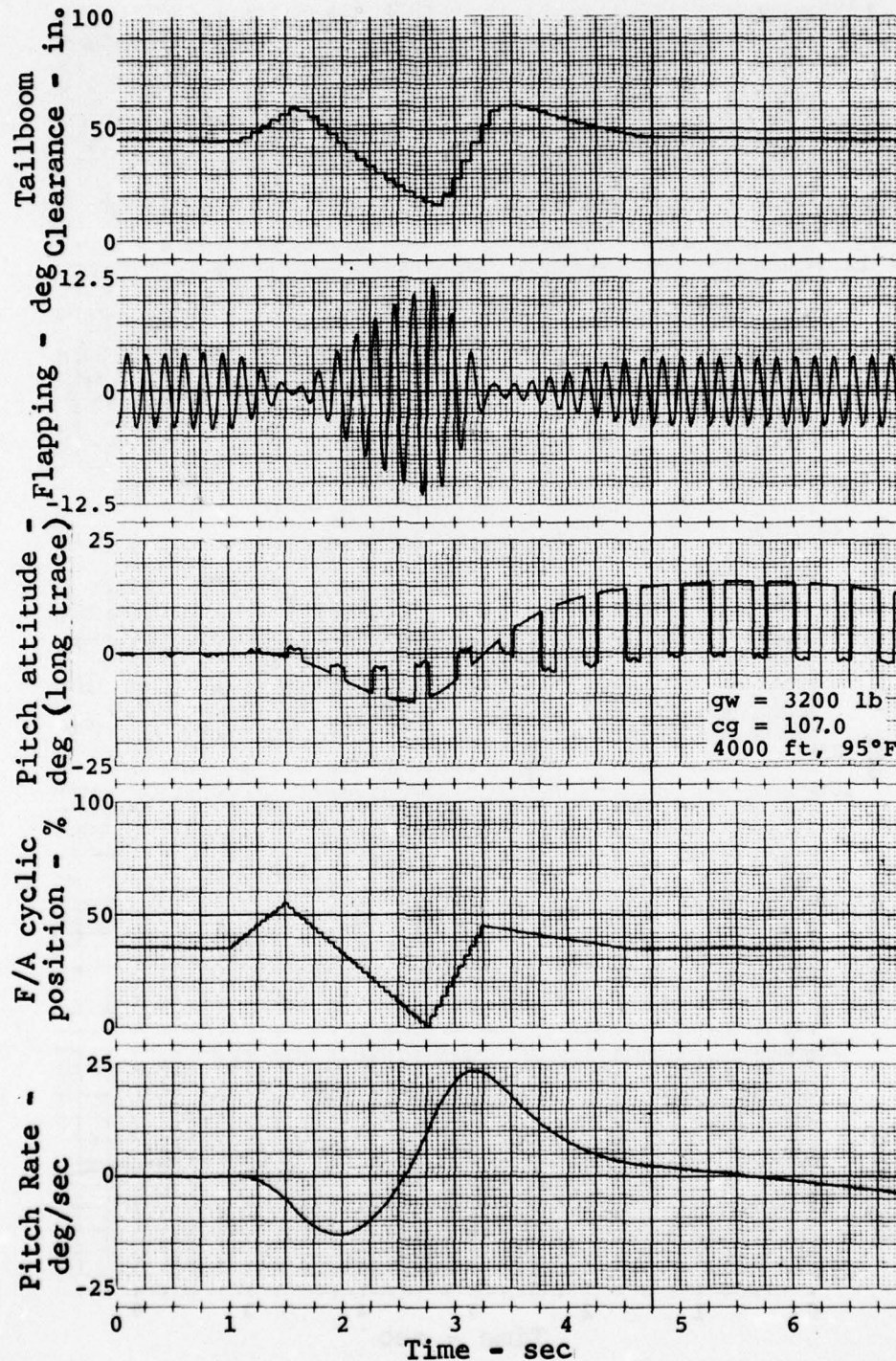


Figure 39. Standard rotor during stick reversal at 20 knots.

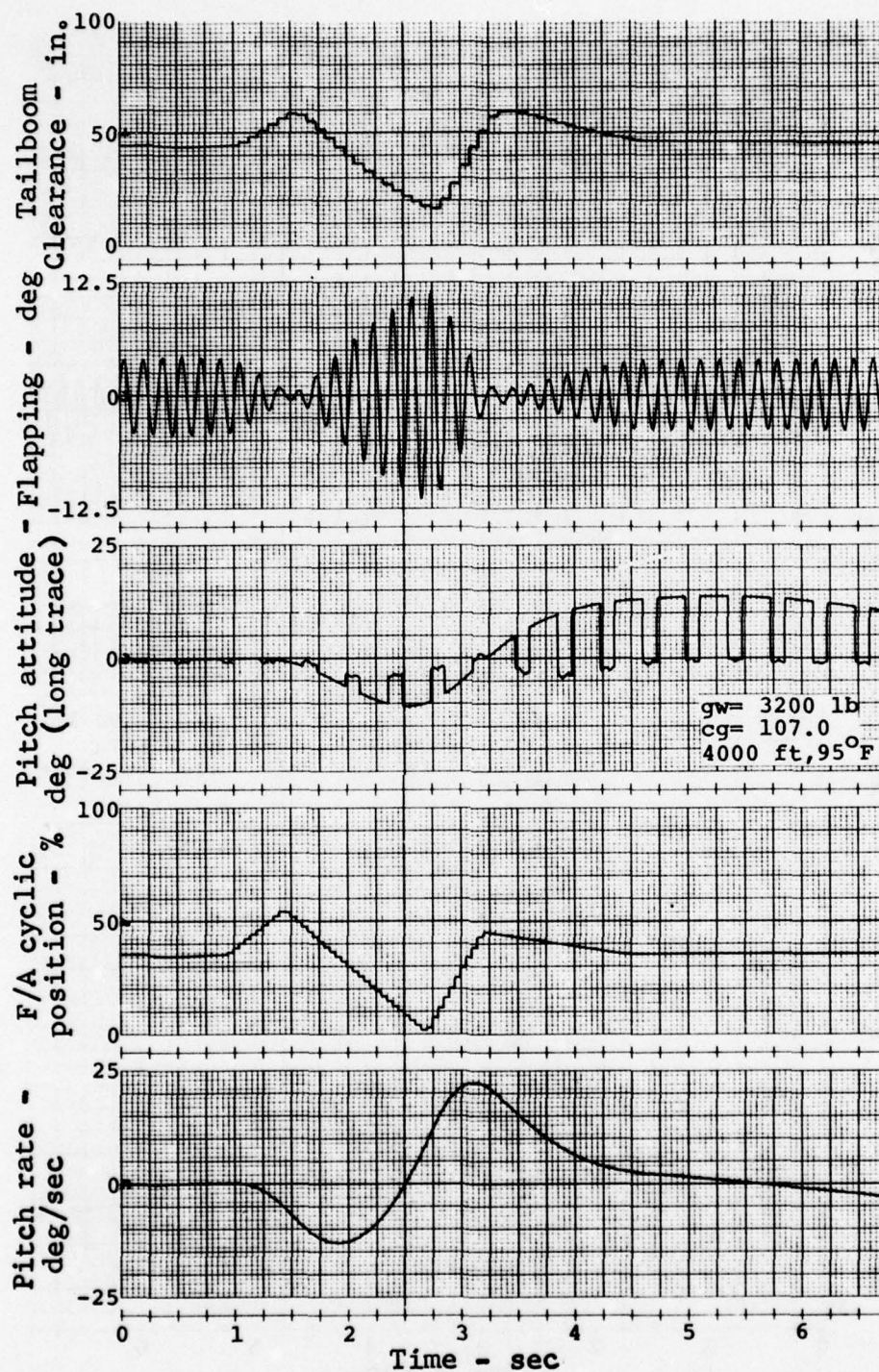


Figure 40. Composite rotor during stick reversal at 20 knots.

4.2.3 Aerodynamic Tests

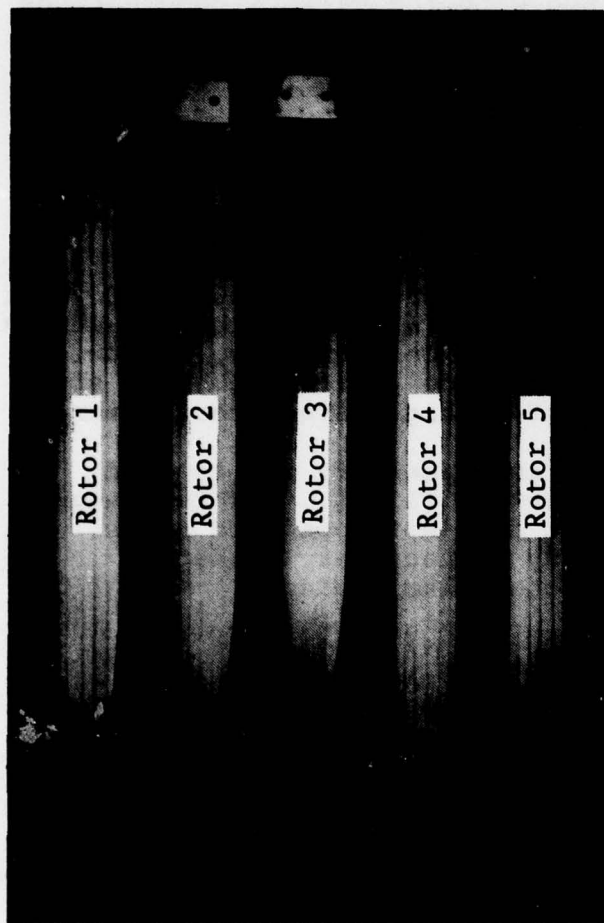
Wind-tunnel tests were conducted to investigate the individual and combined effects of high-lift airfoils, blade taper, and high twist on performance in both hover and forward flight. To accomplish this objective, five sets of 1/14th-scale model blades (defined in Figure 41) were tested at a tip speed of 700 fps.

The performance changes obtained with the various combinations of twist, taper, and airfoil distribution as compared to the performance of the standard blade indicate that:

- The use of high-lift airfoils delays retreating blade stall in forward flight and allows the rotor's thrust-weighted solidity to be reduced for a savings in profile power.
- Blade taper increases performance in both hover and forward flight by reducing the induced and profile power. However, the use of taper alone results in a higher angle-of-attack distribution in the tip region. Consequently, the twist rate must be increased to preclude retreating blade stall during high-speed flight and at high-thrust coefficients.
- Higher twist is beneficial and necessary for tapered blades in both hover and forward flight. For rectangular blades, the increased twist does not appear to be as advantageous. Further study is necessary to better quantify its effects on rectangular blades.

4.2.3.1 Introduction

Prior to this investigation, an experimental aerodynamic performance comparison was conducted between a standard (Rotor 4) and improved (Rotor 1) set of model rotor blades. Through the proper selection of planform taper, twist, and airfoil distribution, it was found that the required hover power could be reduced up to 6 percent and that forward flight power could be reduced by over 10 percent. From these results, the question arose as to how the individual and combined effects of taper, twist, and airfoil contributed to these gains. To properly answer this question would have required up to eight additional sets of blades with the different combinations of taper, twist, and airfoil distribution. From these possible combinations, three sets of blades were chosen that would best determine the components of the performance improvement for a reasonable cost. The hover and forward flight performance of these three sets of blades was then measured. For comparative purposes, the performance for the previously tested standard (Rotor 4) and improved blades (Rotor 1) was repeated.



Rotor No.	Equivalent* Chord (in.)	Radius (in.)	Twist Rates	Planform	Airfoils	Solidity*
Rotor 1	1.30	20	18°, 16°, 14°	tapered	VR-7, 098, 080	0.0414
Rotor 2	1.30	20	18°, 16°, 14°	tapered	NACA 0012	0.0414
Rotor 3	1.30	20	10°	tapered	NACA 0012	0.0414
Rotor 4	1.47	20	10°	square	NACA 0012	0.0468
Rotor 5	1.47	20	18°, 16°, 14°	square	NACA 0012	0.0468

* thrust weighted

Figure 41. Model rotor configurations.

For several reasons, a certain degree of caution must be exercised when extrapolating the model results to full-scale results. This is primarily because of the uncertainty of Reynolds number effects, the influence of Mach number on the data, and the limited number of possible combinations of taper, twist, and airfoil distribution tested. For the model rotor's forward flight comparison, retreating-blade stall occurs at much lower angles of attack, or C_T 's, than for a full-scale rotor because of the retreating blade's low Reynolds number of 40,000 to 50,000. Consequently, performance improvements due to high-lift airfoils show up at lower values of C_T . For the full-scale case, improvements of the same magnitude as the model occur at higher C_T 's or airspeeds where similar amounts of retreating-blade stall are present and the advantage of the high-lift airfoils becomes prominent.

Model Rotors and Test Apparatus

The five rotors compared in this test were fabricated from laminated basswood. An embedded brass strip provided a 25-percent chordwise balance. The five 1/14th-scale blades and their respective geometric parameters are shown in Figure 41. Both the rectangular and tapered planform have the same geometric solidity. However, on a thrust-weighted basis, the solidity of the tapered planform is 11 percent less. The distribution of the chord, twist, and airfoils for the various blades is shown in Figure 42.

Figure 43 shows the test stand in the Vought Corporation's slow-speed wind tunnel. During the performance measurements, a schlieren system was used to monitor the rotor's wake structure for easier interpretation of the performance trends.

A diagram of the test stand is shown in Figure 44. Thrust is measured along the control axis, which is the same as the shaft axis for this direct control rotor system. Summation of forces in the vertical direction gives

$$T \cos \alpha_s + H \sin \alpha_s = W \quad (5)$$

whereas, in the horizontal direction they are

$$T \sin \alpha_s = D + H \cos \alpha_s \quad (6)$$

Eliminating second order terms and substituting $H = T a_1$ gives

$$T \cos \alpha_s = W, \text{ and} \quad (7)$$

$$T \sin \alpha_s = D + T a_1 \cos \alpha_s \quad (8)$$

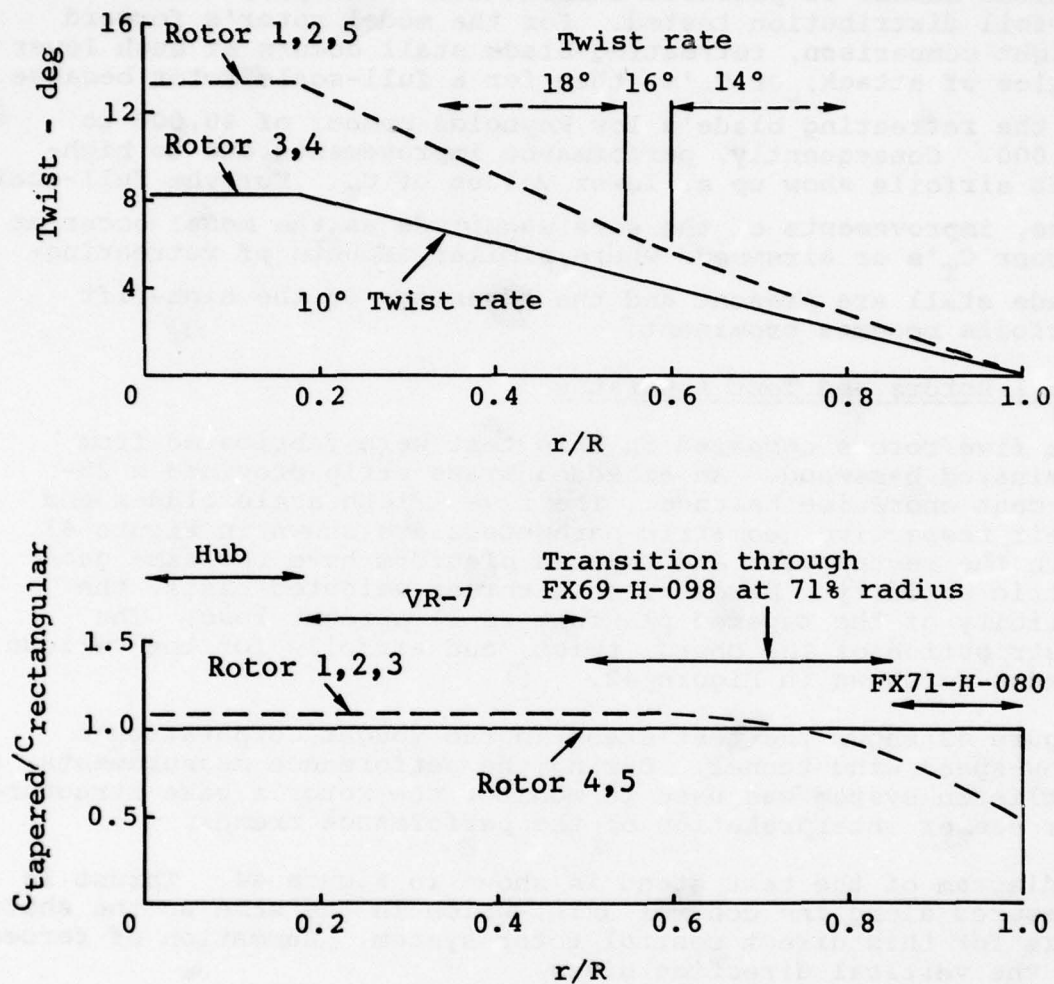


Figure 42. Chord, twist, and airfoil distribution for the model rotors.

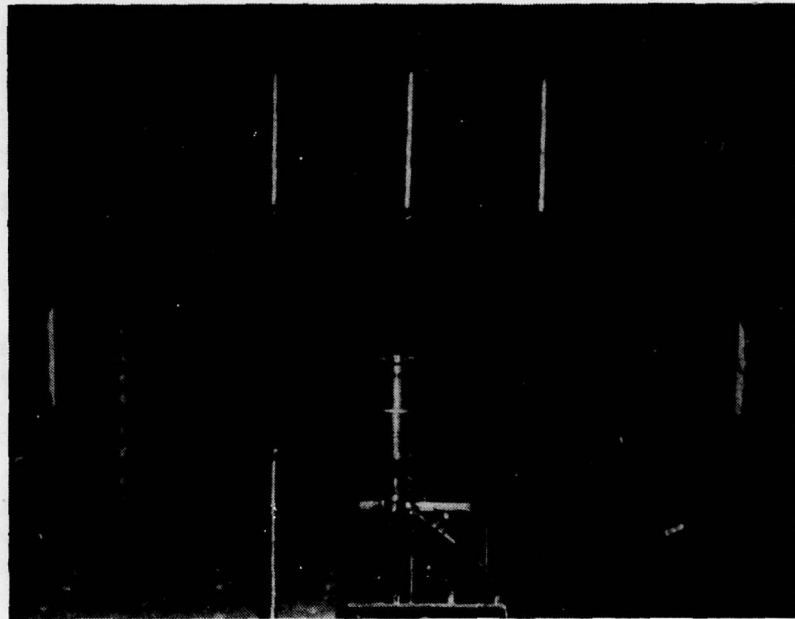


Figure 43. Test stand in anechoic wind tunnel.

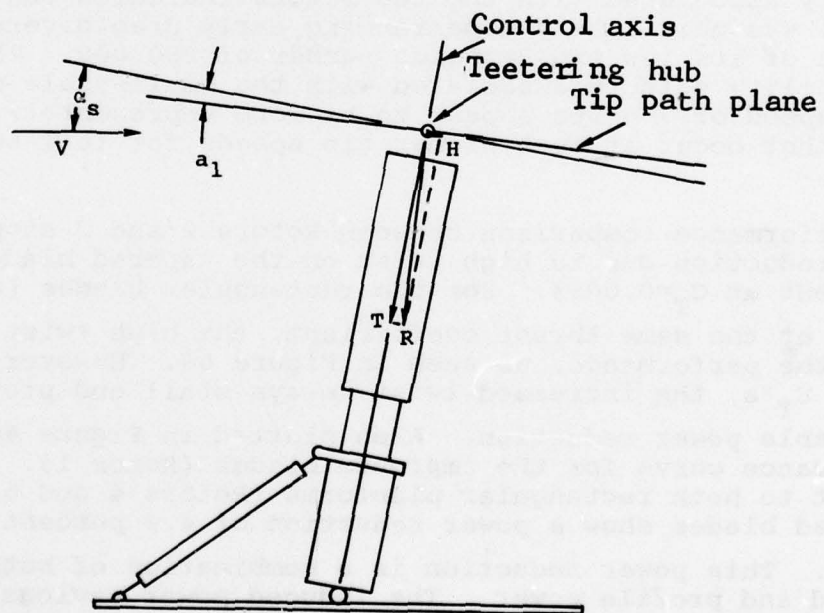


Figure 44. Components of resultant rotor force.

The shaft angle for positioning the rotor in the wind tunnel for a given flight condition is calculated using C81 based on the helicopter's weight (W) and drag (D). The model rotor's flapping angle, a_1 , is measured from schlieren photographs taken of a rotating blade at $\psi_p = 180^\circ$ with and without the wind tunnel operating. From a_1 , the H-force component can be determined.

4.2.3.2 Experimental Hover Results and Discussion

The hover performance comparison between the three sets of tapered blades in Figure 45 illustrates differences due to an improved airfoil distribution and increased twist. For the reference operating condition of $C_T = 0.0033$, the power reduction due to the improved airfoil distribution was measured to be 11 percent at a tip speed of 700 fps. This gain, due to airfoils alone, was much higher than anticipated. Further investigation indicated that compressibility effects contributed to this abnormally high improvement. The performance of Rotor 2 with the NACA 0012 airfoil improved with decreasing tip speed, whereas this was not the case with Rotor 1 with the FX71-H-080 airfoil in the tip region. At reduced tip speeds of 400 and 550 fps, the performance of Rotor 2 improved to where the power reduction due to airfoil distribution is 8 percent rather than 11 percent. Schlieren flow visualization of the tip compressibility associated with the two rotors indicated that the 0012 airfoil was most likely experiencing early drag divergence because of its low tip Reynolds number of 280,000. The compressibility effects associated with the small-scale models at a tip speed of 700 fps appear to be more representative of those that occur at much higher tip speeds for full-scale rotors.

The performance comparison between Rotors 2 and 3 showed the power reduction due to high twist on the tapered blade to be 4 percent at $C_T = 0.0033$. For the rectangular blades (Rotors 4 and 5) at the same thrust coefficient, the high twist did not alter the performance, as seen in Figure 46. However, for higher C_T 's, the increased twist delays stall and provides a noticeable power reduction. Also plotted in Figure 46 is the performance curve for the improved blades (Rotor 1). With respect to both rectangular planforms (Rotors 4 and 5), the improved blades show a power reduction of 4.9 percent at $C_T = 0.0033$. This power reduction is a combination of both power-induced and profile power. The induced power savings is attributed to the tapered planform and high twist, whereas the profile power savings is attributed to these factors along with the improved airfoil distribution. However, as the improved blade approaches stall, the high-twist rectangular

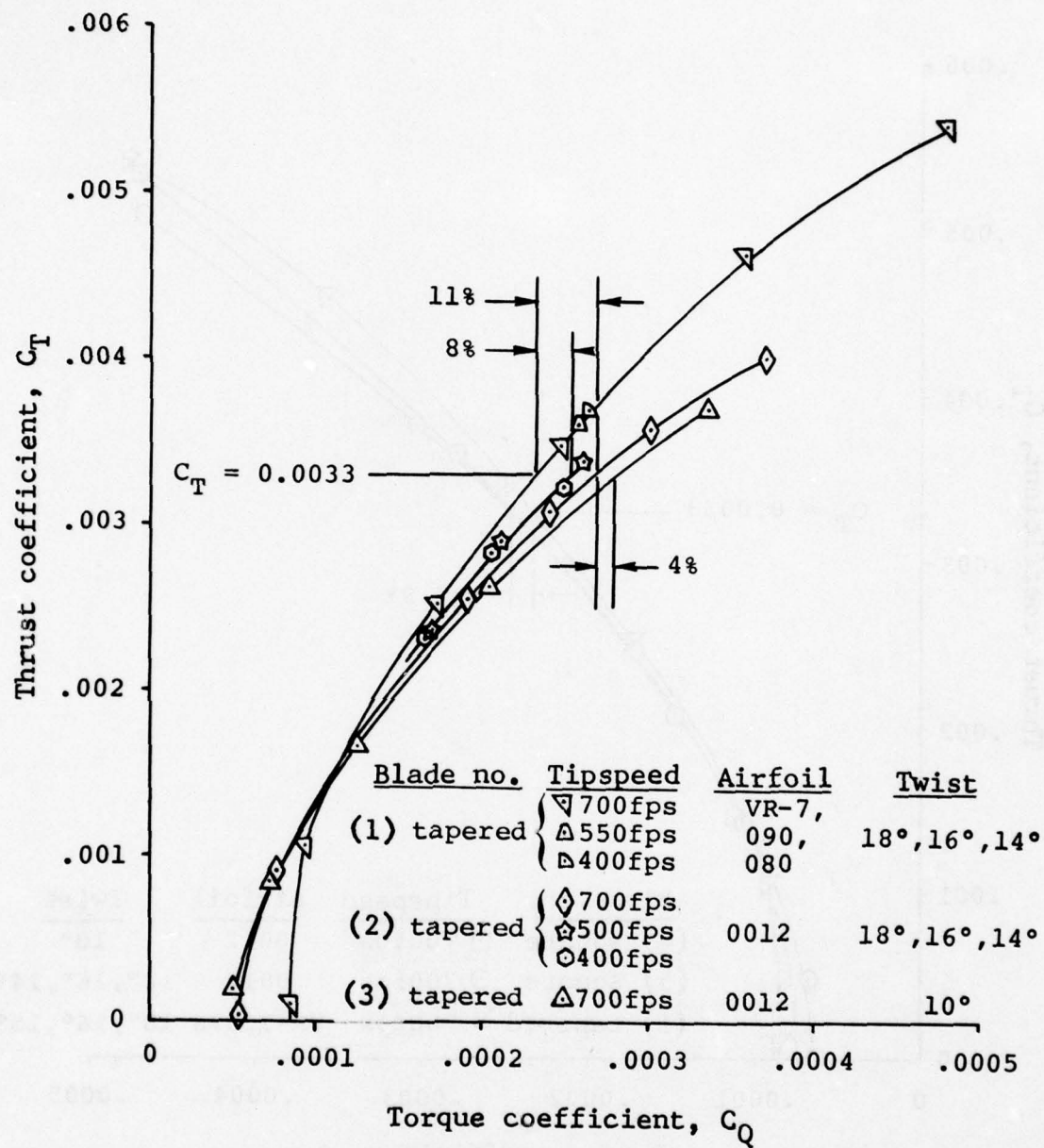


Figure 45. Hover performance comparison for tapered blades.

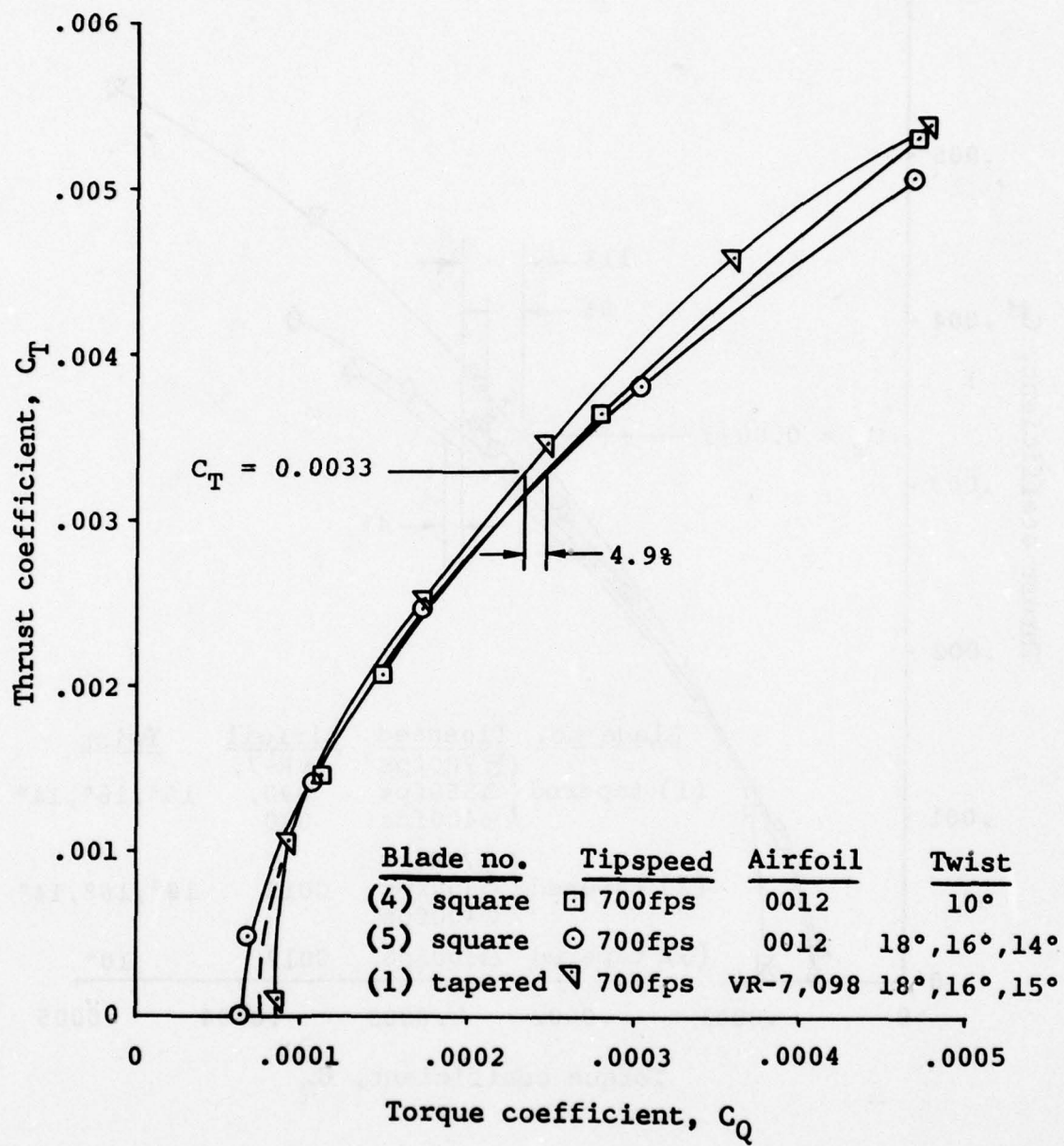


Figure 46. Hover performance comparison for rectangular blades.

blades (Rotor 5) close the performance gap because of higher thrust-weighted solidity.

4.2.3.3 Experimental Forward Flight Results and Discussion

The forward flight performance characteristics of the five sets of blades are shown in Figure 47 for a C_T of 0.0031. The data are presented as a ratio of lift/effective drag versus airspeed where

$$\text{effective drag} = \frac{\text{total power}}{\text{airspeed}} - \text{rotor propulsive force}$$

$$\text{and rotor propulsive force} = T \sin \alpha_s - T a_1 \sin \alpha_s \quad (9)$$

The improved blades (Rotor 1) show an impressive performance gain that increases with airspeed over the standard rectangular blades (Rotor 4). The improvement varies from 8 percent at 60 knots to well over 10 percent at airspeeds greater than 80 knots. The overall performance of the high-twist rectangular blades (Rotor 5) was not significantly different from the standard blades (Rotor 4) at this C_T . The high twist (Rotor 5) required slightly more power up to 85 knots due to negative tip loading on the advancing blade at a low C_T of 0.0031. Above 85 knots, the high twist delays retreating-blade stall, and the performance of Rotor 5 is slightly better than for the low twist (Rotor 4). At higher C_T 's, it is expected that Rotor 5 with the high twist would provide better performance than Rotor 4 over the whole speed range since its advancing blade would experience less negative loading.

A comparison between the two tapered blades with the 0012 airfoil (Rotors 2 and 3) shows the high twist (Rotor 2) to provide a performance improvement over the whole speed range. This trend differs from the rectangular blade comparison mainly because the tapered blades are operating at higher blade loading due to their thrust-weighted solidity being 11 percent less than the rectangular blades. At the higher blade loading, the increased twist provides a more favorable load distribution that results in reduced power. The rapid drop-off in the lift/effective drag ratio above 80 knots is thought to be due to early drag divergence of the 0012 airfoil for an advancing-blade Reynolds number of 350,000, as experienced for the hover data. Without the use of high-lift airfoils on the reduced solidity tapered rotors (Rotors 2 and 3), their performance falls below the rectangular planform rotors (Rotors 4 and 5). For a valid performance comparison between these two sets of blades, they should be at the same thrust-weighted solidity.

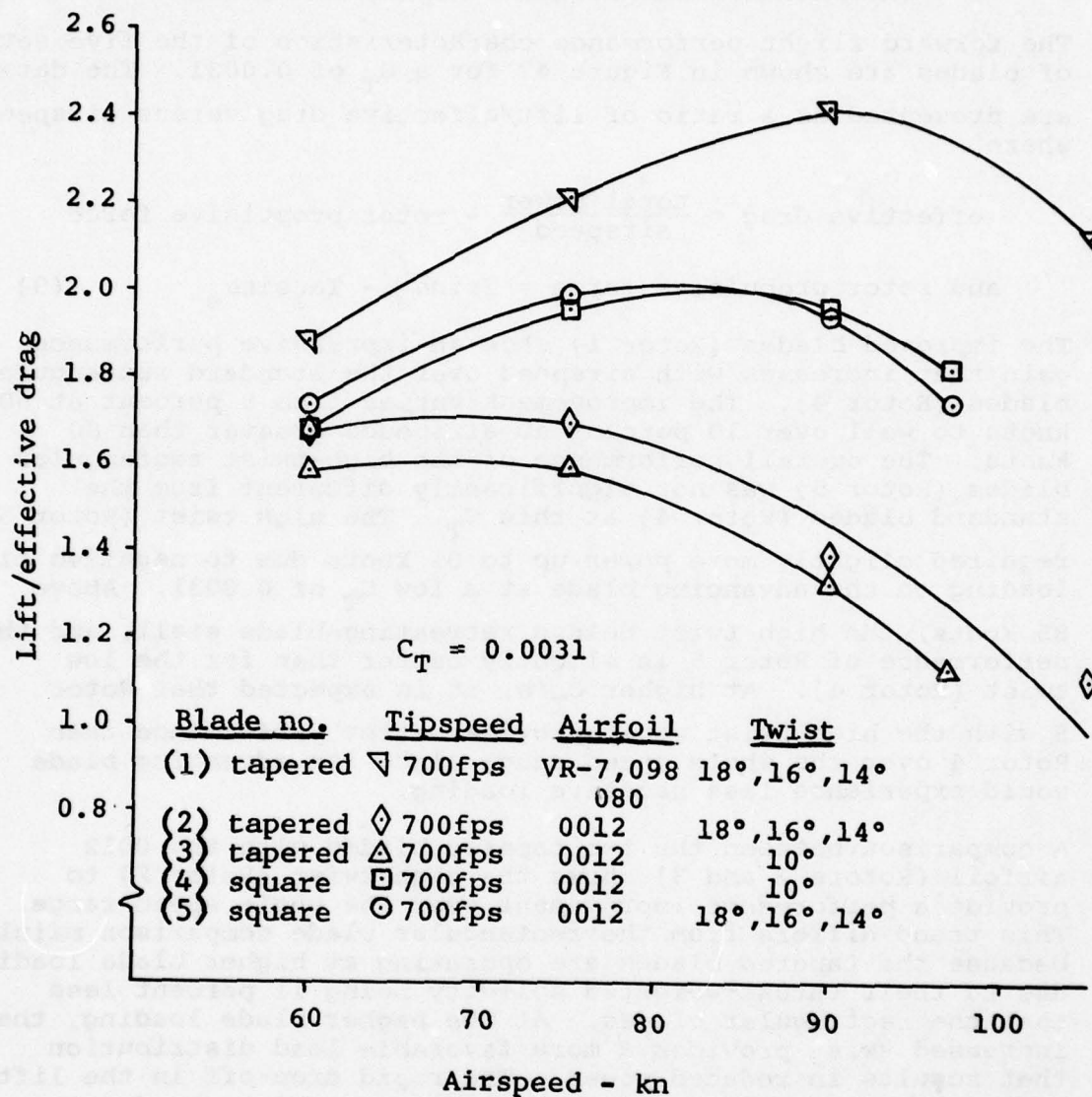


Figure 47. Forward flight performance comparison.

The longitudinal flapping blowback angle, α_1 , for each of the five model rotors is shown in Figure 48 versus airspeed along with the calculated angle for the standard (Rotor 4) full-scale blades. The data shown indicate that for a given twist distribution the flapping is proportional to the amount of retreating blade stall. This trend is reasonable since this angle is dependent on a rotor's lift distribution around blade azimuths of 90 and 270 degrees.

4.2.3.4 Rotor Noise

Various means of reducing blade slap and broadband noise have been investigated with varying degrees of success by both industry and government. Most of these do so at the expense of performance and added blade complexity. The advantage of the improved blades (Rotor 1) is that they provide a substantial reduction in broadband noise and reduced blade slap, while at the same time increasing performance and reducing the oscillatory loads. This is achieved through the proper choice of blade taper, thickness, and airfoil distribution. Through the use of taper, more loading is carried inboard on the blade. This results in a weaker tip vortex that interacts with a following blade to reduce blade slap. Reduced blade thickness in the tip region results in lower broadband noise and reduced high-speed blade slap, while the use of an airfoil having a favorable drag divergence Mach number at negative lift coefficients reduces both partial power descent and high-speed blade slap.

4.3 STRUCTURAL ANALYSIS

4.3.1 Section Properties

Laminate properties used in the structural analysis were calculated by BHT Composite Analysis Program SC1701. Considering lamina material, orientation, and thickness, Program SC1701 performs a linear analysis to produce composite laminate properties. Material properties used in this analysis are given in Table 14. Blade section properties were determined by BHT Program CBCR04. CBCR04 is a combined bending and torsional analysis program. Blade cross section geometry is described to the program as quadrilateral cells with each cell wall having as many layers as the different materials used. The cellular description is required because the program calculates torsional section properties based on thin-walled multicellular theory.

Program CBCR04 produces beam, chord, axial, and torsional stiffnesses as well as weight distribution, mass moments of inertia, and center of gravity, neutral axis, and shear center location. Typical blade sections are shown in Figure 7.

$$C_T = 0.0031$$

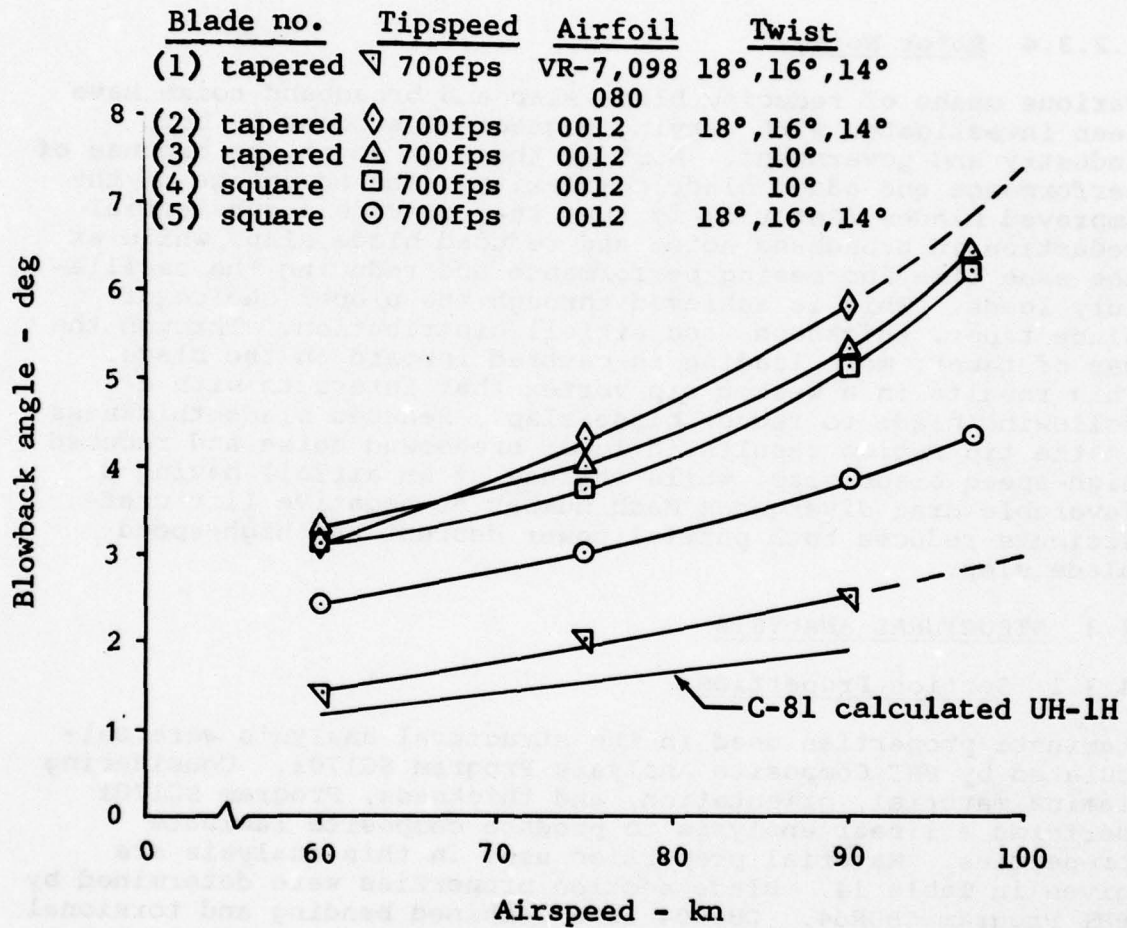


Figure 48. Blowback angle versus airspeed.

TABLE 14. MATERIAL PROPERTIES

	Tension* Modulus $E \times 10^{-6}$ (lb/in. ²)	Shear Modulus, $G \times 10^{-6}$ (lb/in. ²)	Density (lb/in. ³)	Tension* Ultimate F_{tu} (lb/in. ²)	Shear Ultimate F_{su} (lb/in. ²)	Compression Ultimate F_{cu} (lb/in. ²)
1. Uniglass 0° S-Glass	6.75	.76	.069	190,000	11,000	-150,000
2. Torque Wrap** ±45° S-Glass	2.33	1.89	.069	26,000	50,000	-26,000
3. Skin ±45° S-Glass**	2.33	1.89	.069	26,000	50,000	-26,000
4. Doubler -30° S-Glass	1.56	.95	.069	14,400	15,900	-20,300

*Tension properties are in the spanwise direction

**BHT test values

Section property distributions are plotted in Figures 49 through 55.

4.3.2 Load Determination

4.3.2.1 Static Limit Loads

BHT Program SB3301 was used to calculate limit hub and blade loads. The program calculates blade moment and force distributions that result from limit beam, chord, and torsion design loads. The following blade properties are considered: beam and chord stiffnesses, weight, center of gravity, and neutral axis location for each blade segment in the model (24 in this case).

Four load conditions were analyzed. Each condition is a combination of rotor RPM, vertical g's, and root chord moment selected to represent the most severe design situation. Design rotor speeds of 411 and 304 RPM, vertical g's of 2.34 and .5, and gross weight of 3200 pounds were taken from Reference 5. For each condition, loads appear as triangular airloads distributed from the 25 percent blade radius station to the tip. The beam airload magnitude is that required to balance the product of the g-loading and the design gross weight. The chord airload balances an input root-chord moment determined from the mast torque, and an experience factor used to account for observed dynamic peak loads.

This chord moment is given by:

$$M_{CO} = M_T (1/2 + K) \quad (10)$$

with $K = 1$

and $M_T = 53,000$ in.-lb (292 hp continuous at 347 RPM).

Therefore,

$$M_{CO} = 53,000 (1/2 + 1) = 79,500 \text{ in.-lb (power on)}$$

$$\text{and } M_{CO} = 53,000 (-1) = -53,000 \text{ in.-lb (power off)}$$

⁵Jordan, G. L., STRUCTURAL DESIGN CRITERIA FOR 206A-1/OH-58A, Report 206-099-200, Bell Helicopter Textron, Fort Worth, Texas, August 1968.

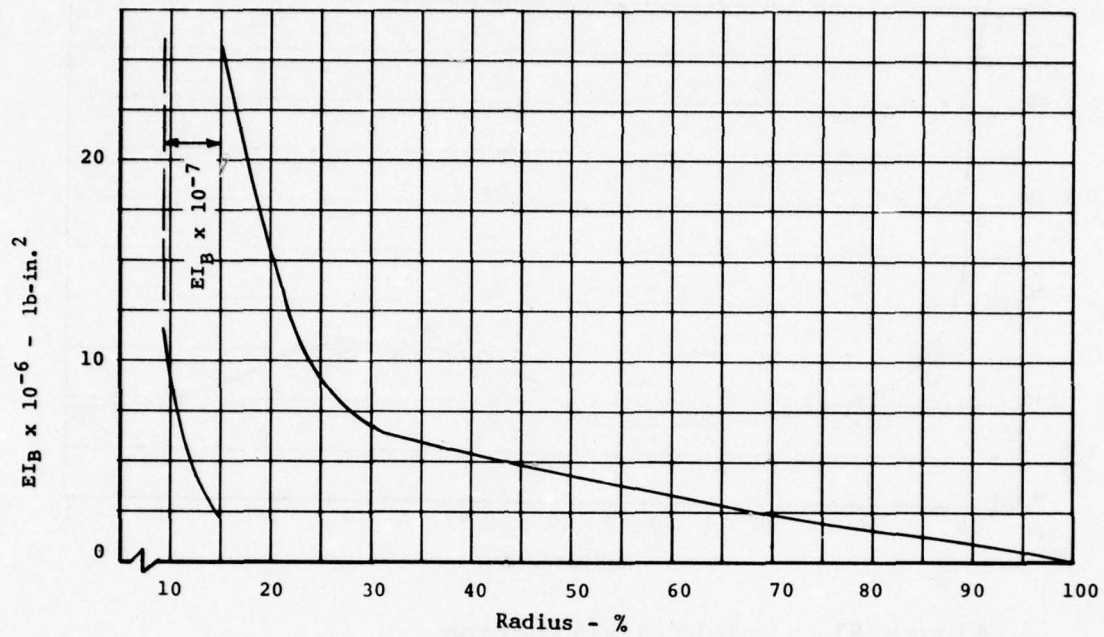


Figure 49. Beamwise stiffness distribution.

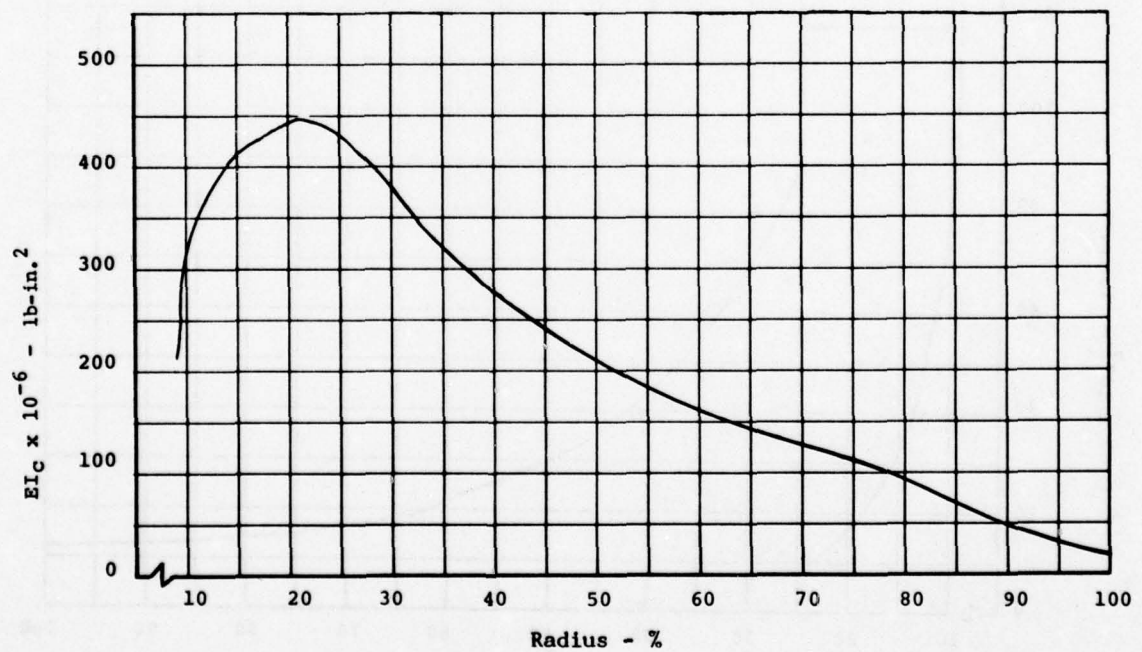


Figure 50. Chordwise stiffness distribution.

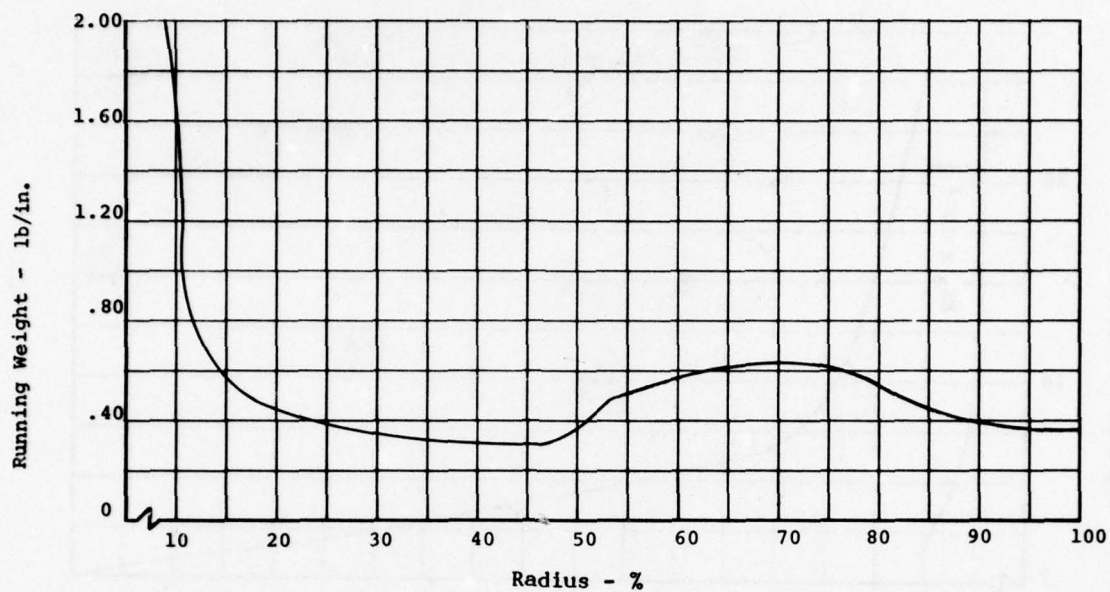


Figure 51. Weight distribution.

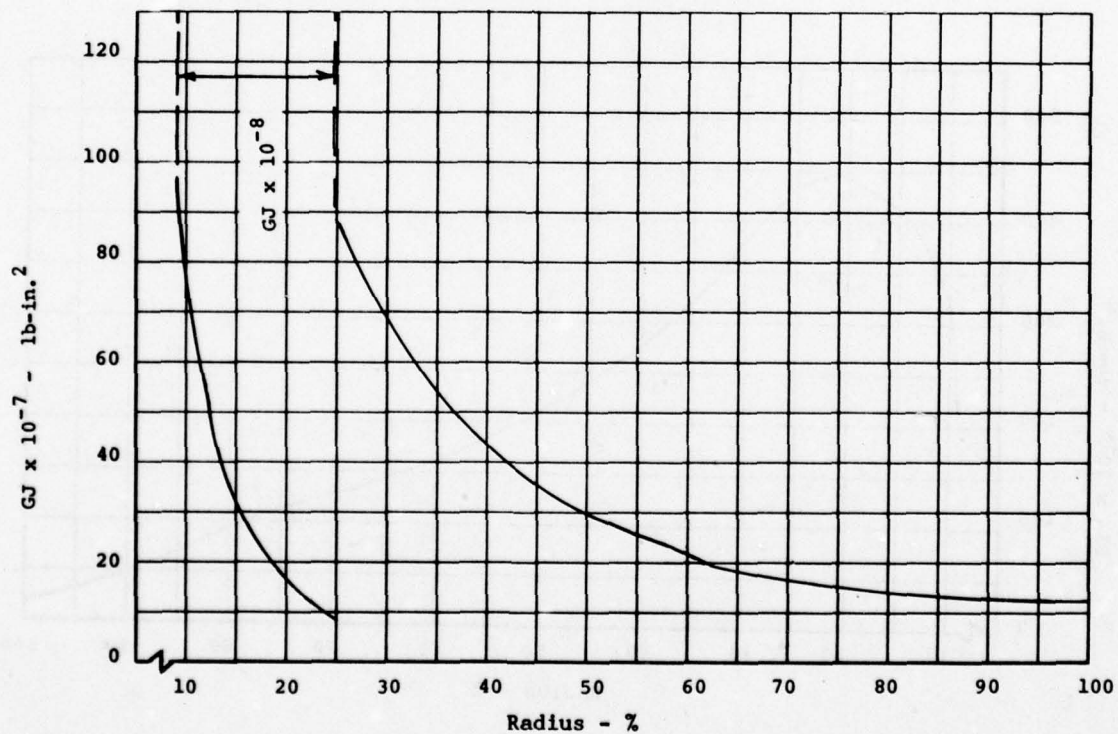


Figure 52. Torsional stiffness distribution.

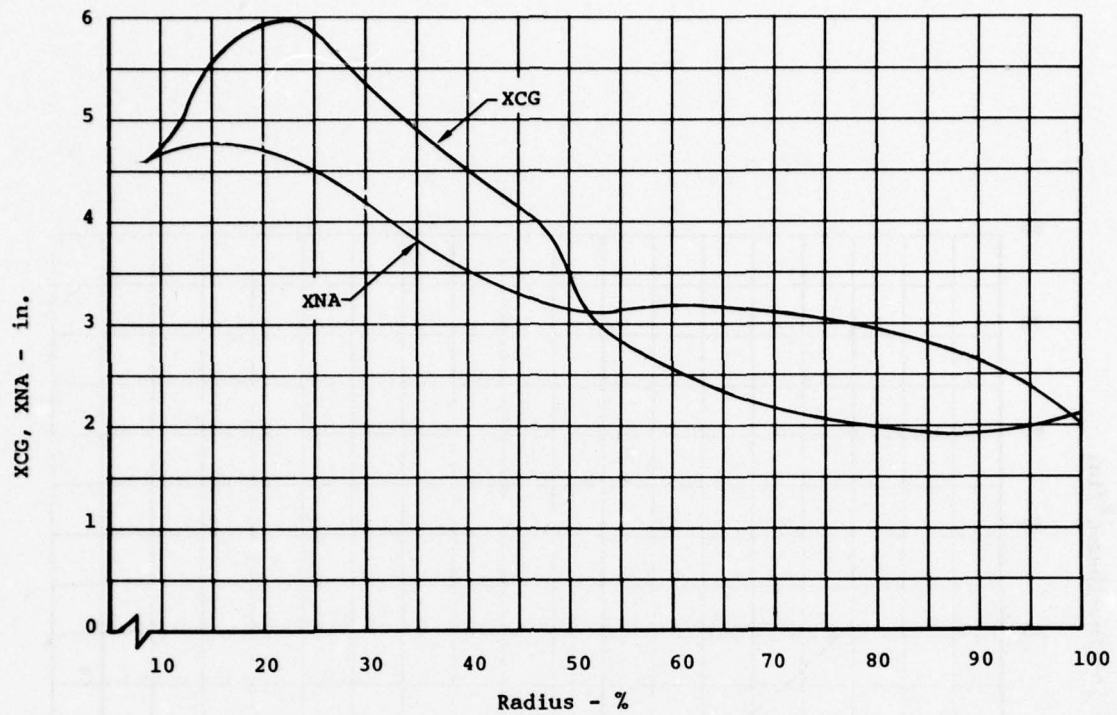


Figure 53. Center of gravity and neutral axis distribution.

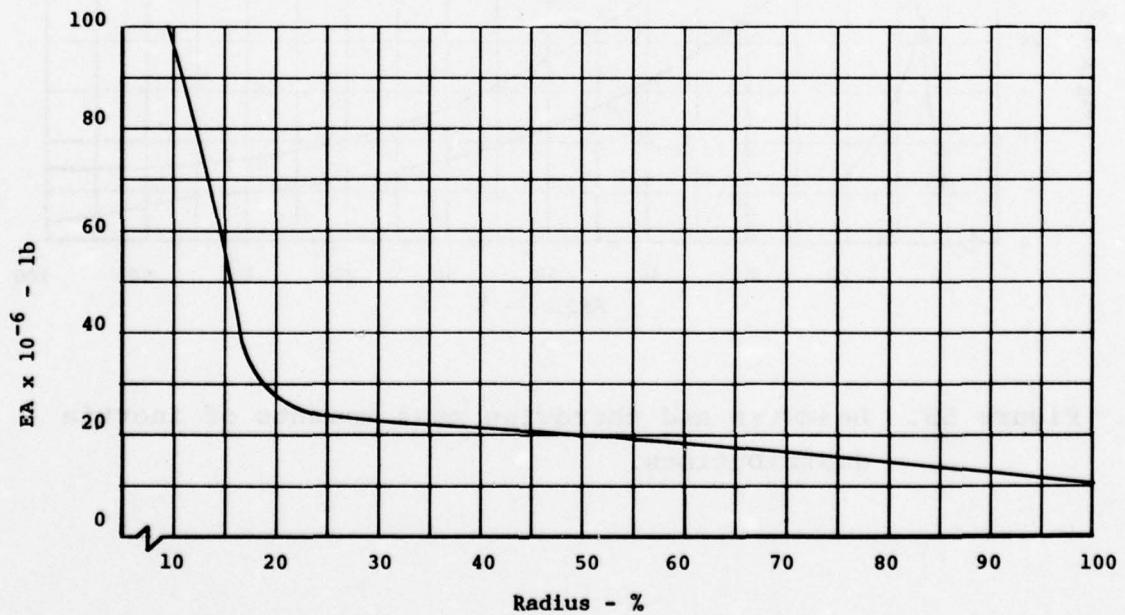


Figure 54. Axial stiffness distribution.

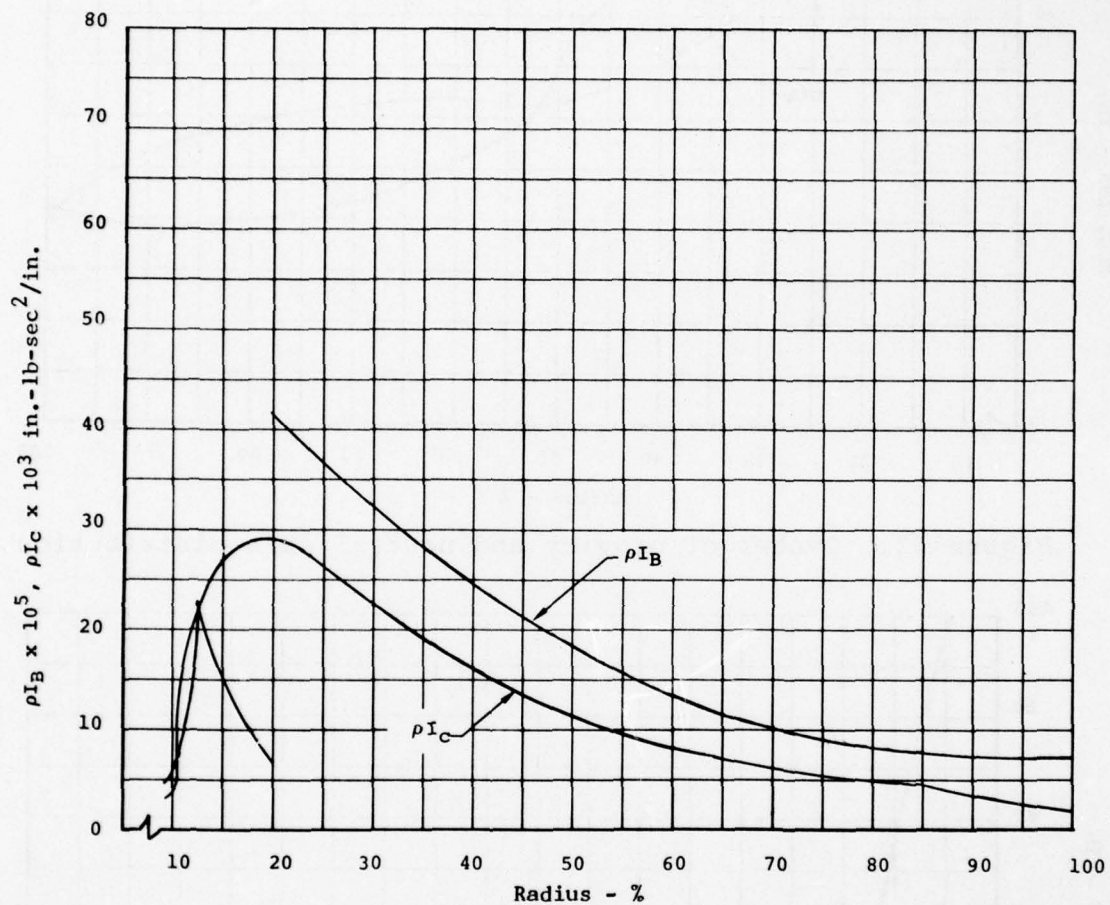


Figure 55. Beamwise and chordwise mass moments of inertia distributions.

Of the possible combinations of RPM, g's, and root-chord moment, the four basic conditions used for analysis were (all at 3200-pound gross weight):

<u>Condition</u>	<u>M_{Co}</u>	<u>RPM</u>	<u>Vertical g's</u>
1	79,500	411	-.5
2	-53,000	411	-.5
3	79,500	304	2.34
4	-53,000	304	2.34

The design torsional moment was calculated from a limit pitch link load of 1200 pounds from Reference 6 and a 7.2-inch pitch horn radius from the pitch change axis. The magnitude of this moment is, therefore, $1200 \times 7.2 = 8640$ in.-lb. The static torsional distribution is the result of offsetting the beam airload by the amount necessary to balance the input torsional load at the pitch horn location.

A condition 5 was added to the four basic cases listed above. This condition combines the effect of static droop and rotor start. Static droop loads were taken at two g's and rotor start loads were calculated to balance two times the maximum design horsepower (317 hp at 347 RPM). Based on the design conditions outlined here, the load distributions shown in Figures 56 through 59 were produced.

4.3.3 Stress Analysis

4.3.3.1 Blade Bolt Hole

A main bolt hole cross section illustrating the uniglass portion of the lug is shown in Figure 60. Only beamwise moment and centrifugal force were considered in this analysis because the chordwise moment was assumed to be coupled out in the grip plates.

⁶Eaton, H., et al., CONTROL SYSTEMS STRUCTURAL ANALYSIS, February 1969.

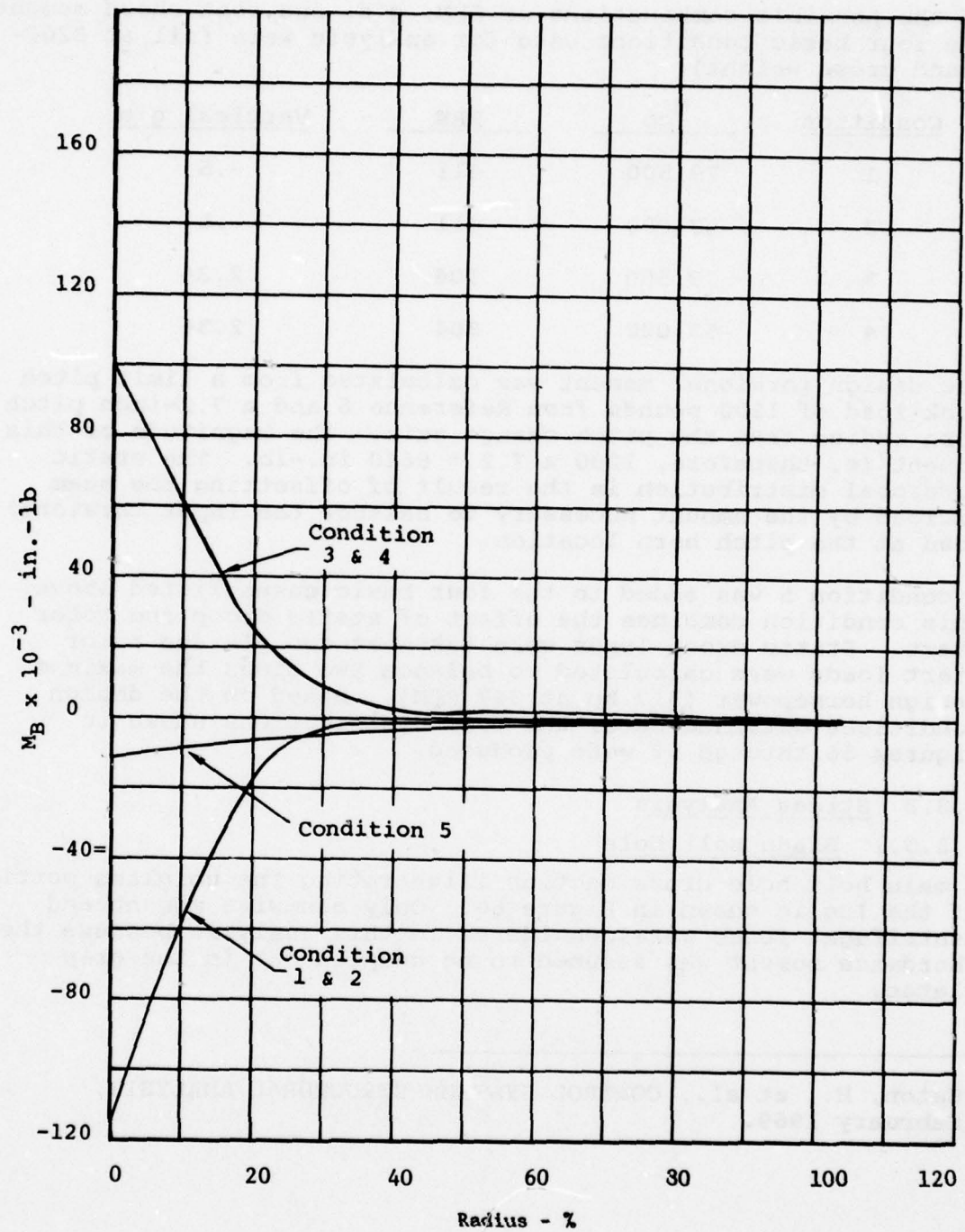


Figure 56. Limit beamwise bending moment distribution.

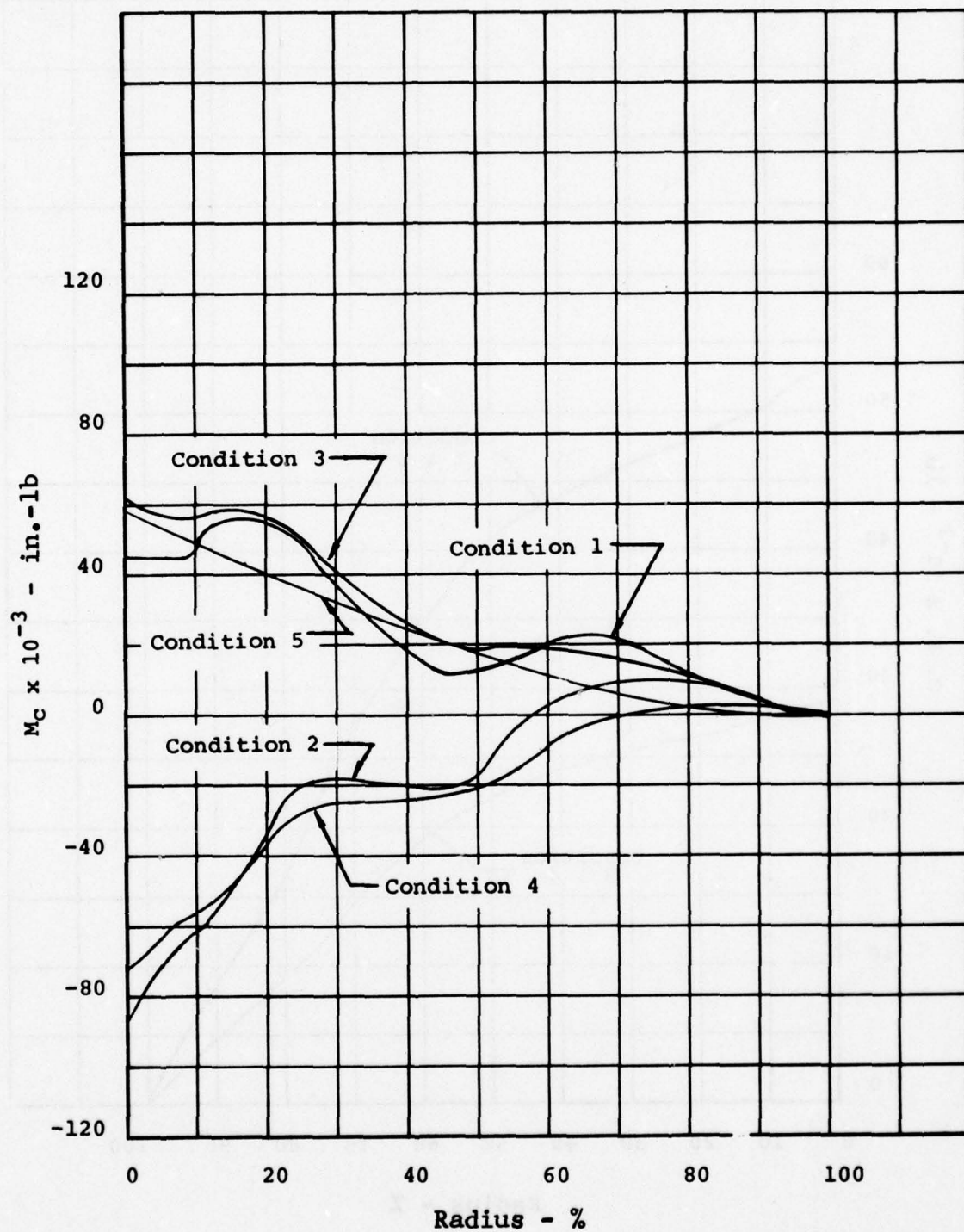


Figure 57. Limit chordwise bending moment distribution.

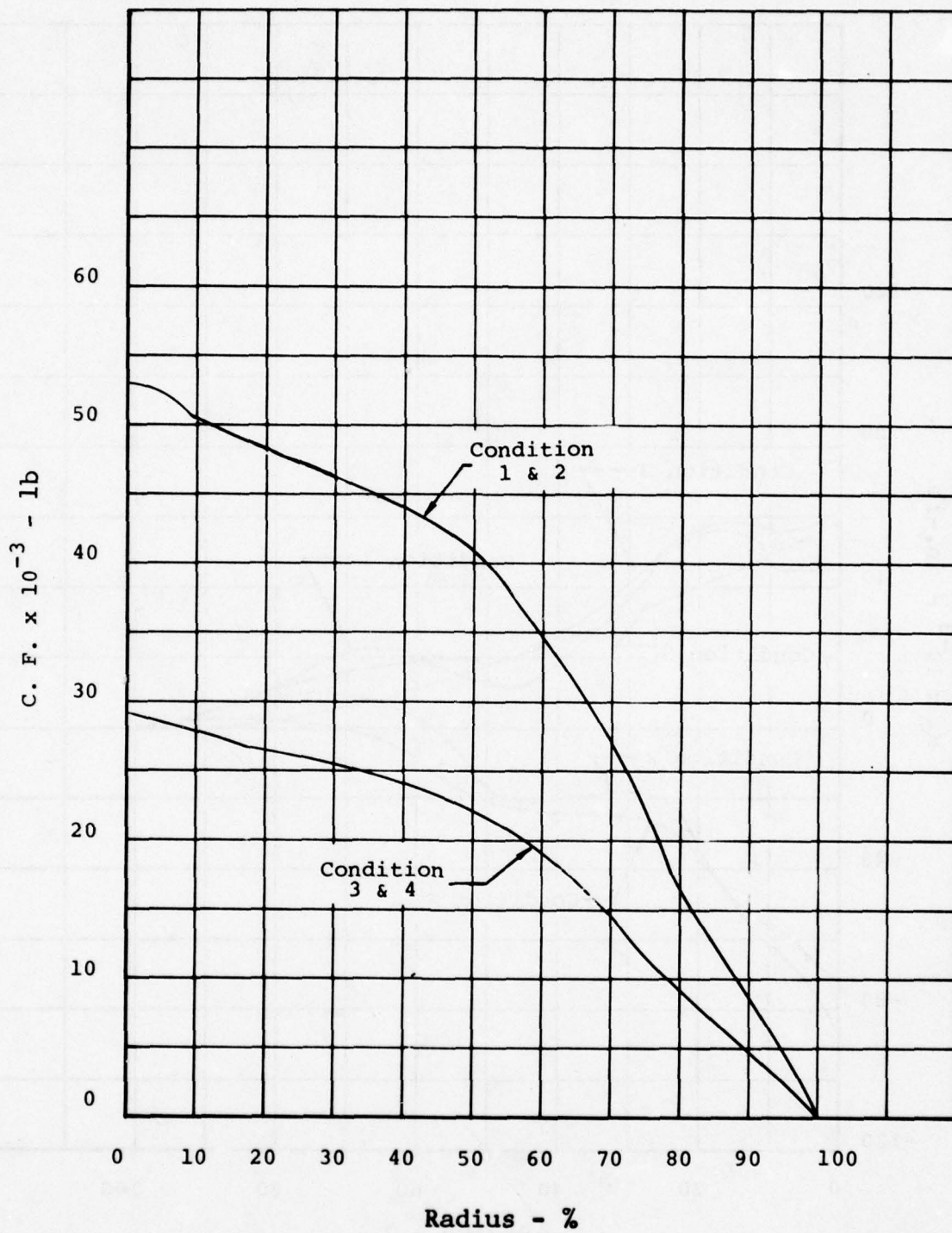


Figure 58. Limit centrifugal force distribution.

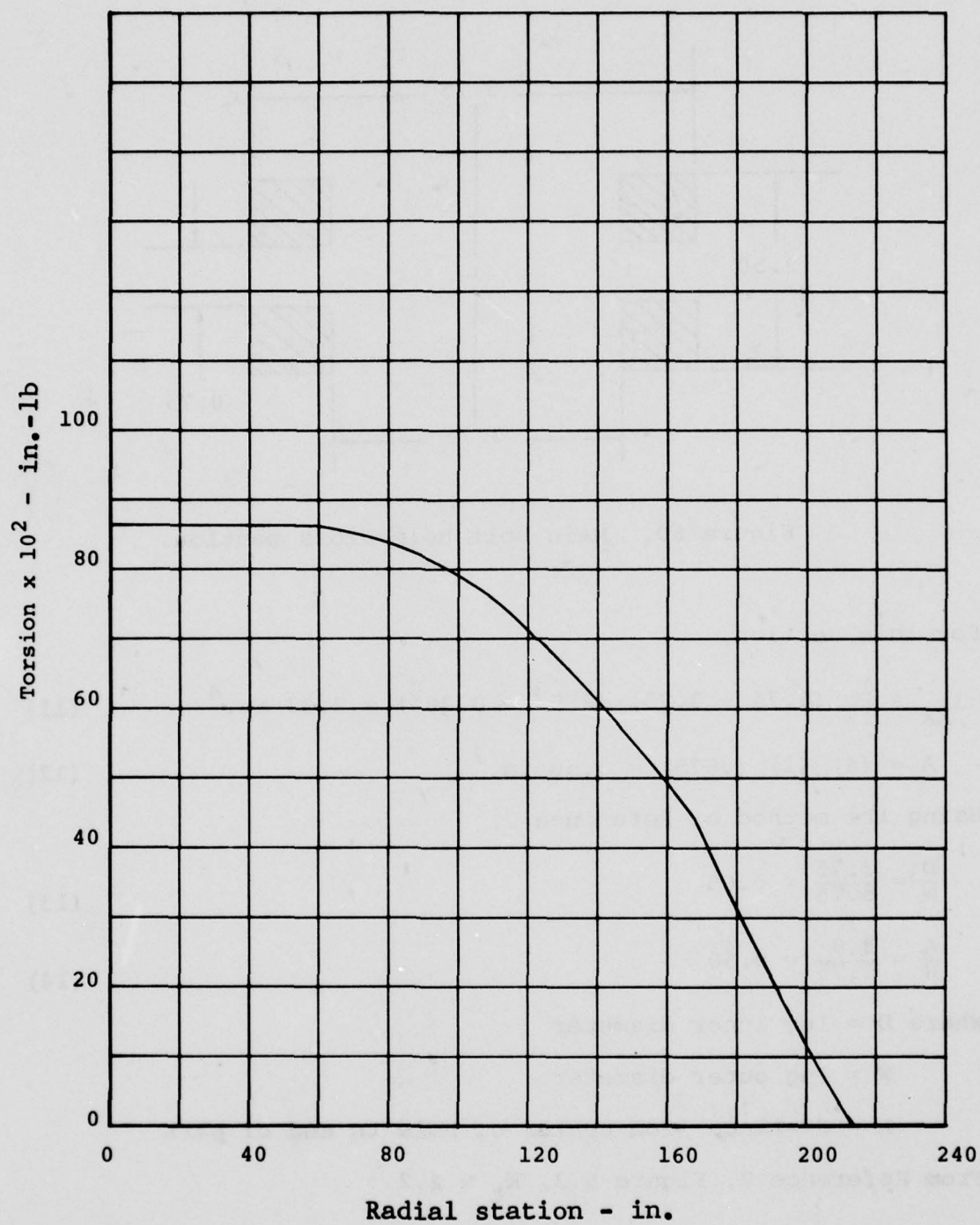


Figure 59. Limit torsional load distribution.

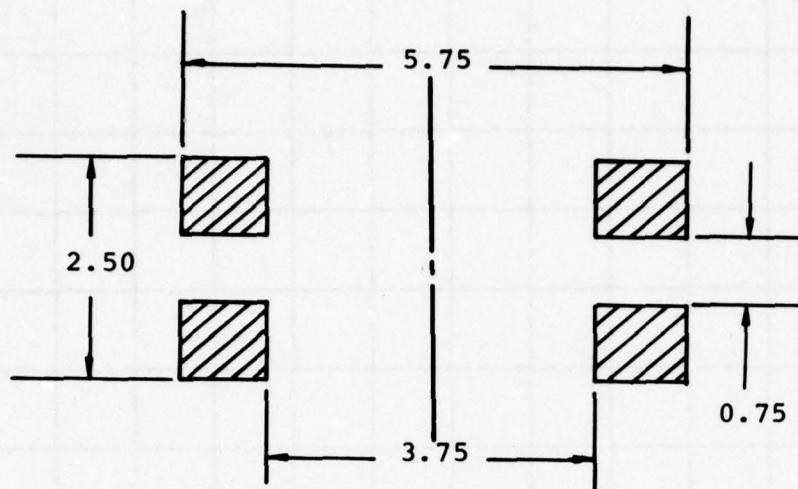


Figure 60. Main bolt hole cross section.

For this section,

$$I_{XX} = \frac{1}{12} (5.75 - 3.75) (2.5^3 - 0.75^3) = 2.53 \text{ in.}^4 \quad (11)$$

$$A = (4) (1) (.875) = 3.50 \text{ in.}^2 \quad (12)$$

Using the method of Reference 7,

$$\frac{D}{W} = \frac{3.75}{5.75} = 0.65 \quad (13)$$

$$\frac{A}{W} = \frac{2.9}{5.75} = 0.50 \quad (14)$$

Where D = lug inner diameter

W = lug outer diameter

A = distance from center of hole to end of part

From Reference 7, Figure 5.3, $K_t = 2.2$

⁷FATIGUE DESIGN HANDBOOK, Report 299-099-076, Bell Helicopter Textron, Fort Worth, Texas, April 1972.

The stress is therefore

$$f_{\max} = 2.2 \left[\frac{CF}{3.50} + \frac{M_B (1.25)}{2.53} \right]$$

$$= 0.629 CF + 1.09 M_B \quad (15)$$

Condition 2 causes the largest stress with loads at station 18.5 of:

$$CF = 50,800 \text{ lb}$$

$$\text{and } M = -64,500 \text{ in.-lb}$$

so that

$$f = 0.629 (50,800) + 1.09 (64,500)$$

$$= 102,000 \text{ psi}$$

For an ultimate allowable of 190,000 psi for 0° S-glass

$$M.S. = \frac{190,000}{1.5 (102,000)} - 1 = +.24 \quad (16)$$

4.3.3.3 Blade Stresses

Blade stresses were analyzed with the aid of BHT Program CBCR04 (discussed previously under Section Properties and evaluated using the Tsai-Hill failure criterion. In CBCR04, beam and chord loads are used to calculate spanwise stresses at five locations in each layer of each wall in the model. The longest wall used in the sections was approximately 2.5 inches long, so stress evaluations were made at a minimum of 0.5-inch intervals. Spanwise stresses at each point are given by

$$f = E_i \left[\frac{M_B Y}{EI_B} + \frac{M_C X}{EI_C} + \frac{CF}{EA} \right]_{\text{section}} \quad (17)$$

Where i = index of each separate layer (material)

E_i = modulus in layer i

M_B = beam moment

M_C = chord moment

CF = centrifugal force

X = chordwise distance from neutral axis

Y = beamwise

EI_B = section beamwise stiffness

EI_C = section chordwise stiffness

EA = section axial stiffness

Since a large amount of information was produced by the procedure outlined above, only a stress summary is presented here. Maximum spanwise stresses are given with an associated torsional stress. These torsional stresses were calculated from the applied torsional load discussed previously and the section torsional properties.

The combined spanwise and torsional stresses were evaluated by the Tsai-Hill criterion. This criterion is described by

$$\left(\frac{1.5 f_t^2}{F_{tu}^2} + \frac{1.5 f_s^2}{F_{su}^2} \right) \leq 1 \quad (18)$$

where f_t = tension (spanwise stress)

f_s = shear stress (due to torsion)

F_{tu} = tensile ultimate stress

F_{su} = shear ultimate stress

1.5 = ultimate safety factor

A margin of safety was calculated as one divided by the square root of the left-hand side of the above relation minus one. The resulting stresses and margins are given in Table 15. The minimum margin of safety was 1.63 occurring in the 50-percent radius torque wrap at the leading edge of the airfoil.

4.3.4 Fatigue Life Estimation

To investigate the fatigue strength of the OH-58 composite main rotor blade, it is necessary to establish the spectrum of loads to which the blade would be subjected during its flight operation and also to establish the fatigue strength of the various materials used in its construction.

TABLE 15. CRITICAL BLADE LIMIT STRESSES

A. 25% (Sta 53)

<u>Condition</u>	<u>I.D.</u>	<u>x</u>	<u>y</u>	<u>Max fn</u>	<u>fs</u>	<u>M.S.</u>
1	TW	2.75	1.09	7310	-1850	>1
	UG	2.75	1.03	20700	- 742	>1
	SKIN	2.75	1.13	7410	-1660	>1
	DBLR	13.1	.723	2520	-1120	>1
2	TW	5.40	1.21	7340	-1570	>1
	UG	5.90	1.12	20500	- 630	>1
	SKIN	7.15	1.20	7400	-3860	>1
	DBLR	13.1	.723	4520	-1120	>1
3	TW	2.75	-.48	6210	1850	>1
	UG	2.75	-.42	17200	742	>1
	SKIN	2.75	-.52	6380	1660	>1
	DBLR	13.1	-.39	2090	1120	>1
4	TW	5.40	-.566	6240	1570	>1
	UG	18.3	-.128	17500	74	>1
	SKIN	13.1	-.487	6920	2230	>1
	DBLR	13.1	-.387	4340	1120	>1
5	TW	3.41	1.155	3300	0	>1
	UG	18.26	-.128	-11400	0	>1
	SKIN	15.1	-.386	- 4200	0	>1
	DBLR	18.3	-.128	- 2640	0	>1

B. 40% (Sta 84.8)

1	TW	.25	.320	5310	-5990	>1
	UG	.45	.330	15300	-	>1
	SKIN	2.75	1.073	5070	-4500	>1
2	TW	4.89	1.118	5360	-3600	>1
	UG	16.89	.146	22200	-87	>1
	SKIN	16.97	.146	7690	- 218	>1
3	TW	.25	-.196	3780	5990	>1
	UG	.10	0.0	10500	-	>1
	SKIN	2.75	-.495	3470	5990	>1
4	TW	4.89	-.521	3740	2180	>1
	UG	16.89	-.126	17200	87	>1
	SKIN	16.97	-.126	5950	218	>1
5	TW	2.75	1.073	2980	0	>1
	UG	16.9	-.126	-13000	0	>1
	SKIN	17.0	-.126	- 4490	0	>1

TABLE 15. (Concluded)

C. 50% (Sta 106)

<u>Condition</u>	<u>I.D.</u>	<u>x</u>	<u>y</u>	<u>Max fn</u>	<u>fs</u>	<u>M.S.</u>
1	TW	.04	0.0	5250	-7680	>1
	UG	.48	.336	15100	-	>1
	SKIN	2.75	1.028	4910	-2300	>1
2	TW	4.65	1.053	5100	-2880	>1
	UG	15.91	.146	20300	0	>1
	SKIN	15.99	.146	7010	0	>1
3	TW	.12	-.094	3440	7680	>1
	UG	1.80	-.313	9230	840	>1
	SKIN	2.75	-.476	3060	2300	>1
4	TW	4.65	-.490	3250	3390	>1
	UG	15.91	-.124	14700	0	>1
	SKIN	15.99	-.124	5090	0	>1
5	TW	4.65	-.490	-2410	0	>1
	UG	15.9	-.124	-10600	0	>1
	SKIN	16.0	-.124	-3680	0	>1

D. 75% (Sta 159)

1	TW	.12	.139	4190	-6270	>1
	UG	1.26	.594	11200	-	>1
	SKIN	2.75	.862	3380	-1560	>1
2	TW	.12	.139	3670	-6270	>1
	UG	1.26	.594	10300	-	>1
	SKIN	2.75	.862	3330	-1560	>1
3	TW	.63	-.204	3140	6270	>1
	UG	2.75	-.326	7950	629	>1
	SKIN	2.75	-.406	2890	1560	>1
4	TW	2.75	-.386	2780	1560	>1
	UG	2.75	-.326	7750	629	>1
	SKIN	2.75	-.406	2820	1560	>1
5	TW	2.75	.842	893	0	>1
	UG	12.7	-.117	-4100	0	>1
	SKIN	12.7	-.117	-1420	0	>1

TW = Torque Wrap UG = Uniglass

Design loads for a new rotor blade must be determined analytically, but loads data from dynamically similar rotor systems can be used as a check on the new calculated loads. Over a period of several years, a large quantity of flight loads data has been recorded for numerous flight conditions and helicopter loadings. The C81 computer program was used to compare the dynamic loading of the new blade with that of the existing blade. Having made this comparison, the previously recorded flight data were adjusted and used to estimate the fatigue life of the new blade.

Since the use of glass fiber composite materials in helicopter dynamic components is relatively new, there is little fatigue strength data on full-scale components. However, extensive testing for basic material fatigue strength has been performed and reported in References 8, 9, and 10. These tests are considered to be an appropriate basis for the design of the new blade.

4.3.4.1 Endurance Limits

The fatigue strength of unidirectional S-glass presented in the modified Goodman diagram in Figure 61 was derived from data contained in Reference 8 and 9. For the steady stress range calculated for the OH-58 blade, an endurance limit of $\pm 17,500$ psi was established.

The fatigue strength of $\pm 45^\circ$ S-glass presented in the modified Goodman diagram in Figure 62 was derived from data contained in Reference 11. For the steady stress range calculated for the OH-58 blade, an endurance limit of ± 3800 psi was established.

⁸Boller, K. H., FATIGUE CHARACTERISTICS OF TWO NEW PLASTIC LAMINATES, REINFORCED WITH UNWOVEN S-GLASS FIBERS, UNDER CYCLIC AXIAL OR SHEAR LOADING, AFML Technical Report 66-54, U.S. Air Force Materials Laboratory, Wright-Patterson AFB, Ohio, May 1966.

⁹Cutler, M. G. and Pickney, R. L., STATIC AND FATIGUE TEST PROPERTIES FOR WOVEN AND NONWOVEN S-GLASS FIBERS, Boeing Vertol Company; USAAVLABS Technical Report 69-9, U.S. Army Aviation Material Laboratories, Fort Eustis, Virginia, April 1969, AD688971.

¹⁰Hoffstedt, D. J., ADVANCED GEOMETRY, GLASS-FIBER-REINFORCED PLASTIC ROTOR BLADE TEST PROGRAM, Boeing Vertol Company; USAAMRDL Technical Report 71-42, Eustis Directorate, U.S. Army Air Mobility Research and Development Laboratory, Fort Eustis, Virginia, September 1971, AD738203.

¹¹Brogdon, V. H., FATIGUE ALLOWABLES FOR SP-250-SF1 S-GLASS PREPREG LAMINATES USING NORMAL DISTRIBUTION, Memo 81:VHB:gs-8147, Bell Helicopter Textron, Fort Worth, Texas, 9 December 1976.

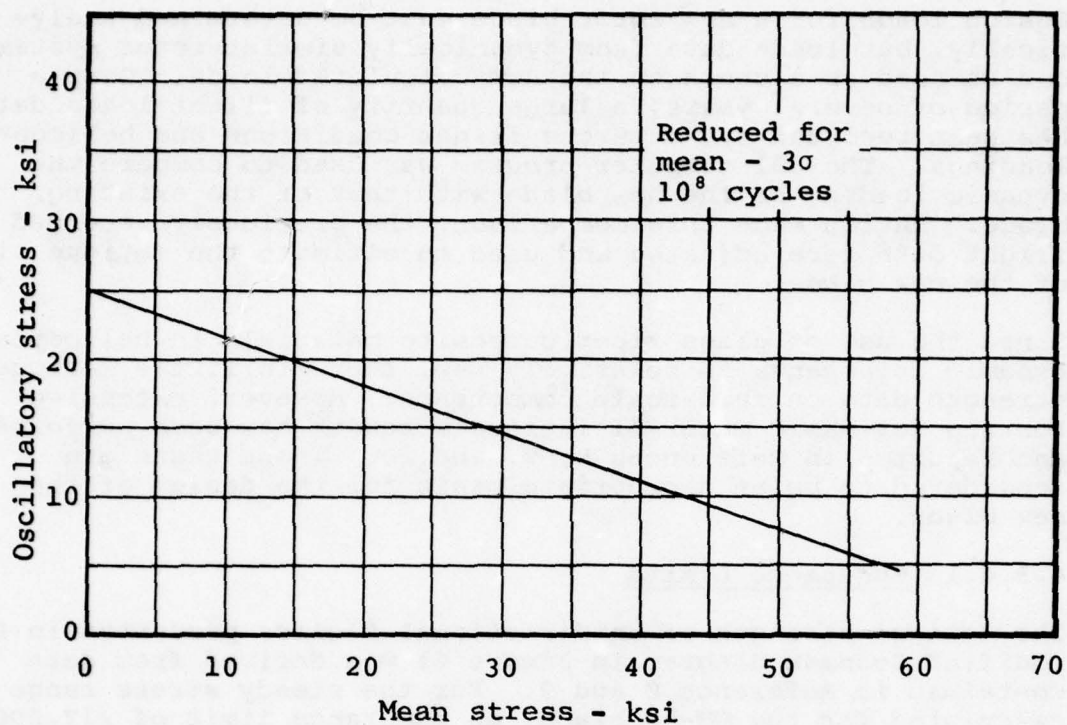


Figure 61. Goodman diagram for unidirectional S-glass.

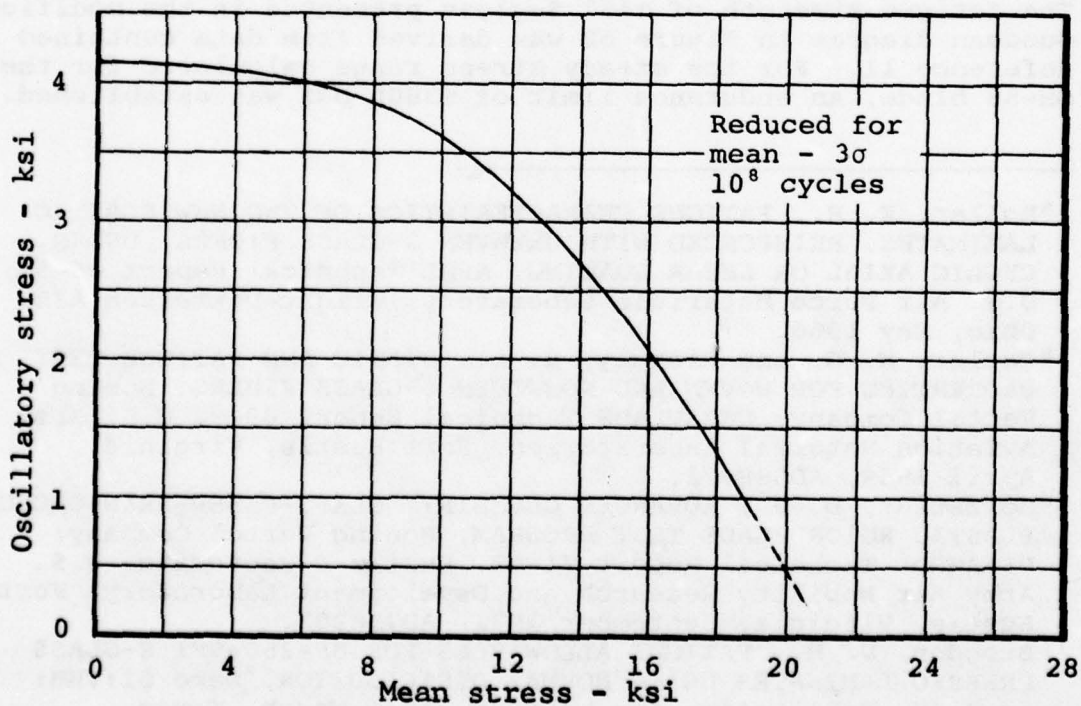


Figure 62. Goodman diagram for $\pm 45^\circ$ S-glass.

4.3.4.2 Fatigue Analysis

The oscillatory loads used in the fatigue analysis were derived from a combination of previously measured flight loads for the production OH-58 blade and loads calculated for both blades with computer program C81. Although C81 calculated loads seldom correlate completely with measured loads for all flight conditions, they are extremely useful in evaluating how variations in dynamic or aerodynamic parameters influence oscillatory loads. Thus, for a given helicopter flight condition, the relationship of calculated oscillatory loads for the production blade and the composite blade may be used to establish load ratios. These load ratios may then be used as a factor on the measured loads to establish a total spectrum of new loads for the use in the fatigue life analysis for the improved blade.

As an example, consider the calculated loads presented in Figure 75. At 50-percent radius, the beamwise oscillatory moment for the improved blade is approximately 0.91 times that for the production blade. Similarly, the chordwise oscillatory moment for the improved blade is 0.58 times that of the production blade. The measured beamwise and chordwise moments at 50-percent radius would be multiplied by 0.91 and 0.58, respectively. These loads would be used to calculate the fatigue life.

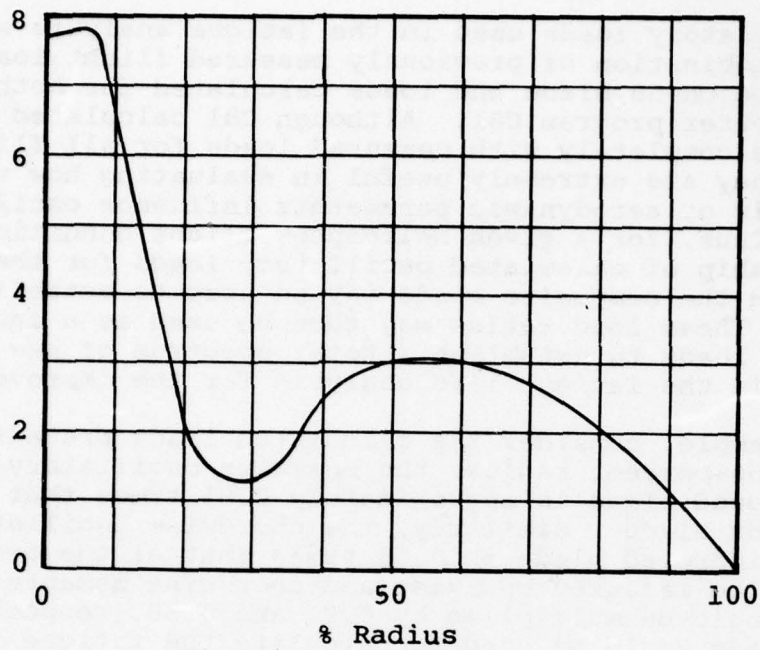
This method has several advantages over the alternative method of using strictly calculated loads.

- The effects of variables in operating conditions, which could not be simulated by calculated loads, are introduced into the analysis.
- The use of measured flight loads as a baseline is more realistic than the use of loads from analysis only.
- The probability of not including a particular maneuver that might generate high loads is reduced.

This procedure was used to evaluate the fatigue strength of the composite blade at: (1) the main retention hole (Station 18.5), and (2) at 50-percent radius (Station 106).

At Station 106, the critical area was determined to be the $\pm 45^\circ$ fiberglass skin at the extreme trailing edge. At this point, the most critical combination of beamwise and chordwise bending moments was measured during a full autorotation landing at 2530 pounds gross weight, neutral cg, as shown in Figure 63. Using these measured loads with the appropriate ratios of calculated improved blade loads to production blade loads, a maximum stress at the critical point of ± 1578 psi was calculated.

Oscillatory chordwise bending moment
in.-lb $\times 10^{-2}$



Oscillatory beamwise bending moment
in.-lb $\times 10^{-3}$

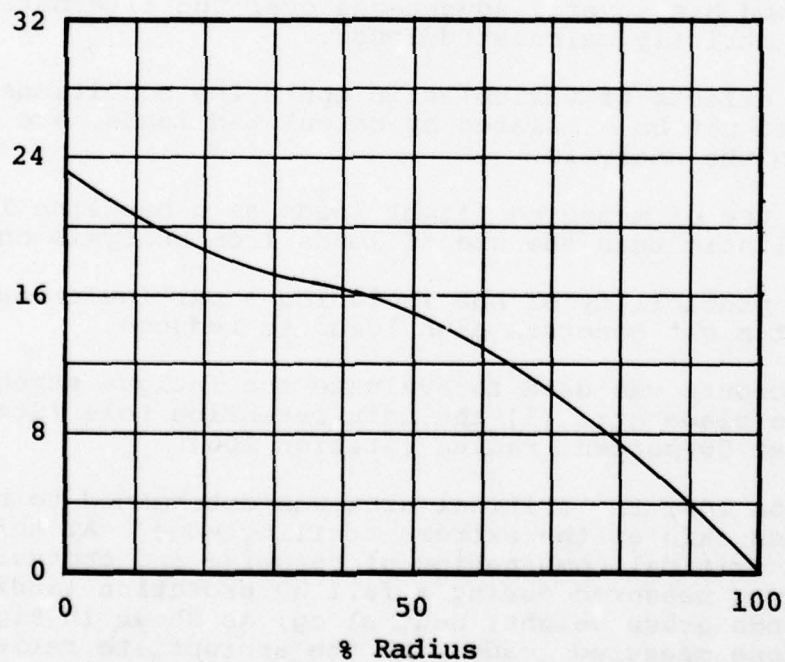


Figure 63. Spanwise moment distribution for a full autorotation landing at 2530 pounds gross weight and neutral cg.

At Station 18.5, the critical area is the unidirectional spar. This section is fatigue loaded only by an oscillatory beamwise bending moment as discussed in paragraph 4.3.3.1. The maximum stress of $\pm 10,569$ psi was calculated by adjusting the load for a fore- and aft-control reversal at V_H , 2760 pounds gross weight, forward cg, and 3000 feet density altitude, shown in Figure 64.

4.3.4.3 Summary of Fatigue Life Estimation

Since none of the maximum calculated stresses in paragraph 4.3.4.2 exceeded the appropriate material endurance limit from paragraph 4.3.4.1, an unlimited fatigue life is indicated for the OH-58 composite main rotor blade.

4.3.5 Environmental Effects

Tests were conducted at BHT to investigate environmental effects on the strength of S-2 glass/epoxy. Specimens were conditioned at 120°F and 95 percent relative humidity for 42 days. These specimens were then statically tested at 75°F and 165°F. Table 16 shows the resulting static strength reductions from the room temperature control values. Using these reduction factors, no negative margins of safety were encountered for the blade.

TABLE 16. PERCENT REDUCTION IN STATIC STRENGTH
DUE TO TEMPERATURE AND MOISTURE

Specimen (S2-Glass)	Test Temperature (°F)		
	Control 165	Environmentally Exposed 75	165
0° Tension	4	1	16
$\pm 45^\circ$ Tension	7	6	42
0° Shear	23	15	52
90° Tension	22	-	-

Fatigue tests of spar loop joints similar to those used in the main rotor blade attachment have been conducted to determine the effects of moisture absorption. These test results showed that specimens conditioned for 42 days at 120°F and 95 percent relative humidity exhibited a fatigue strength approximately 7 percent lower than the control specimens.

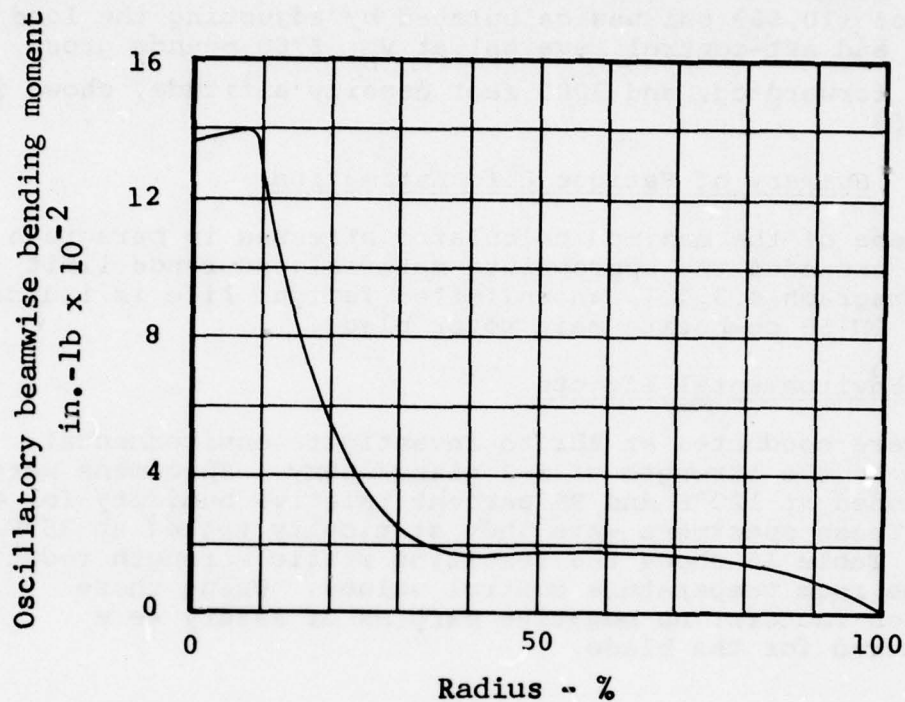


Figure 64. Spanwise moment distribution for fore/aft cyclic control reversal at V_H , 2760 pounds gross weight, forward cg, and 3000 feet density altitude.

In addition, fatigue tests of conditioned skin-type laminates indicate an acceptable reduction in strength. It was concluded that environmental effects will not reduce the fatigue life of the blade.

4.4 DYNAMIC ANALYSIS

4.4.1 Main Rotor Natural Frequencies

Natural frequencies of both the production OH-58 rotor blade and the OH-58C/A composite rotor blade were calculated using BHT computer program DN9100 (Myklestad Analysis). A 24-unequal-segment model was used for the standard and improved rotor blades in order to provide a detailed math model of the hub. The effect of the rotor support system on rotor frequencies was accounted for by the effective inplane restraint (HSOFT). A value of -100 for HSOFT was used to best represent the OH-58 pylon. The control system stiffnesses were obtained from a load/deflection test conducted on an OH-58A helicopter. The values were found to be 172,000 in.-lb/rad and 108,000 in.-lb/rad for collective and cyclic loadings, respectively.

Computed natural frequencies of collective and cyclic modes for the production blade, based on the structural properties given in Table 17, are shown in Figure 65. Computed natural frequencies for the rotor with the composite blade, based on the structural parameters presented in Table 18, are shown in Figure 66. Computed frequencies at mid-collective and 354 rpm for both rotors are also tabulated in Table 19 for a direct comparison. The results indicate that, at 100 percent normal rotor operating speed, the collective torsion mode of the production rotor is located near 6/rev, and the fourth cyclic mode is in 5/rev resonance. Also, natural frequencies of the rotor with the composite blade are well removed from coincidence with the rotor aerodynamic forces (at rotor harmonic frequencies) through the practical operating regime.

The frequency placements for the rotor with the composite blade show two areas of improvement over those for the production rotor: the frequency of the first inplane mode for the composite blade rotor is at 1.30/rev, well removed from 1/rev, and the frequency of the fourth cyclic mode for the composite blade rotor is at 4.01/rev thereby eliminating the possibility of 5/rev resonance.

The OH-58C/A composite blade has been designed such that the blade weight, flapping inertia, spanwise effective center of gravity, and the centrifugal force at the hub closely agree with those of the production rotor. These design parameters for the production rotor and the composite blade rotor are

TABLE 17. DN9100 INPUTS FOR OH-58C/A PRODUCTION ROTOR

BMC PROGRAM DN9100 -COMPILED 05/02/77
NATURAL BLADE MODES
02/28/78
206212

OH58-A/C PRODUCTION H/R

	SEGMENT LENGTH (IN)	EI (LB-IN**2) MEAN (E-6)	CHORD (E-6)	WT/IN (LB/IN)	TWIST AT INBD END (DEG)	CF AT INBD END (LB/RPM**2)
1	3.00	130.80	374.30	2.1330	.0	.31171
2	2.00	123.10	123.60	1.5750	.0	.31131
3	4.50	138.00	142.00	2.9640	.0	.31014
4	3.00	388.40	344.50	2.8180	.0	.30720
5	4.00	292.00	117.00	1.7730	.0	.30444
6	4.70	141.60	209.00	1.8590	.0	.30074
7	10.60	34.100	488.30	.84400	-1.0600	.29529
8	10.60	18.100	470.00	.57100	-1.5900	.28833
9	10.60	10.650	420.20	.40700	-2.1200	.28209
10	10.60	5.8500	343.80	.30300	-2.6500	.27643
11	10.60	5.8200	280.00	.28800	-3.1800	.27078
12	10.60	5.8200	250.00	.28800	-3.7100	.26435
13	10.60	5.8200	235.00	.28800	-4.2400	.25700
14	10.60	6.2600	237.60	.84900	-4.7700	.24069
15	10.60	6.2600	237.60	.84900	-5.3000	.21361
16	10.60	5.8200	233.60	.28800	-5.8300	.19367
17	10.60	5.8200	233.60	.28800	-6.3600	.18265
18	10.60	5.8200	233.60	.28800	-6.8900	.17071
19	10.60	5.8200	233.60	.28800	-7.4200	.15786
20	10.60	5.8200	233.60	.28800	-7.9500	.14408
21	10.60	5.8200	233.60	.28800	-8.4800	.12939
22	10.60	7.5500	263.20	.64700	-9.0100	.10404
23	10.60	7.5500	263.20	.64600	-9.5400	.61539E-01
24	10.60	6.4000	244.50	.50400	-10.070	.21005E-01

RADIUS= 212.00 IN

6 HUB SEGMENTS

ROTOR RPM 324.00 354.00 384.00

ROOT COLL (DEG) 7.50 16.00 24.50

PREG SWEEP (CPH) 32.40 384.00 96.00

INITIAL FINAL DELTA

TWIST AT TIP= -10.600 DEG

BALANCE WT. .020 LBM HAST TORSION 0.0 *1.E6 IN-LB/RAD

VSOFT .0 /LB VMASS .0 LBM/BLADE

HISOFT -100. /LB HMASS .0 LBM/BLADE

FLAP SPRING/BLADE 0.0 FT-LB/DEG PITCH HORN OFFSET 5.0000 INCH

HUB TYPE GIMBALED CHORD 13.000 INCHES

BLADE MASS 137.4541 LBM FLAP INERTIA 335.6768 SLUG-FT**2/BLADE

BLADE LOCK NUMBER 4.284 FLAP HINGE ANGLE 0.0

FLAP-LAG COUPLING 0.0 DEG PITCH-LAG COUPLING 0.0 DEG

PITCH LINK OFFSET 0.0 INCH

CONTROL DAMPING 0.0 PERCENT

EFFECTIVE BLADE CG 0.13 INCH AHEAD OF PCA

RIGID TORSION FREQ 50.448 HERTZ BLADE TORSION INERTIA 1.712 IN-LB-SEC**2

PITCH ARM LENGTH 7.18 INCHES IMPLANE SPRING .0 FT-LBF/DEG

FLAP HINGE AT 0.0 INCHES LAG HINGE AT .0 INCHES

NUMBER OF BLADES 2. FIRST MASS MOMENT 28.42 SLUG-FT

FREQUENCY PLOT REQUESTED COLLECTIVE CONTROL SPRING .1720E+06 IN-LB/RAD

TORSION OPTION IS ON CYCLIC CONTROL SPRING .1080E+06 IN-LB/RAD

NONLINEAR TWIST IS USED

UNEQUAL SEGMENTS ARE USED

TABLE 17. (Concluded)

	IBS IN-LB-SEC**2/IN	BEAM RADIUS OF GYRATION - INCH	ICC IN-LB-SEC**2/IN	CHORD RADIUS OF GYRATION - INCH
1	.0	.0	.0	.0
2	.0	.0	.0	.0
3	.0	.0	.0	.0
4	.44170E-03	.24610	.29990E-02	.64126
5	.44170E-03	.31026	.29990E-02	.80845
6	.44170E-03	.30360	.29990E-02	.78953
7	.12422E-02	.73687	.13190E-01	2.4011
8	.54990E-03	.61002	.12750E-01	2.0384
9	.27430E-03	.51031	.11206E-01	3.2617
10	.17470E-03	.47200	.90320E-02	3.3938
11	.15010E-03	.44876	.69980E-02	3.0641
12	.15010E-03	.44876	.68320E-02	3.0276
13	.15010E-03	.44876	.68320E-02	3.0276
14	.34200E-03	.39453	.82040E-02	1.9323
15	.31300E-03	.37743	.79930E-02	1.9073
16	.14900E-03	.44711	.68060E-02	3.0218
17	.14900E-03	.44711	.68060E-02	3.0218
18	.14900E-03	.44711	.68060E-02	3.0218
19	.14900E-03	.44711	.68060E-02	3.0218
20	.14900E-03	.44711	.68060E-02	3.0218
21	.14900E-03	.44711	.68060E-02	3.0218
22	.20800E-03	.35245	.78190E-02	2.1609
23	.24000E-03	.33346	.83860E-02	1.9711
24	.18900E-03	.38066	.74920E-02	2.3966

	SHEAR CENTER OFFSET(IN). BEAM CHORD		C.G. OFFSET (IN) BEAM CHORD		GJ(LB-IN**2) (E-6)
1	0.0	0.0	0.0	0.0	0.95000E+02
2	0.0	0.0	0.0	0.0	0.95000E+02
3	0.0	0.0	0.0	0.0	0.95000E+02
4	-0.119	0.335	0.112	-0.102	0.96290E+02
5	-0.119	0.335	0.112	-0.102	0.96290E+02
6	-0.119	0.335	0.112	-0.102	0.96290E+02
7	-0.006	0.675	0.005	-0.800	0.48000E+02
8	-0.008	0.745	0.007	-0.890	0.21370E+02
9	-0.011	0.565	0.010	-0.730	0.11470E+02
10	-0.015	0.555	0.014	-0.730	0.73130E+01
11	-0.016	0.475	0.015	-0.680	0.69800E+01
12	-0.016	0.285	0.015	-0.550	0.69800E+01
13	-0.016	0.018	0.015	-0.385	0.69800E+01
14	-0.014	-0.160	0.006	0.550	0.69800E+01
15	-0.014	0.140	0.007	0.429	0.69800E+01
16	-0.016	-0.050	0.015	-0.250	0.69800E+01
17	-0.016	-0.050	0.015	-0.250	0.69800E+01
18	-0.016	-0.050	0.015	-0.250	0.69800E+01
19	-0.016	-0.050	0.015	-0.250	0.69800E+01
20	-0.016	-0.050	0.015	-0.250	0.69800E+01
21	-0.016	-0.050	0.015	-0.250	0.69800E+01
22	-0.012	-0.030	0.010	0.430	0.69800E+01
23	-0.009	-0.050	0.007	0.810	0.69800E+01
24	-0.013	-0.050	0.011	0.210	0.69800E+01
TW			0.0	0.0	

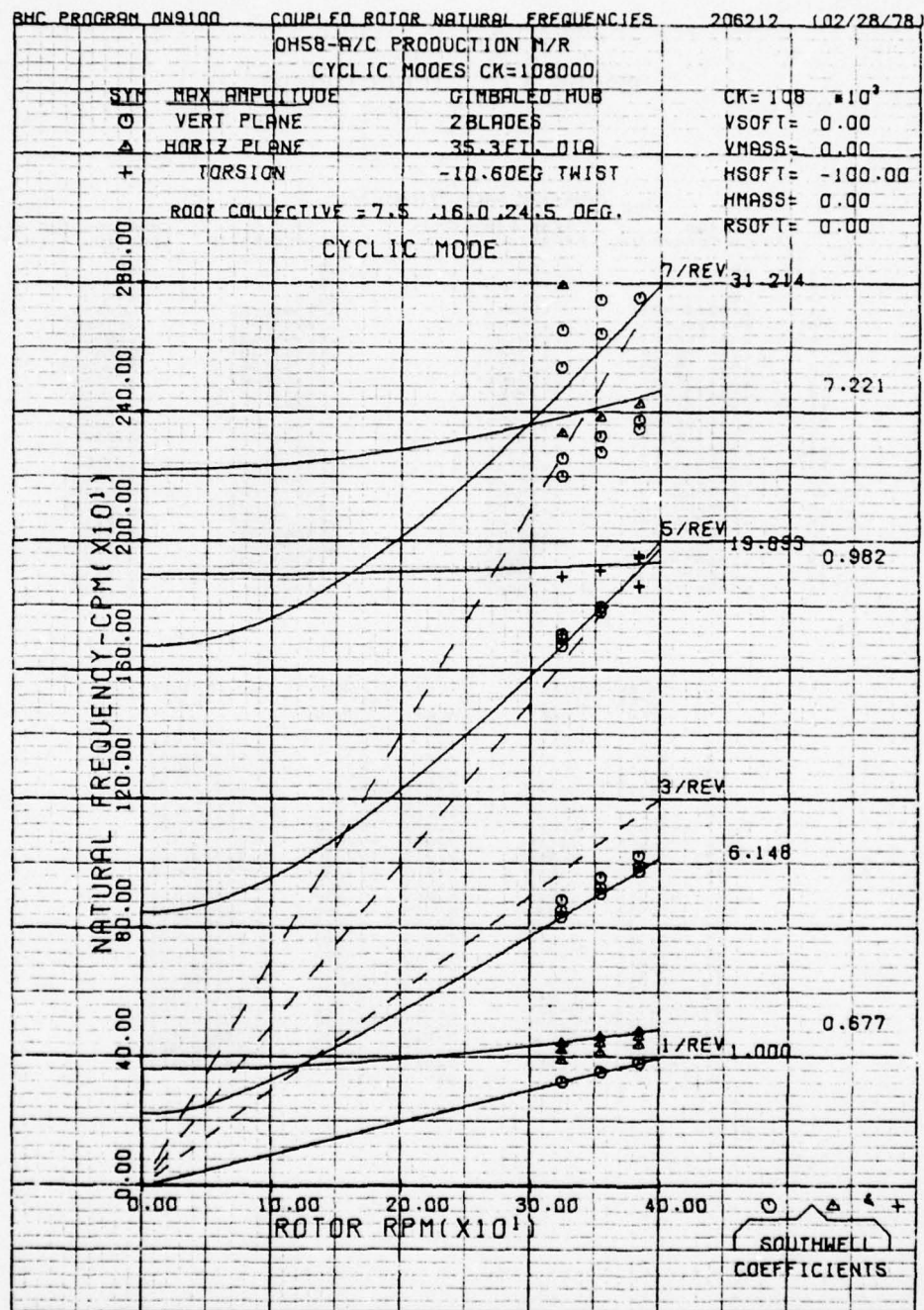


Figure 65. Calculated natural frequencies for OH-58C/A production rotor.

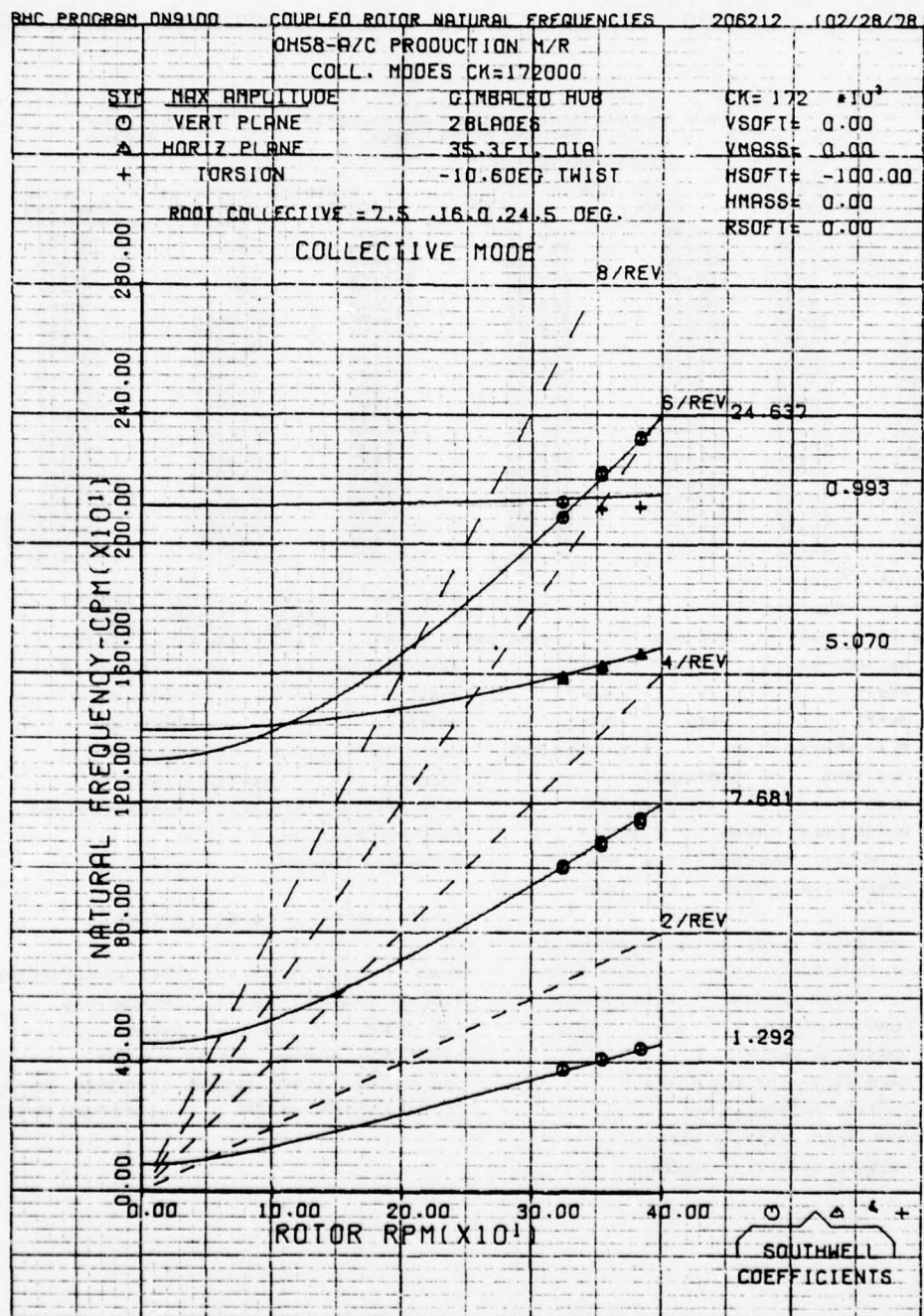


Figure 65. (Concluded)

TABLE 18. DN9100 INPUTS FOR OH-58C/A COMPOSITE BLADE ROTOR

BMC PROGRAM DN9100 -COMPILED 05/02/77
NATURAL BLADE MODES02/28/78
206312

206 COMPOSITE M/R

	SEGMENT LENGTH (IN)	E1 (LB-IN**2) BEAM (E-6)	CHORD (E-6)	WT/IN (LB/IN)	TWIST AT INBD END (DEG)	CF AT INBD END (LB/RPM**2)
1	3.00	130.00	374.30	2.1330	.0	.31165
2	2.00	123.10	123.60	1.5750	.0	.31125
3	4.50	138.00	142.00	2.9640	.0	.31008
4	3.00	388.40	344.50	2.9180	.0	.30714
5	4.00	292.00	117.00	1.7730	.0	.30438
6	4.70	131.10	183.70	2.0240	.0	.30050
7	10.60	43.300	379.00	.72200	-9.2900	.29533
8	10.60	20.800	432.00	.52500	-6.5100	.28937
9	10.60	11.000	445.00	.41800	-3.7300	.28335
10	10.60	7.4500	408.00	.36200	-9.9500	.27713
11	10.60	6.4000	347.50	.34000	-1.6500	.27042
12	10.60	5.7000	297.50	.32200	-2.3500	.26303
13	10.60	5.0800	258.00	.31000	-3.0500	.25497
14	10.60	4.5500	226.00	.29500	-3.7500	.24629
15	10.60	4.0700	198.00	.45500	-4.4500	.23433
16	10.60	3.6200	172.50	.54700	-5.1500	.21676
17	10.60	3.1800	153.50	.58900	-5.8500	.19502
18	10.60	2.7500	136.00	.63100	-6.5500	.16973
19	10.60	2.3000	120.50	.62900	-7.2500	.14161
20	10.60	1.9000	107.00	.59000	-7.9500	.11245
21	10.60	1.4500	83.500	.47500	-8.6500	.08285E-01
22	10.60	1.0500	56.500	.42500	-9.3500	.00891E-01
23	10.60	.65000	40.000	.38000	-10.050	.37788E-01
24	10.60	.70000	26.000	.35000	-10.750	.15673E-01

RADIUS= 212.00 IN

6 HUB SEGMENTS

TWIST AT TIP= -11.450 DEG

BALANCE WT.	.750	LBH	MAST TORSION	0.0	*1.E6 IN-LB/RAD
VSOFT	.0	/LB	VMASS	.0	LBH/BLADE
MSOFT	-100.	/LB	WMASS	.0	LBH/BLADE
FLAP SPRING/BLADE	0.0 FT-LB/DEG		PITCH HORN OFFSET	5.0000 INCH	
HUB TYPE	GIMSALED		CHORD	13.300 INCHES	
BLADE MASS	137.3645 LBH		FLAP INERTIA	327.2773 SLUG-FT**2/BLADE	
BLADE LOCK NUMBER	4.495		FLAP HINGE ANGLE	0.0	
FLAP-LAG COUPLING	0.0 DEG		PITCH-LAG COUPLING	0.0 DEG	
PITCH LINK OFFSET	0.0 INCH				

CONTROL DAMPING 0.0 PERCENT

EFFECTIVE BLADE CG 0.77 INCH AHEAD OF PCA

RIGID TORSION FREQ 39.869 HERTZ

PITCH ARM LENGTH 7.18 INCHES

FLAP HINGE AT 0.0 INCHES

NUMBER OF BLADES 2.

FREQUENCY PLOT REQUESTED

TORSION OPTION IS ON

NONLINEAR TWIST IS USED

UNEQUAL SEGMENTS ARE USED

BLADE TORSION INERTIA 2.741 IN-LB-SEC**2

INPLANE SPRING .0 FT-LBF/DEG

LAG HINGE AT .0 INCHES

FIRST MASS MOMENT 28.42 SLUG-FT

COLLECTIVE CONTROL SPRING .1720E+06 IN-LB/RAD

CYCLIC CONTROL SPRING .1080E+06 IN-LB/RAD

TABLE 18. (Concluded)

206 COMPOSITE M/R				
	ICC IN-LB-SEC**2/IN	BEAM RADIUS OF GYRATION - INCH	ICC IN-LB-SEC**2/IN	CHORD RADIUS OF GYRATION - INCH
1	.0	.0	.0	.0
2	.0	.0	.0	.0
3	.0	.0	.0	.0
4	.44170E-03	.24610	.29990E-02	.64126
5	.44170E-03	.31026	.29990E-02	.60845
6	.44170E-03	.29039	.29990E-02	.75866
7	.22920E-02	1.1075	.22390E-01	3.4616
8	.10390E-02	.67447	.28340E-01	4.3671
9	.38900E-03	.59889	.27600E-01	5.0785
10	.33900E-03	.60154	.24440E-01	5.1097
11	.30000E-03	.58390	.20570E-01	4.8350
12	.26100E-03	.55964	.17340E-01	4.5616
13	.22900E-03	.53426	.14620E-01	4.2689
14	.19700E-03	.50797	.12290E-01	4.0122
15	.17100E-03	.48108	.10350E-01	3.7647
16	.14800E-03	.45234	.89300E-02	3.5116
17	.12700E-03	.42864	.76300E-02	3.2373
18	.11100E-03	.40771	.66000E-02	2.9104
19	.97000E-04	.38411	.59000E-02	2.5338
20	.86700E-04	.35829	.54300E-02	2.1094
21	.78900E-04	.33334	.47900E-02	1.7970
22	.73100E-04	.30130	.40100E-02	1.5094
23	.72500E-04	.27152	.28500E-02	1.7024
24	.72500E-04	.28291	.20700E-02	1.5117

	SHEAR CENTER OFFSET (IN)		C.G. OFFSET (IN)		GJ (LB-IN**2) (E-6)
	BEAM	CHORD	BEAM	CHORD	
1	0.0	0.0	0.0	0.0	0.95000E+02
2	0.0	0.0	0.0	0.0	0.95000E+02
3	0.0	0.0	0.0	0.0	0.95000E+02
4	-0.119	0.335	0.112	-0.102	0.96290E+02
5	-0.119	0.335	0.112	-0.102	0.96290E+02
6	-0.119	0.335	0.112	-0.102	0.96290E+02
7	0.250	0.280	-0.240	-0.280	0.48000E+02
8	0.250	0.100	-0.240	-0.650	0.21370E+02
9	0.250	-0.100	-0.240	-1.000	0.11470E+02
10	0.247	-0.300	-0.237	-0.950	0.78500E+01
11	0.241	-0.550	-0.233	-0.600	0.59500E+01
12	0.234	-0.750	-0.228	-0.250	0.47500E+01
13	0.228	-0.950	-0.224	0.0	0.39000E+01
14	0.224	-1.100	-0.212	0.330	0.32000E+01
15	0.226	-0.950	-0.192	1.150	0.28500E+01
16	0.222	-0.800	-0.188	1.300	0.24000E+01
17	0.218	-0.650	-0.185	1.370	0.19000E+01
18	0.212	-0.500	-0.180	1.420	0.16700E+01
19	0.204	-0.360	-0.174	1.350	0.15200E+01
20	0.192	-0.250	-0.164	1.230	0.14200E+01
21	0.177	-0.100	-0.152	1.050	0.13600E+01
22	0.160	0.050	-0.138	0.750	0.13000E+01
23	0.140	0.220	-0.122	0.500	0.12700E+01
24	0.118	0.360	-0.105	0.300	0.12500E+01
TW			0.0	-2.125	

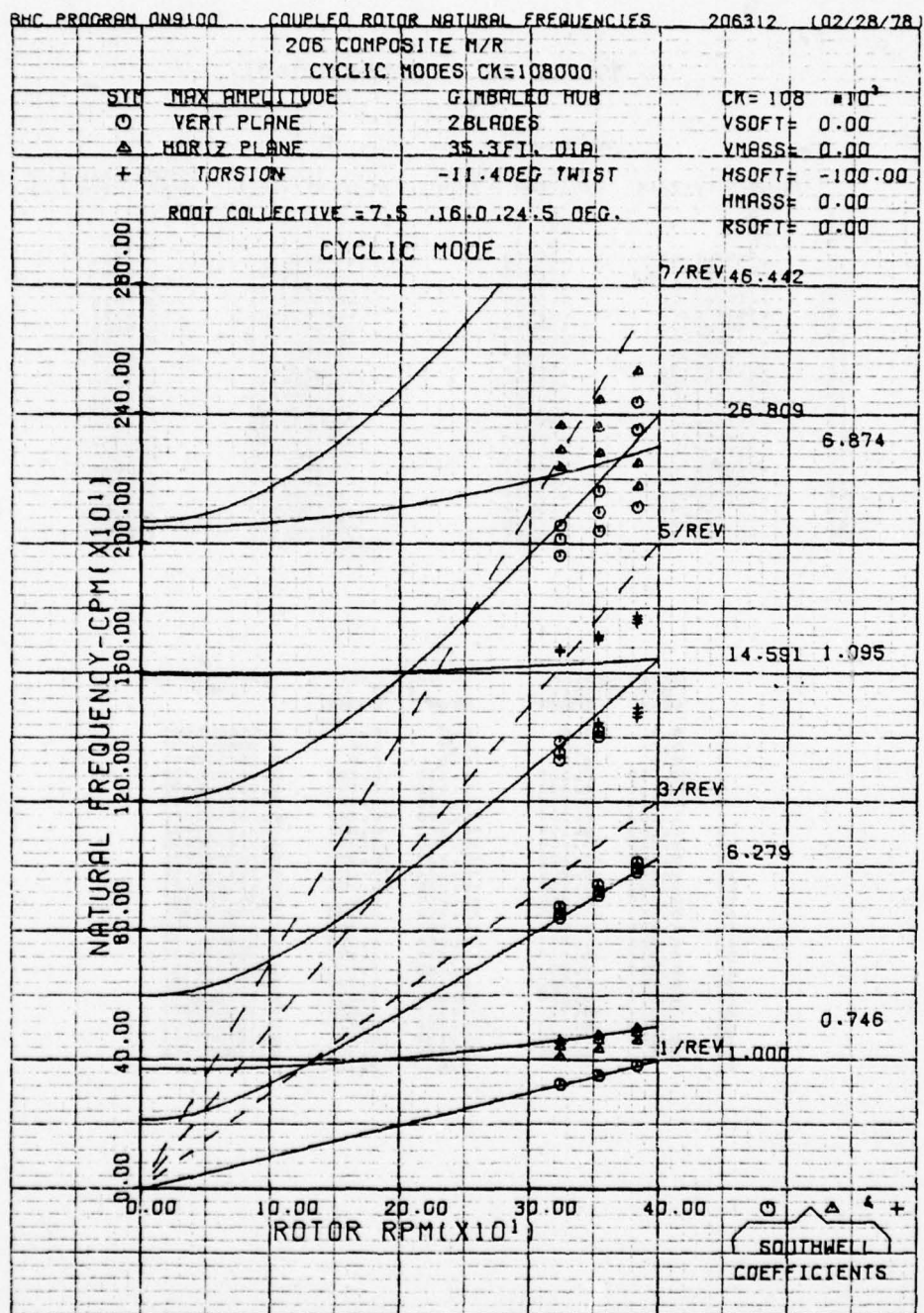


Figure 66. Calculated natural frequencies for OH-58C/A composite blade rotor.

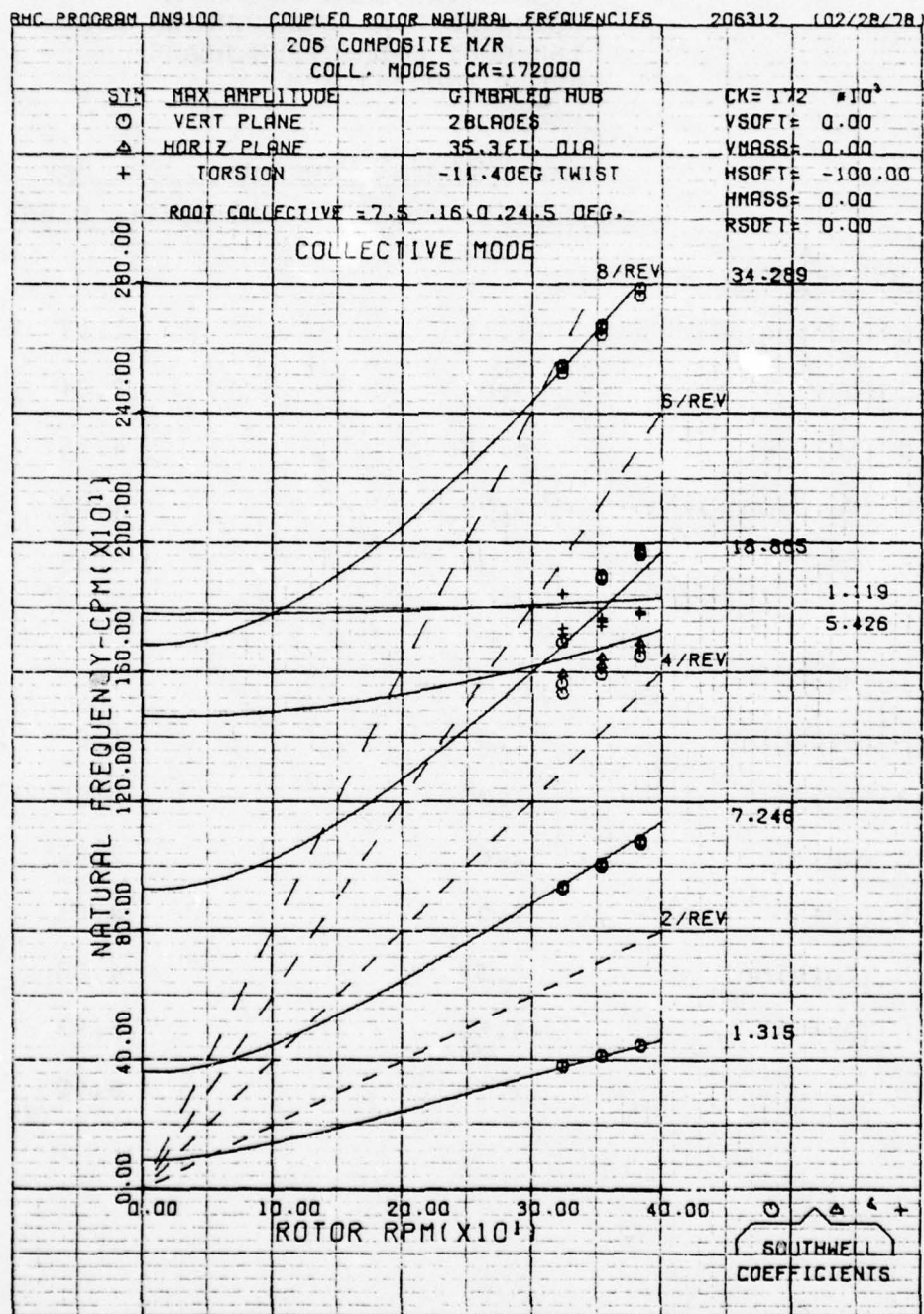


Figure 66. (Concluded)

TABLE 19. COMPARISON OF PRODUCTION AND
COMPOSITE BLADE OH-58C/A
ROTOR NATURAL FREQUENCIES FOR
16° ROOT COLLECTIVE BLADE
ANGLE AND 354 RPM

	<u>Natural Frequency, Per Rev</u>	
	<u>Production Rotor</u>	<u>Composite Blade Rotor</u>
<u>Collective Mode</u>		
1st (Coning)	1.16	1.17
2nd (OP)	3.05	2.84
3rd (IP)	4.58	4.58
4th (Torsion)	5.96	4.97
5th (OP)	6.27	5.35
<u>Cyclic Mode</u>		
1st (Flapping)	1.0	1.0
2nd (IP)	1.25	1.30
3rd (OP)	2.61	2.61
4th (OP)	5.07	4.01
5th (Torsion)	5.39	4.83
6th (OP)	6.54	5.93
7th	7.76	6.65

listed in Tables 17 and 18, respectively. These properties were retained to assure the adaptability of the composite blade to the existing hub with no degradation of autorotation characteristics.

4.4.2 Main Rotor Loads

Main rotor beamwise and chordwise oscillating bending moments were computed by the Rotorcraft Flight Simulation Program C81 (C8176 version). All loads were calculated using the coupled beam-chord-torsion mode shapes and natural frequencies generated by the DN9100 program. These modes were generated for a root-collective pitch of 16 degrees and a rotor speed of 354 rpm. The effects of pylon motions on the rotor modes (hub impedance) are represented by the HSOFT value of -100. This method was also used in the rotor natural frequency calculations (Section 4.4.1). Four collective and five cyclic modes with frequencies up to 6/rev were used for the blade loads calculations.

NACA 0012 airfoil data tables (C_l , C_d , and C_m) were used for the production blade. The tables are based on the two-dimensional NASA-Army Langley wind-tunnel data, except that a ΔC_d of .0045 was added to all elements of the C_d tables in order to achieve good correlation in performance.

FX098 airfoil data were used for the composite blade. The data tables are based on the two-dimensional NASA-Army Langley wind-tunnel data. Since the airfoil data table for the FX098 was obtained from the same source as that for the 0012, the same ΔC_d value as that used for 0012 was added to all elements of the C_d table for the FX098. The selected twist distribution and the curved leading- and trailing-edge planform for the composite blade were properly considered in defining the aerodynamic properties.

In order to substantiate the C81 analysis for computing main rotor loads, a comparison of computed blade loads (overall oscillatory) with loads obtained from flight test data for a production OH-58A helicopter is presented in Figure 67. The data was obtained from a level flight condition at an airspeed of 102.5 knots, a density altitude of 3618 feet, an outside air temperature of 24°C, cg station 112.1, and a gross weight of 3000 pounds. Good correlation between the computed and measured loads is shown for both the beam and chord bending moments at most blade stations.

During the blade correlation study, it was observed that the six-harmonic rotor-induced velocity distribution which would

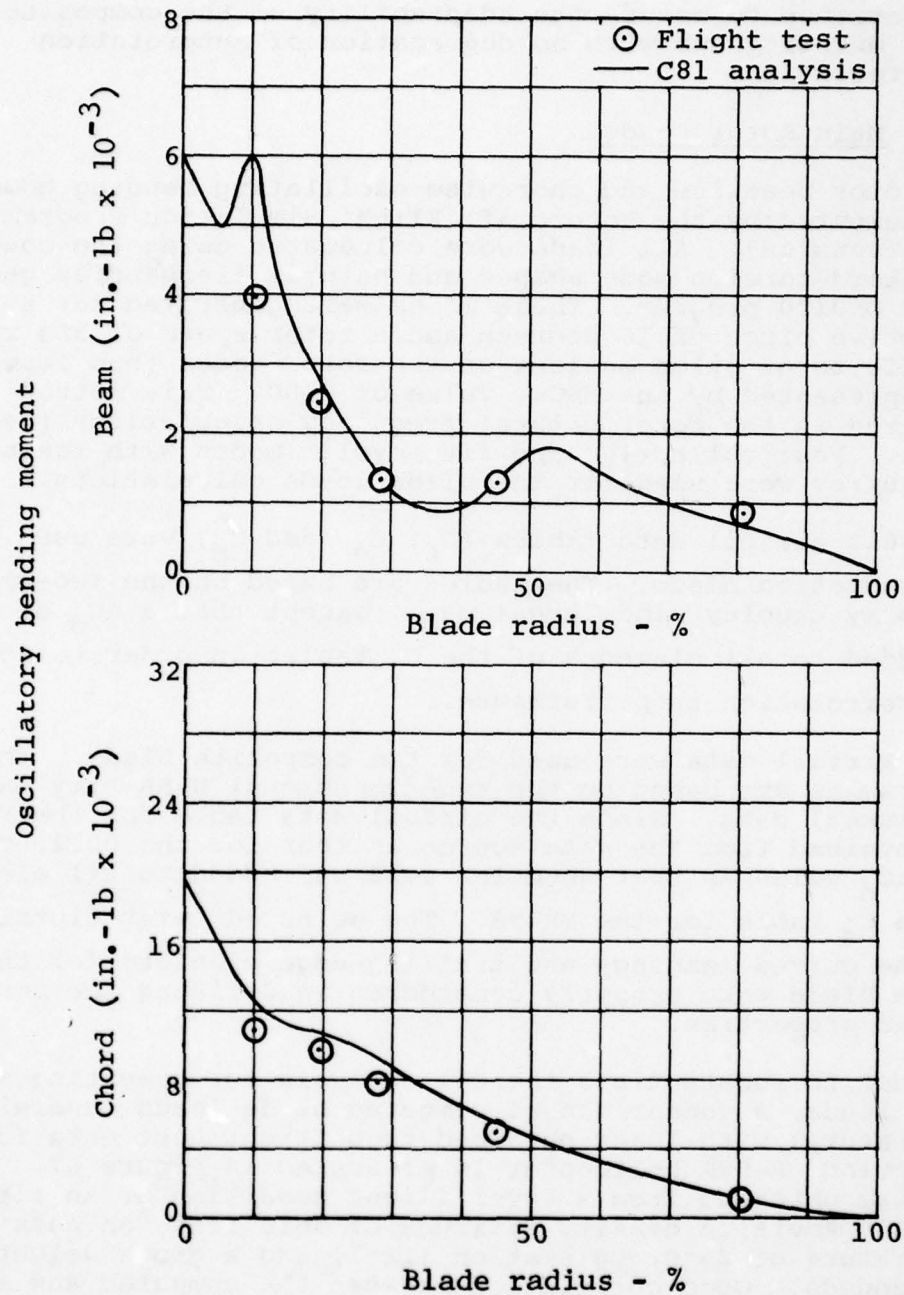


Figure 67. Correlation of calculated and measured main rotor loads for the OH-58A: gross weight = 3000 lb, cg = 112.2, 2100 feet, 76°F, airspeed = 102.5 kn.

account for higher-harmonic airload forcing functions did not noticeably affect the calculated overall oscillatory blade loads for this rotor. Inasmuch as the inclusions of the higher-harmonic induced velocity distribution in the rotor loads calculations is a very time-consuming procedure, the six-harmonic rotor-induced velocity was omitted in all the rotor loads computations.

Rotor loads for the composite blade on an OH-58C helicopter were predicted for several flight conditions. Loads were also computed at the same conditions for the production blade. Flight conditions at which these calculations were made are given in Table 20. The maneuvering flight loads for both rotors were calculated at a load factor of 1.5g.

Spanwise distributions of computed overall oscillatory loads for the two different rotor blades are given in Figures 68 through 76. Comparing these results, the following observations are made:

- In level flight, beam bending moments for the composite blade are slightly higher than those for the production blade at some blade stations. On the other hand, chord bending moments for the composite blade are considerably lower than those for the production blade at all blade stations. This is primarily due to the change in frequency of the fourth cycle made. Refer to Table 19.
- In the cyclic pullup and right and left turns, both the beam and chord loads for the composite blade are lower than those for the production blade at all critical blade stations (blade bolt hole and midspan).

4.4.3 Control Loads

Main rotor pitch-link loads were computed for both unaccelerated and maneuvering flight conditions using BHT computer program C81. To substantiate the accuracy of the C81 analysis in predicting pitch-link loads, correlations of computer steady and oscillatory pitch-link loads with those measured in flight for several airspeed conditions are shown in Figure 77. It is evident that the calculated loads are in good agreement with those measured.

Computed steady and overall oscillatory pitch-link loads for both production and composite blade rotors on an OH-58C helicopter in level flight conditions are presented in Figure 78. Computed pitch-link-load waveforms for the cyclic pullup and the right and left turns are depicted in Figures 79, 80, and 81, respectively. The data demonstrate that both steady and oscillatory pitch-link loads for the composite blade rotor are close to those for the production rotor in all flight conditions. The existing main rotor control system can, therefore, be used with the composite blade without any modifications or reinforcements.

TABLE 20. FLIGHT CONDITIONS FOR
CALCULATIONS OF MAIN
ROTOR LOADS

<u>Flight Condition</u>	<u>Gross Weight (lb)</u>	<u>Center of Gravity (Station)</u>	<u>Rotor Speed (rpm)</u>	<u>Airspeed (knots)</u>	<u>Density Alt, H_D (ft)</u>	<u>OAT (°F)</u>
Level Flt:						
1	3200	112.2	354	70	7122	95
2	3200	112.2	354	90	7122	95
3	3200	112.2	354	100	7122	95
4	3200	112.2	347	90	7122	95
5	3200	112.2	354	90	10000	95
6	2500	112.2	354	90	7122	95
Cyclic Pullup (1.5g)	3200	108	354	70	7122	95
Right Turn (1.5g)	3200	108	354	70	7122	95
Left Turn (1.5g)	3200	108	354	70	7122	95

<u>Legend</u>	<u>Note</u>
— C81, Production blade	See Table 20 for
- - - C81, Composite blade	flight conditions

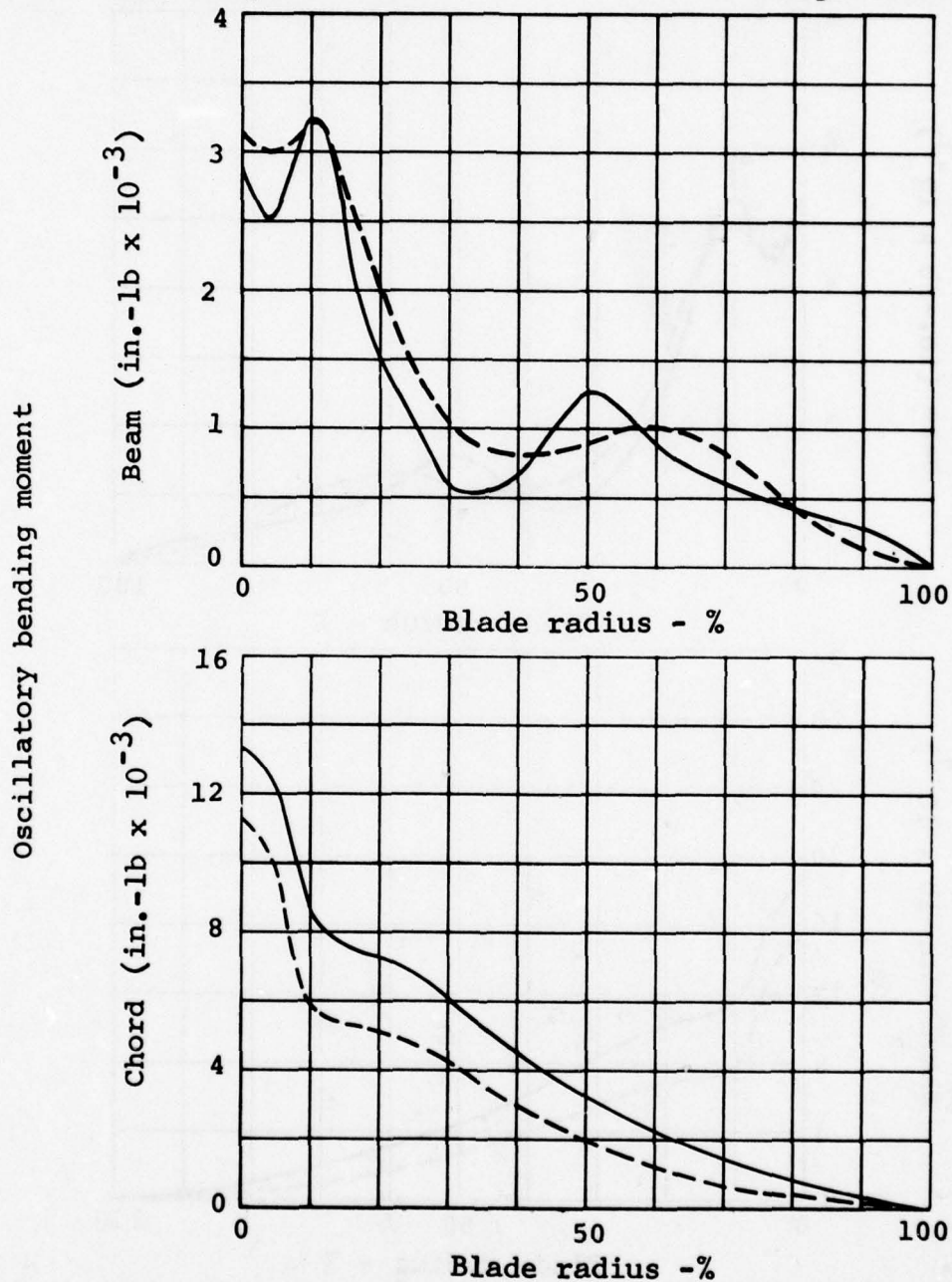


Figure 68. Calculated main rotor loads for OH-58C with production and composite blades: flight condition 1.

Legend
 — C81, Production blade
 - - - C81, Composite blade

Note
 See Table 20 for
 flight conditions

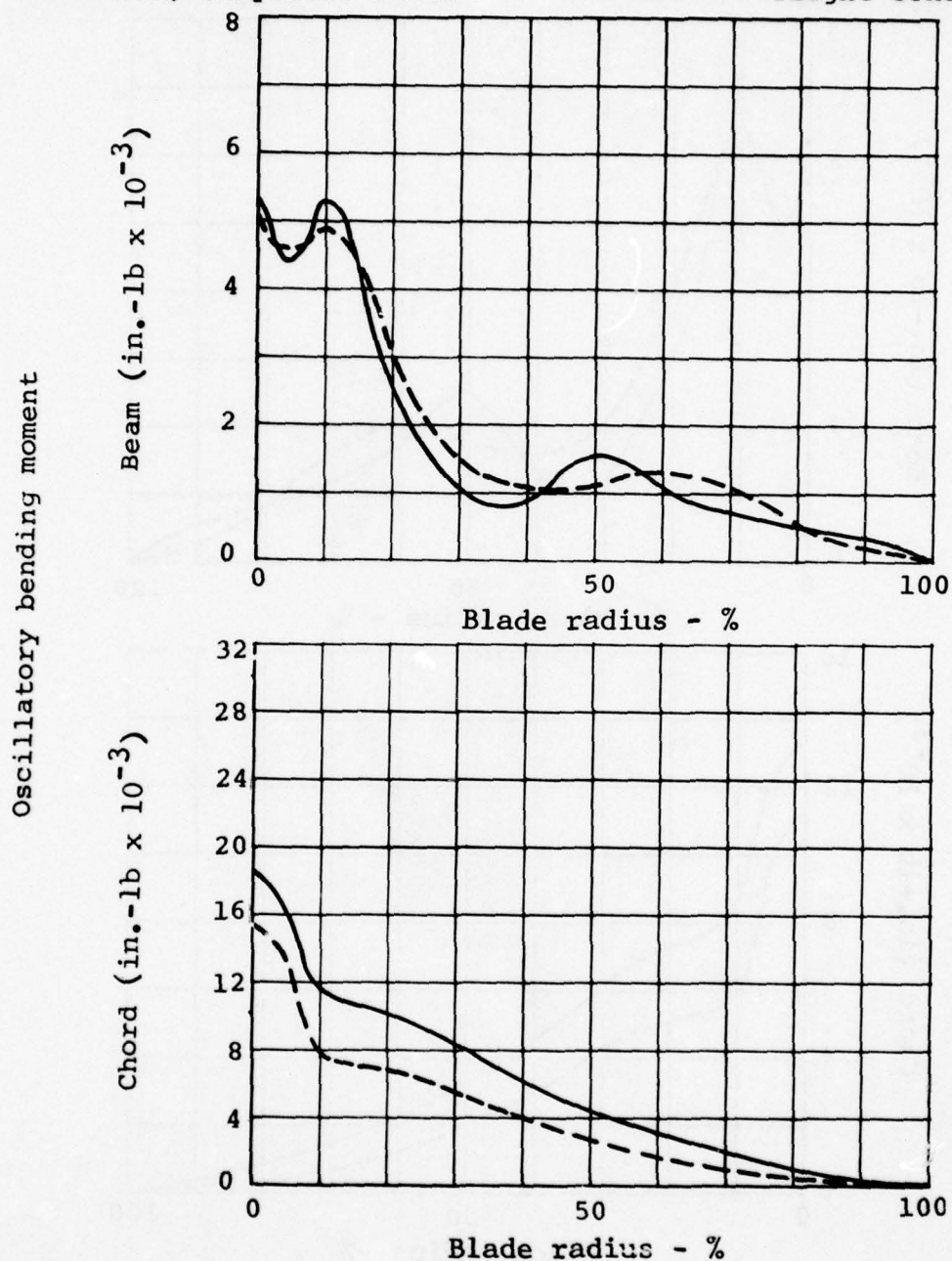


Figure 69. Calculated main rotor loads for OH-58C with production and composite blades: flight condition 2.

Legend
 — C81, Production blade
 - - - C81, Composite blade

Note
 See Table 20 for flight conditions

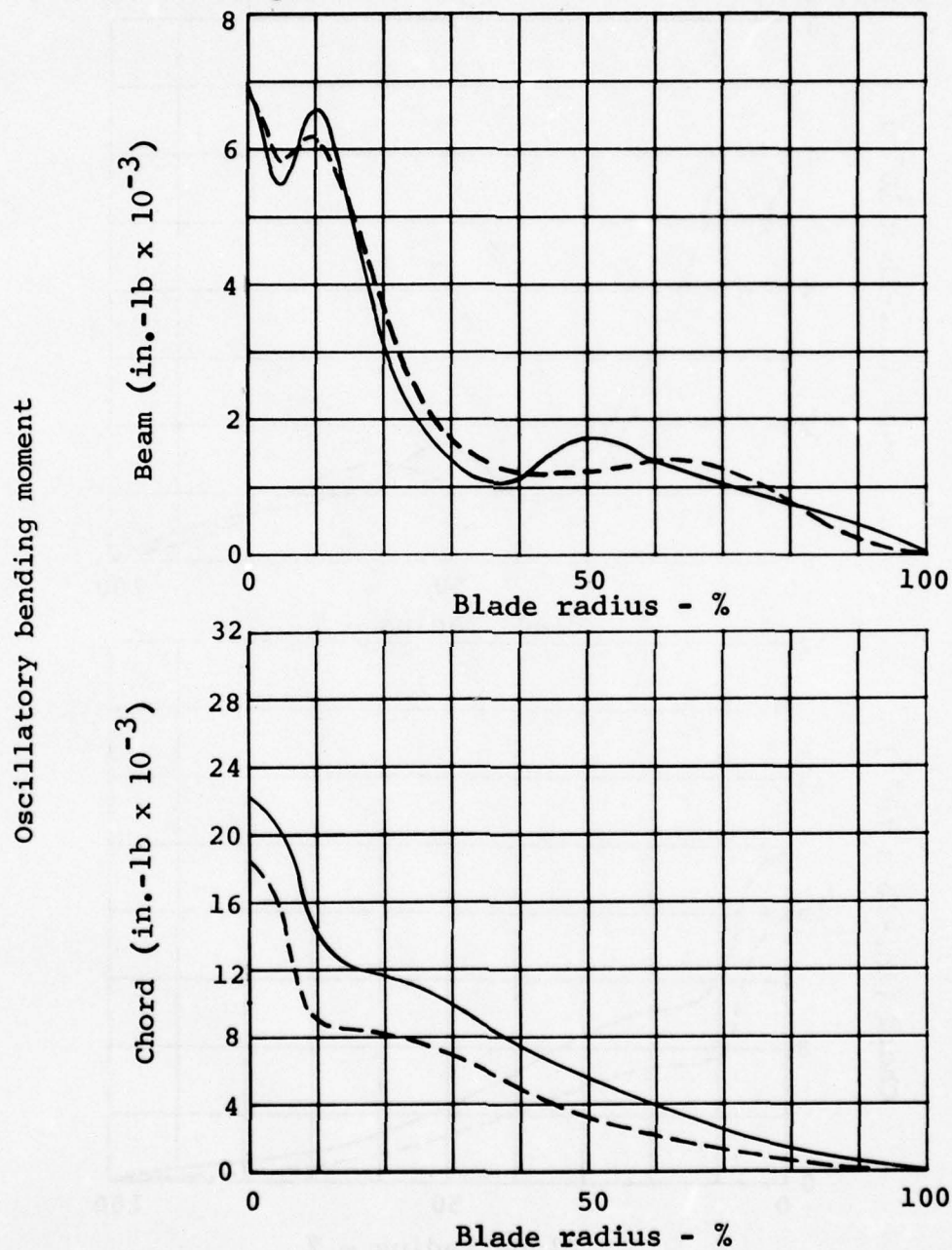


Figure 70. Calculated main rotor loads for OH-58C with production and composite blades: flight condition 3.

Legend
 — C81, Production blade
 - - - C81, Composite blade

Note
 See Table 20 for
 flight conditions

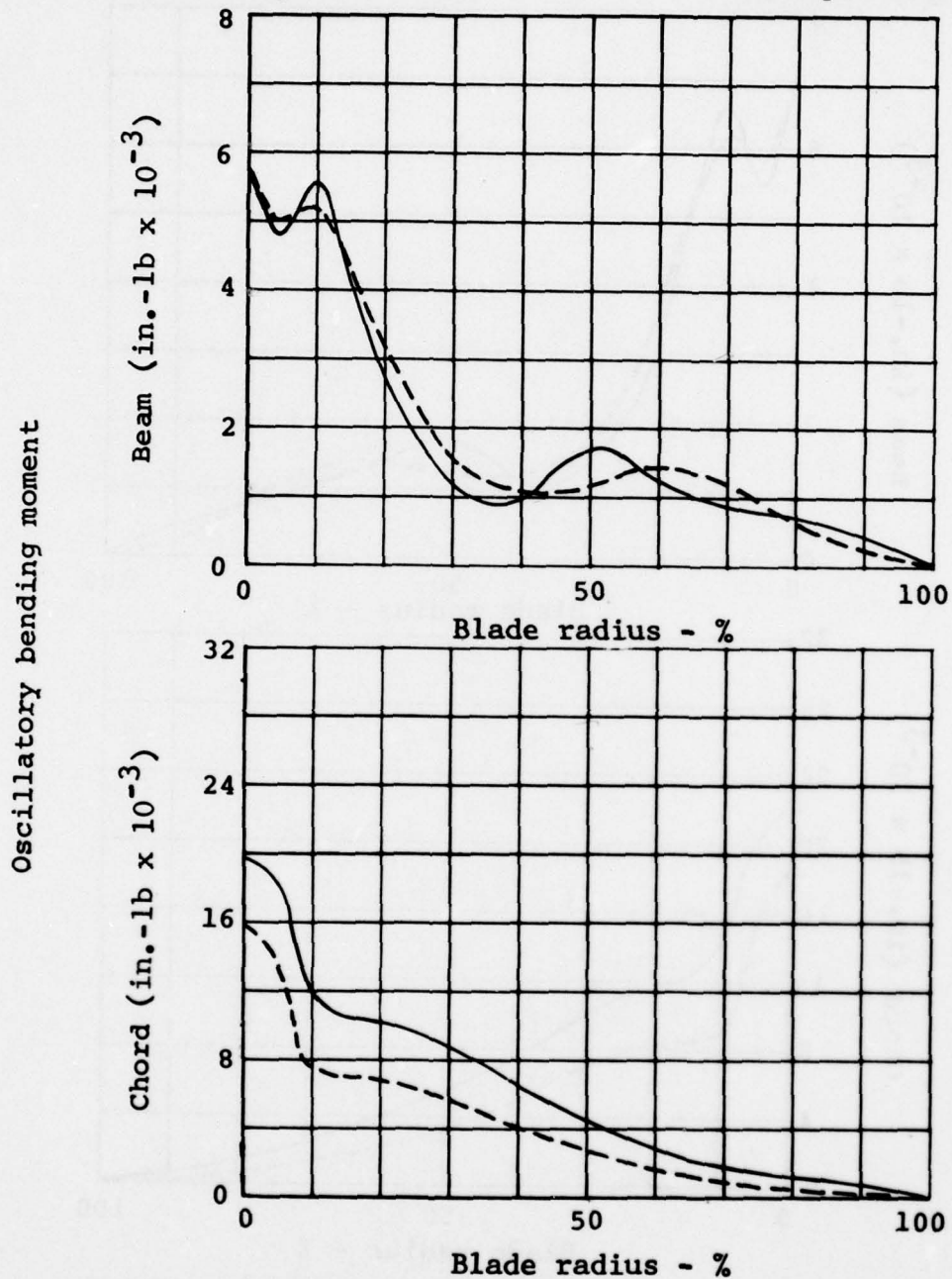


Figure 71. Calculated main rotor loads for OH-58C with production and composite blades: flight condition 4.

Legend
 — C81, Production blade
 - - - C81, Composite blade

Note
 See Table 20 for
 flight conditions

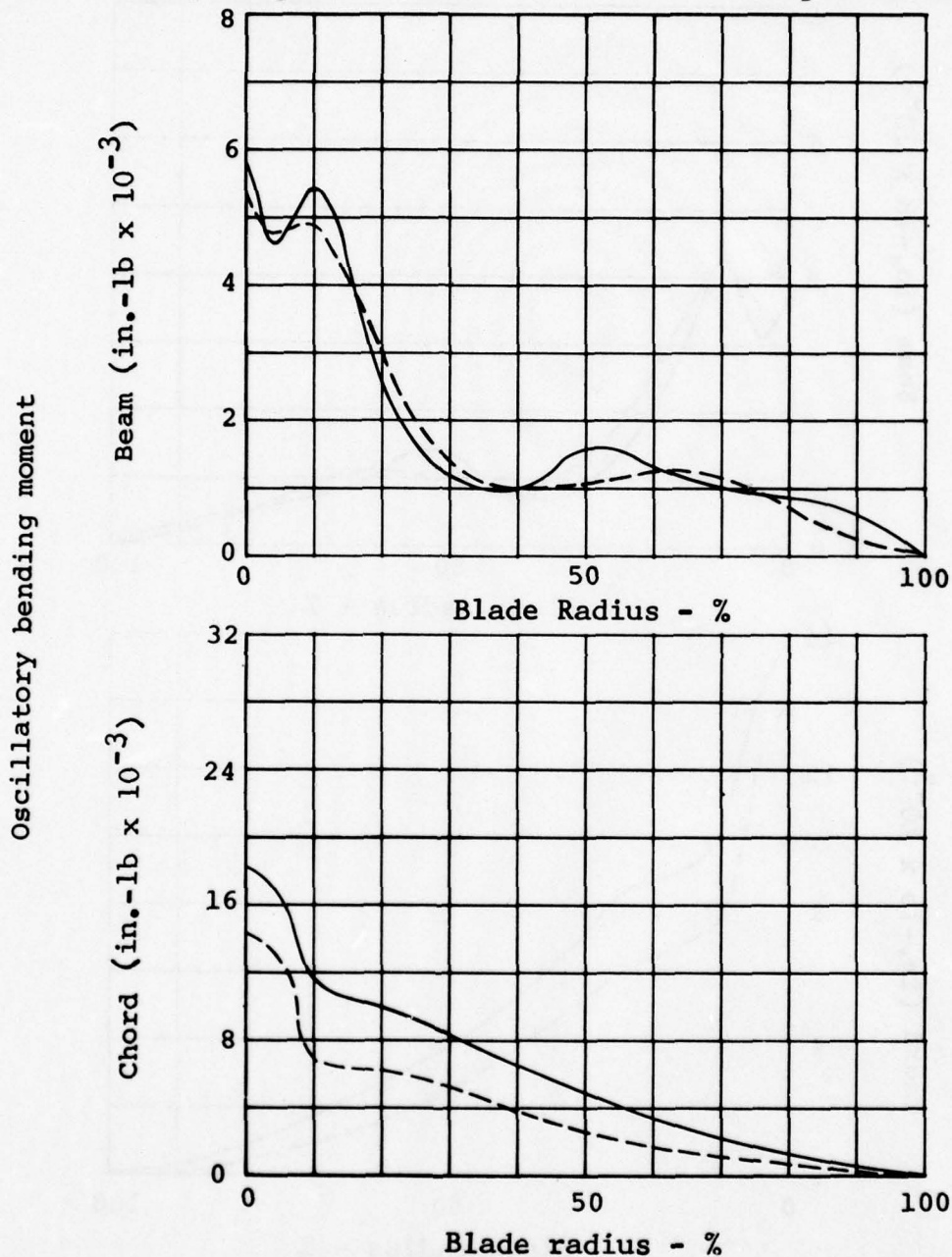


Figure 72. Calculated main rotor loads for OH-58C with production and composite blades: flight condition 5.

Legend
 — C81, Production blade rotor
 - - - C81, Composite blade rotor

Note
 See Table 20 for
 flight conditions

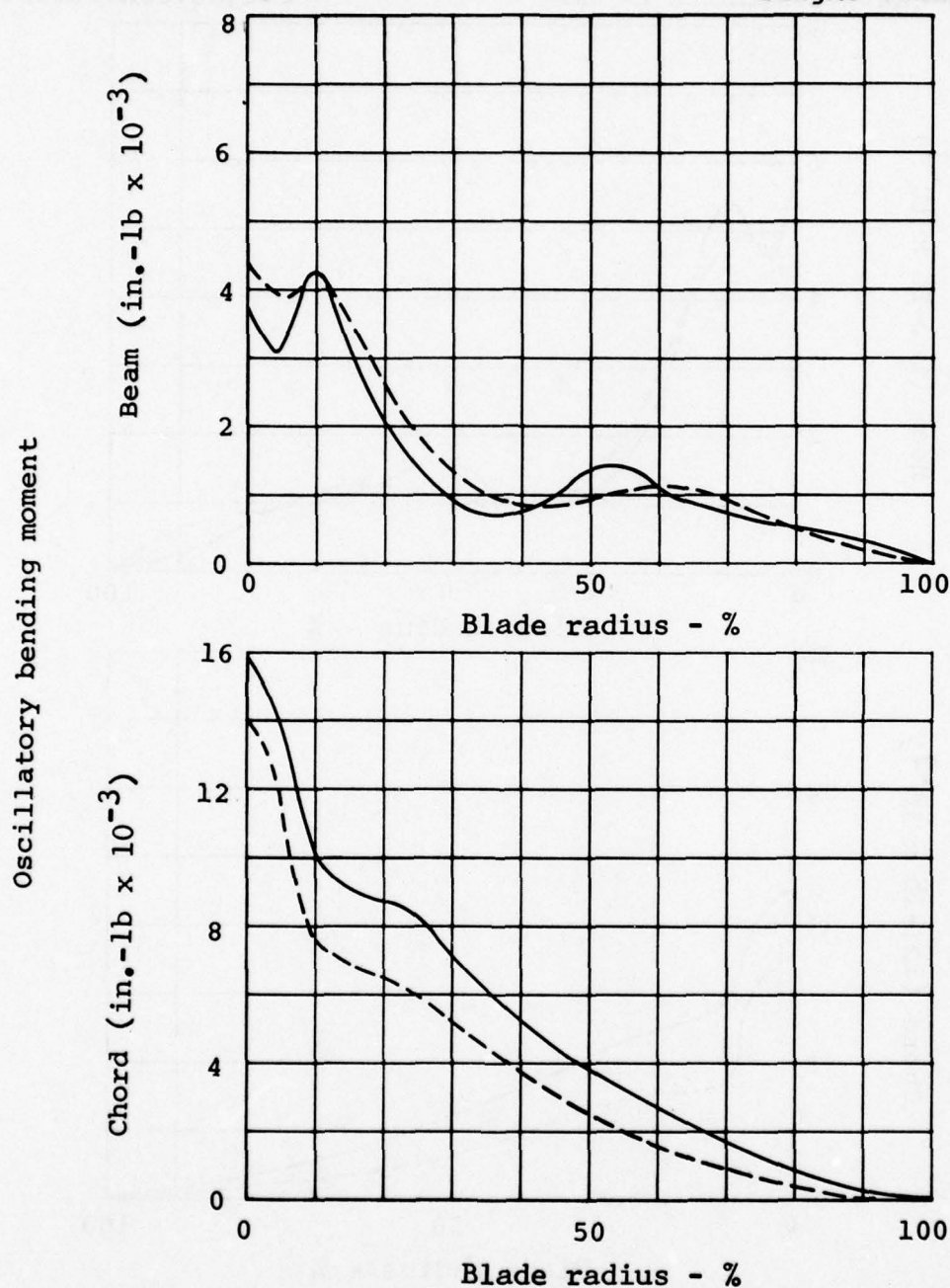


Figure 73. Calculated main rotor loads for OH-58C with production and composite blades: flight condition 6.

Legend
 — C81, Production blade rotor
 - - - C81, Composite blade rotor

Note
 See Table 20 for
 flight conditions

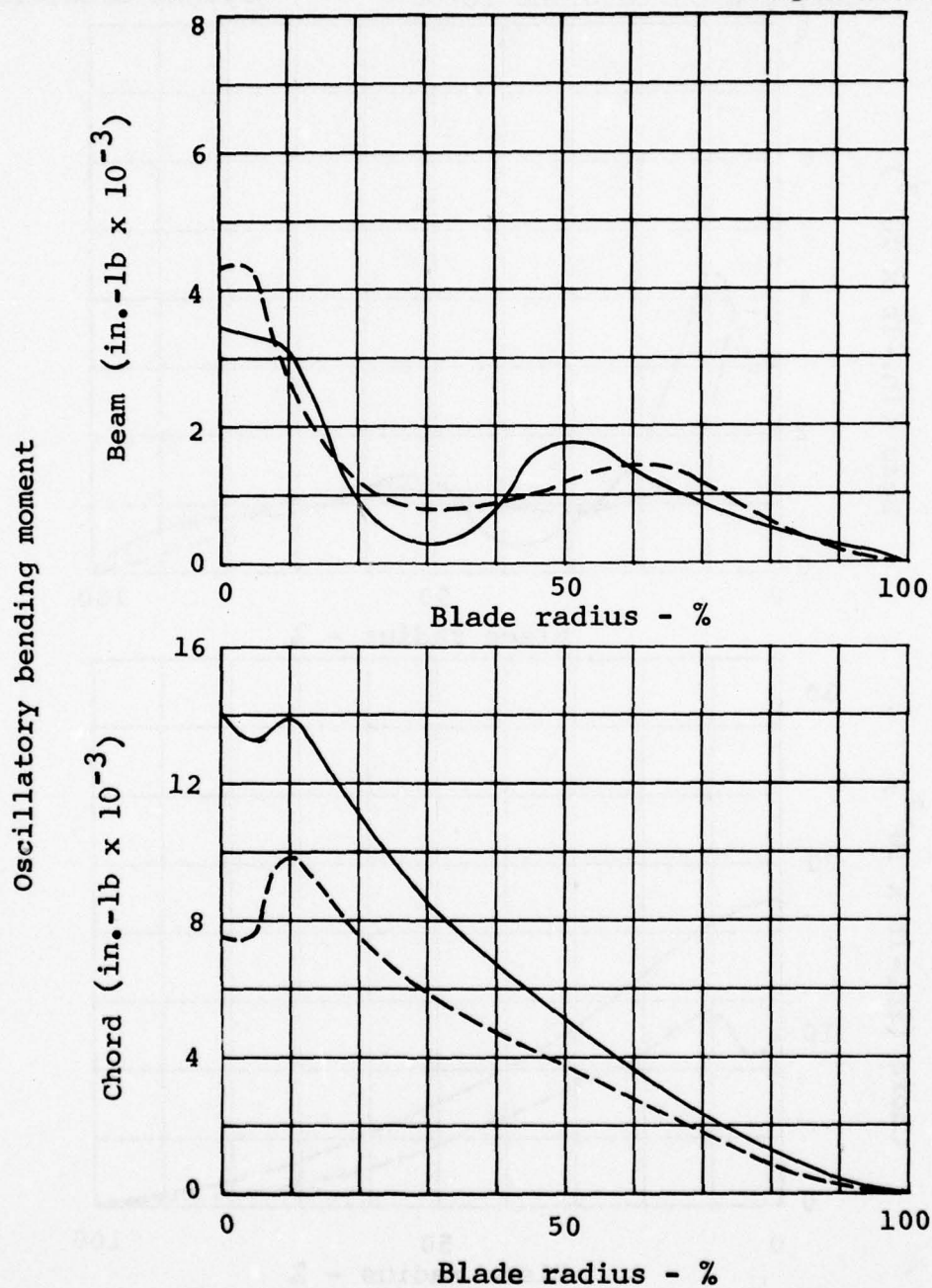


Figure 74. Calculated main rotor loads for OH-58C with production and composite blades: cyclic pullup.

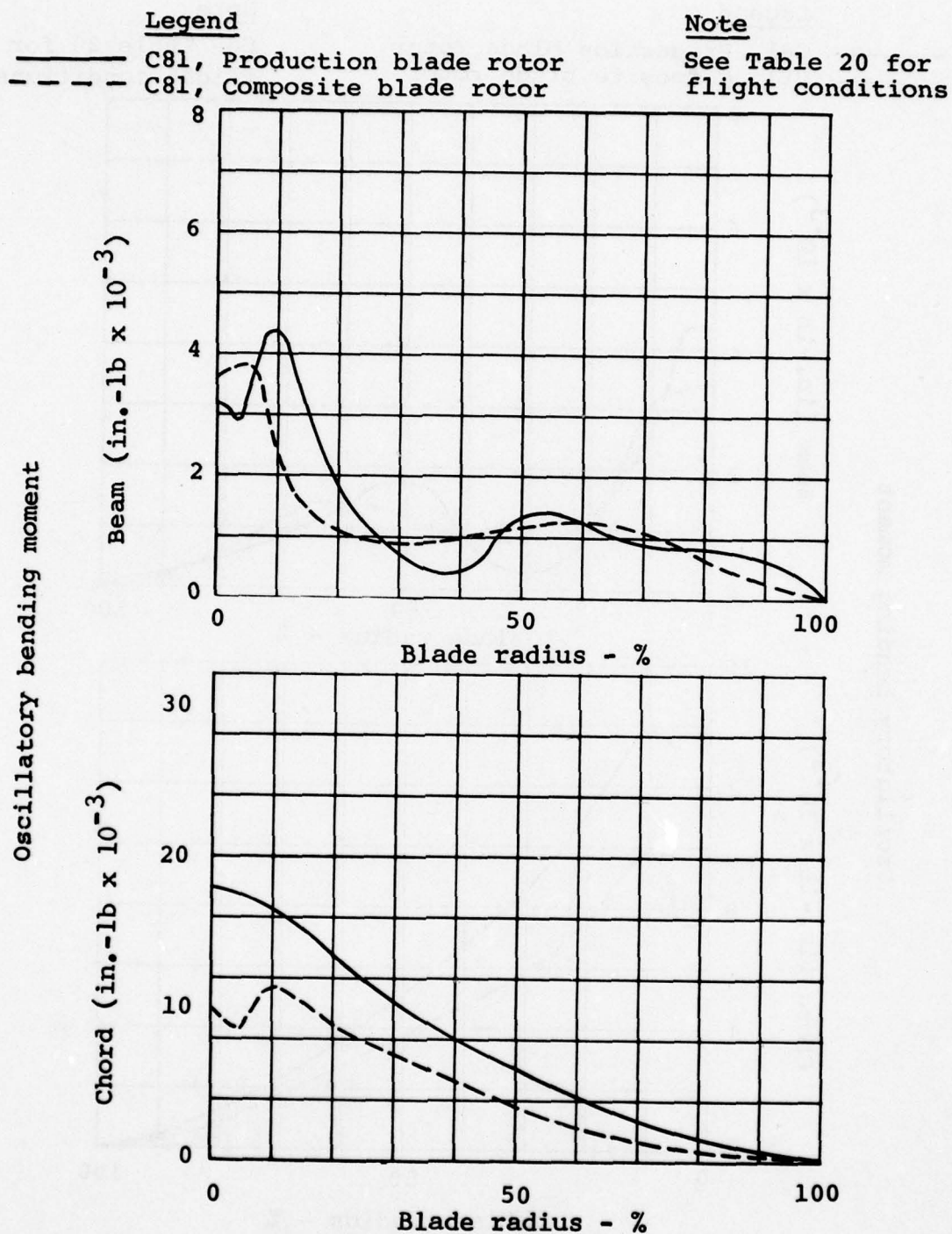


Figure 75. Calculated main rotor loads for OH-58C with production and composite blades: right turn.

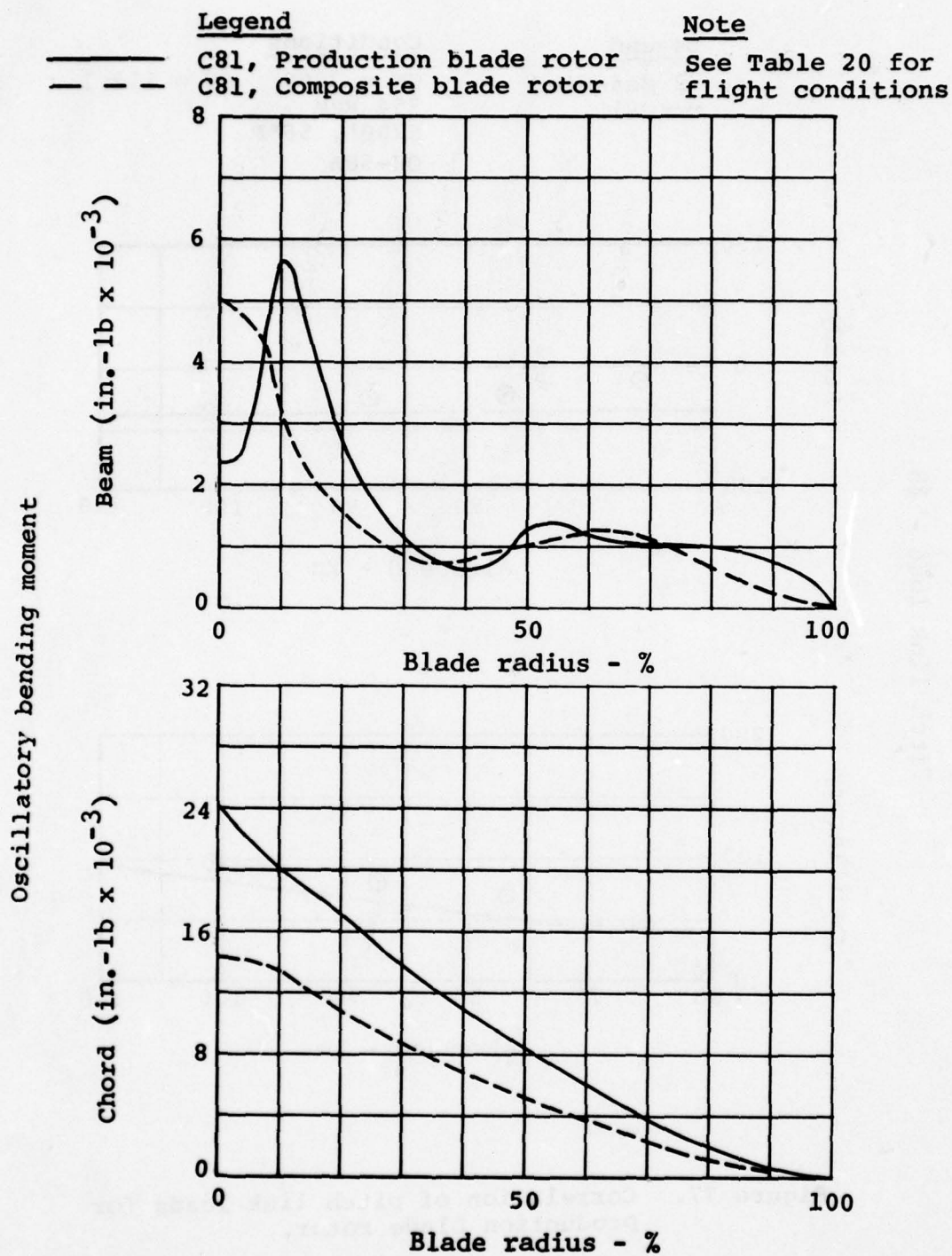


Figure 76. Calculated main rotor loads for OH-58C with production and composite blades: left turn.

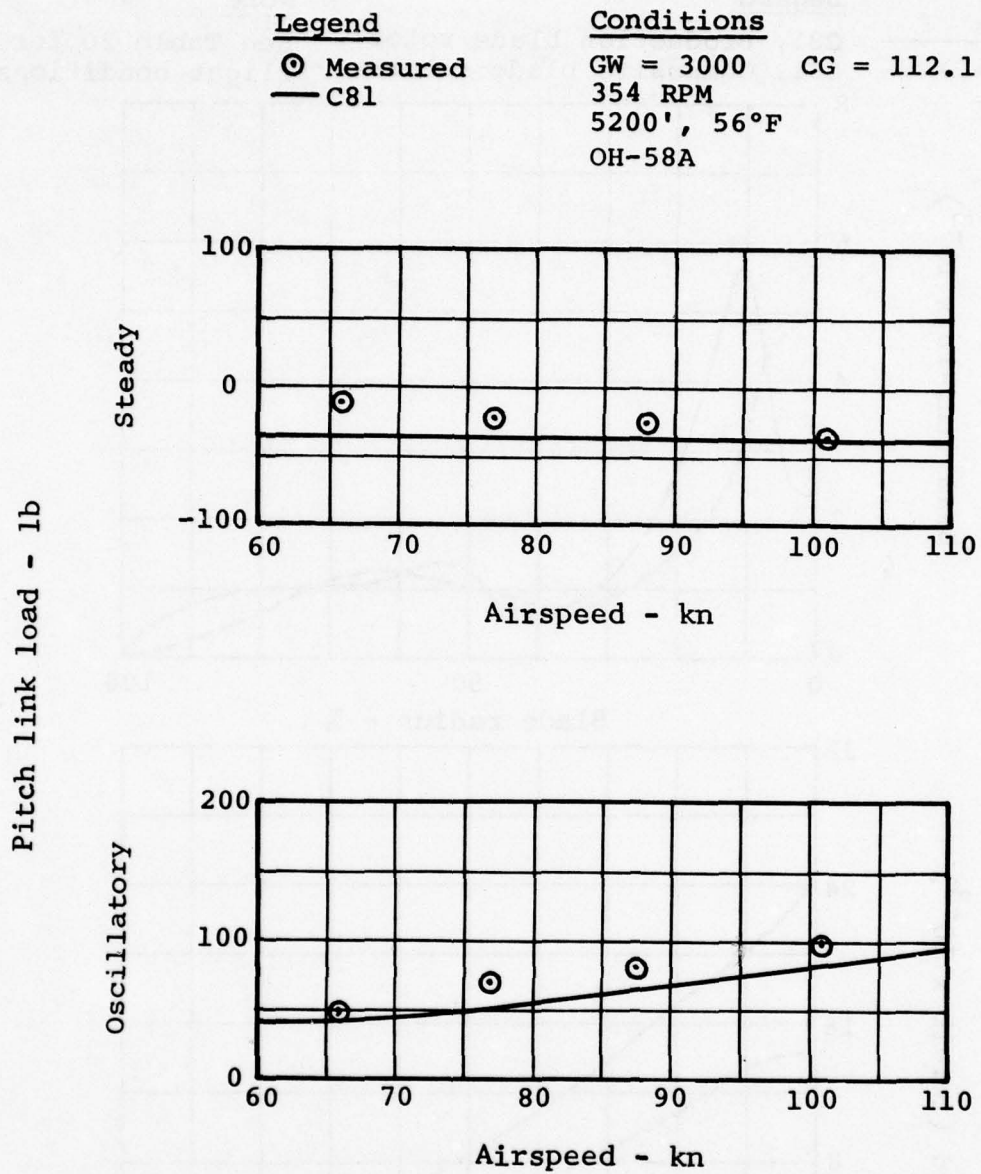


Figure 77. Correlation of pitch link loads for production blade rotor.

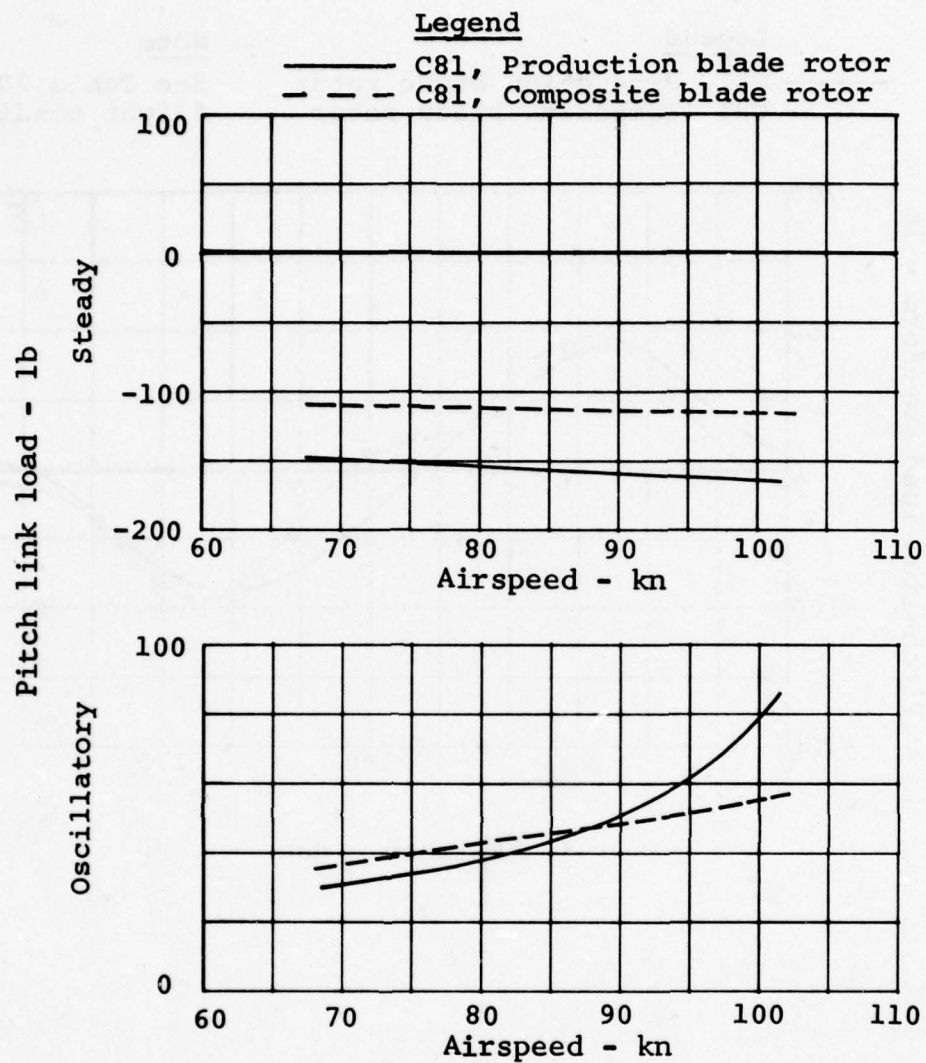


Figure 78. Calculated pitch link loads in level flight for OH-58C with production and composite blade rotors: ground weight = 3200 lb, aft cg, 4000 feet and 95°F.

<u>Legend</u>		<u>Note</u>
—	C81, Production blade rotor	See Table 20 for flight conditions
- - -	C81, Composite blade rotor	

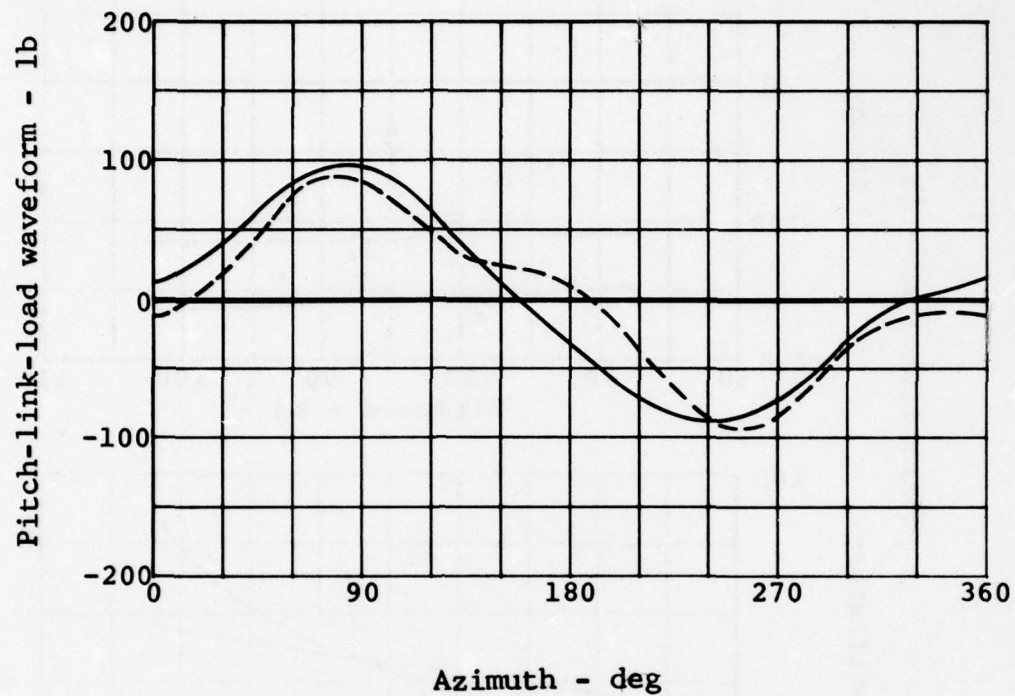


Figure 79. Computed pitch-link-load waveforms for the production and composite blade rotors: cyclic pullup at 1.5g.

Legend

— C81, Production blade rotor

- - - C81, Composite blade rotor

Note

See Table 20 for flight conditions

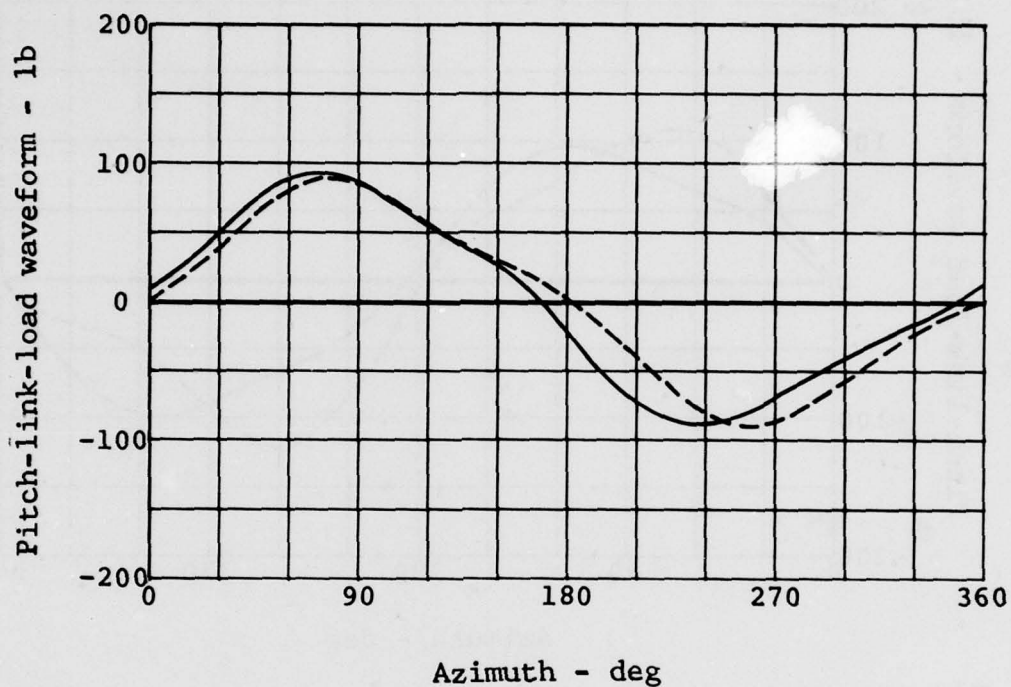


Figure 80. Computed pitch-link-load waveforms for the production and composite blade rotors: right turn at 1.5g.

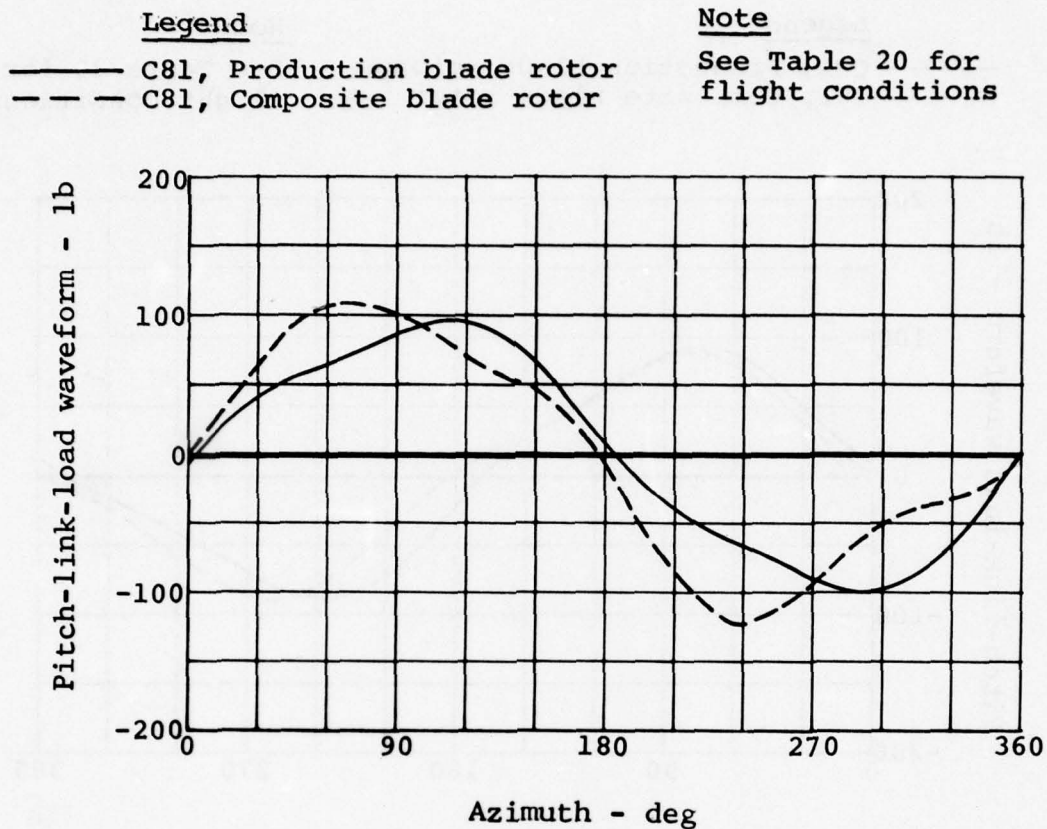


Figure 81. Computed pitch-link-loads waveforms for the production and composite blade rotors: left turn at 1.5g

The effect of the blade's elastic torsional deflection on performance for both production and composite blade rotors was also assessed by C81 during the rotor loads evaluation. The results indicate that the elastic twist for both rotors is so small that the aeroelastic effects on performance are negligible.

4.4.4 Rotor/Pylon Subharmonic Instability

The OH-58C/A helicopter equipped with the production rotor is free from rotor/pylon subharmonic instability. The primary reason for the inherent stability is the fact that the pylon and rotor system are completely decoupled from each other. To demonstrate this, BHT computer program DFAL5 was used. Figure 82 presents the computed stability boundaries for swashplate/pylon cyclic couplings in hover for the OH-58C/A with the production rotor. As shown, the design point is well removed from instabilities.

The composite blade was designed to have dynamic properties similar to those of the production rotor. The blade flapping inertia for the composite blade is 327.3 slug-ft^2 , while that for the production rotor is 335.7 slug-ft^2 . The Lock number for the composite blade rotor is 4.36 at 4000 feet, 95°F , while that for the production rotor is 4.40. With these small differences, the instability boundaries in hover for the OH-58C/A with the composite blade are essentially unchanged from those with the production rotor.

BHT computer program DYN5 was used to study the rotor/pylon subharmonic instabilities in forward flight. The analysis was conducted for both production and composite blade rotors on an OH-58C helicopter at 100 knots, 3200-pound gross weight, 4000 feet, and 95°F . To excite the rotor/pylon cyclic modes, a pylon plucking in the longitudinal direction was conducted. Time histories of the rotor/pylon response to the pylon plucking for the production and composite blade rotors are presented in Figures 83 and 84, respectively. No subharmonic instabilities are found for either rotor.

Swashplate/pylon collective couplings do not exist for the OH-58 helicopter in all flight conditions since the pylon does not move vertically with respect to the fuselage. Therefore, there is no possibility of subharmonic instabilities with the composite blade due to rotor/pylon collective couplings.

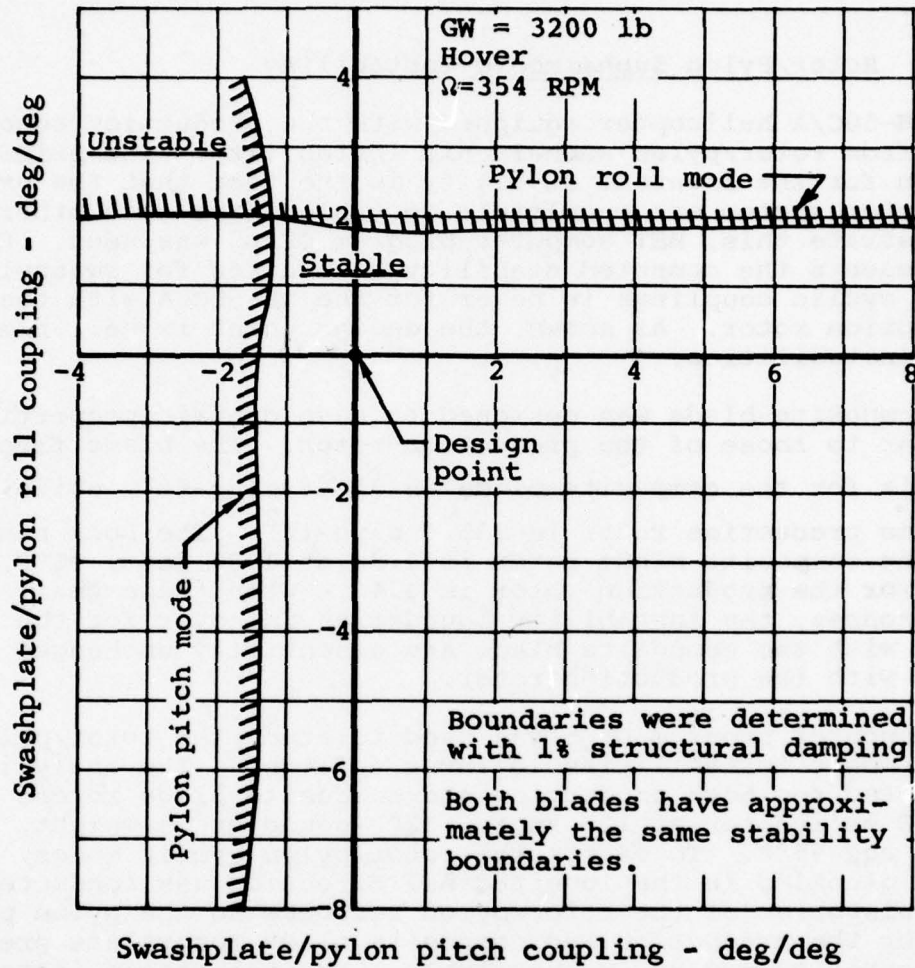


Figure 82. Stability boundary with swashplate/pylon coupling for both production and composite blade rotors.

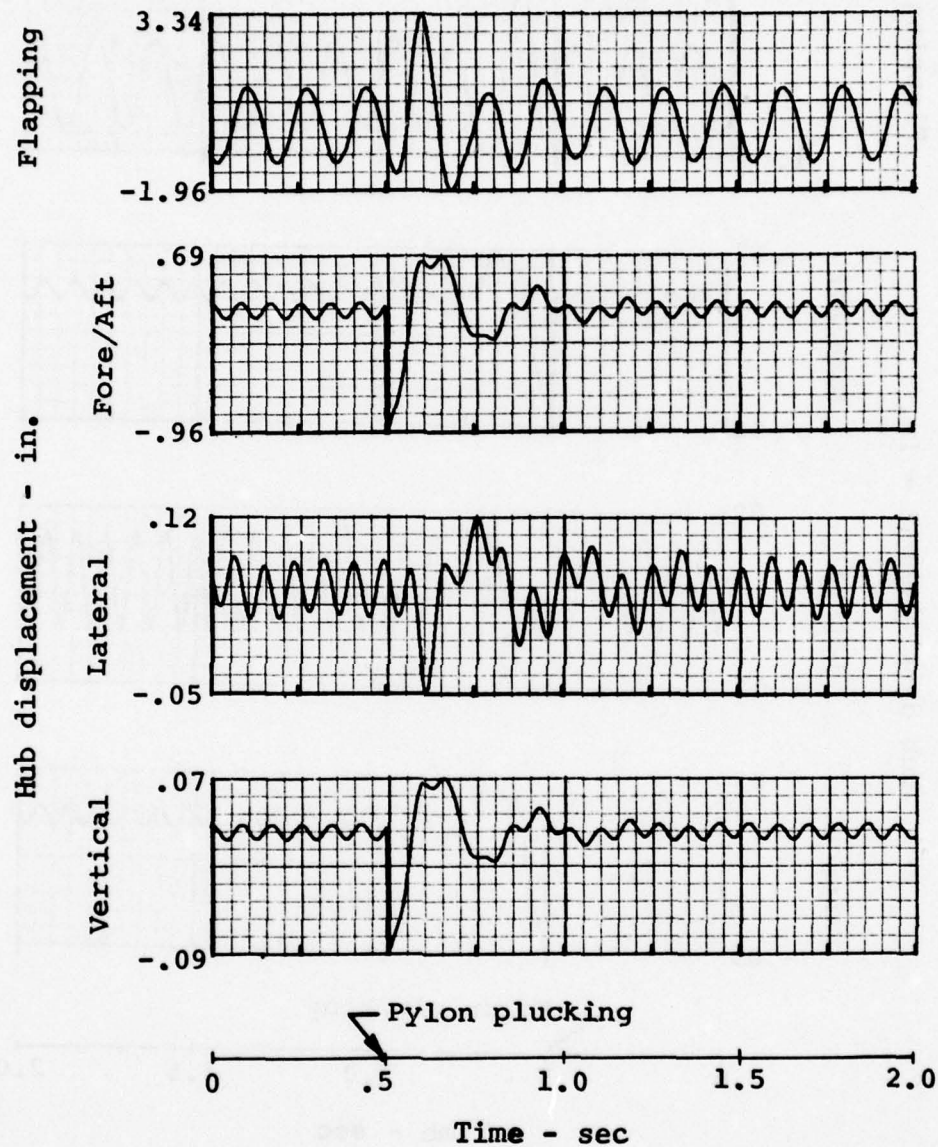


Figure 83. Production rotor and pylon response to pylon plucking at 100 knots, 354 rpm, level flight.

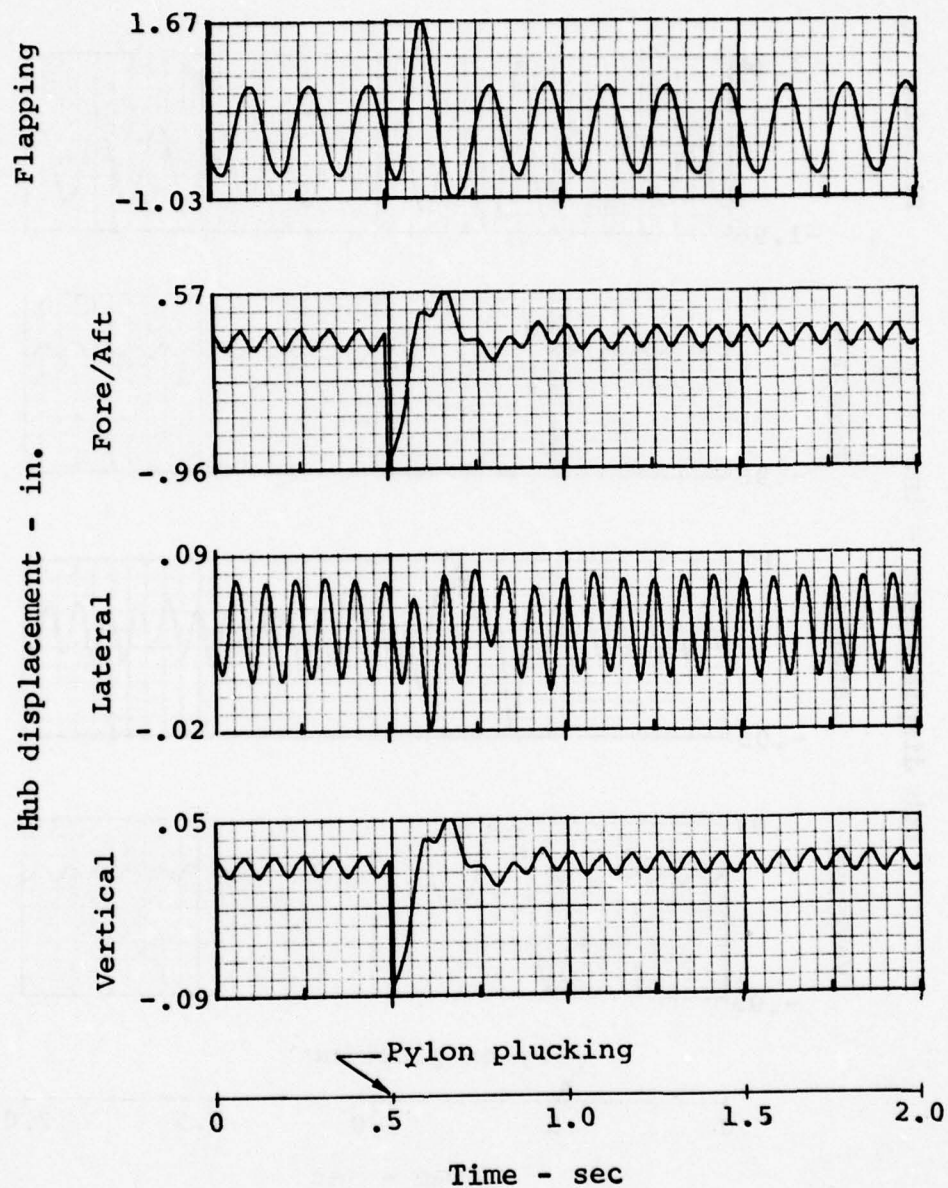


Figure 84. Composite blade rotor and pylon response to pylon plucking at 100 knots, 354 rpm, level flight.

4.4.5 Blade Flap-Lag Instability

The OH-58C/A helicopter with the production main rotor is free from flap-lag instability. To demonstrate this analytically, BHT computer program DR0620-A was used. Root loci of the blade flapping and first inplane modes are given in Figure 85. Both modes are stable.

The analysis was then repeated for the rotor with composite blades. Due to dynamic similarities between the two rotors, the calculated root loci for this rotor is very close to those for the production rotor. Since the rotor with composite blades has better first lead-lag frequency placement (1.30/rev) than that for the production rotor (1.25/rev), better blade flap-lag stability characteristics for the improved rotor are expected.

4.4.6 Blade Bending-Torsion Flutter

BHT computer program DFAV05 was used to analyze both the production and composite blades for classical flutter phenomena. Four collective and five cyclic coupled blade modes at flat pitch were obtained from BHT computer program DN9100 (Section 4.4.1) and were input to DFAV05. Variations in aerodynamic center locations and lift curve slopes with Mach number for the NACA 0012 and the FX098 airfoil were employed to account for compressibility effects. Figures 86 through 89 show the calculated frequency and damping versus airspeed at 354 rpm for the production and composite rotors. The results indicate that neither flutter nor divergence is present throughout the flight envelope.

4.4.7 Blade Stall Flutter

The C81 analysis has been substantiated by comparing measured and computed level flight pitch-link loads (Section 4.4.3). Stall flutter characteristics for the composite blade rotor on an OH-58C helicopter were then investigated using C81 to determine the value of C_T/σ at the onset of retreating blade stall for an advance ratio of 0.23. The results are shown in Figure 90. The onset of retreating blade stall is indicated by a noticeable change in slope in the plot of the shaft horsepower and oscillatory root chordwise bending moments versus C_T/σ . Since there is not a sharp increase in the oscillatory pitch-link load, it is evident that stall flutter does not occur. To further demonstrate the stall-flutter-free phenomenon, the computed pitch-link-load waveform at the maximum C_T/σ in Figure 90 is given in Figure 91. As observed, there is no limit cycle oscillation in the pitch-link load when the blade is in the fourth gradient of the blade azimuth. The absence of such

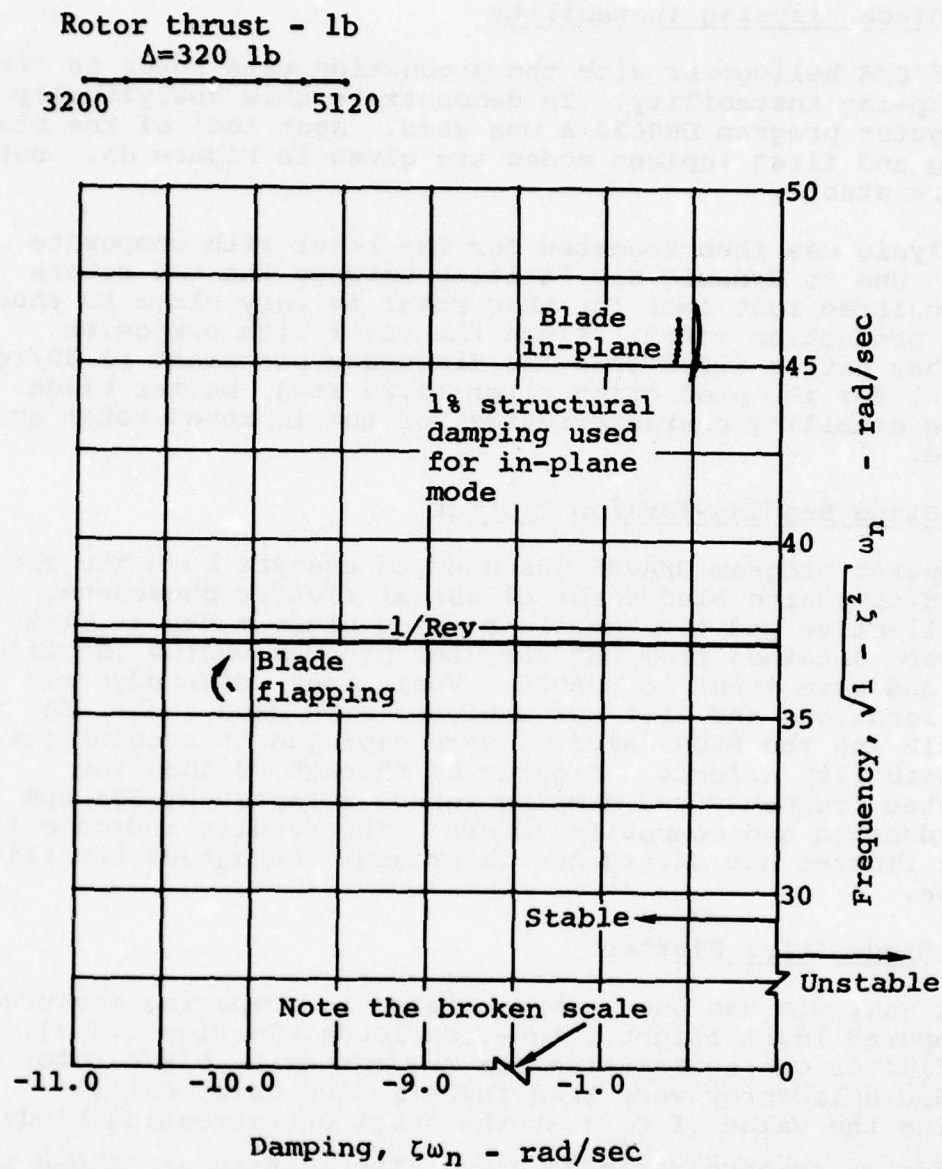


Figure 85. Flap-lag stability for OH-58C/A production blade rotor.

1. First collective (coning)
2. Second collective
3. Third collective (inplane)
4. Fourth collective (torsion)
5. First cyclic (flapping)
6. Second cyclic (inplane)
7. Third cyclic
8. Fourth cyclic
9. Fifth cyclic (torsion)

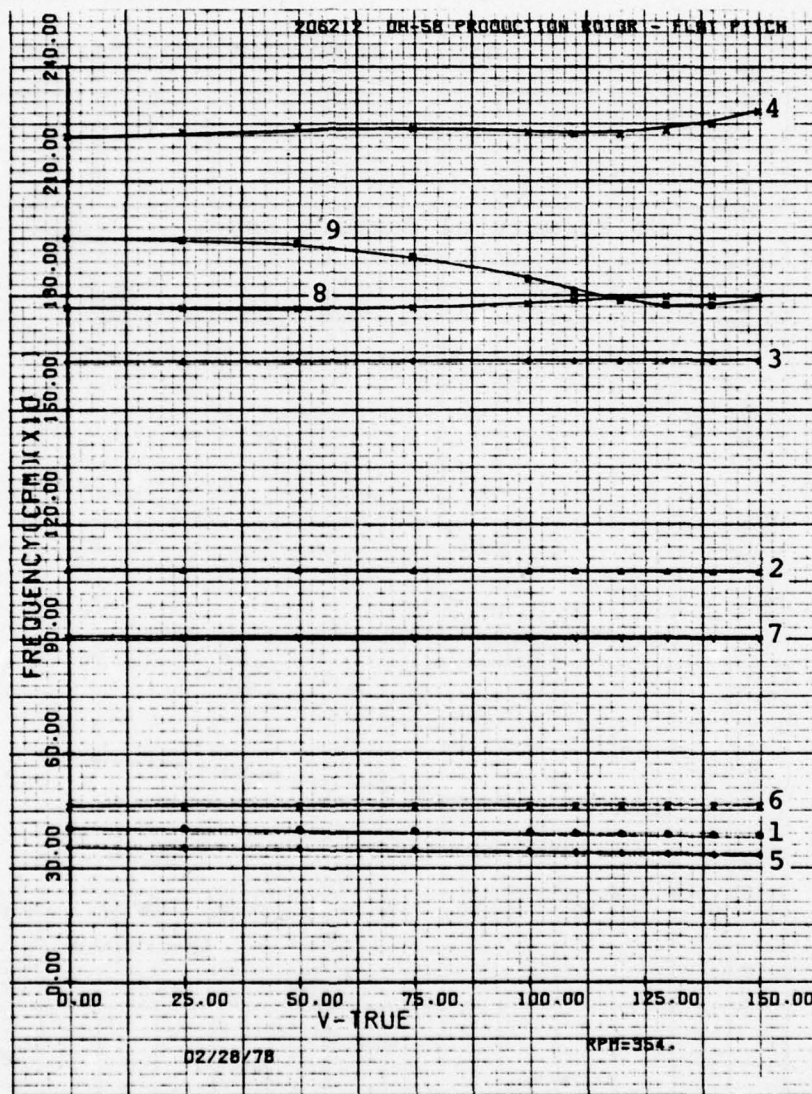


Figure 86. Production blade frequency variation with airspeed.

1. First collective (coning)
2. Second collective
3. Third collective (inplane)
4. Fourth collective (torsion)
5. First cyclic (flapping)
6. Second cyclic (inplane)
7. Third cyclic
8. Fourth cyclic
9. Fifth cyclic (torsion)

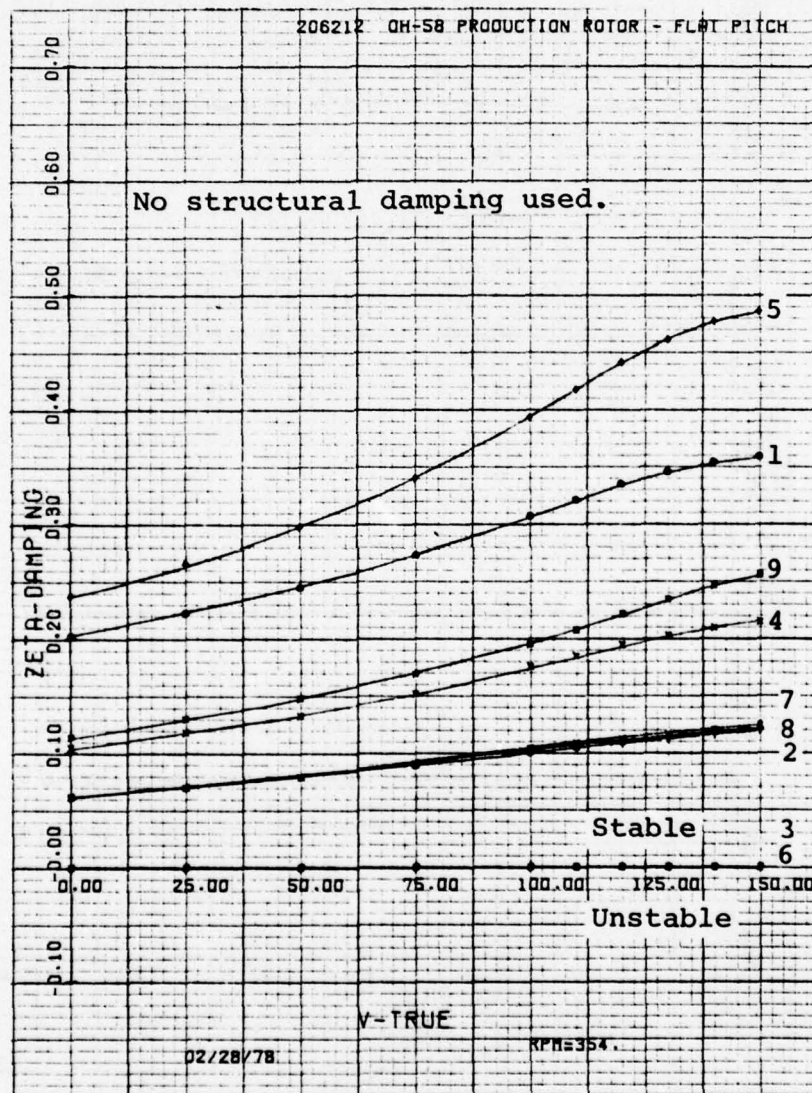


Figure 87. Production blade damping variation with airspeed.

1. First collective (coning)
2. Second collective
3. Third collective (inplane)
4. Fourth collective (torsion)
5. First cyclic (flapping)
6. Second cyclic (inplane)
7. Third cyclic
8. Fourth cyclic
9. Fifth cyclic (torsion)

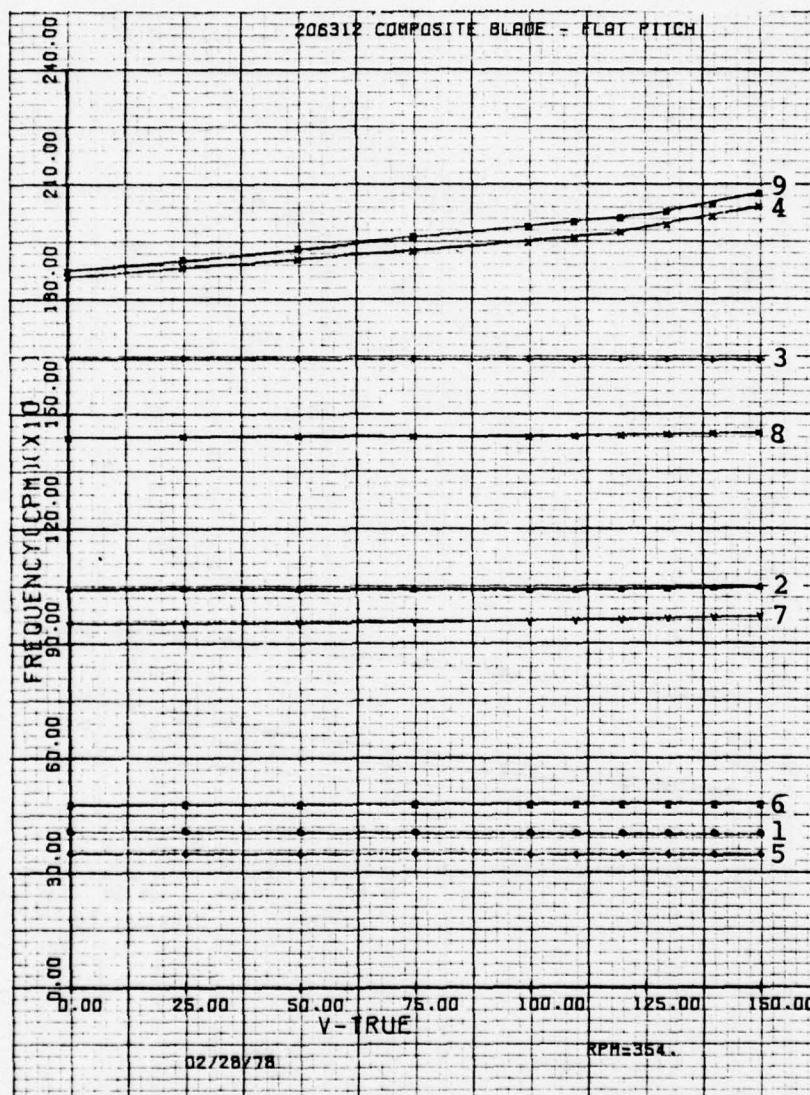


Figure 88. Composite blade frequency variation with airspeed.

1. First collective (coning)
2. Second collective
3. Third collective (inplane)
4. Fourth collective (torsion)
5. First cyclic (flapping)
6. Second cyclic (inplane)
7. Third cyclic
8. Fourth cyclic
9. Fifth cyclic (torsion)

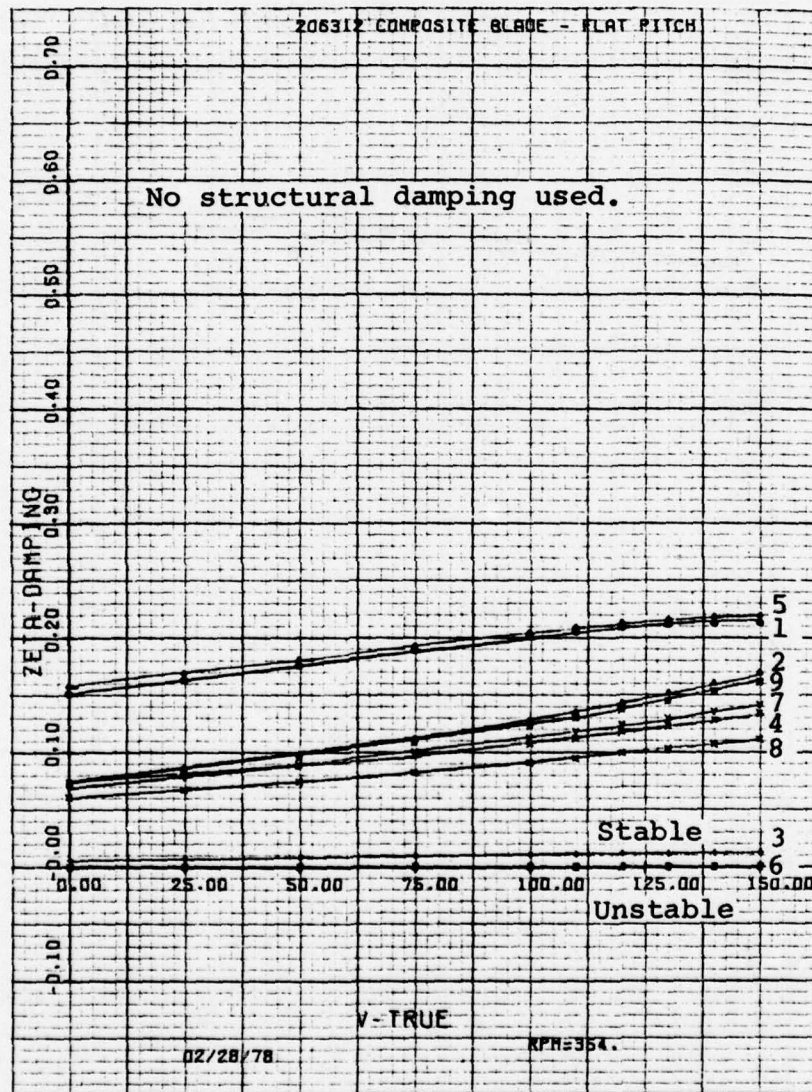


Figure 89. Composite blade damping variation with airspeed.

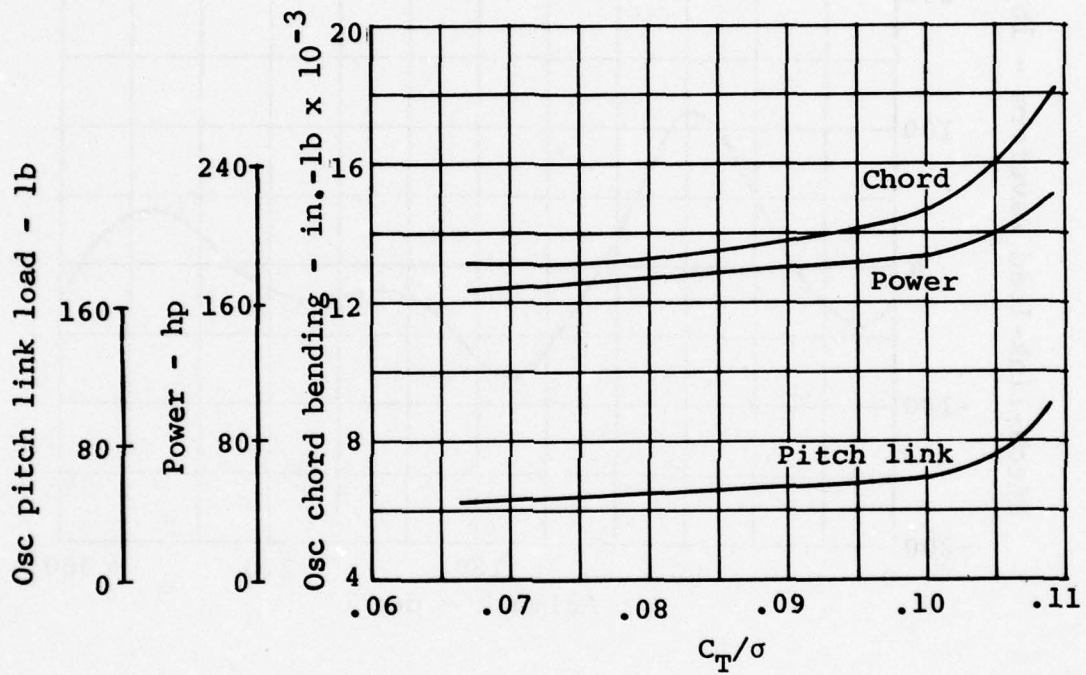


Figure 90. Plot for determination of onset of retreating blade stall at $\mu = .23$.

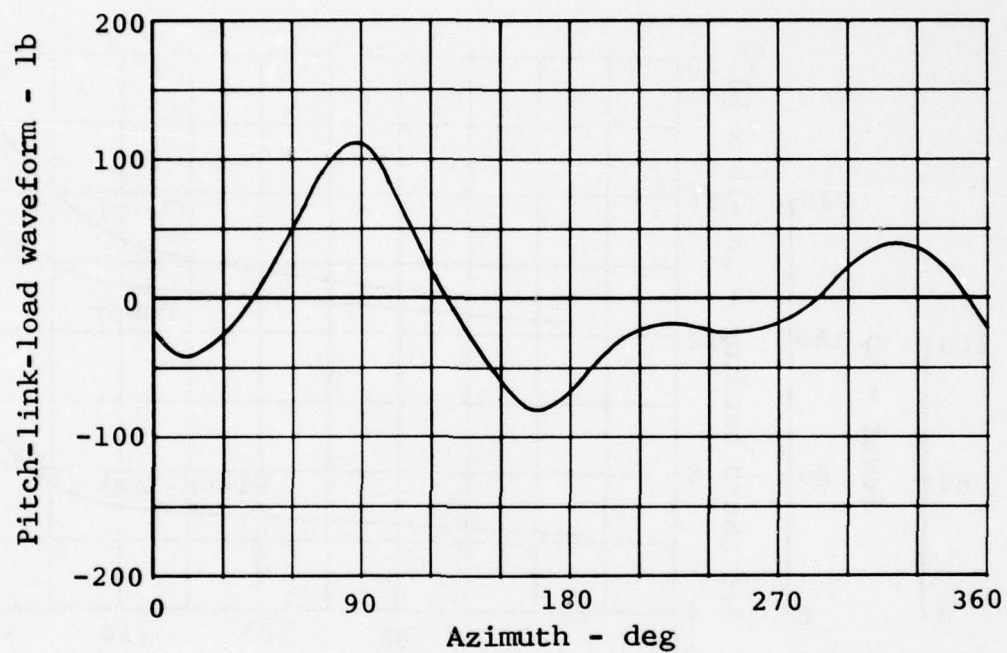


Figure 91. Computed pitch-link-load waveform
for the composite blade rotor:
 $C_T/\sigma = 0.109$, $\mu = .23$.

large loads in a flight condition with retreating blade stall is a clear indication that the composite blade rotor is not susceptible to stall flutter.

4.4.8 Vibration Characteristics

BHT computer program C81 was used to predict hub vibrations in level flight for the composite blade rotor on a standard OH-58C hub/pylon/airframe. To present the results in better perspective, hub vibrations for the production rotor were also computed at the same flight conditions. Figure 92 shows the 2/rev longitudinal, lateral, and vertical vibration levels for both rotors. The results indicate that vibration levels with the composite blade rotor are close to those with the production blade rotor.

4.5 MANUFACTURING METHODOLOGY

4.5.1 Blade Manufacturing Background

BHT has been conducting extensive manufacturing research and development under IR&D funding to establish cost-effective methods for producing rotor blades and effective methods for producing rotor blades and other structures from composite materials. These programs have resulted in the development of several experimental glass fiber/epoxy rotor blades including the model 649 main rotor blade, shown in Figure 93, and the Model 654 rotor shown in Figure 94. Based on the Model 649 rotor development program, the Model 214 fiberglass rotor blade has been placed in production. Approximately 20 of these blades have been produced and both FAA certification and military qualification under government cognizance are in progress.

This extensive manufacturing experience has been the basis for judgements in the manufacturing trade-off studies on the proposed OH-58C/A blade. The following areas are significant:

- Internal pressure systems for curing of parts
- Mechanized filament placement techniques
- Basic material control processes vital to a successful manufacturing operation

2/rev component of vibrations
at hub - g's

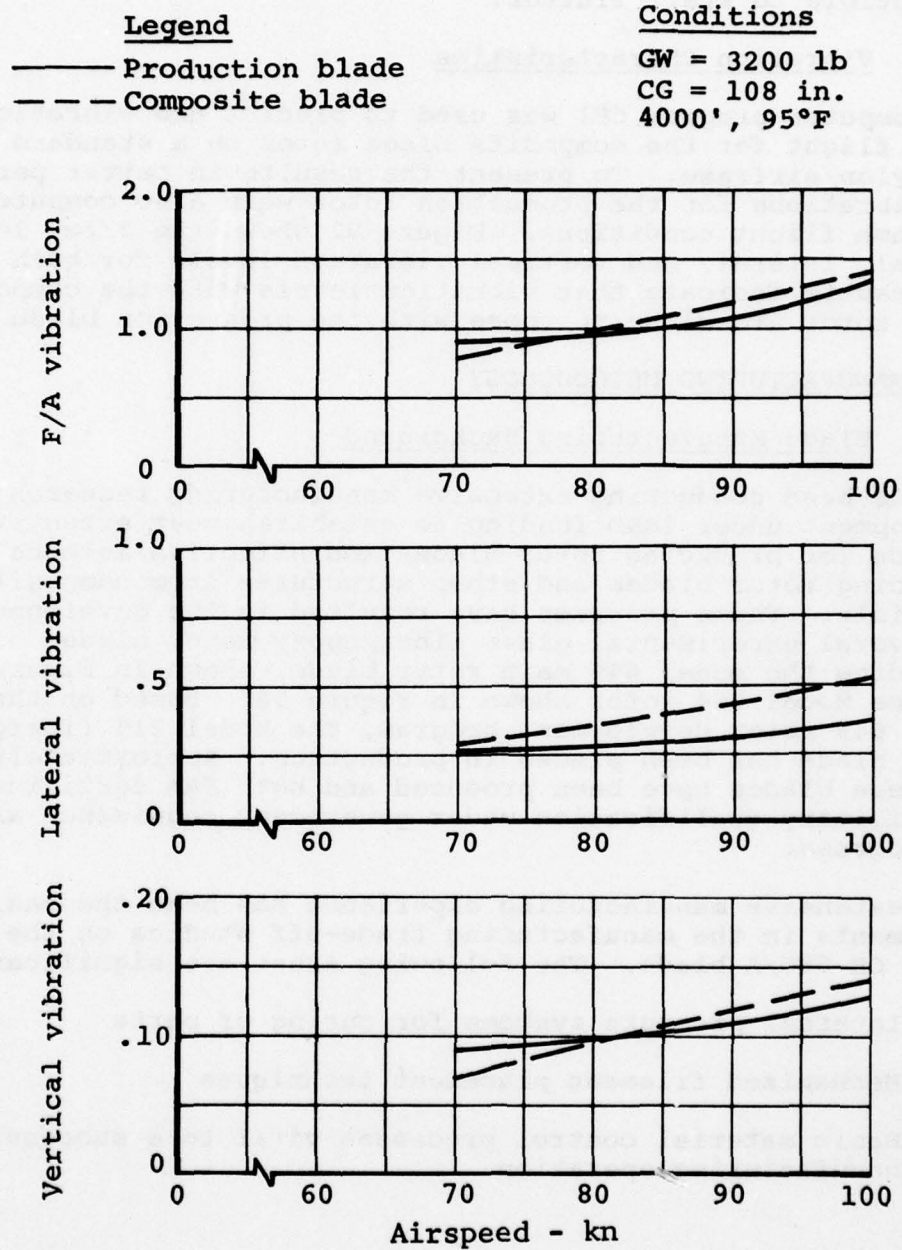


Figure 92. Computed hub vibrations of OH-58C with production and composite blade rotors.



Figure 93. Model 649 fiberglass main rotor blade.

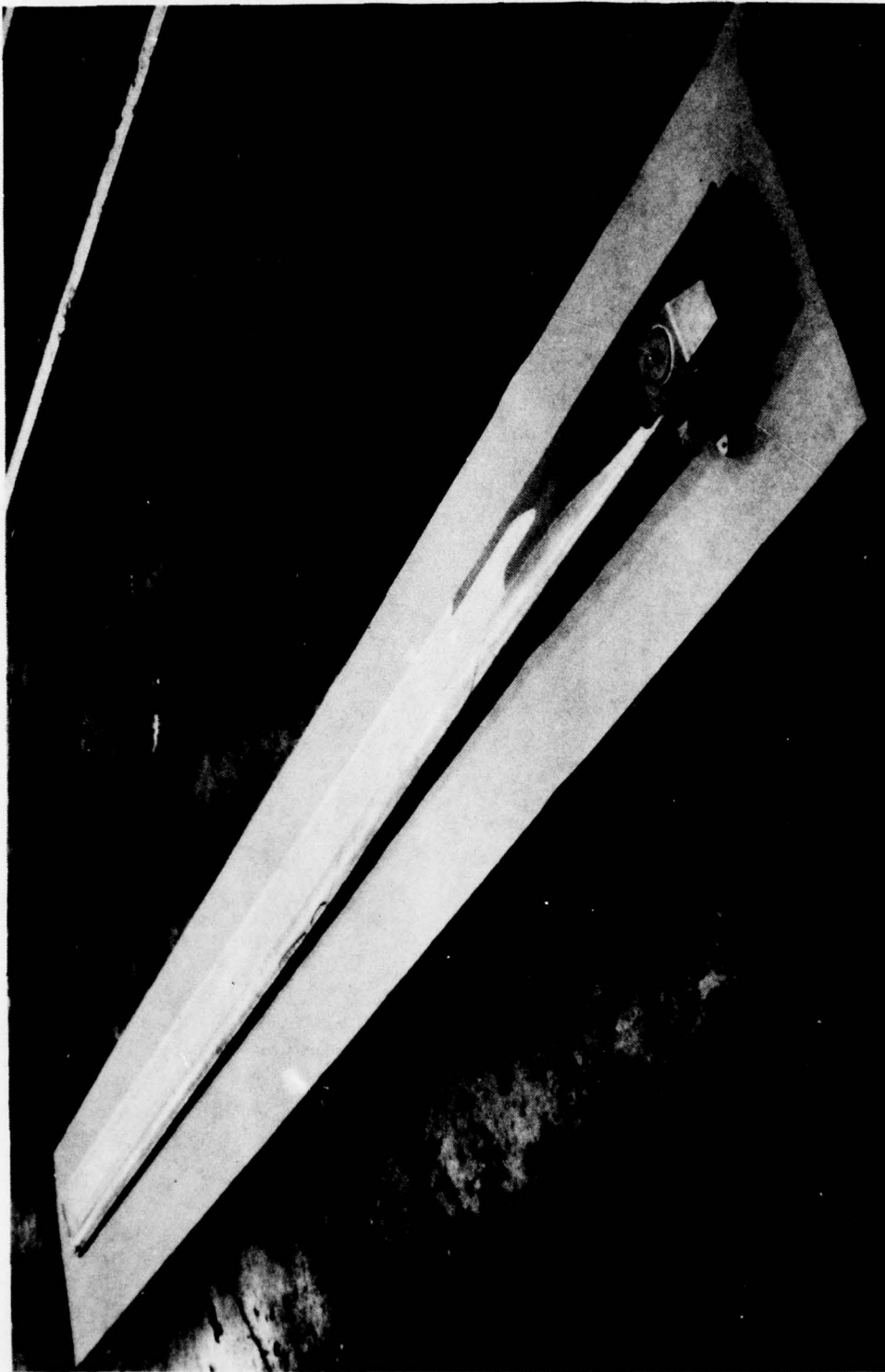


Figure 94. Model 206LM composite main rotor blade.

4.5.2 Blade Manufacturing

There are basic fabricating trade-offs that must be considered in preparing a composite main rotor blade manufacturing plan to preserve product reliability, ensure uniformity, and offer producibility at minimum cost.

- Mechanization in the manufacturing process offers the most significant benefit to cost and consistency of the end article. Hand lay-up in selected applications, however, may be more compatible in the manufacturing procedure. An example is the case of the "slip plane" created by a broadgoods hand layup of the inner spar torque tube. The tube may be mechanically produced by filament winding; however, the hoop strength of such a wound part inhibits bonding/laminating pressure internally applied to mold the external shape. In isolated applications such as this, hand layup may be logical, but overall, the objective is to utilize mechanization of the manufacturing process wherever possible.
- Number of cure cycles affects tooling requirements and labor content. The ideal situation is to create a final blade assembly from uncured details in a single "one-shot" curing operation. The trade-off consideration here is to what extent quality assurance and product uniformity are compromised.

In this manufacturing plan, spars are created in detail to assure that all surfaces and sections are subjected to proper laminating pressures. In a "one-shot" situation, laminating pressure at the closure would be reactive against supported honeycomb columns or uncured tube elements in the afterbody - either of which would produce questionable results. Quality assurance functions are more effectively applied at the detail level.

- Cocuring of honeycomb skins offers labor reduction, quality benefits, and simplified fabrication.

The sculptured honeycomb afterbody wedge presents the problems of dimensional change during transport, a flexible target for inspection, and difficulty of location during assembly.

The trade-off advantage rests heavily with the concept of cocuring a skin to one side of a warped-to-shape honeycomb wedge. The next sequence is to sculpture only the opposite side. In that configuration it is stable for inspection purposes, is readily machinable, and can be easily tooled for accurate location at assembly. The second skin is cocured in the final blade assembly bond operation.

- Filament winding was chosen as the basic fabricating method for the blade structure, to take advantage of the design and manufacturing versatility that the process offers. Unidirectional reinforcement fibers can be strategically placed to obtain optimum strength-to-weight, stiffness, and other structural properties in a routine manufacturing environment. Trade-off studies have shown the justification for development of specialized filament placement equipment that performs variations of the basic filament-winding operation.
- Material considerations for the blade were wet filament winding, prepreg roving, and prepreg tape. Factors in making the choice between these methods were material costs, labor content, and control of the end item. Wet filament winding was chosen as the best approach because it offers the lowest material cost and the good possibility of low labor content. Prepreg rovings are second in cost and second in labor content. Prepreg tapes are last in all categories and are therefore ruled out.

The manufacturing sequences and process choices that follow are based on manufacturing experience gained from several successful fiberglass blade programs.

4.5.3 Tooling

The basic tools to be used to fabricate the selected composite blade components are as follows:

Tool Description

Winding/compacting tools
Spar cap assembly mold
Spar assembly mold
Core chuck tool
Skin/core bonding mold
Compression molds
Cold storage mold
Tip-shoe form die
Boring and milling fixtures
Balance fixture
Main blade bonding mold

Numerical surface definition is used in all phases of tool fabrication to maintain coordination of critical matching surfaces and to ensure accurate airfoil shapes.

4.5.4 Fabrication

The manufacturing procedure established for the composite blade involves fabrication of the following major assemblies:

- Spar cap assemblies
- Spar
- Lower skin/core
- Blade body
- Final assembly

The manner in which each is fabricated and the method of final assembly are discussed in the following paragraphs. Processes such as drilling, trimming, bagging procedure, autoclaving, preparation for bonding, and inspection are considered standard practice and are not described in detail.

4.5.4.1 Spar Caps

The caps are made by orbital-winding machine (Figure 95). This machine places impregnated S2-glass roving between the facing plates of a winding/compacting tool that controls the general size and shape of the cross section. After the appropriate amount of S2-glass has been wound onto the tool, a compacting (or debulking) operation removes the air and compacts the material into an approximation of its cured configuration as shown in Figure 96. The wedge-shaped area at the root is the fid. an upper and lower cap are required for each blade. Root-end reinforcement plies produced from unidirectional prepreg tape are added during the winding sequence. These reinforcement plies are cocured with the spar cap.

4.5.4.2 Spar Cap Assembly

This assembly is fabricated by having a hand lay-up of the inner wrap over a mandrel enclosed by the upper and lower caps and nose blocks. The steel mandrel, which is covered by an inflatable silicone rubber bag, controls the interior shape of the spar and stiffens the assembly during the fabrication (see Figure 97).

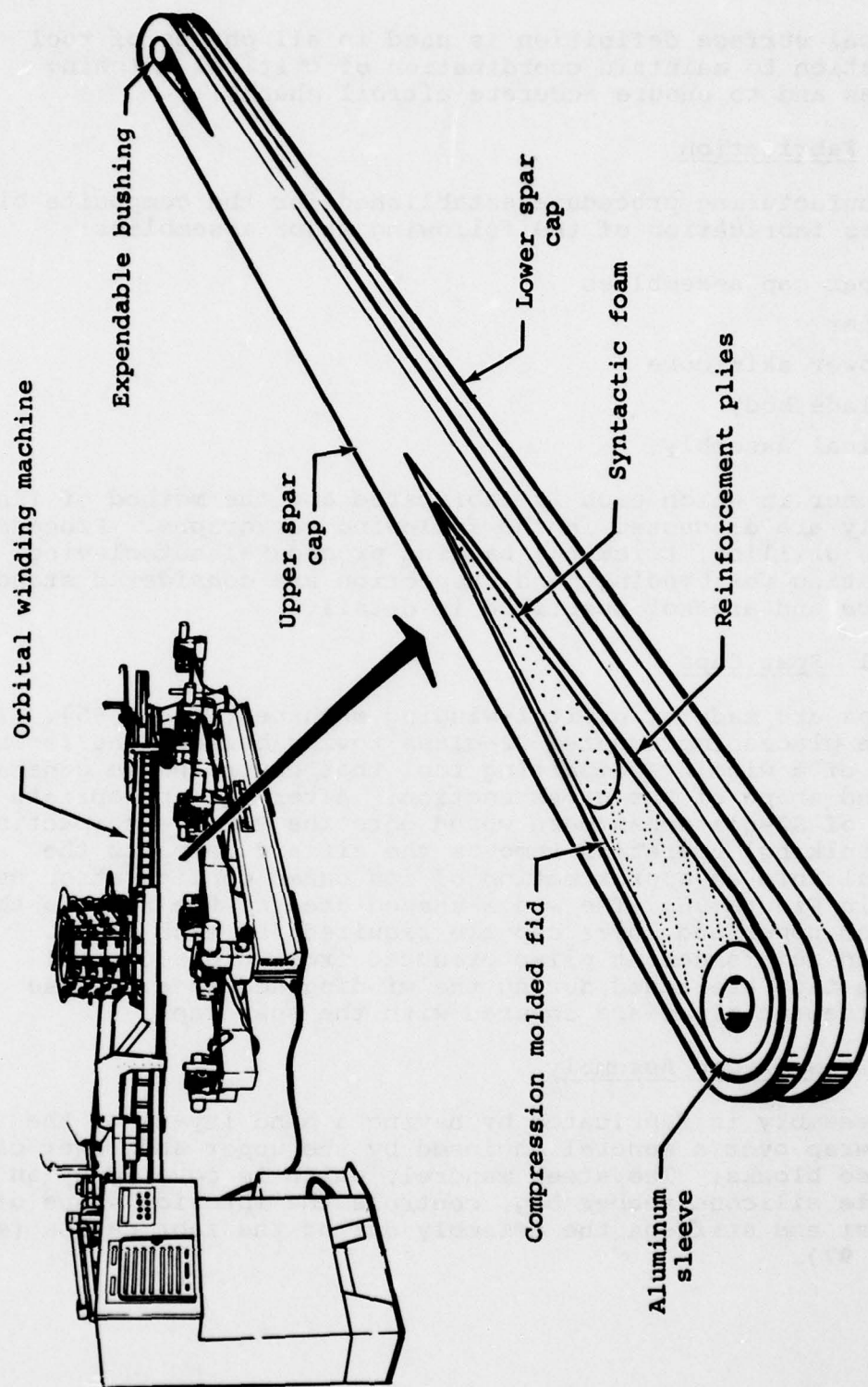


Figure 95. High capacity orbital filament-winding machine.

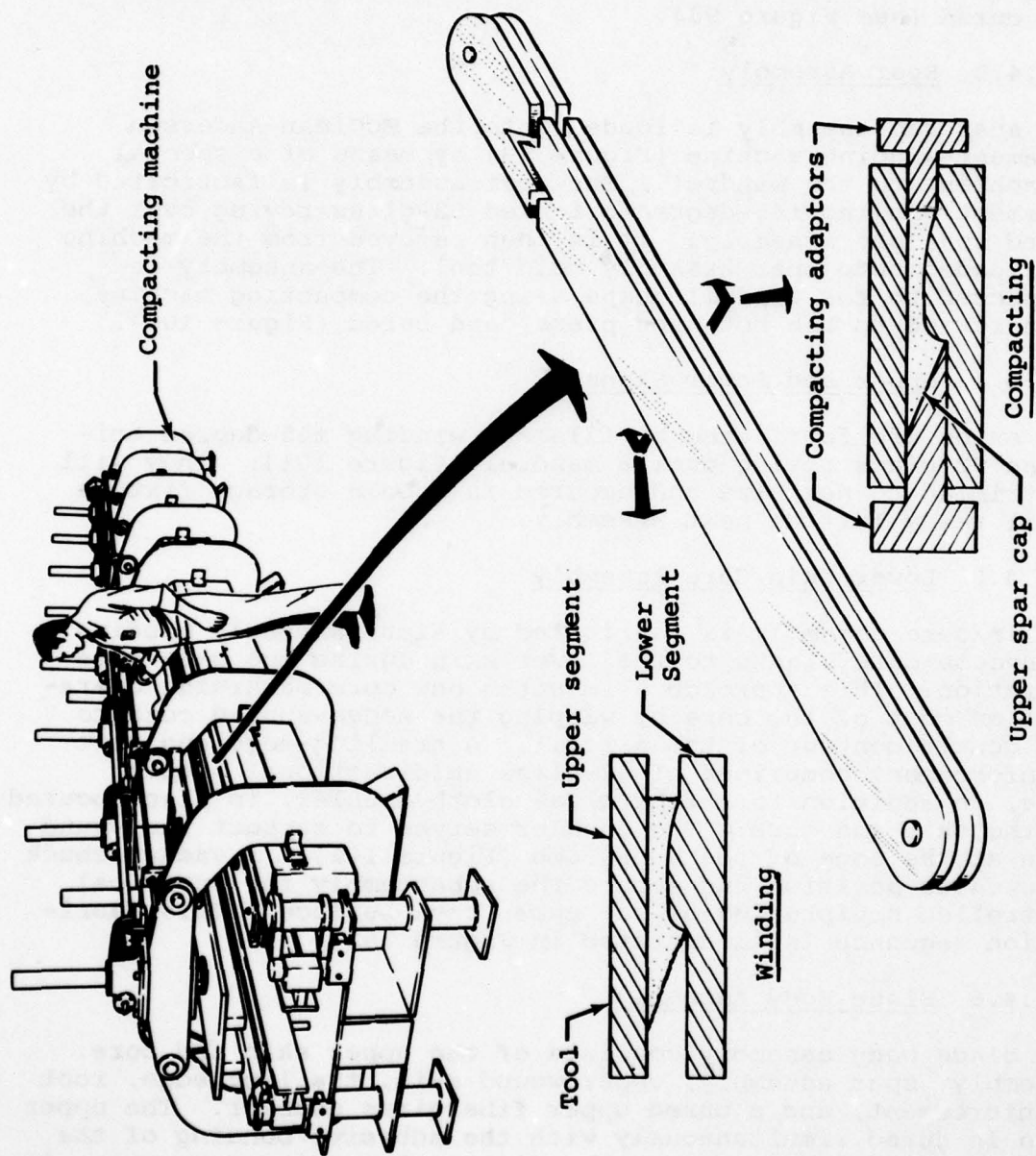


Figure 96. Compacting procedure for filament-wound blade spar caps.

The spar cap assembly is then loaded into a mold-type tool and the rubber bag is pressurized to force the components outwards against the mold surfaces, which results in precise reproduction of contours. The tool is loaded into the hotbond press and cured (see Figure 98).

4.5.4.3 Spar Assembly

The spar cap assembly is loaded onto the McClean-Anderson filament-winding machine (Figure 99) by means of a special attachment to the mandrel. The spar assembly is fabricated by filament winding ± 45 -degree-oriented S2-glass roving over the cured spar cap assembly. It is then removed from the machine and loaded onto spar assembly mold tool. The assembly is compacted to the airfoil shape using the compacting machine, transferred to the hot-bond press, and cured (Figure 100).

4.5.4.4 Upper and Lower Skins

The skins are fabricated by filament winding ± 45 -degree oriented S2-glass roving over a mandrel (Figure 101). They will be trimmed to net size and secured in a cold storage fixture until ready for the next assembly.

4.5.4.5 Lower Skin/Core Assembly

A skin/core assembly is fabricated by simultaneously bonding honeycomb core blanks to the lower skin during the skin cure operation. This approach eliminates one core machining operation on most of the core by warping the wedge-shaped core to the gentle contour of the airfoil. A trailing-edge and root reinforcement comprised of S2-glass unidirectional prepreg tape, in addition to a fiberglass cloth doubler, is also cocured to the skin and core. The doubler serves to support the wound skin at the edge of the honeycomb (Figure 102). A vacuum chuck is used to position and secure the subassembly for numerical controlled sculpturing of the upper core surface. This fabrication sequence is illustrated in Figure 103.

4.5.4.6 Blade Body Assembly

The blade body assembly consists of the upper skin and core assembly, spar assembly, upper wound skin, trailing edge, root reinforcement, and a cured upper fiberglass doubler. The upper skin is cured simultaneously with the adhesive bonding of the subassembly components. The bonding tool for this operation is a full-blade cavity mold designed for use in a hot-bond press. Detail arrangements of the blade body are illustrated in Figure 104.

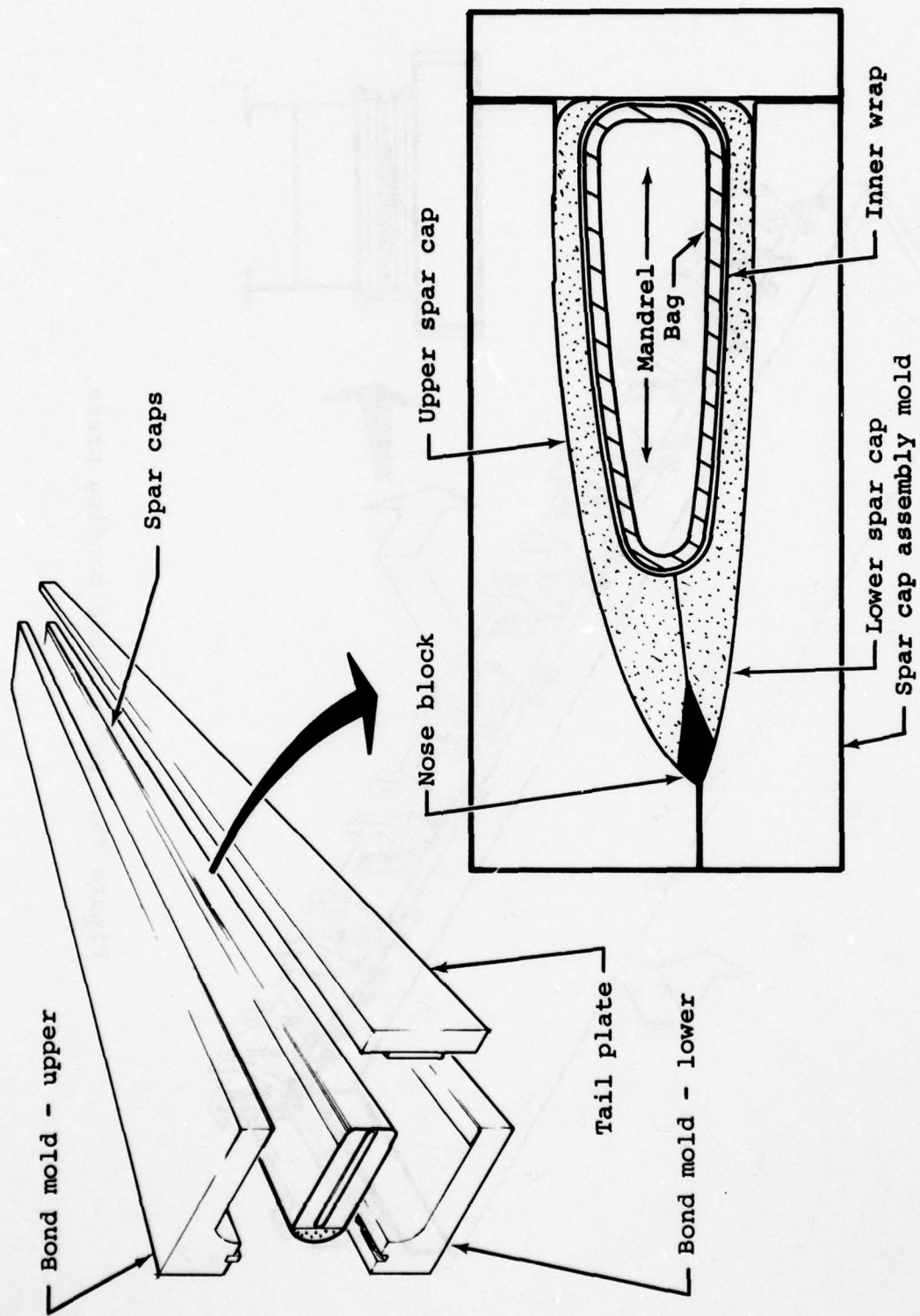


Figure 97. Assembly tool and procedure for spar cap subassembly.

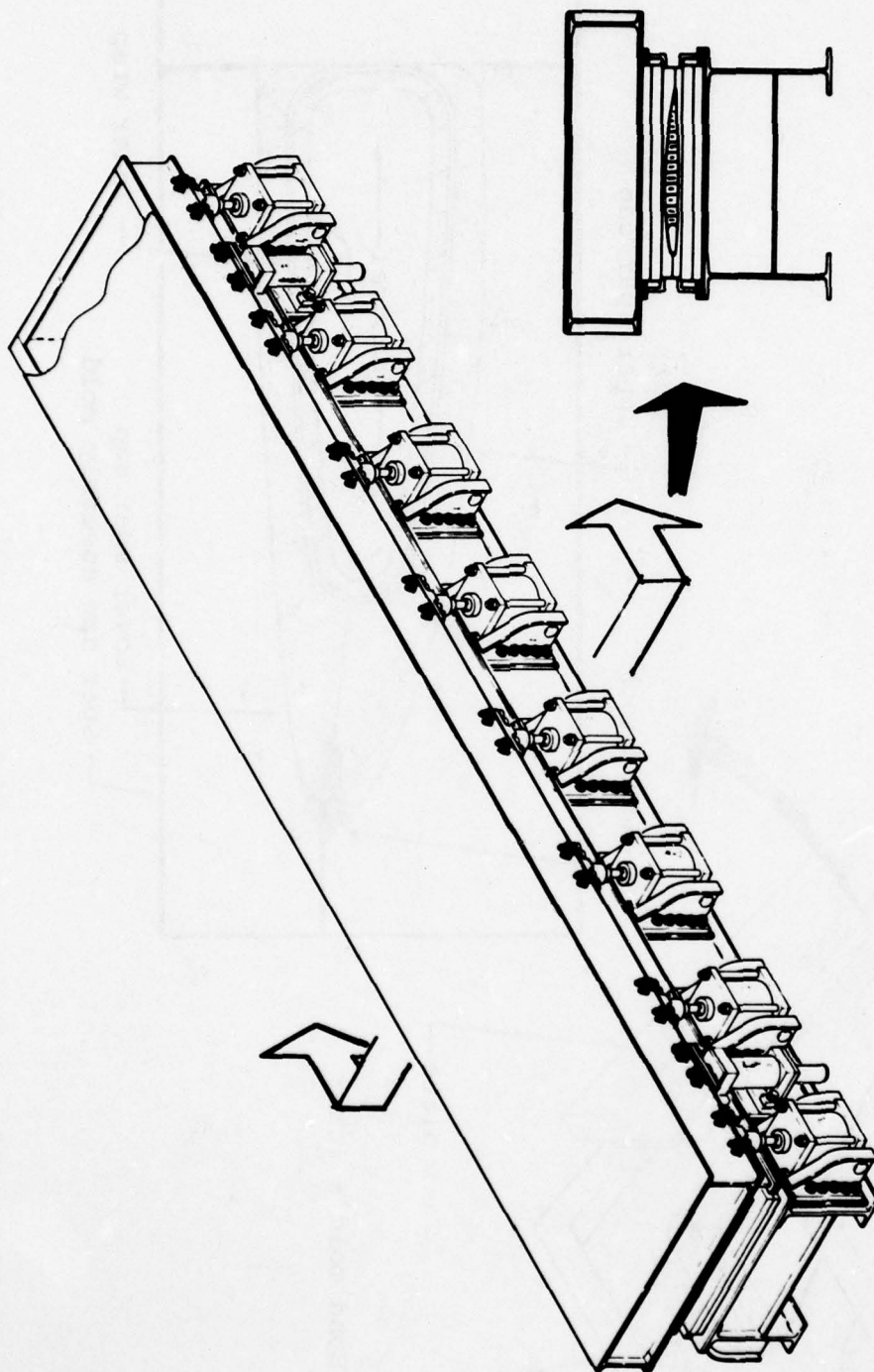


Figure 98. Rotor blade bonding press.

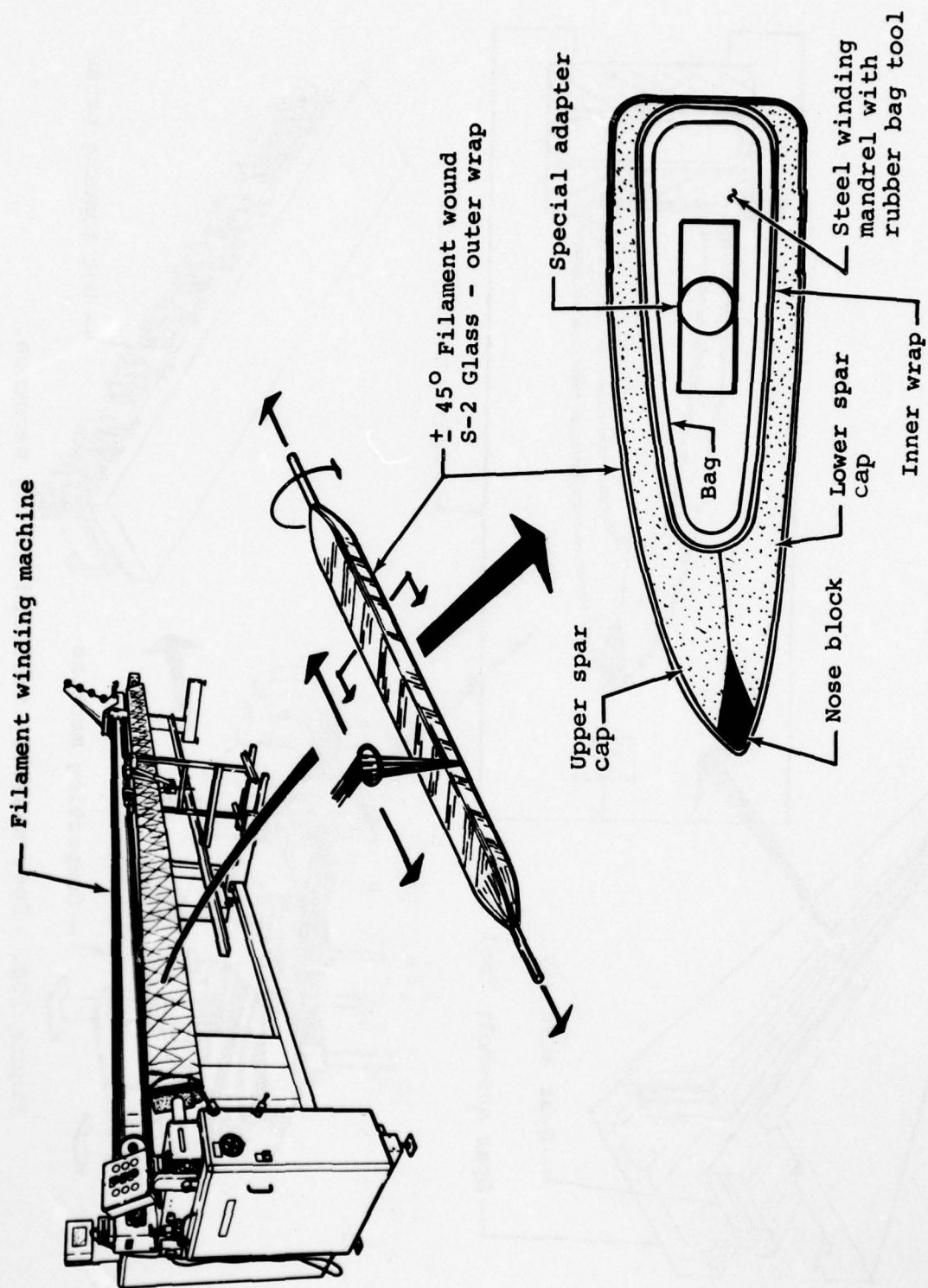


Figure 99. Filament-winding machine and blade spar outer torque wrap application.

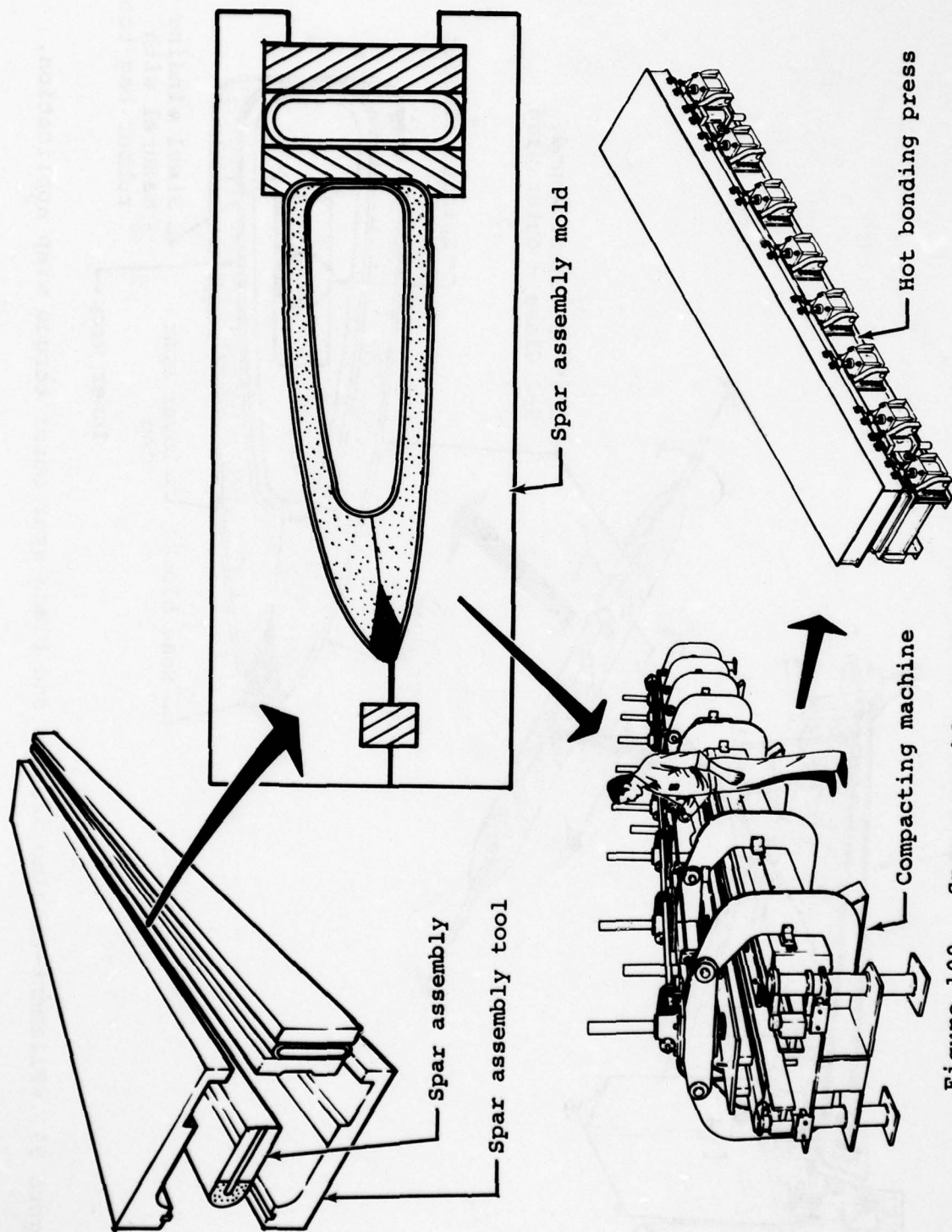


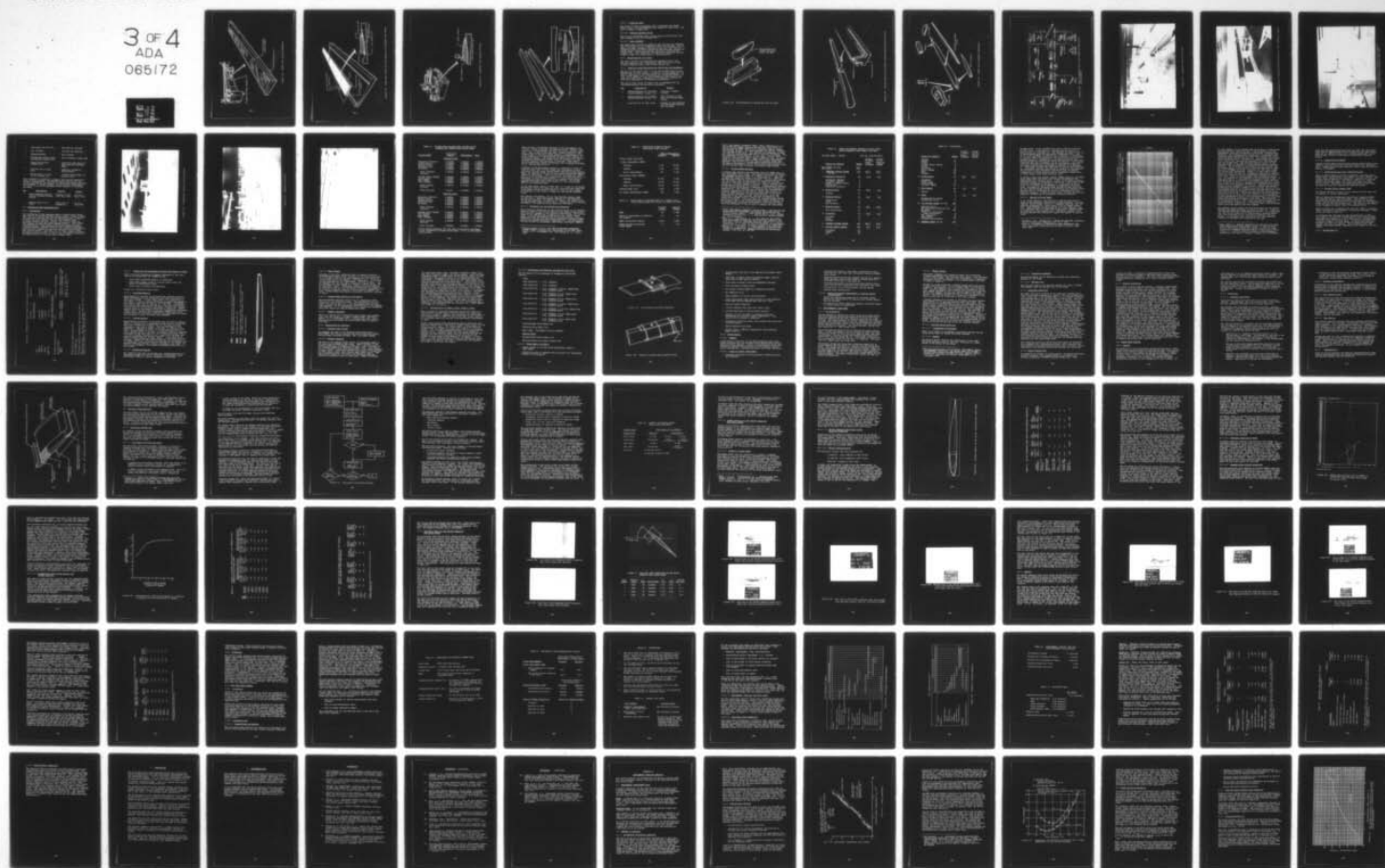
Figure 100. Spar assembly tool and curing sequence.

AD-A065 172

BELL HELICOPTER TEXTRON FORT WORTH TEX
OH-58 COMPOSITE MAIN ROTOR BLADE. PRELIMINARY DESIGN INVESTIGAT--ETC(U)
DEC 78 V H BROGDON, J BRASWELL, F FREEMAN DAAJ02-77-C-0073
699-099-086 USARTL-TR-78-38A NL

UNCLASSIFIED

3 OF 4
ADA
065172



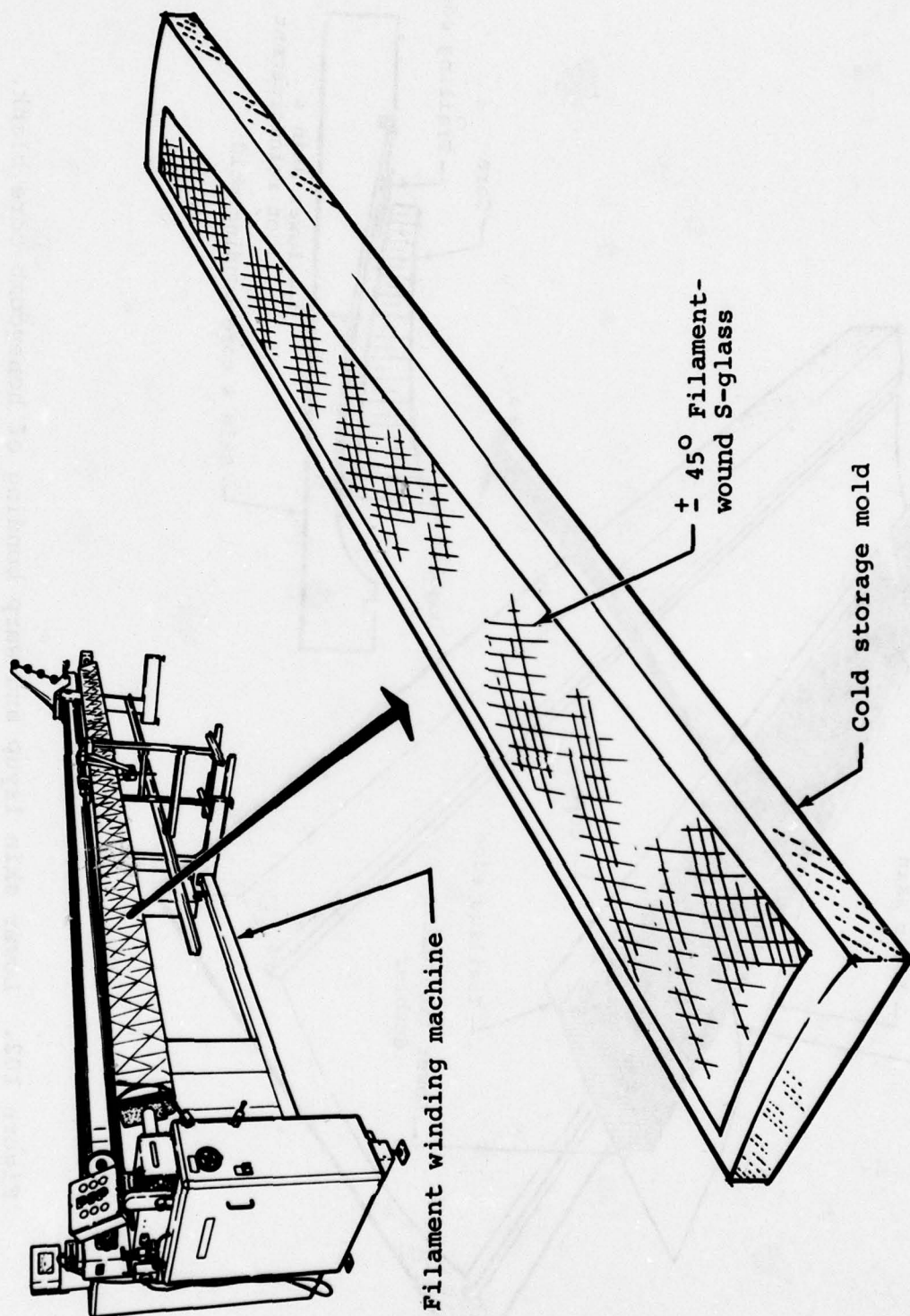


Figure 101. Blade skin winding procedure.

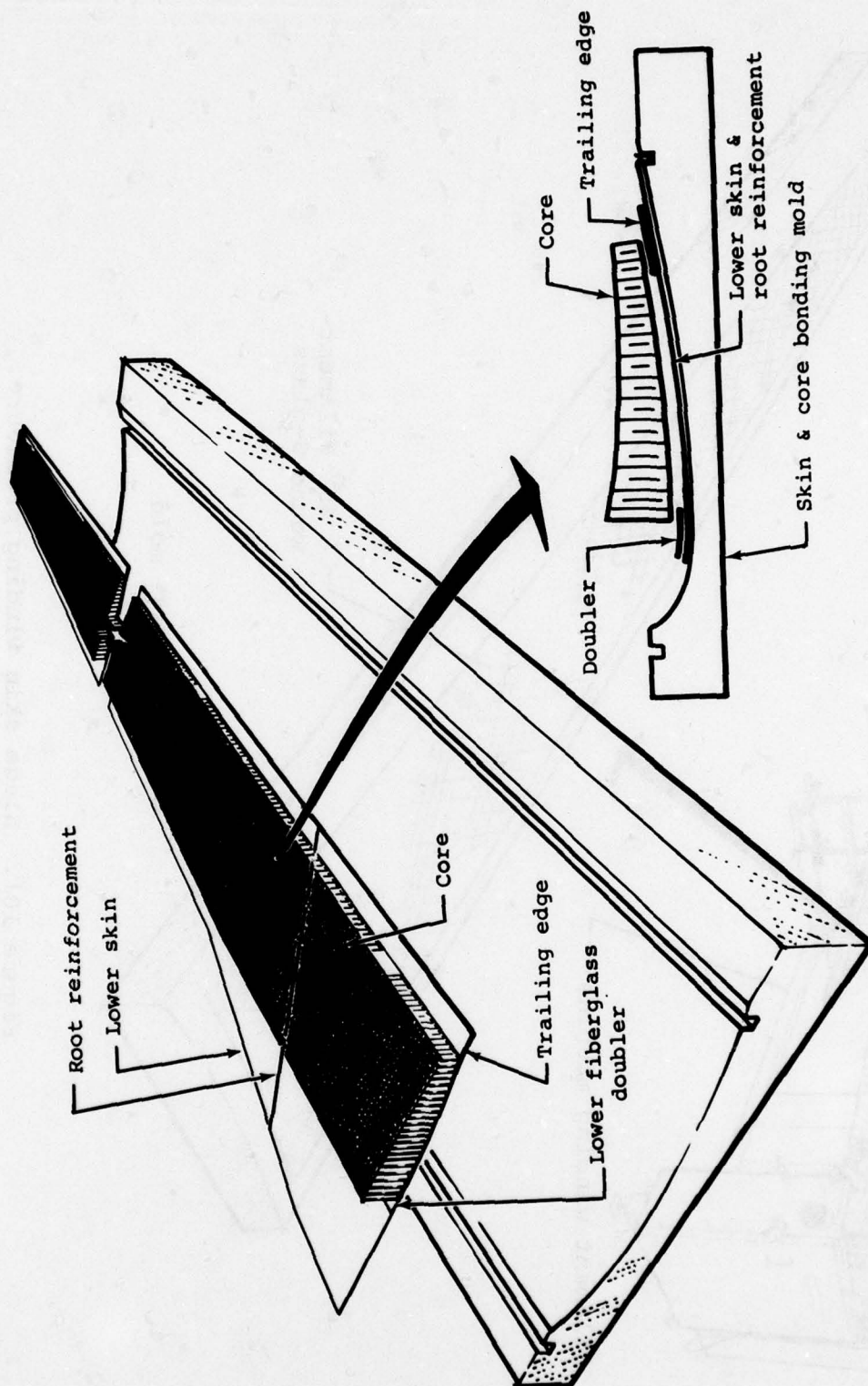


Figure 102. Lower skin layup and warp bonding of honeycomb core blank.

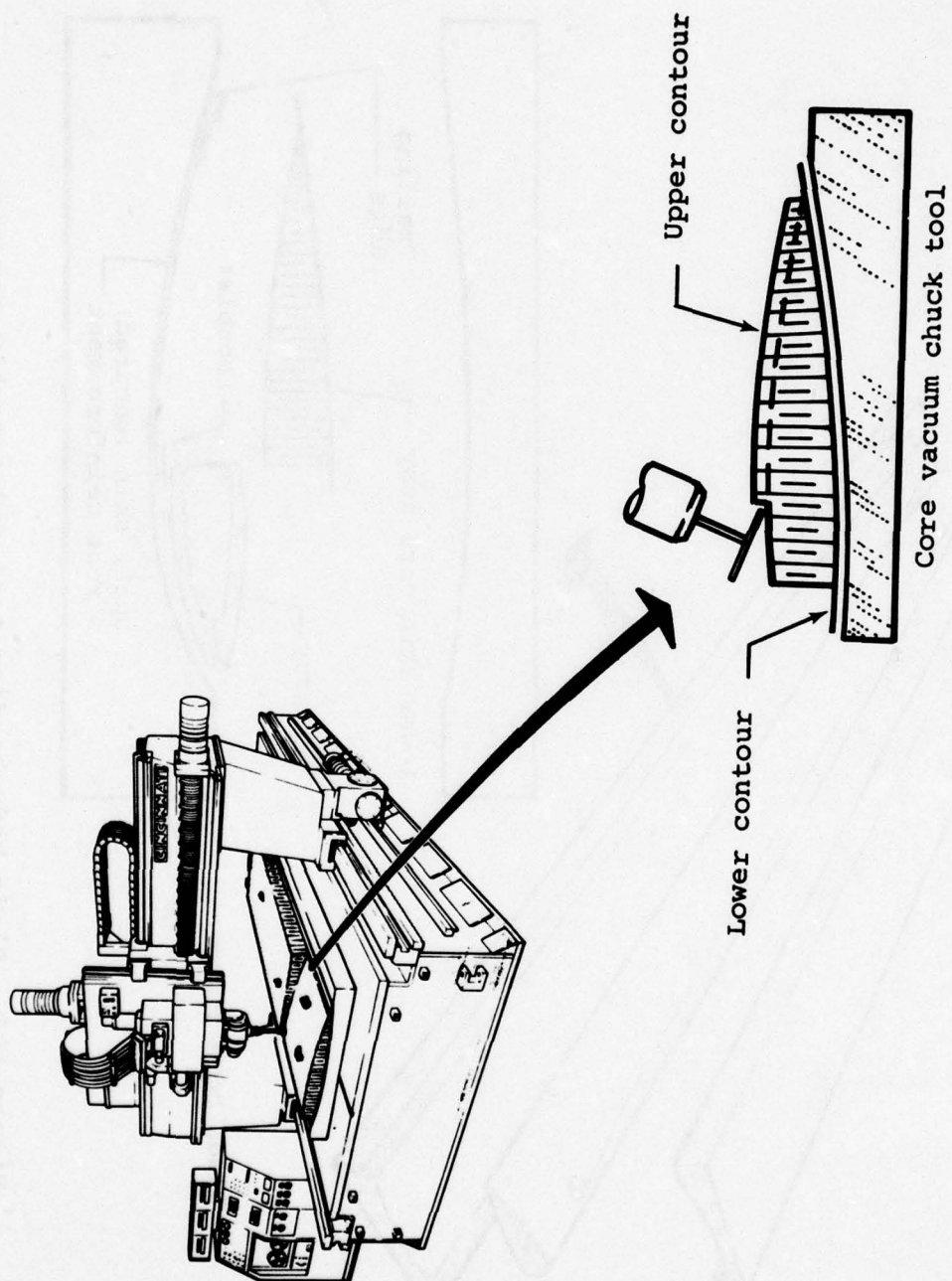


Figure 103. Honeycomb core contour carving.

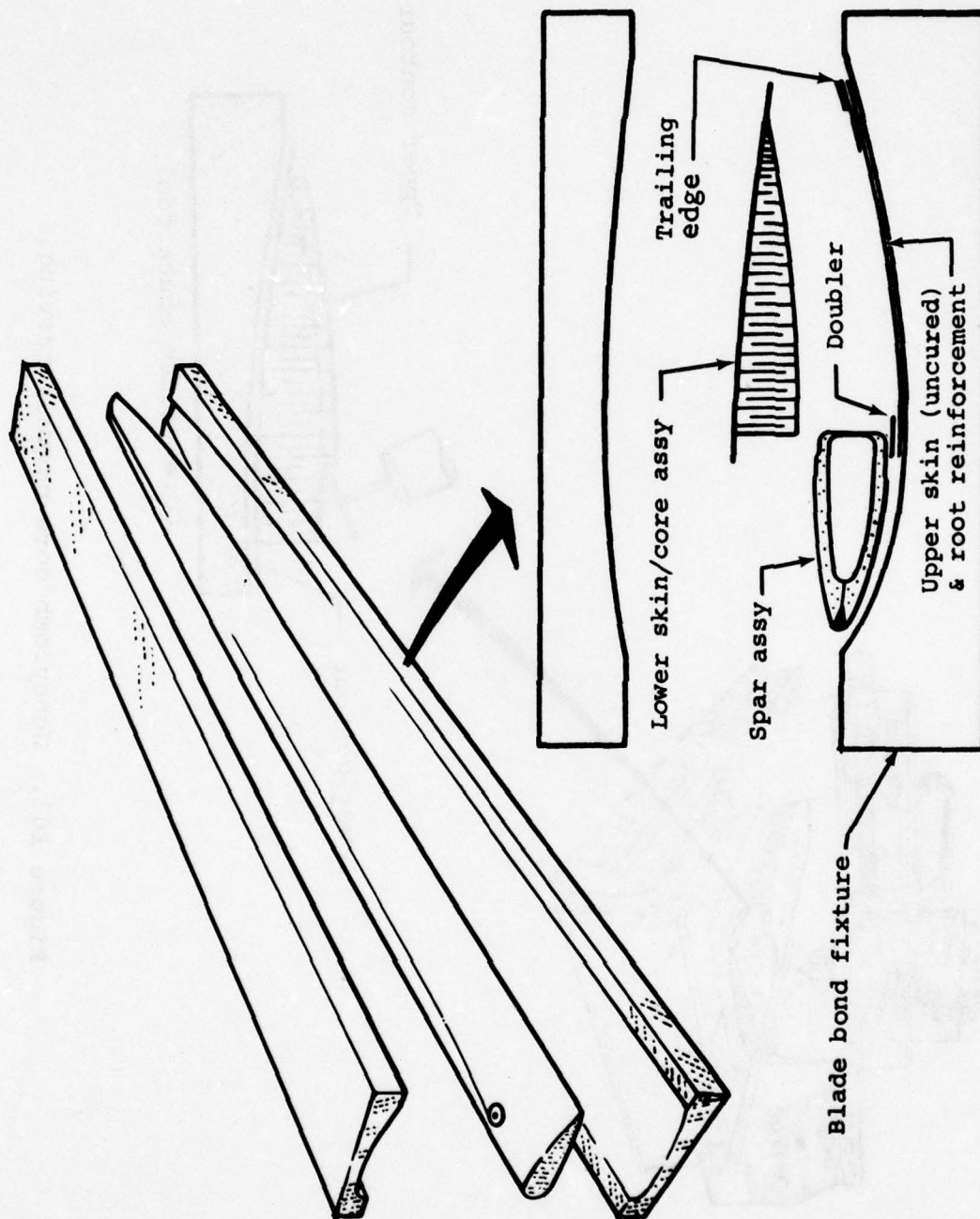


Figure 104. Blade body bonding tool and assembly sequence.

4.5.4.7 Blade Tip Shoe

The blade tip shoe is produced from a preformed and welded blank, which is electrohydraulically formed to final size. The tool is shown in Figure 105.

4.5.4.8 Urethane Abrasive Strip

The strip is preformed under vacuum using a hot-form tool and then trimmed to net size (Figure 106).

4.5.4.9 Final Assembly

The blade body is sawed to length at the root and tip stations, and the tooling tab is trimmed from the trailing edge. The tip shoe, grip pads, closures, abrasion strip, and trim tabs are bonded in place followed by machining the grip pads, boring the attach holes, filling and fairing, painting, and balancing (Figure 107). This completes the fabrication sequence and the blade is ready for installation on the helicopter.

4.5.5 Manufacturing Flow Chart

The chart outlines the manufacturing sequence flow of the various component parts required for the fabrication of the selected composite main rotor blade (Figure 108).

4.5.6 Composite Blade Manufacturing Facilities and Equipment

BHT has 135,000 square feet of floor space being used for the manufacture of rotor blades. Currently, 12,915 square feet of this is dedicated to the manufacture of fiberglass blades. Of this, 8,852 square feet is environmentally controlled to provide the cleanliness, temperature, and humidity essential to fault-free manufacture of fiberglass structures.

The lay-up area, shown in Figure 109, is equipped with the following machines and processing equipment:

<u>Qty</u>	<u>Description</u>	<u>Purpose</u>
1	McLean-Anderson W-2 filament-winding machine (Figure 110)	Cross-ply filament winding
1	McLean-Anderson W-2 filament-winding machine (Figure 111)	Polar winding or spar caps and trailing edge strips
1	Cold box (25 ft long, 40°F)	Storage of raw materials and full-length uncured spar windings

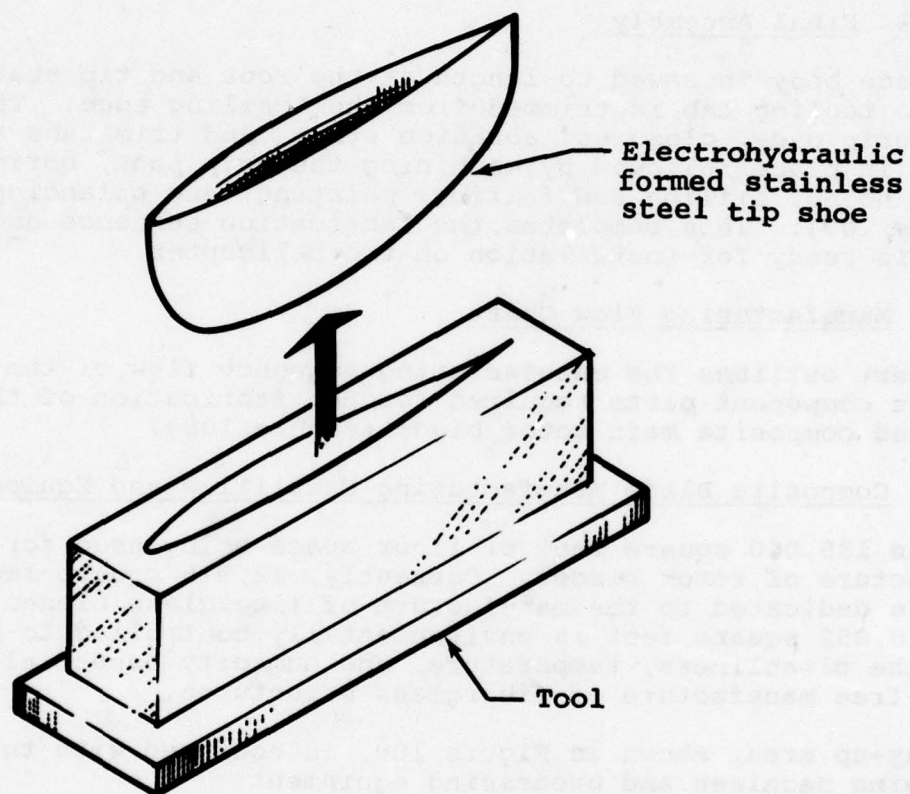


Figure 105. Electrohydraulic forming die for tip shoe.

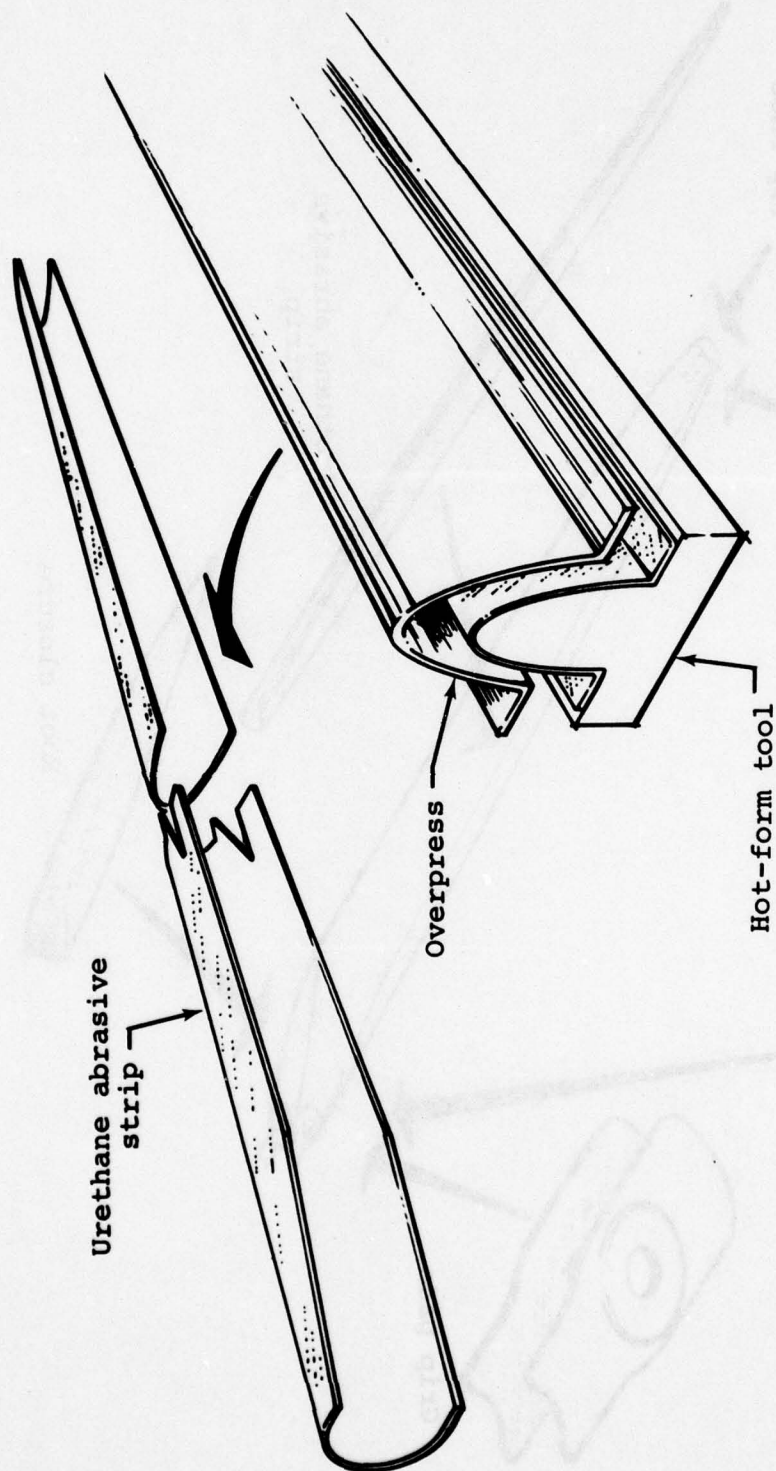


Figure 106. Vacuum forming of urethane leading-edge protective strip.

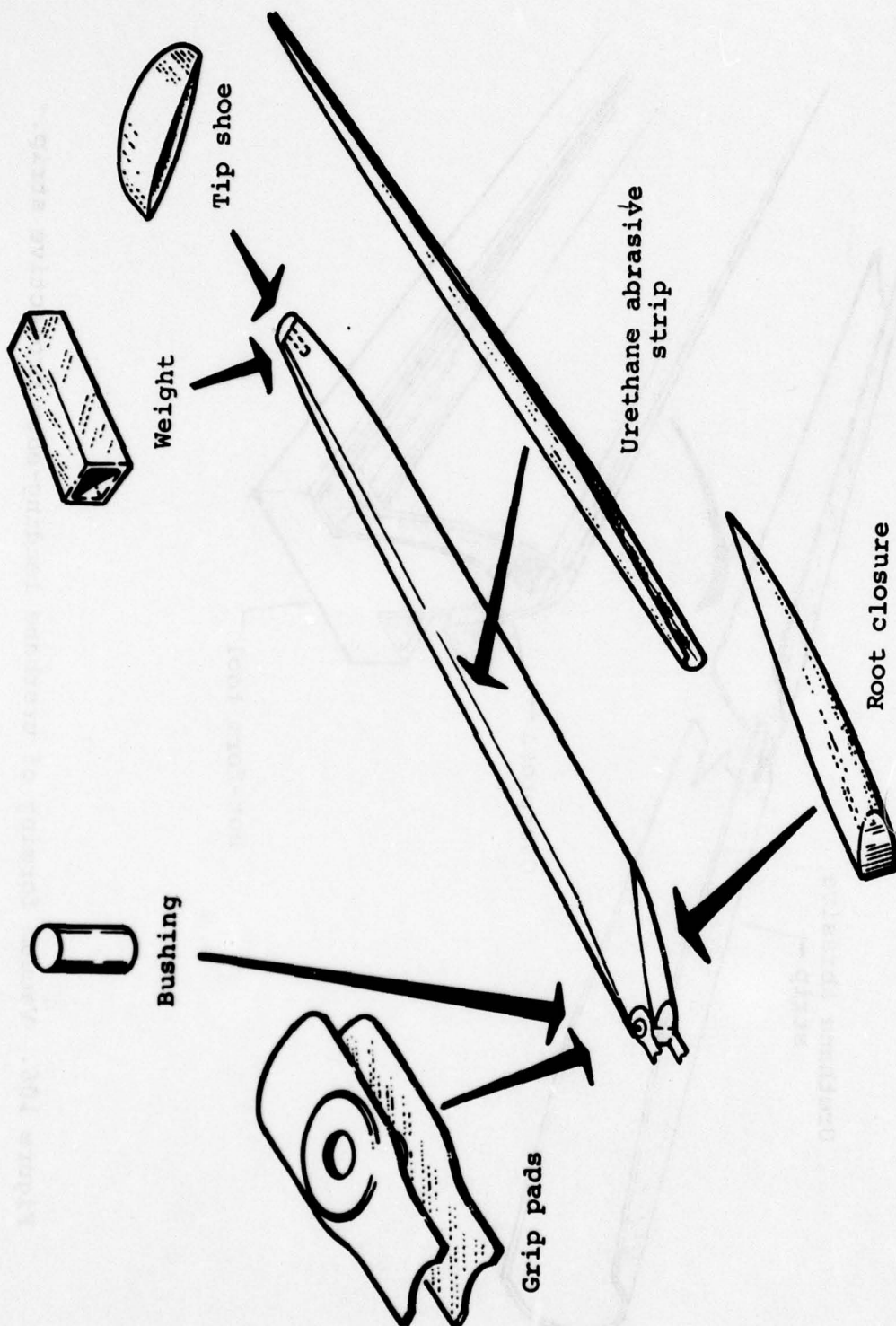


Figure 107. Blade final assembly operations.

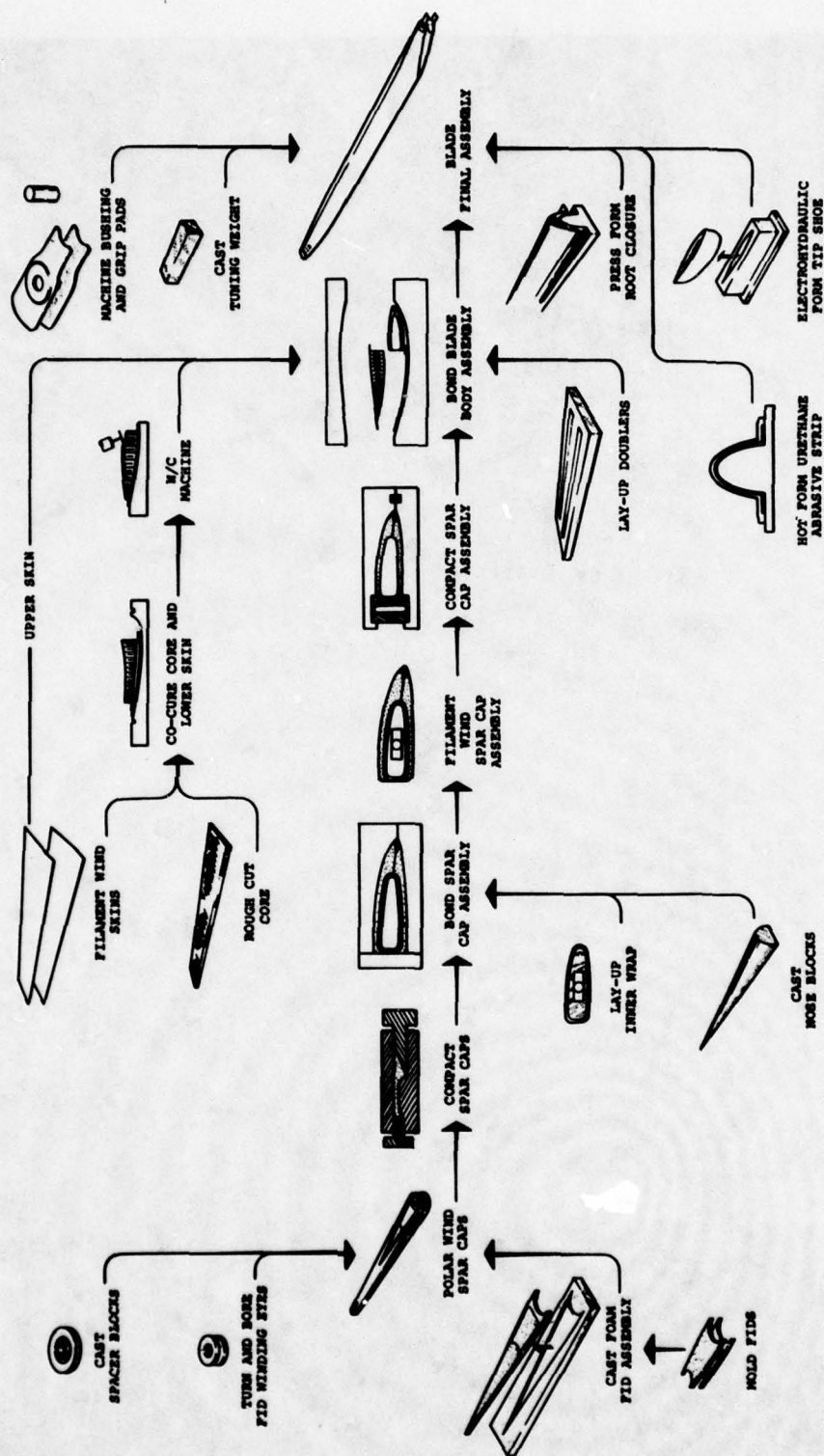


Figure 108. OH-58 composite main rotor blade manufacturing flow sequence.

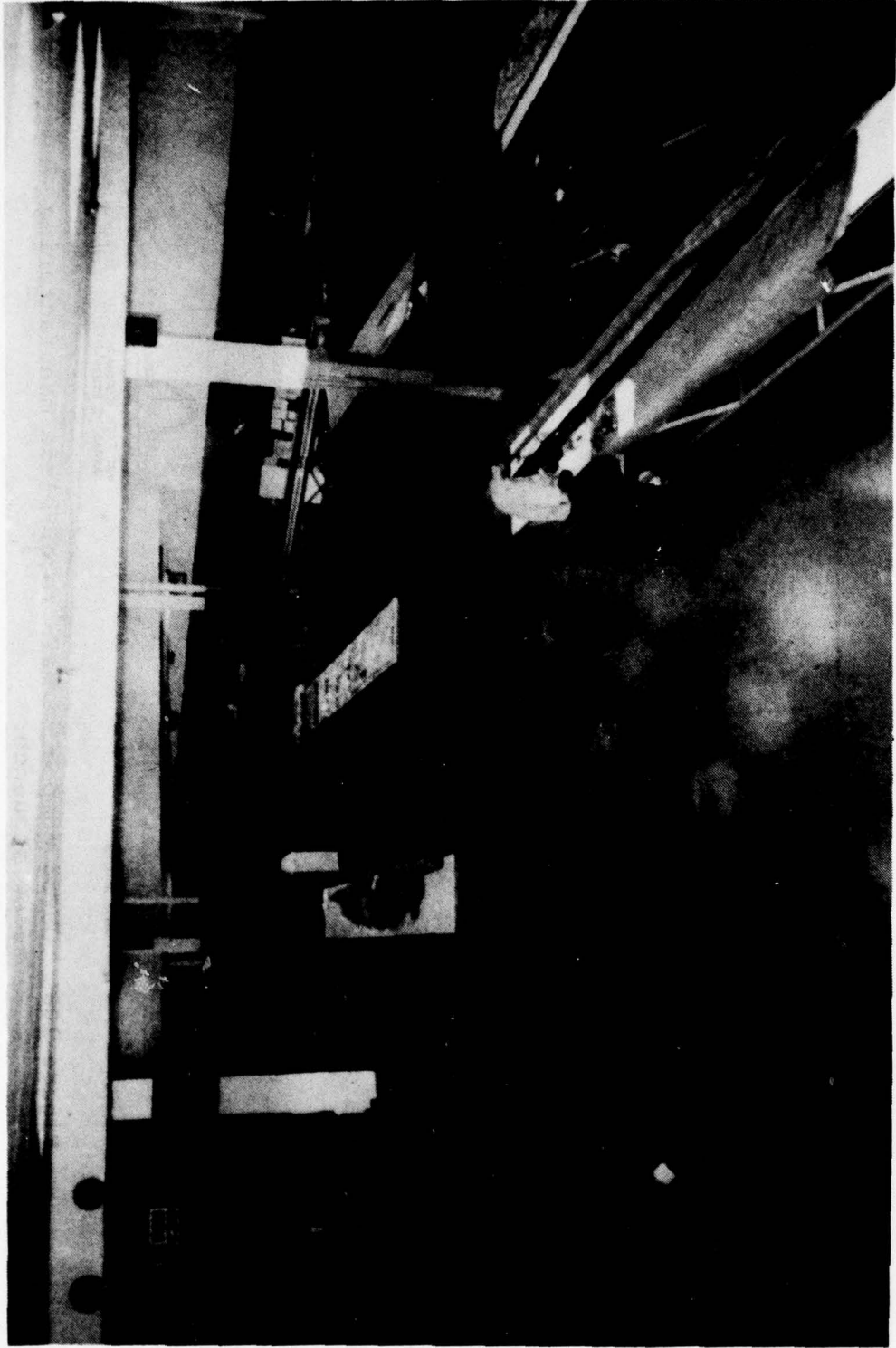


Figure 109. Composite blade lay-up area.

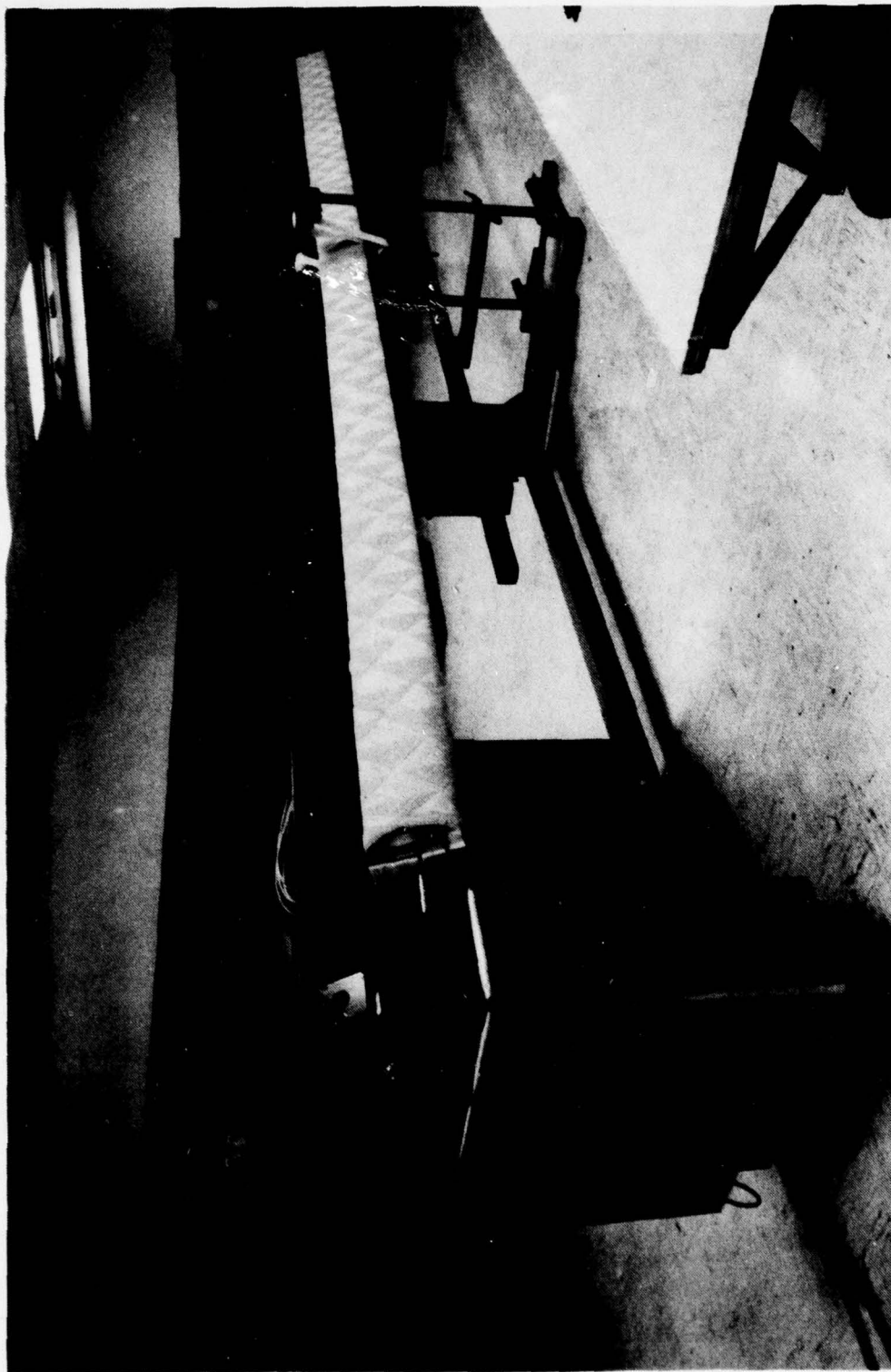


Figure 110. McLean-Anderson W-2 filament-winding machine for $\pm 45^\circ$ winding of spars.

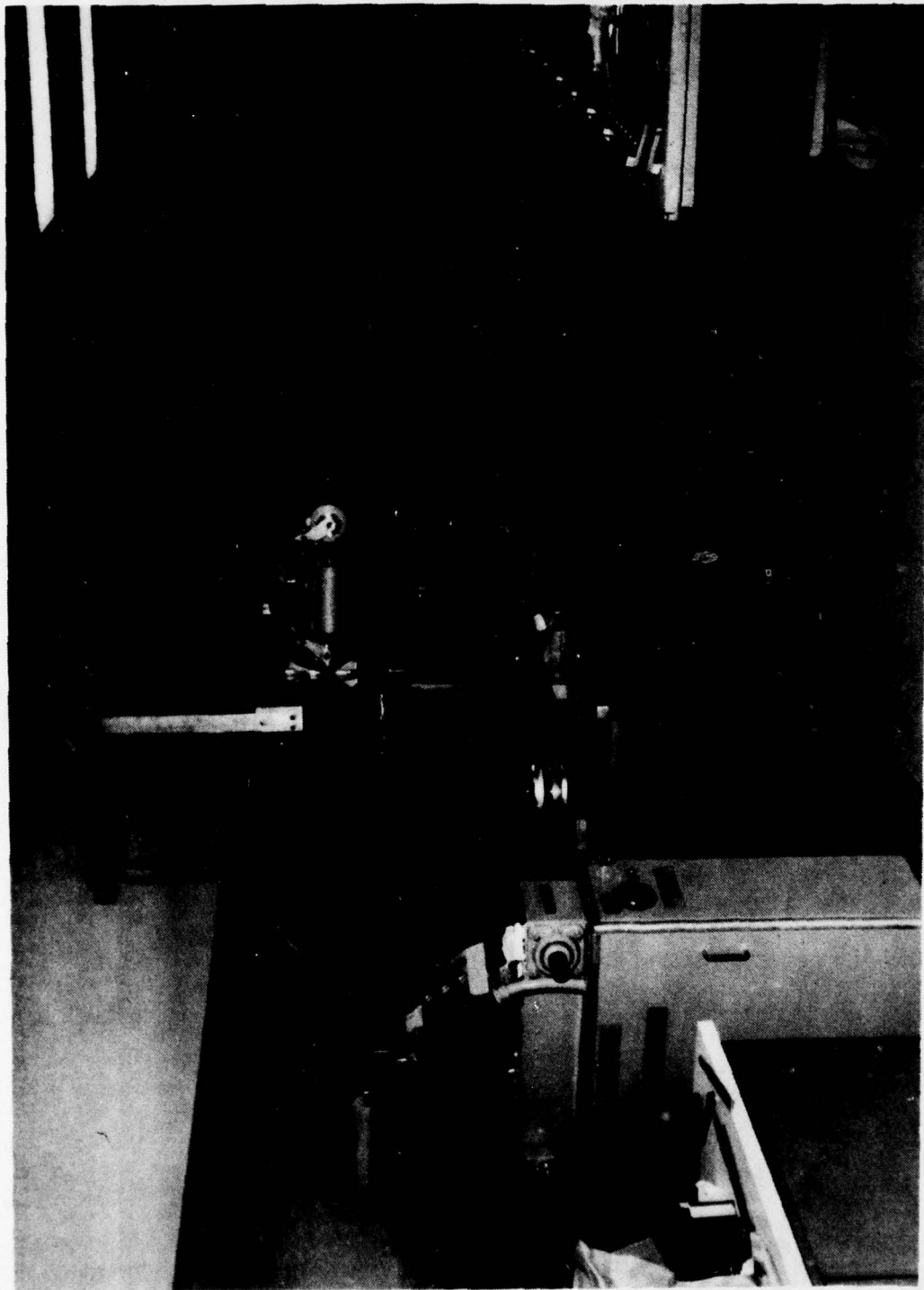


Figure 111. McLean-Anderson W-2 filament-winding machine adapted for orbital winding of spar caps.

2	Cold boxes (36 ft ³ 0°F)	Raw material storage
1	Saw, slicing	Cutting roll material
1	Bagging machine	Heat sealing
1	Goldsworthy orbital-winding machine (Figure 112)	Polar winding of spar caps
1	Compacting machine (Figure 113)	Compacting and sizing of spar caps and trailing edges
1	Cold box (30 ft long, 40°F)	Temporary storage of uncured parts
1	K&T N/C mill (5 ft by 32 ft) (Figure 114)	In-house manufacturer of bonding tools

This equipment is adequate to support the critical production phase of this program. The manufacturing capacity will be further extended by the addition of specialized modern machines and equipment to support higher rate production requirements. Following is a list of equipment either planned or currently on order:

<u>Qty</u>	<u>Description</u>	<u>Purpose</u>	<u>Status</u>
1	McLean-Anderson digital control filament-winding machine	Winding of $\pm 45^\circ$ cross ply wraps	On line April 1978
1	Bonding press (30 ft long)	Press cure of assemblies	On line July 1978

4.6 RELIABILITY AND MAINTAINABILITY

4.6.1 Reliability

The reliability of the improved blade is significantly better than that of the OH-58A standard (metal) blade. Table 21 shows that the total failure rate for the improved blade is almost one-half the total failure rate for the standard blade (0.000621 versus 0.001216). (Note: All failure rates are expressed as failures per blade operating hour.) This reduction applies to both the total inherent failures and total induced failures. The reduction for total inherent failures (0.000195 versus 0.000357) is due to the virtual elimination of deterioration, bonding failure, and corrosion failure modes from the new design. The reduction for total induced failures (0.000426 versus 0.000859) is due to the increased tolerance of the improved blade to foreign object damage (FOD).

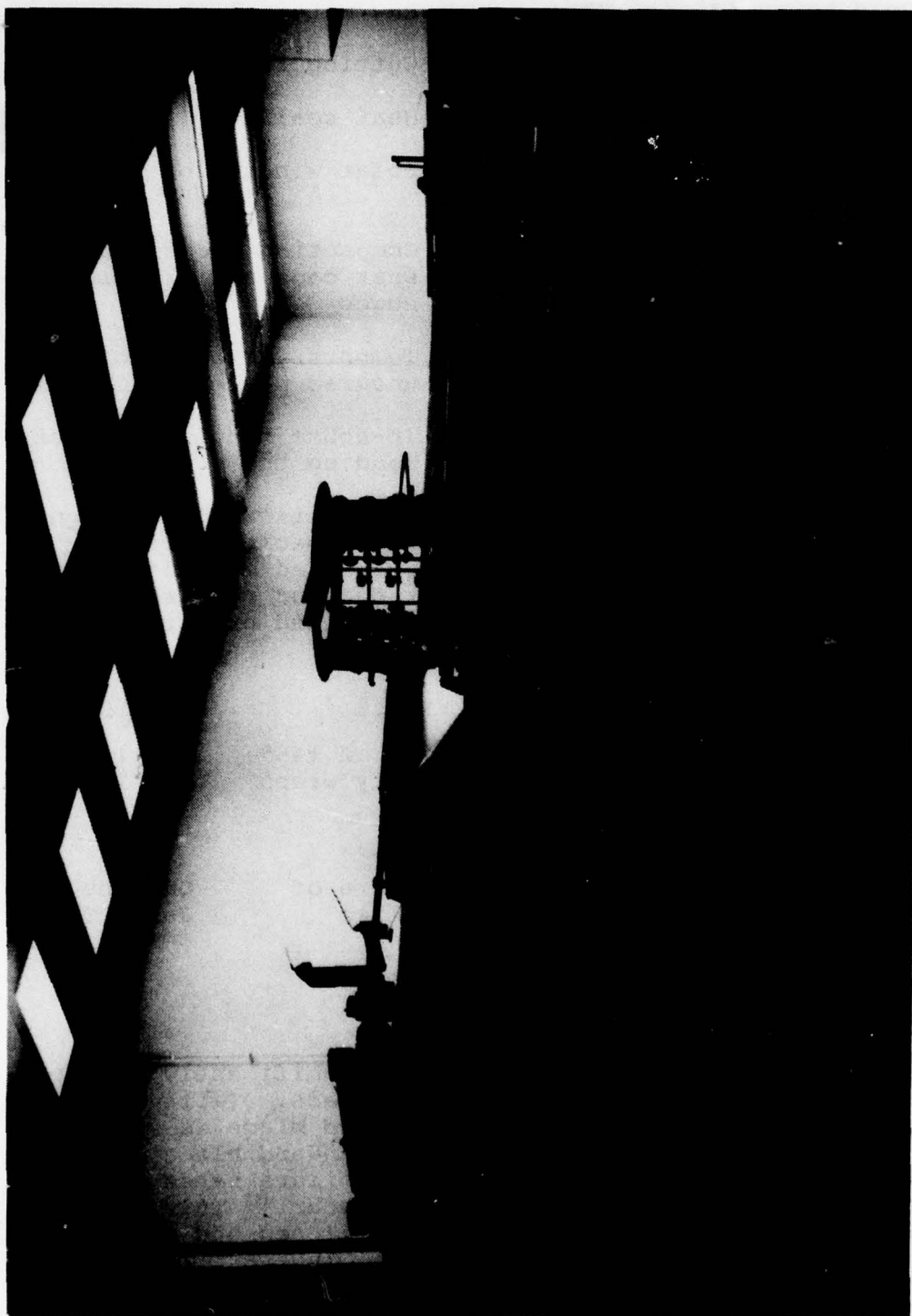


Figure 112. Goldsworthy orbital winding machine.

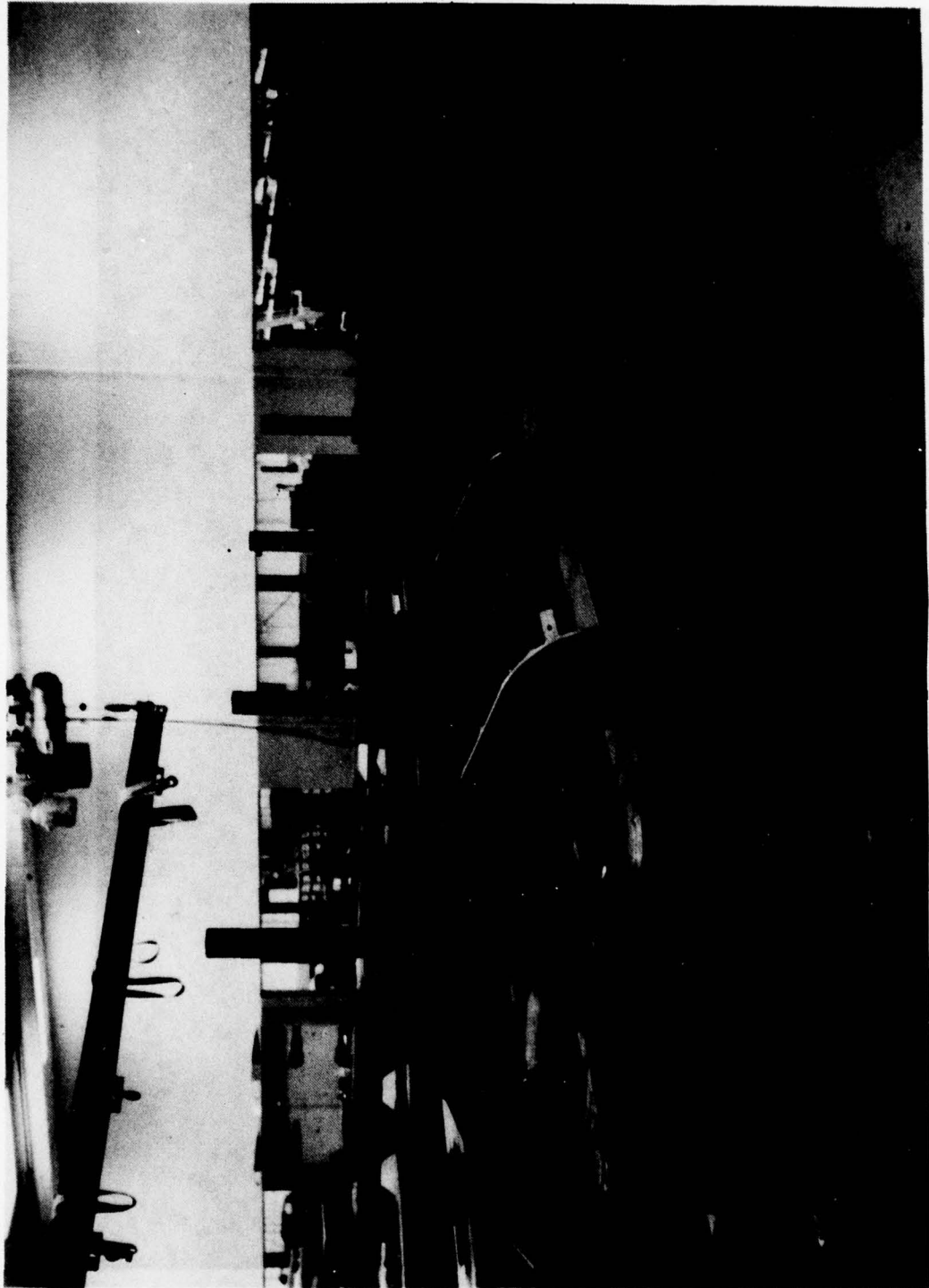


Figure 113. Compacting machine.

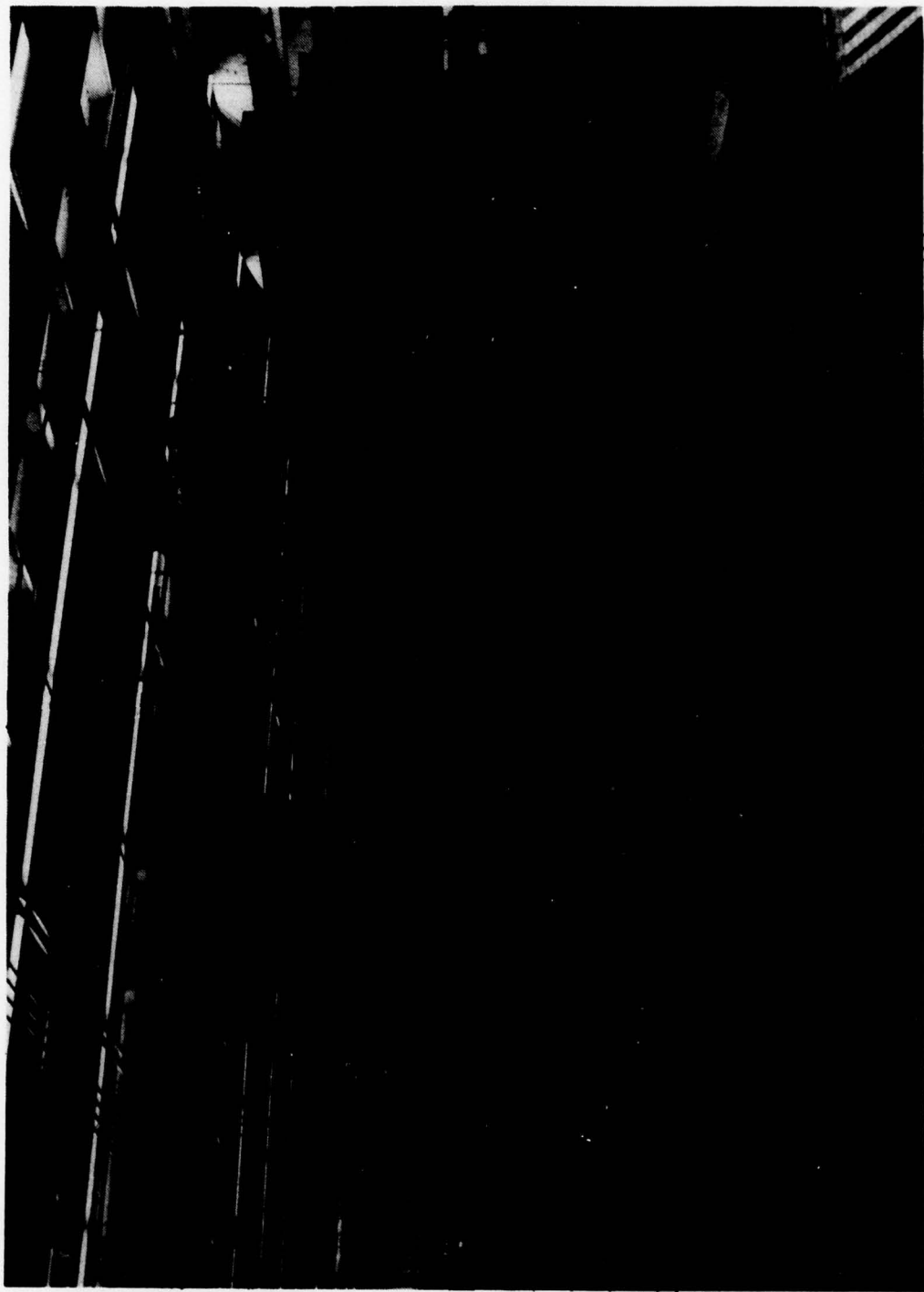


Figure 114. K&T 5 ft x 32 ft numerical control mill.

TABLE 21. FAILURE MODE FAILURE RATES FOR THE OH-58A
STANDARD AND IMPROVED MAIN ROTOR BLADE

<u>Failure Mode</u> ¹	<u>On-Aircraft Repair</u>	<u>Replacement</u>	<u>Both</u>
<u>Standard Blade</u>			
Excessive Vibration	0.000008	0.000022	0.000030
Deterioration	0.000004	0.000052	0.000056
Bonding Failure	0.000003	0.000042	0.000045
Excessive wear	0.000006	0.000169	0.000175
Corrosion	<u>0.000018</u>	<u>0.000033</u>	<u>0.000051</u>
Total Inherent Failures	0.000039	0.000318	0.000357
Foreign object damage	0.000047	0.000602	0.000649
Overstressed	0.000009	0.000111	0.000120
Heat damage	0.000023	0.000054	0.000077
Other induced	<u>0.000000</u>	<u>0.000013</u>	<u>0.000013</u>
Total Induced Failures	0.000079	0.000780	0.000859
Total Failures	0.00118	0.001098	0.001216
<u>Improved Blade</u>			
Excessive vibration	0.000008	0.000022	0.000030
Deterioration	0.000000	0.000000	0.000000
Bonding failure	0.000000	0.000000	0.000000
Excessive wear	0.000148	0.000017	0.000165
Corrosion	<u>0.000000</u>	<u>0.000000</u>	<u>0.000000</u>
Total Inherent Failures	0.000156	0.000039	0.000195
Foreign object damage	0.000016	0.000200	0.000216
Overstressed	0.000009	0.000111	0.000120
Heat damage	0.000023	0.000054	0.000077
Other induced	<u>0.000000</u>	<u>0.000013</u>	<u>0.000013</u>
Total Induced Failures	0.000048	0.000378	0.000426
Total Failures	0.000204	0.000417	0.000621

¹ Rotor system unbalance that has been corrected by adjustment is not included as a blade failure mode. It is a rotor system failure mode.

There is also a 90-percent decrease in the replacement rate (0.000017 versus 0.000169) for excessive wear. However, this results in a corresponding increase in the on-aircraft repair rate. This is due to the fact that, whereas wearout of the leading edge of the metal blade results in replacement of the blade, wearout of the polyurethane abrasion strip results in on-aircraft repair. The blade can be repaired at the Aviation Intermediate Maintenance (AVIM) level by stripping off the worn-out material and replacing it with new. This repair action should also reduce considerably the scrappage of blades due to leading-edge erosion.

A summary of the preceeding results is presented in Table 22. Table 22 shows that if both blades were considered to have unlimited life for those failure modes requiring blade replacement, the improved blade would have a mean-time-between-removal (MTBR) of 2398 hours. Table 23, derived from Table 22, shows that if each helicopter in a fleet flies 300 hours per year, in peacetime, it will be approximately 5.5 years before half of the improved blades would have to be replaced. The OH-58A standard blade has about three-eighths of the failure mode MTBR of the improved blade.

On the other hand, Table 23 shows that in a fleet of 100 OH-58A helicopters flying 300 hours per year, an on-aircraft improved-blade repair can be expected every 4.2 weeks on the average, as compared to once every 7.3 weeks for the OH-58A standard blade.

The limited (retirement) life of the standard (metal) blade is 2400 hours. When these blade removals are included with the failure removals, the MTBR is 845 hours. The limited life of the improved blade is 3600 hours. Considering these removals, the MTBR of the improved blade should be 1864 hours.

4.6.1.1 Rationale for the Reliability Estimates

The reliability comparison of the improved blade to the standard blade is based on the failure modes of the metal blade and how they would be changed by the improved blade design. The failure rates of the improved and standard main rotor blade failure modes, for both replacements and on-aircraft repairs, were determined from the Army Maintenance Management Systems (TAMMS) data on the OH-58A helicopter (Reference 12). The Reliability and Maintainability Management Improvement Techniques (RAMMIT)

¹²Technical Manual 38-750, THE ARMY MAINTENANCE MANAGEMENT SYSTEM (TAMMS), Headquarters, Department of the Army, Washington, D.C., 21 November 1972, with Change No. 1, 1 April 1974.

TABLE 22. COMPARISON OF MTBF OF OH-58A
MAIN ROTOR BLADE DESIGNS

	<u>MTBF (blade hours)</u>	
	<u>Standard</u>	<u>Improved</u>
Failure modes requiring:		
Blade replacement (MTBR)		
Inherent	3,145	25,641
Induced	1,282	2,646
Total (replacement)	911	2,398
On-aircraft repair (MTBUM)		
Inherent	25,641	6,410
Induced	12,658	20,833
Total (on-aircraft)	8,475	4,902
Limited blade life	2,400	3,600
All blade replacements (MTBR)	845	1,864

TABLE 23. SIGNIFICANCE OF IMPROVED MTBF TO A FLEET OF 100
OH-58A HELICOPTERS EACH FLYING 300 HOURS PER YEAR

	<u>Standard Blade</u>	<u>Improved Blade</u>
MTBR	911	2,398
Years to replacement of one-half the blades	2.1	5.5
MTBF (on-aircraft repair)	8,475	4,902
Weeks between on-aircraft blade repair	7.3	4.2

Major Item Removal Frequency (MIRF) report (Reference 13) on the OH-58A helicopter contains data on main rotor blade removals based on TAMMS DA2410 form (Component Removal, Repair, and Overhaul Record). The data represent the period 1 October 1969 through 31 May 1974. The removals are presented in tabular form for each failure mode and in 100-hour increments. The data represent first removals of new items. Failure rates obtained from the MIRF report are for removals only. To obtain rates for on-aircraft repair, TAMMS DA2407 form (Maintenance Request) data obtained from the Army on computer tapes were analyzed. The ratio of nonreplacement maintenance actions to the replace maintenance actions was obtained and applied to the replace failure rates to obtain on-aircraft repair rates.

4.6.1.2 Failure Modes Analysis

A failure mode analysis was performed using the TAMMS data for the OH-58A main rotor blade. The reasons for repair or removal were grouped by failure mode in a manner similar to that used in USAAVLABS Technical Report 71-9 (Reference 14). Table 24 presents the reason for removal analysis. Since blades removed for "No Defect" type failure codes are reinstalled on the aircraft, they have the opportunity to either be removed eventually for a failure reason or retired. Hence, the data are multiplied and progressively censored. A nonparametric estimate of the failure distribution is obtained using the technique of Reference 15. The technique for obtaining the (unconditional) survival probability at the end of a given time interval is based on computing the conditional probability of surviving each 100-hour increment of time given survival, up to the beginning of the time interval, and then multiplying the conditional probabilities to obtain the (unconditional) probability of survival. Since the data are already grouped in the MIRF report, and if the censored removal times are assumed to be approximately uniformly distributed in the interval, Equation (4b) Reference 15 can be used to compute the conditional

¹³MAJOR ITEM REMOVAL FREQUENCY, OH-58A FLEET, A RELIABILITY AND MAINTAINABILITY MANAGEMENT IMPROVEMENT TECHNIQUES REPORT, Period Covered October 1, 1969 through May 31, 1974, Systems Engineering Directorate, U. S. Army Aviation Systems Command, St. Louis, Missouri.

¹⁴Carr, P. V., and Hensley, O. L., UH-1 AND AH-1 HELICOPTER MAIN ROTOR BLADE FAILURE AND SCRAP RATE DATA ANALYSIS, Bell Helicopter Textron; USAAVLABS Technical Report 71-9, Eustis Directorate, U. S. Army Air Mobility Research and Development Laboratory, Fort Eustis, Virginia, January 1971, AD8811322.

¹⁵Kaplan, E. L. and Meier, P., NONPARAMETRIC ESTIMATION FROM INCOMPLETE OBSERVATIONS, American Statistical Association Journal, June 1958, pp. 456-480.

TABLE 24. REASON FOR REMOVAL ANALYSIS OF MAIN ROTOR
BLADE ASSEMBLIES FROM RAMMIT MRF DATA

Aircraft Model: OH-58A

Part No. 206-011-250-3

<u>Reason For Removal</u>	<u>Number</u>	<u>Percent of Major Cause Category</u>	<u>Percent of all Failures Causes</u>
<u>ALL CAUSES (100.0%)</u>	<u>1387</u>		
I. <u>INHERENT FAILURE CAUSES</u> (10.3%)	<u>143</u>	<u>100.0</u>	<u>24.8</u>
A. <u>Excessive Vibration</u>	<u>16</u>	<u>11.2</u>	<u>2.8</u>
Adjustment improper	1		
Alignment improper	2		
Unable to adjust limits	2		
Unbalanced	1		
Vibration excessive	10		
B. <u>Deterioration</u>	<u>26</u>	<u>18.2</u>	<u>4.5</u>
Cracked	26		
C. <u>Bonding Failure</u>	<u>21</u>	<u>14.7</u>	<u>3.6</u>
Delaminated	1		
Loose	15		
Poor bonding	5		
D. <u>Excessive Wear</u>	<u>61</u>	<u>42.7</u>	<u>10.6</u>
Worn excessively	61		
E. <u>Corrosion</u>	<u>19</u>	<u>13.3</u>	<u>3.3</u>
Corroded	11		
Dirty	5		
Leaking	3		
II. <u>INDUCED FAILURE CAUSES</u>	<u>434</u>	<u>100.0</u>	<u>75.2</u>
A. <u>Foreign Object Damage</u>	<u>330</u>	<u>76.0</u>	<u>57.2</u>
Collapsed	23		
Broken	130		
Cut	3		

TABLE 24. (Concluded)

<u>Reason for Removal</u>	<u>Number</u>	<u>Percent of Major Cause Category</u>	<u>Percent of all Failure Causes</u>
Damaged	2		
Dented	10		
Folded	1		
foreign object damage	4		
Nicked	3		
Punctured	5		
Battle damage	26		
Bent	23		
Chipped	90		
B. <u>Overstressed</u>	<u>73</u>	<u>16.8</u>	<u>12.7</u>
Overspeed	2		
Sudden stop	3		
Crash damage	2		
Accident damage	66		
C. <u>Heat Damage</u>	<u>26</u>	<u>6.0</u>	<u>4.5</u>
Burned	26		
D. <u>Other</u>	<u>5</u>	<u>1.2</u>	<u>0.9</u>
Transportation damage	1		
Maintenance error	4		
III. <u>NO FAILURE CAUSES</u> (50.3%)	<u>698</u>		
Cannibalization	4		
MWO previously complied with	5		
No defect	590		
Removed to facilitate other maintenance	9		
MWO compliance	8		
Time change	10		
Scheduled maintenance	72		
IV. <u>UNKNOWN CAUSES</u> (8.1%)	<u>112</u>		

probabilities. Since the MIRF data were in effect truncated at 1700 hours, we can obtain an average failure rate for a Equation (20.9), Reference 16. The integral in Equation (20.9) is approximated using the well-known trapezoidal rule. The value of the integral is referred to in Section 2.3, Reference 15, as the "mean life limited to time 1700 hours," and as shown by Equation (20.2), Reference 16, is actually a mean time between premature removals and scheduled removals at 1700 hours (assuming that the retirement life is 1700 hours). The failure rates for each mode of failure may be obtained by using the "accidental death" model by Sampford referred to in Reference 17. This model assumes that each mode of failure and censoring are independent and that each blade is subject to each mode of failure and to being withdrawn (censored) from the sample irrespective of which failure mode or withdrawal occurs first. In other words, every blade has many lives.

To obtain a mean time between removal (MTBR) based on retirement times other than 1700 hours, the failure distribution was approximated by a Weibull curve. A plot of the data on Weibull probability paper is presented in Figure 115. The slope of the curve was determined to be about 1.2. Since this is fairly close to 1.0 (which would represent an exponential distribution), the MTBR for the metal blade retired at 2400 hours and for the improved blade retired at 3600 hours was computed using Equation (20.3), Reference 16, which is sufficient for comparative purposes. A more accurate result could be obtained by numerical integration of the Weibull survival function.

4.6.1.3 Inherent Failure Modes

In all blade removals, the decision to replace the blade is based on the immediate evaluation of blade condition. For most inherent failure modes, there is a judgement decision that the mode has progressed to a point where it is no longer acceptable. Most inherent failure modes do not occur abruptly, and it is probable that all blades build up several inherent modes concurrently as they acquire time. Generally, however, only one mode becomes the statistical reason for removal of any one blade.

¹⁶Bazovsky, Igor. RELIABILITY: THEORY AND PRACTICE, Englewood Cliffs, New Jersey, Prentice-Hall, Inc., 1961.

¹⁷Herd, W., ESTIMATION OF RELIABILITY FROM INCOMPLETE DATA, Sixth Symposium on Reliability and Quality Control, page 206, 1960.

Component M/R Blade
 Part No. 206-011-250-3 Model OH-58A
 Data Source RAMMIT MRF Report

WEIBULL PROBABILITY

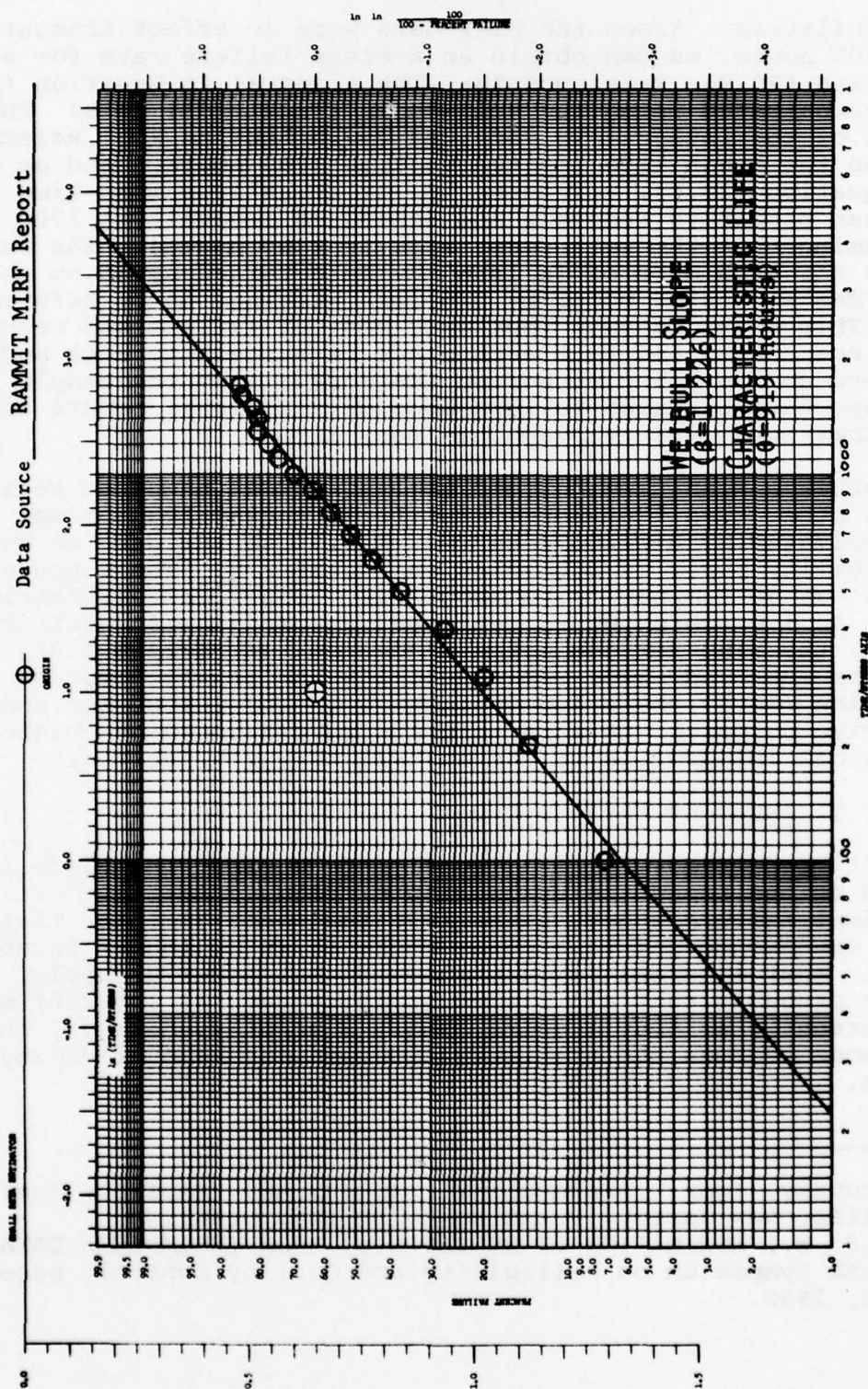


Figure 115. Distribution of removals due to all failures.

For the analysis it was assumed that 90 percent of those blade failures coded as "excessive wear," which results in blade replacement, were due to wearout of the blade's leading edge. Therefore, the standard blade failure rate for excessive wear requiring blade replacement was modified to obtain the corresponding improved blade failure rate. The present metal blade has no abrasion strip. The blade is replaced when more than 0.125 inch of the leading-edge outboard tip of the aluminum spar has eroded away. The proposed abrasion strip for the improved blade is "TUFTANE," a polyurethane material made by Goodrich. The thickness of the abrasion strip is 0.040 inch. No erosion tests of this material have been performed at BHT. Data from USAAMRDL TR-76-40A, Reference 18, was used to make the failure rate adjustment. Figure 2 of that report shows that the time-to-failure for elastomeric materials is approximately the same for material thicknesses ranging from 0.020 to 0.040 inch. Data on a polyurethane material made by Dunlop, Ltd. is compared to the aluminum on the OH-6A metal blade. An adjustment factor is computed which assumes a flight environment of flight in clear air for an unspecified period of time, plus flight in an erosive atmosphere of 80 percent sand and 20 percent rain the remainder of the time. Whereas the all-metal blade would be scrapped at the end of its mean-time-between-unscheduled-maintenance (MTBUM) erosion period, the use of the polyurethane erosion strip would allow the improved blade to be used indefinitely by stripping off the worn-out material and replacing it with new. Since the operation can be accomplished on the aircraft at AVIM, this will result in an increased on-aircraft maintenance action rate corresponding to the decreased remove-and-replace maintenance action rate. The adjusting factor using the data of Table 3 and the equation given on page 14 of Reference 18 was 0.936. This estimate is judgmental since the actual wearability of different types of polyurethane varies even when made by the same company.

The inherent failure modes and rates predicted for the OH-58A standard and improved blades are shown in Table 21. Those for the improved blade were determined as follows. It is expected that the failure modes due to deterioration, bonding separation, and corrosion will be virtually eliminated from the design. On the other hand, the failure rate for excessive vibration is assumed to be essentially the same.

¹⁸Head, Robert E., EROSION PROTECTION FOR THE AH-1G LOW RADAR CROSS-SECTION MAIN ROTOR BLADE, Volume I - Sand and Rain Erosion Evaluation, Hughes Helicopters, Division of Summa Corporation; USAAMRDL Technical Report 76-40A, Eustis Directorate, U. S. Army Air Mobility Research and Development Laboratory, Fort Eustis, Virginia, January 1977, AD A035961.

Since the failure-mode failure rates are very low, the procedure used to compare these rates to those for the same failure modes on the improved blade is to consider them equal if the mode exists, or zero if the mode is eliminated in the new design.

4.6.1.4 Induced Failure Modes

Induced failure modes causing blade removal almost always occur abruptly, and evaluation of the blade condition is generally easy. Induced failure modes generally result from the aircraft mission environment.

4.6.1.5 Overstressed and Other Induced Failures

Table 24 shows induced failures classified as foreign object damage (FOD), overstressed, heat damage, or other induced. The latter three categories are primarily a function of pilot and mechanic skills and care. At present, there is no reason to expect that design changes will have much effect on these failure rates. Therefore, the observed OH-58A failure rates are used for both the standard and improved blades.

4.6.1.6 Foreign Object Damage (FOD)

FOD causes the major portion of the induced failure rates and is amenable to design improvement.

Table 25 shows the dimensional and material changes between the standard and the improved blades. Also shown are the observed FOD failure rates and MTBF values for the standard blade, and the estimated failure rate and MTBF for the improved blade derived from the OH-58A rates. The materials and dimensional changes and impact tests are discussed below.

These estimates are judgmental but show the effect of improvements in materials and increases in material thickness. These values are used in Table 21.

To determine the tolerance of the improved blade to FOD, a core sample of 0.030-inch fiberglass skin over 3-pound Nomex honeycomb was compared to a core sample from a scrapped Model 214 metal blade (0.032-inch skin). A test was performed by dropping an object of known weight and shape from different heights onto the core samples. This simulated small dent damage or puncture damage, depending on the shape of the test object.

4.6.2 Maintainability

TABLE 25. ESTIMATE OF BLADE FOREIGN OBJECT DAMAGE FAILURE RATES¹

	Standard	Improved
λ FOD		
Repair	0.000047 ²	0.000016 ³
Replace	0.000602 ²	0.000200 ³
TOTAL	0.000649 ²	0.000216 ³
MTBF FOD	1541 hr	4630 hr
<u>MATERIAL AND DIMENSIONAL CHANGES</u>		
Outboard abrasion strip	N/A ⁴	0.040-in. polyurethane
Skin thickness		
Upper	0.016-in. aluminum	0.020-in. fiberglass, outbd
Lower	0.016-in. aluminum	0.020-in. fiberglass, 65%
		0.040 in. to 35% radius
		0.060 in. to root

¹Failures per blade flight hour

²From TAMMS DATA

³Estimates based on dimensions and materials shown

⁴No abrasion strip. The blade is replaced when more than 0.125 in. of the leading edge of the aluminum spar has eroded away.

4.6.2.1 Inspection and Acceptance Criteria for Repair of Scrap

There are three categories of damage, depending on the location on the blade where the damage occurs:

- Areas where unlimited repairs are permitted
- Areas where higher loads or critical parts limit the amount of permissible repair
- Areas where no repairs are permitted

Figure 116 illustrates these areas.

4.6.2.2 Unlimited Repairs


Approximately 55 percent of the blade area consists solely of Nomex honeycomb core and fiberglass skin where unlimited repairs are allowed. In this area, there is no restriction on the number or size of repairs permitted providing the damage is more than 1 inch from the spar or trailing edge. Fiberglass skin patches must have an overlap of 1 inch over the adjacent skin and will be feathered at the edges, although the original contour need not be strictly maintained in this area. These repairs should be performed at Aviation Intermediate Maintenance (AVIM) level. Aviation Unit Maintenance (AVUM) level maintenance should be confined to removal and replacement of blades and treatment of minor scratches and blemishes.


4.6.2.3 Limited Repairs


Approximately 20 percent of the blade area can have a limited number of repairs and is repairable within certain limitations. This area includes the outboard half of the spar with the exception of the last 8 inches. The trailing edge is also repairable. Repairable damage to the spar is limited to that which can be cleaned out with a 0.75-inch diameter hole or less. Damaged glass in the spar is removed, a plug is inserted and bonded in the spar cap hole, and a fiberglass patch with a 0.50-inch overlap is bonded on top. Repairs in the spar will require maintaining the original contour. There must be at least 8 inches between each spar repair, or the blade must be scrapped. Repairs to the trailing edge may not be practical in all cases due to the difficulty of cleaning out the damage and reestablishing the original contour and edge of the blade. If repairs are attempted, the minimum recommended patch size is 2 by 8 inches.


4.6.2.4 Prohibited Repairs

The noseblock and areas of the spar not covered above are not repairable (except for nicks, scratches, and abrasion strip replacement) and will require scrapping of the blade.

 No repair allowed except nicks and surface scratches in skin and abrasion strip replacement.

 Limited repair allowed.

 Unlimited repair allowed. No limit on patch size or number of patches allowed in this area.

 Depot replacement.

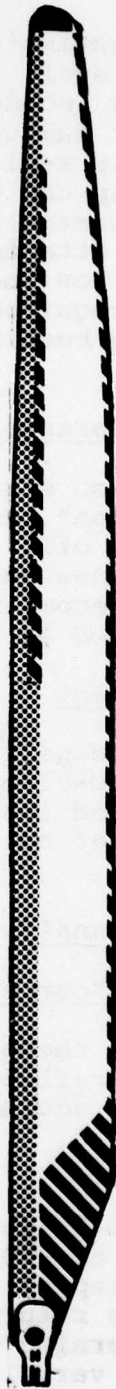


Figure 116. Blade repair areas.

4.6.2.5 Depot Repair

Although it was first estimated that all repairs could be performed below depot level, analysis of the blade shows that it is probable that any incident damaging the tip cap would likely cause structural damage to the blade also. A hot bond is also required for tip replacement. Because of this, it is recommended that the tip cap be replaced at depot level. The low incidence of such damage will require very few blades to be returned to depot. Attachment bushings could be replaced at AVIM level, but the low incidence of bushing replacement will not justify equipment required at that level to support the task. Blades requiring bushing replacement should be returned to depot.

4.6.2.6 Leading Edge Abrasion Strip Repair

The polyurethane abrasion strips will be replaced at AVIM level on an "on-condition" basis. The old material will be relatively easy to peel off. The area beneath must be thoroughly cleaned and the new section attached with a low temperature adhesive. It is recommended that a heated tool (abrasion-strip caul sheet) be used to hasten cure time.

4.6.2.7 Support Equipment

While all repairs may be performed using common and standard tools such as routers, C-clamps, wooden blocks, and micrometers, it is recommended that a pressure heat pack, and an abrasion-strip caul sheet be used at AVIM level to shorten cure time.

4.6.3 Maintainability Analysis

4.6.3.1 Analysis Data Source

An analysis was made of the proposed blade based upon U. S. Army RAMMIT data which reflected 650,000 flying hours and 25 failure modes including accident, FOD, and combat damage.

4.6.3.2 Analysis Results

The data on the present blade reflect an unscheduled MTBR of 475 hours and an MTBUM of 380 hours. Thirty percent of the removed blades were scrapped at AVUM level, and 70 percent of all removed blades were returned to depot level. No information is available concerning disposition of the blades returned to depot level. Since very limited field repair is authorized for the present blade, most require depot-level repair. The same failure modes are related to the proposed blade and reflected 30-percent scrap at AVUM level. Modes considered

for scrap were crash, burn, accident, overspeed, sudden stop, and some collapsed, broken, and battle damage. There was also 40-percent repair at AVUM level and 30-percent repair at AVIM level before the abrasion strip on the proposed blade was considered. An MTBUM of 850 hours for the polyurethane abrasion strip was obtained from Reference 18. This value is considered reasonable for world-wide usage. Deterioration of the present blade caused some scrappage because of the lack of an abrasion strip. Introduction of the abrasion strip changes the scrap value of the proposed blade to 15 percent of all maintenance actions, decreases the AVUM level repair to 15 percent, and increases the AVIM level repair to 70 percent. The MTBF for unscheduled removals (scrap and depot repairs) is 988 hours. The MTBUM for AVUM and AVIM level repairs is 476 hours. While the replacement of the abrasion strip lowers the MTBUM because of its frequency, the blade need not be removed and sent to depot level, thus reducing the number of spare blades required in the supply pipeline. The total maintenance generated for the proposed blade will require only .006096 MMH/FH and a MTTR of 2.62 hours.

4.6.3.3 Determination of Repair Level (AVUM or AVIM)

The repairability rationale developed during the study is to limit repairs at AVUM level to minor repairs not requiring patching or bonding. Removal and replacement of some blades is also accomplished at AVUM for those that meet scrap criteria, or for blades requiring tip and retaining bushing replacement at depot.

Blades requiring patching and bonding repairs should be temporarily repaired by a tape wrap to permit ferry flight to AVIM level for final repair. All blade repair at AVIM should be accomplished in a hangar if on-aircraft repair is to be performed. This includes replacement/repair of the polyurethane abrasion strip. Damaged blades that have been exposed to weather and have internal water that has entered through the damaged area should be thoroughly dried out with hot-air blowers or heat lamps before bonding is attempted. In such cases, it might be more effective from the operational readiness aspect to replace the blade at AVUM level and transport the blade to AVIM level for repair.

4.6.3.4 Preliminary Kit Material and Special Tool List

The following will be necessary to accomplish authorized repairs:

Kits

- Skin Patch Kit - 3-in. diameter
- Skin Patch Kit - 5-in. diameter
- Plug Patch Kit - 3-in. diameter x 1/2-in. depth plug
5-in. diameter patch
- Plug Patch Kit - 3-in. diameter x 2-in. depth plug
5-in. diameter patch
- Plug Patch Kit - 3-in. diameter x 3-in. depth plug
5-in. diameter patch
- Plug Patch Kit - 1-in. diameter x 1/2-in. depth plug
3-in. diameter patch
- Plug Patch Kit - 1-in. diameter x 1-1/2-in. depth plug
3-in. diameter patch
- Plug Patch Kit - 1-in. diameter x 2-in. depth plug
3-in. diameter patch
- Plug Patch Kit - 1-in. diameter x 3-in. depth plug
3-in. diameter patch

Trailing-Edge Patch Repair Kit

Abrasion-Strip Repair Kit

Spar Plugs - Preformed 3/4-inch diameter

Special Tools

Pressure Heat Pack (Figure 117)

Abrasion-Strip Caul Sheet (Figure 118)

4.6.3.5 Blade Repair Procedure

- Support blade at tip end using maintenance stand or step ladder.
- Determine extent of damaged area and select kit containing proper size plug/patch.

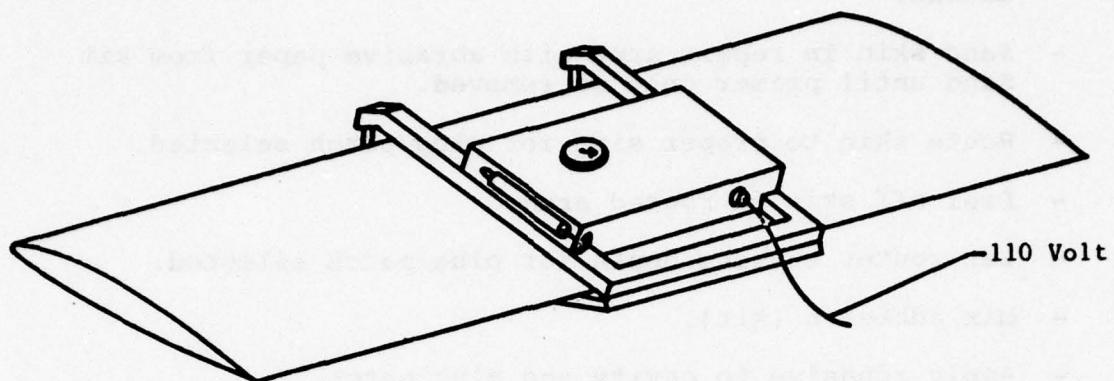


Figure 117. Heat-pressure patching apparatus.

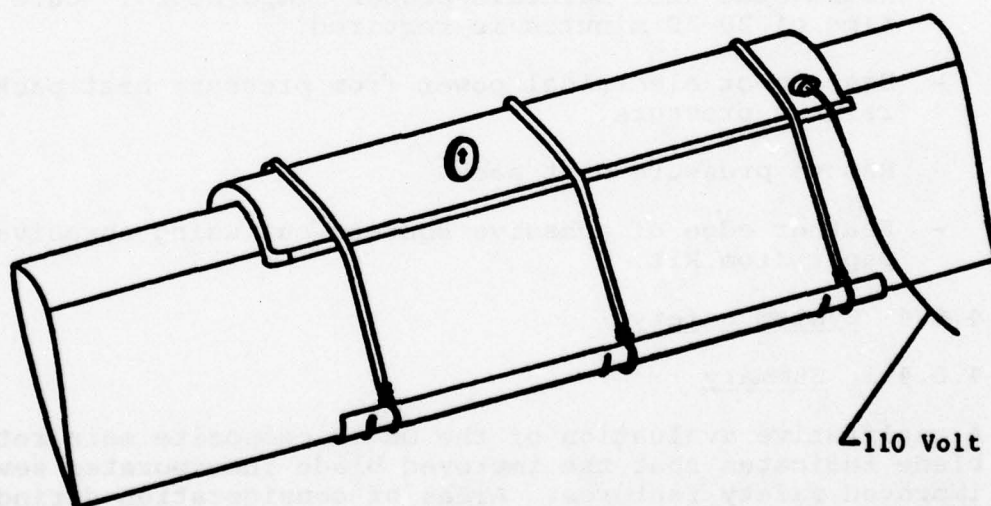


Figure 118. Replacing leading-edge abrasion strip.

- Remove paint from area to be repaired with methyl ethyl ketone.
- Sand skin in repair area with abrasive paper from kit. Sand until primer only is removed.
- Route skin to proper size for plug/patch selected.
- Peel off skin in routed area.
- Set router cutting depth for plug/patch selected.
- Mix adhesive (kit).
- Apply adhesive to cavity and plug patch.
- Insert plug patch under hand pressure to seat properly. Patch must overlap damaged skin area by 1 inch.
- Wipe off excess adhesive.
- Install pressure heat pack over repair area.
- Actuate hand pump to obtain proper pressure.
- Connect 110-volt AC power to pressure heat pack. Thermostat will maintain proper temperature. Cure time of 20-30 minutes is required.
- Disconnect electrical power from pressure heat pack and relieve pressure.
- Remove pressure heat pack.
- Feather edge of adhesive squeeze-out using abrasive paper from kit.

4.6.4 System Safety

4.6.4.1 Summary

A qualitative evaluation of the OH-58 composite main rotor blade indicates that the improved blade incorporates several improved safety features. Areas of consideration during this evaluation included FOD tolerance and fail-safety, environmental degradation, lightning protection and blade retention.

4.6.4.2 Areas of Safety Improvement

- Increased resistance to deterioration, bonding failure, and corrosion

- Increased tolerance of the blade to ballistic strikes, tree strikes, and other FOD; increased residual strength after strike
- Improved erosion protection through the use of a polyurethane abrasion strip on the blade's leading edge and a stainless steel cap at the blade tip
- Titanium grip plates, which provide good fatigue resistance and are more compatible with fiberglass than steel
- Incorporation of an electrothermal deicing system
- Reduced radar reflectivity

4.6.4.3 Areas of Possible Improvement or Special Safety Consideration

- Method for monitoring integrity of the blade (blade monitoring characteristic or device) until blade experience is attained
- Procedures for blade inspection/checkout following repair to insure blade is flightworthy

4.7 ENVIRONMENTAL SUBSYSTEMS

4.7.1 Ice Protection

Several methods of deicing the OH-58 blade were investigated. The electrothermal method was chosen as being the most cost-effective method that has been technically proven by flight testing. Two other methods, ice phobic materials and vibratory deicing, show important weight and cost advantages but neither method has been flight tested to the extent that they have been proven technically feasible. The electrothermal concept has been proven by U.S. Army flight tests.

The electrothermal method involves heating the blade leading edge. A small thickness of ice is allowed to form; heat from an electric heater is then cyclically applied under the blade leading edge. The heat raises the leading edge temperature above 32°F, and thus sheds the ice. The heater is turned off, ice is allowed to form, and the cycle is repeated. The cycle time will depend upon the icing rate.

Preliminary design has shown that a heating element for an electrothermal deicing system is feasible for the OH-58 rotor blade. The design provides for a metallic heating element to be installed under the leading-edge abrasion strip. When this deicing capability is desired, the strip of radar-absorbing material (RAM) in the spar is eliminated to make space for the heating element. The blade contour will remain the same for either configuration.

4.7.1.1 Heater Design

The heater elements will consist of metal foil-resistance elements photoetched from stainless steel alloy. Foil thickness will be 0.005 inches. The foil will be bonded to a single-ply fiberglass carrier and bonded to the leading edge of the spar as shown in Figure 8.

Because it is not practical to supply enough electrical power to heat the entire unit, the foil heater must be installed in segments. The segments can be oriented either span or chordwise. Spanwise segments have simpler lead connections because each segment extends to near the inboard edge of the blade. A decision on segment orientations will be made during detailed design. The heating element will extend to 10 percent of the upper surface and to 15 percent of the lower surface.

A thermal analysis will be made to determine the power density requirements of the heating elements along the blade. This analysis will be accomplished to meet the requirements of the meteorological conditions defined by Figures 2 and 3 of MIL-E-38453A (USAF) (Reference 19) as amended in the work statement for this contract. Power densities and the time increment of power application for shedding are related. The heat flow as well as heat sinks and the thermal resistance between the heater and blade breeze surface must be considered. Because of the change in aerodynamic heating due to varying air velocity along the blade, it is estimated that the power density can be gradually reduced from the inboard to the outboard ends of the blade. Power density will be varied by changing the resistivity (by size) and spacing of the foil heating ribbons.

4.7.1.2 Deicing System Penalties

4.7.1.2.1 Aerodynamic Performance

There is no effect on aerodynamic performance because the deicing heater does not change the blade envelope.

4.7.1.2.2 Weight

The deicing heater requires the elimination of the radar-absorbing material strip in the spar, resulting in a small change to the weight of the blade.

¹⁹Military Specification, MIL-E-38453A, ENVIRONMENT CONTROL, ENVIRONMENTAL PROTECTION, AND ENGINE BLEED AIR SYSTEMS, AIRCRAFT AND AIRCRAFT-LAUNCHED MISSILES, GENERAL SPECIFICATION FOR, Department of Defense, Washington, D. C., 2 December 1971.

4.7.1.2.3 Structural Dynamics

The deicing heater is not expected to affect the structural dynamics of the blade.

4.7.1.2.4 Fatigue Life

The stainless steel alloy heating element will have a fatigue life greater than the fatigue life of the blade.

4.7.2 Lightning Protection

The upper and lower surfaces of the blade are covered with a layer of 120-mesh aluminum wire screen. The wire extends from 1-1/2 inches aft of the leading edge to 2-1/2 inches forward of the trailing edge, over the full span of the blade. Over the outboard half of the blade leading edge, in the area of the nose ballast weight, 1/2-inch-wide strips of aluminum screen wire are placed on 6-inch centers. These strips extend from the upper screen wire cover over the blade leading edge to the lower screen wire cover, forming a protective cage over the exposed leading-edge ballast weight. This cage will prevent a lightning strike from penetrating to the metal leading-edge ballast weight. The tip balance weight package, the leading-edge balance weight, and the tip cap are electrically connected to the screen wire covers at the tip of the blade. The screen wire covers provide an electrical ground path from the tip of the blade to the blade bolt-hole at the butt of the blade. The screen wire covering over the blade surfaces provides protection for the internal structural elements by providing an external conductive path to ground for lightning. Additionally, the screen covering functions to prevent the buildup of electric charges caused by precipitation on the blade surface, eliminating the possibility of "P" static radio interference. For radar cross section reduction purposes, the conductive wire surface shields the back surface of the blade spar and other internal features from the radar. An auxiliary function of the wire covering, unrelated to electrical phenomena, is that it provides an effective abrasion-resistant and damage-resistant covering over the glass blade skins.

The lightning protection system described above is calculated to be adequate for lightning protection, and to provide the best possible interrelationship between static electric, radar reflection, and lightning protection measures for the blade.

4.7.3 Static Electricity

To minimize the effects of precipitation, and static and tribo-electric charging, the proposed blade is provided with a surface covering of 120-mesh aluminum screen wire. This

coating provides a continuous conductive path to allow the drainage of surface charges to the main blade retention plate without arcing or flashovers. This will allow the bleed-off of accumulated static charges prior to their reaching corona levels.

4.7.4 Erosion Protection

As a result of the trade-off studies, a urethane leading-edge protective strip was chosen over a metal leading edge. The urethane material has good sand erosion resistance, is transparent to radar energy, and is easily replaced in the field. Unless exposed to considerable flight in rain, the urethane material will provide the required 1200-hour life in service. Urethane is substantially less expensive than metal for leading-edge erosion protection, both in material cost and in forming costs. Loss of portions of the urethane leading edge material would not be as serious in its effect on rotor dynamics as partial loss of a metal leading edge. On a previous government-sponsored composite blade program, the AH-1Q blade, a urethane leading-edge material was chosen. The "Q" rotor has a significantly higher tip speed than the OH-58, and since the severity of the erosion of the leading edge of a rotor blade is a function of velocity, the OH-58 blade is considered to be a relatively better candidate for a urethane leading edge than the "Q" blade. Erosion protection of a rotor blade involves more than the protection of the leading edge of the blade. While the erosion of the leading edge is the most severe problem in protection of the blade, the blade skin surfaces are also subjected to erosion. In particular, the lower surface of the blade of a small helicopter that operates in a forward area is subjected to: erosion and scuffing from dirt, small pebbles, and sticks picked up by rotor downwash in unprepared landing areas; a high incidence of strikes by small limbs from trees and brush. The choice of the aluminum screen wire for the rotor will enhance the durability of the blade skins by providing a relatively durable surface layer of wire mesh imbedded in a tough resin layer. This surface layer will improve the ability of the blade skins to resist penetration by small limbs or pebbles and prolong the life of the blade.

4.8 RADAR CROSS SECTION

4.8.1 General

One objective of this preliminary design program was to investigate and evaluate methods of reducing the radar cross section (RCS) of the OH-58C/A composite main rotor blade. In support of this effort a subcontract was placed with Rockwell International, Tulsa Division, to assist BHT in the analysis, diagnostic treatment, and testing of a reduced RCS blade. Evaluations were made at two frequencies (I and J bands), two

polarizations, 0 to ± 30 degrees blade pitch aspect angles taken over 90 degrees of azimuth for three sectors of interest. The leading edge, tip, and trailing edge scattering centers were evaluated.

The results obtained are considered realistic and significant for the conditions stated. The average RCS reduction is on the order of 90 percent for a treated composite blade versus an untreated blade. The following paragraphs briefly summarize the approach. Details are presented in Volume II of this report.

4.8.2 Discussion

4.8.2.1 Treatment Approaches

The blade has three (excluding the root) prime scattering centers: leading edge, tip, and trailing edge. Each center must be addressed individually for optimum reduction.

Two methods were considered in reducing the RCS: shaping, when feasible, and the application of radar-absorbent materials (RAM). The primary requirements for any reduction technique are that they do not alter the aerodynamic shape in a detrimental way, are compatible with other design disciplines and requirements, and effectively suppress radar reflections over a range of frequencies, polarizations, and viewing angles. The preferred approaches are those that offer the best compromise for the design concept.

The inherent benefits of leading- and trailing-edge curvature and tip shaping of the proposed blade are also advantageous in terms of reducing the specular peak values of the blade RCS. In addition to shaping, the following approaches were considered in treating the blade with RAM.

- Application of a magnetic absorbing material in the leading edge of the blade. The parameters involved in the electrical design are the thickness of the material, location of the material with respect to the leading edge, and the electrical characteristics.
- The use of discrete element-absorbent materials in the leading edge as considered early in the design concept phase, but was rejected on the basis that the small leading-edge radius would prevent their successful application.
- Reduction of the blade tip can be best controlled by shaping. The proposed taper thin tip is an effective method of reducing this area as a significant scattering center. Application of RAM was not considered.

- Treatment of the trailing edge by applying carbon loading to the afterbody core makes it lossy. Also, the use of woven mesh in the upper and lower skins of the blade is effective, making those surfaces reflective.

4.8.2.2 Absorber Performance

Performances of the absorber systems were computed using transmission line techniques and the known electrical properties of the structural laminates and absorber elements. A theoretical optimization was derived by varying the values of controllable material properties and spacing.

4.8.2.3 RCS Substantiation

Past experience has shown that material parameter changes and the effect of highly curved surfaces may change the theoretical values during fabrication. To verify the theoretical design, a series of tests were made using a short-length loose stack blade model. Loose stack models are specimens which are taped to or tack bonded together so that various material arrangements may be evaluated. BHT supplied these model specimens to Rockwell for measurement in their anechoic chamber facility. The models provided were midspan, full-scale in chord, and 24 inches in length. Measurements were made for two frequencies, two polarizations, and two attitudes.

4.8.2.4 Test Results

Test results obtained indicate that the proposed configuration (shown in Figure 119) provides a significant reduction in blade radar signature. This configuration consists of a magnetic sheet absorber in the leading edge of the blade. The afterbody core is treated to be made lossy. The upper and lower skins, from the leading-edge absorber to 3 inches from the trailing edge, are made reflective by a woven mesh installed in the skin.

Average RCS data for this configuration indicates a reduction of approximately 90 percent over an all-composite untreated blade. This average is identified as an average of four 90-degree spheres of influence centered about the leading edge, tip, and trailing edge for a window of 0 to ± 30 degrees in pitch, 360 degrees in azimuth, at two frequencies and two polarizations.

4.8.3 Compatability

Aside from blade geometry and material characteristics, other diverse requirements such as erosion and lightning protection and deicing interact with RCS reduction.

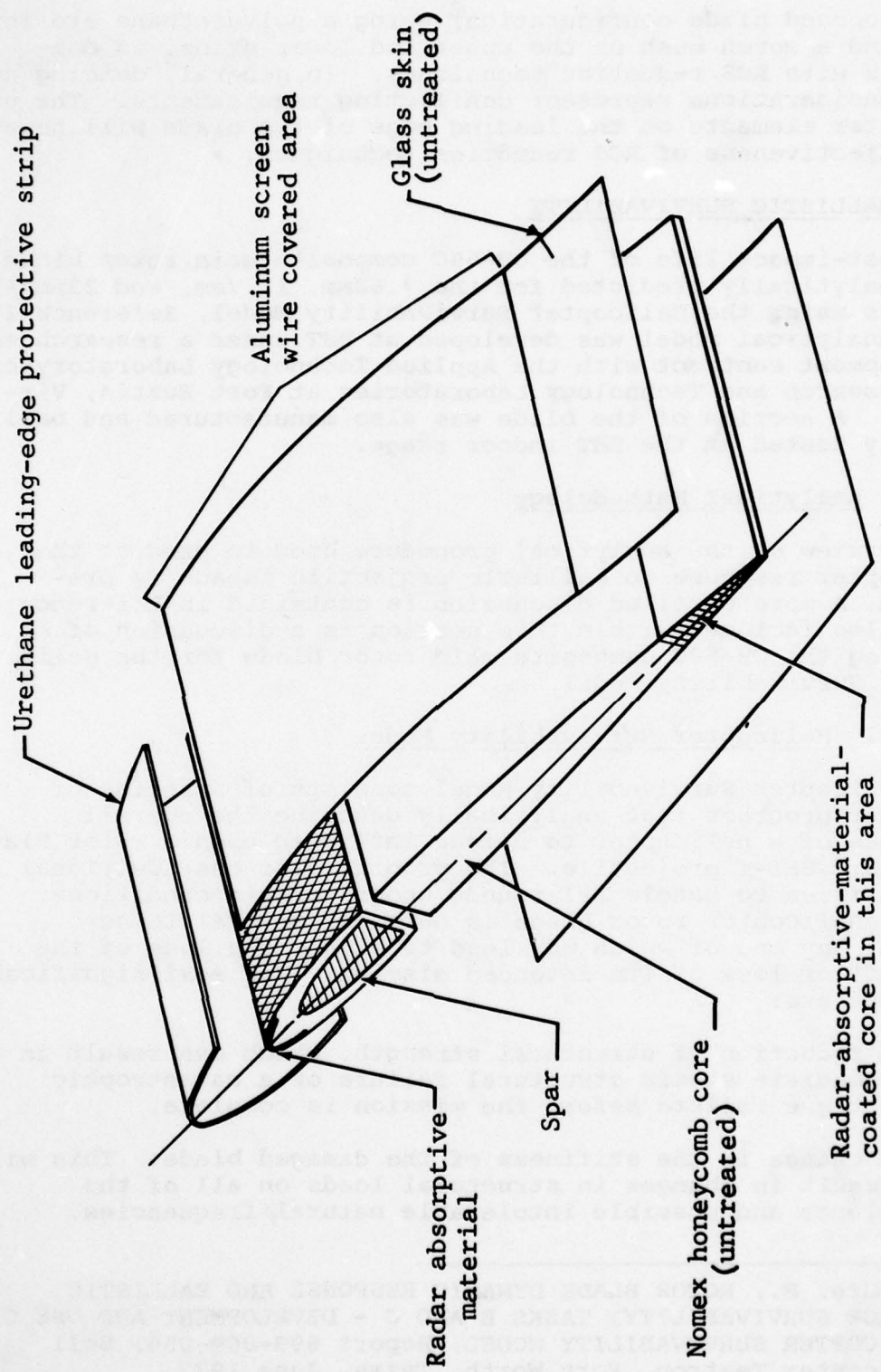


Figure 119. RCS reduction concept for the OH-58C/A composite rotor blade.

The proposed blade configuration, using a polyurethane erosion boot and a woven mesh on the upper and lower skins, is compatible with RCS reduction techniques. In general, deicing and RCS considerations represent conflicting requirements. The use of heater elements on the leading edge of the blade will negate the effectiveness of RCS reduction techniques.

4.9 BALLISTIC SURVIVABILITY

The post-impact life of the OH-58C composite main rotor blade was analytically predicted for the 7.62mm, 12.7mm, and 23mm API threats using the Helicopter Survivability Model, Reference 20. This analytical model was developed at BHT under a research and development contract with the Applied Technology Laboratory of the Research and Technology Laboratories at Fort Eustis, Virginia. A section of the blade was also manufactured and ballistically tested at the BHT indoor range.

4.9.1 Analytical Methodology

An overview of the analytical procedure used to predict the helicopter response to ballistic projectile impact is presented. A more detailed discussion is contained in Reference 20. Also included within this section is a discussion of modeling the OH-58C composite main rotor blade for the Helicopter Survivability Model.

4.9.1.1 Helicopter Survivability Model

The Helicopter Survivability Model consists of a series of computer programs that analytically describe the overall response of a helicopter to damage inflicted upon a rotor blade by a 23mm HEI-T projectile. The program also has additional capabilities to handle API rounds under certain conditions. When a helicopter rotor blade is damaged, several things happen, any one of which may lead to either the loss of the aircraft or loss of its intended mission. The most significant of these are:

- A reduction of structural strength, which can result in an immediate static structural failure or a catastrophic fatigue failure before the mission is complete.
- A change in the stiffness of the damaged blade. This will result in changes in structural loads on all of the blades and possible intolerable natural frequencies.

²⁰Zinburg, H., ROTOR BLADE DYNAMIC RESPONSE AND BALLISTIC DAMAGE SURVIVABILITY, TASKS B AND C - DEVELOPMENT AND USE OF HELICOPTER SURVIVABILITY MODEL, Report 699-099-054, Bell Helicopter Textron, Fort Worth, Texas, June 1977.

- A loss of mass in one blade, which can cause large oscillatory hub shears at the top of the mast. These shears not only induce high loads throughout the helicopter, but may impose sufficiently high accelerations on the pilot to make him incapable of controlling the aircraft.
- A change in the aerodynamics of the rotor blade that can increase the power required to maintain flight.

The Helicopter Survivability Model analytically addresses these problems.

The major elements of the model, shown in Figure 120, are the Damage Model, the Myklestad Analysis, the Dynamic Analysis, and the Fatigue Analysis.

The Damage Model simulates the damage caused by the impacting projectile. The inputs to the program are the blade structural elements (those used to compute section properties), the airfoil geometric description, and such projectile data as impact velocity, are spanwise and chordwise obliquity. The outputs are the damaged blade section properties (EA , EI_b , EI_c , KG , ρA , ρI_b , ρI_c) at five spanwise locations between and including the extremities of the damage. (The five stations are automatic, but there is a program option wherein the user may call for as many intermediate stations as he desires.) In addition to the computed section properties, the output contains computer plots of the blade cross section showing the material removed by the projectile.

The Dynamic Analysis consists of the Myklestad Analysis to compute mode shapes and natural frequencies, and a modified version of computer program C81 to compute the response of the aircraft to the damage, and to compute rotor blade loads.

The Myklestad Analysis uses the section properties of both the damaged and undamaged blades to compute mode shapes and frequencies. Section property data for the analysis are taken from the output of the Damage Model. The data can take one of two forms at the option of the user. He may either use it directly from the tapes, where the properties are computed for five sections along the damage line and then weighted to give average properties, or he may take the properties from the computer printouts at as many damaged stations as he desires and do his own weighted averaging. The mode shapes and frequencies are then used in the modified version of C81.

Computer program C81, which was developed by BHT, is a rotorcraft simulation program that contains a time-variant aeroelastic rotor analysis to compute rotor oscillatory loads. It

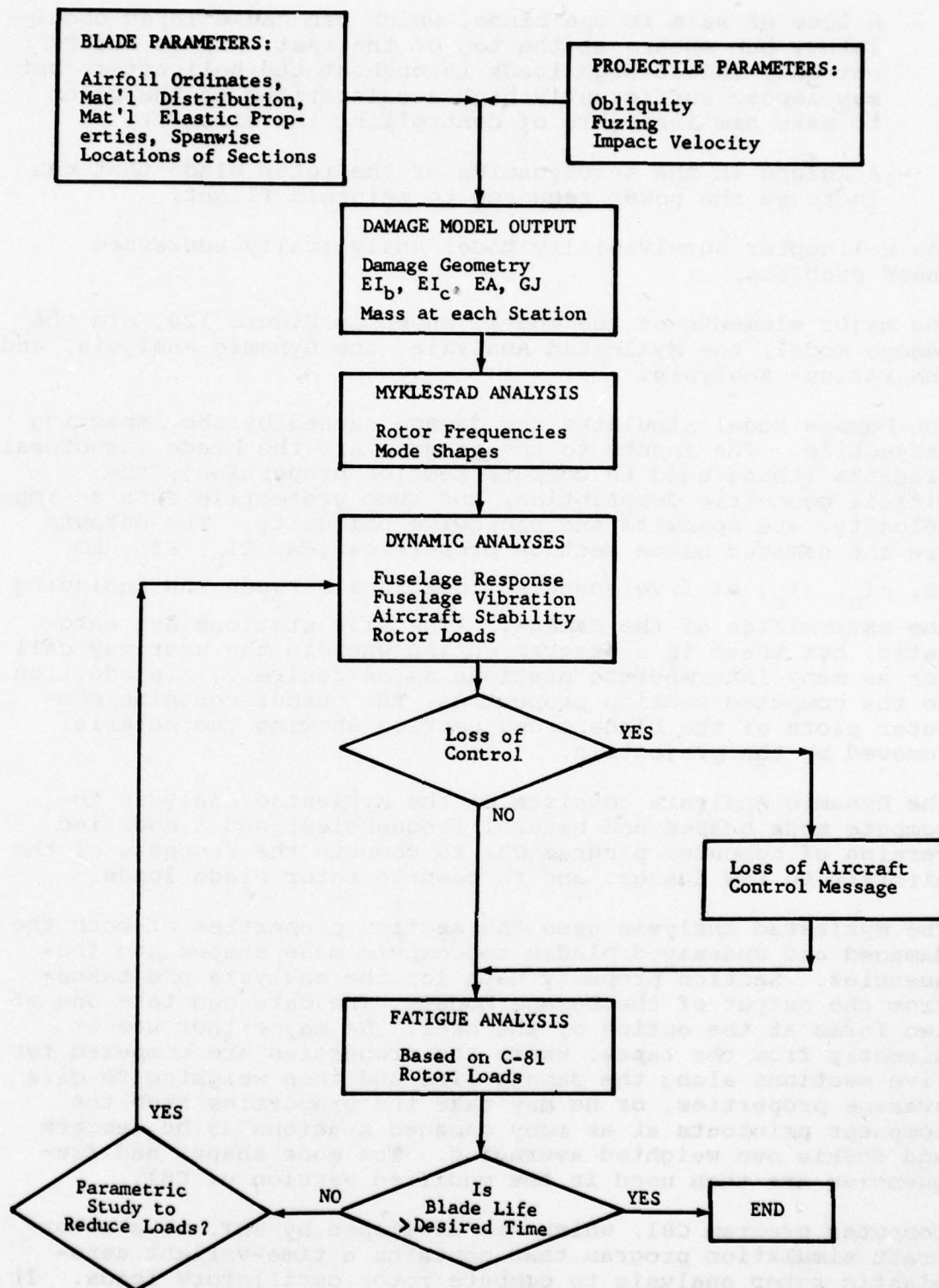


Figure 120. Helicopter survivability model.

uses the modal approach to analyze the aeroelastic rotor and can be used with rotors having up to seven blades. The program, however, does not account for dissymmetry at the hub caused by a change in mass and stiffness of one blade. Because of this, the Helicopter Survivability Model uses a modified version of C81 called SLAMUR (Straight Line Analytical Method for Unsymmetrical Rotors) which accounts for this dissymmetry.

The possible outputs of the Dynamic Analysis are many. The more significant ones pertaining to helicopter response to ballistic damage are:

- Beam and chord bending moments
- Torsional moments
- Hub shears
- Pylon motion
- Control forces

The above factors are used to compute rotor blade stresses, control forces, rates, and position. (It should be noted that centrifugal force, for computing axial stress, is not an output of C81. It is computed in another program.)

All of the outputs are printed as standard C81 outputs. The data are also stored for use in the structural analyses and to check against other helicopter failure criteria.

The structural analysis, the final segment of the Helicopter Survivability Model, contains the following:

- A check for static strength
- A fatigue analysis for metallic blades based on linear fracture mechanics concepts
- A fatigue analysis for composite blades using Goodman diagrams and stress concentration factors

The bending moments for the static and fatigue analyses are outputs of the SLAMUR/C81 program. The output from SLAMUR/C81 also contains values for computing the centrifugal force at the damage. Section properties for the damaged section are taken from the output of the Damage Model. Steady state and oscillatory stresses are computed at the damaged section in the conventional manner. The check for residual life is made for metallic or composite blades using equations contained in the program for metal and Goodman diagrams for composite materials.

An automatic looping feature, shown in Figure 120, removes the requirement for user intervention in determining the residual life of the blade. If the fatigue analysis shows

the residual life of the blade to be less than the desired time of high-speed flight, the Survivability Model driver program will reduce the aircraft speed by a specified increment and return to SLAMUR/C81 to recompute loads and then stresses. This is repeated until either failure is no longer indicated or a specified low speed is reached, indicating a nonsurvivable rotor.

Loss of the aircraft or mission may occur in one of the following ways, and is accounted for in the Survivability Model.

- Structural failure; static or fatigue
- Inadequate control power available to maintain flight
- Excessive control rate is required to maintain flight
- Pitch, yaw, or roll rates are excessive
- Excessive power is required to maintain flight

The structural analysis contains an analysis for both static strength and residual fatigue life. The time criterion for an acceptable residual life at high-speed flight is established by the user. (It is undoubtedly also acceptable if, following damage, the speed can be reduced to a value which will also give the desired time of flight.)

Control and flight limits for the Survivability Analysis were developed from flight test data and are shown in Table 26. Beyond these limits, the pilot will abort a maneuver because of the sensation of the onset of loss of control. It was determined that flight path angle of itself was not the important criterion, but the combination of angle with rate (pitch, yaw, or roll) that led to loss of control. To establish a loss-of-control criterion for the Survivability Model, it was assumed that the maximum allowable rate is twice the rate shown in Table 26. The maximum control rate of full throw in .5 second (Table 26) is representative of the maximum control rates of most boosted control systems, and loss of control is considered to occur if control rate requirements exceed this value.

The acceleration at the pilot's seat is an output of the Dynamic Analysis. The criterion for failure is a lateral acceleration of $\pm 1g$. Considering that a helicopter with a blade damaged by a projectile represents an emergency short-term condition, the value of $\pm 1g$ (lateral) is a reasonable value for the maximum value of acceleration during which a pilot can control an aircraft. The pilot's seat acceleration is a printed output of the Dynamic Analysis, but if the value of $\pm 1g$ is exceeded, the Survivability Model does not stop. It

TABLE 26. CONTROL LIMITATIONS FOUND
FROM FLIGHT EXPERIENCE

<u>Control Rate</u>	<u>100% Throw in 0.5 Second</u>		
	<u>Absolute</u>	<u>Combination</u>	
<u>Flight Path</u>			
Pitch Angle	50 deg	+20 deg	-20 deg
Pitch Rate	20 deg/sec	with +15 deg/sec	with -10 deg/sec
Roll Angle	70 deg		55 deg
Roll Rate	60 deg/sec		with 25 deg/sec
Yaw Rate	55 deg/sec hover		
	15 deg/sec forward flight		

is left to the discretion of the user to decide what acceleration he wishes to use as a limit, although on the basis of available data, 11g lateral is recommended.

In severe cases the drag caused by ballistic damage may increase the power required to sustain forward flight to a level greater than is available. As part of the SLAMUR/C81 analysis, the power required for flight is computed and printed. As with the pilot seat accelerations, this is not an item that will automatically stop the Survivability Model, but a warning message is included in the output if the power required for flight exceeds the power available, and it is noted on the summary page.

4.9.1.2 Damage Analysis of The OH-58C Composite Main Rotor Blade

Evaluating the OH-58C composite main rotor blade for ballistic damage consists of the development of required input data for program DAMAGE in the Helicopter Survivability Model by determining the section properties of the damaged rotor blade. These data are used for dynamic and fatigue analysis. The undamaged blade inputs were previously developed in Sections 4.3 and 4.4 of this report.

The Damage Model requires two packages of input data. The first package contains a geometrical description of the rotor blade and projectile parameters. The second package contains an elemental description of the blade cross section in the area of the shot for determining the blade material removed by the projectile.

4.9.1.2.1 Geometric Target Model

The Damage Model uses the combinatorial geometry (COMGEOM) technique to form the geometrical representation of the blade. This technique makes use of combining preprogrammed solids to form regions that are parts of the rotor blade. When these regions are combined, they form a three-dimensional description of the rotor blade. The COMGEOM procedure is used in a program called GIFT, Reference 21. This program was used in the initial development of the OH-58C glass blade geometrical description for the Damage Model. The GIFT model was used because of available options that greatly aid the model development, which

²¹Bain, L. W., Jr., and Reisinger, M. J., THE GIFT CODE USER MANUAL; VOLUME 1. INTRODUCTION AND INPUT REQUIREMENTS, USABRL Report No. 1802, U. S. Army Ballistic Research Laboratory, Aberdeen Proving Ground, Maryland, July 1975.

are not available in the Damage Model. One option, called PICTURE, provides computer-generated CALCOMP plots of the model at any user-requested aspects.

The OH-58C composite main rotor blade was analyzed in a section where maximum stresses are predicted to occur. Since the threats were all API rounds, the damage produced would generally be local. This meant that the required COMGEOM model would need to be developed for a small spanwise section of the blade. The model represents a section of the blade from Station 103 through blade Station 109. The resultant model is shown in the CALCOMP drawing, Figure 121. This represents a view of the blade cross section at blade Station 103. For the short span of the blade that was modeled, the taper was not enough to affect the ballistic damage results for this analysis. Therefore it was not programmed into this geometrical model. The box surrounding the model is only a frame that the computer draws and is not part of the geometrical description.

4.9.1.2.2 OH-58C Composite Main Rotor Blade Material Properties

Properties of the composite materials from which the OH-58C blade is constructed are not among those that are available in the Damage Model. Therefore, these materials properties were input using an optional method which allows for up to six additional materials to be defined in program DAMAGE. Table 27 lists the parts of the blade and their materials and properties that are required by program DAMAGE.

4.9.1.2.3 Threat Characteristics

The ballistic threats that were analyzed are:

7.62mm API, fully tumbled at 2500 ft/sec

12.7mm API, fully tumbled at 2500 ft/sec

23mm API, aligned at 200 ft/sec

To model the tumbled API rounds using the Damage Model, an aligned projectile whose diameter was equal to the effective cutting length of the tumbled round had to be determined. This was necessary because the Damage Model was developed to analyze impacts from aligned rounds. To determine the effective cutting length, the ballistic damage results on the rotor blade specimen (discussed in Section 4.9.2) were measured. At the time of the analysis, the specimen had been shot with the aligned 23mm API and a tumbled 12.7mm API projectile. The effective cutting length of the 12.7mm API was measured at 2.7 inches. The

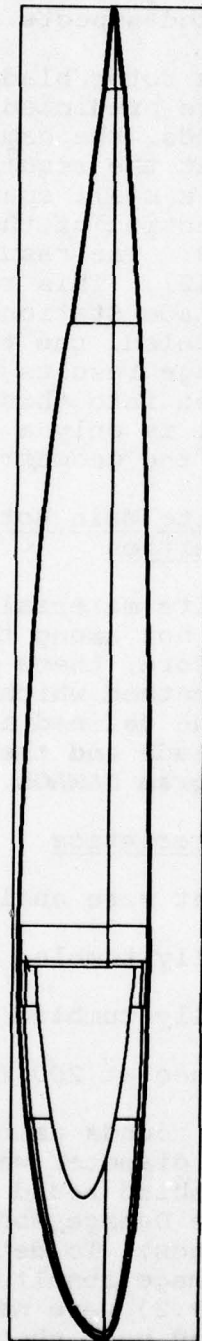


Figure 121. CALCOMP drawing of the OH-58C composite main rotor blade.

TABLE 27. OH-58C COMPOSITE MAIN ROTOR BLADE MATERIAL PROPERTIES

Blades (materials)	Density $\frac{\text{lb}}{\text{in}^3}$ ($\frac{\text{sec}^2}{\text{in}^4}$) $\times 10^4$	Young's modulus (psi) $\times 10^{-6}$	Bulk modulus (psi) $\times 10^{-6}$	Shear yield (psi) $\times 10^{-4}$	Shear strength (psi) $\times 10^{-4}$	Brinell Hardness
Abrasion Strip (urethane)	1.115	.000001	1.9	.0001	.0001	1.0
Unidirectional spar (S-Glass, 0°)	1.787	7.1	5.9	1.1	1.1	70
Outer Spar Rap (S-Glass, +45°)	1.787	2.3	1.9	4.0	4.0	70
Skin (S-Glass, +45°)	1.787	3.0	2.5	1.39	1.39	65
Trailing Edge (S-Glass, Tape)	1.787	7.1	5.9	1.1	1.1	70
Honeycomb (Nomex core)	.0463	.000001	1.0	.0001	.0001	1.0

diameter of the 23mm API entrance on the blade was measured at 1.2 inches. Since the specimen had not been shot with the 7.62mm API round, the tumbled cutting length was determined using a ratio of the 7.62mm round length to the 12.7mm round length times the measured effective cutting length of the 12.7mm API projectile. The result was a 1.54-inch cutting length for the 7.62mm API projectile. This projectile was modeled in the same manner as the 12.7mm API projectile discussed above.

Since these rounds were inert and the blade model was symmetrical about the shot line, the damage would be symmetrical about that shot line (Station 106). Therefore, several cross sectional cuts were requested between blade Stations 103 and 106. The damage would be determined from this region and applied equally to the region bounded by blade Stations 106 through 109. For the tumbled rounds, these cuts were located within one half the normal projectiles diameter from blade Station 106. For the 12.7mm API, damage was confined to blade Stations 105.75 to 103.0 and for the 7.62mm API, blade Stations 105.85 to 105.0. The 23mm API damage was between blade Stations 105.4 and 106.0.

The projectiles were modeled to strike the rotor blade from two directions. These directions were chosen because they represent typical type cases for ballistic impact in an area of questionable survivability. In case one, the shot line for the projectiles intersects the rotor blade from below at an angle of 45° with respect to the blade's chord. It enters the blade approximately 3.5 inches aft of the leading edge, passes through the spar closure and exits the top surface approximately 1 inch aft of the closure. In the second case, the shot line intersects the blade from below at an angle of 60° with respect to the chord. It enters the blade approximately at the same location as the first case shot line. However, the shot line exits the blade at the top corner of the spar closure. All three projectiles were analyzed by the Helicopter Survivability Model for both of these cases. They were centered about the shot lines with the tumbled rounds orientated such that the projectile length was perpendicular to the rotor blade's leading edge.

The two cases are certainly not "worst case shots." Projectiles that penetrate the forward portion of the rotor blade spar will do more lethal damage to the blade's structure. When considering the projectile cutting lengths and velocities, strikes on the rotor blade at the nose-on or near nose-on aspects will remove enough of the spar to render the blade incapable of withstanding the forward flight static and fatigue loads. The cutting lengths of these projectiles are as large or larger than the thickness of the blade. Therefore, they theoretically would sever the blade from these aspects if the

projectiles' energy is great enough so that they pass through the spar of the blade. Ballistic tests of a specimen of this rotor blade, discussed later in Section 4.9.2, showed that these projectiles, traveling at these velocities, contained enough energy to completely penetrate this blade. Impacts of the tumbled 12.7mm API and the aligned 23mm API projectiles passed completely through the main portion of the spar. Although the tumbled 7.62mm API projectile did not pass completely through the spar, it did penetrate far enough to bulge the top surface of the blade and therefore render the spar's structural integrity questionable.

Currently, there is limited data on penetration relationships for composite materials. The Damage Model contains material properties and penetration equations for metallic materials that are impacted by an aligned 23mm HEI-T projectile. These equations are used to calculate the projectile's deceleration as it passes through the material. Even with a change in properties and coefficients, it is doubtful that the equations would properly calculate the deceleration profile for the threats used in this report, especially when the projectiles are tumbled. However, if the projectile has enough energy to pass completely through the blade, these properties and coefficients will not affect the results.

4.9.1.2.4 Elemental Description Model

To predict material removal from the main rotor blade, an elemental description of the cross section was formed. This is the second package of input data required by the Damage Model. Each region of the blade at Station 103 was divided into small elements. Element size was approximately .25 inch x .25 inch from the nose to the torque wrap closure and 1 inch x .050 inch aft of the closure. Element dimensions in the spar region of the blade were selected to be on the order of the size of the 7.62mm API threat. This was done to insure that the algorithm for material removal in the Damage Model would work for this size threat. Centroid location, area, and material properties were calculated and supplied to the Damage Model for the code element of the model.

4.9.1.2.5 Damaged Blade Section Properties

Section properties were computed by program DAMAGE using the API threats described in Section 4.9.1.2.3. Figure 122 shows a printer plot of the damaged OH-58C composite blade. Shown are predicted damage results at the shot line (blade Station 106.0) from impact by an aligned 23mm API projectile. The Damage Model computes and prints this information for each requested cross section. The shot line has been drawn on this

plot to indicate the projectile's path. Note that the vertical scale begins at 1.06 inches. This is because the leading edge of the COMGEOM blade model was set 1 inch from the reference.

The stiffness properties (EI_B for blade beamwise bending and EI_C for blade chordwise bending) are recorded for each cross section within the projectile-damaged area of the blade. These values are then averaged as a function of the blade length between the cross sections for a section of the blade that defines the blade model for the Myklestad and Dynamic Analysis programs. This blade section may or may not be the same length as the section used in the Damage Model. However, a Myklestad section must end at the shot line on the blade. For this model, the Myklestad sections extend from blade Station 95.4 through Station 106.0 and from 106.0 through 116.6. For the portion of the blade section that is beyond the damage, stiffness values derived for the undamaged blade are used in the averaging process. The averaged values derived from the Damage Model program were applied equally to the Myklestad sections bounding the damaged blade's shot line because the blade model was symmetrical. However, there were differences in the undamaged stiffness values predicted by the Damage Model using a symmetrical model, and those determined by a finite stress analysis using a taper in the blade. To account for these differences, the predicted damaged blade stiffness values were altered by the ratio of these differences.

Torsion stiffness was determined using Figure 123, Reference 18. A set of effective torsion stiffnesses (KG) were determined across the Myklestad blade sections on either side of the shot line. These values were averaged with respect to the lengths of these sections to determine the values printed in Table 28.

4.9.1.2.6 Damaged Main Rotor Blade Dynamic and Fatigue Analysis

The values in Table 28 were inserted into the undamaged blade data for the Myklestad and Dynamic Analysis programs to determine blade mode shapes, frequencies, and loads for the damaged blade. The Dynamic Analysis program, C81/SLAMUR, applies helicopter operating conditions and determines whether control limits of the helicopter have been exceeded. If loss of control is predicted, then a warning message is printed. For this problem an operating condition of 100 knots forward flight was used in the analysis.

From time/history plots produced by the Dynamic Analysis program, beamwise and chordwise bending moments were extracted for input into the fatigue analysis program. The values of the bending moments for both cases were almost identical. Therefore, the values listed in Table 29 apply for both cases.

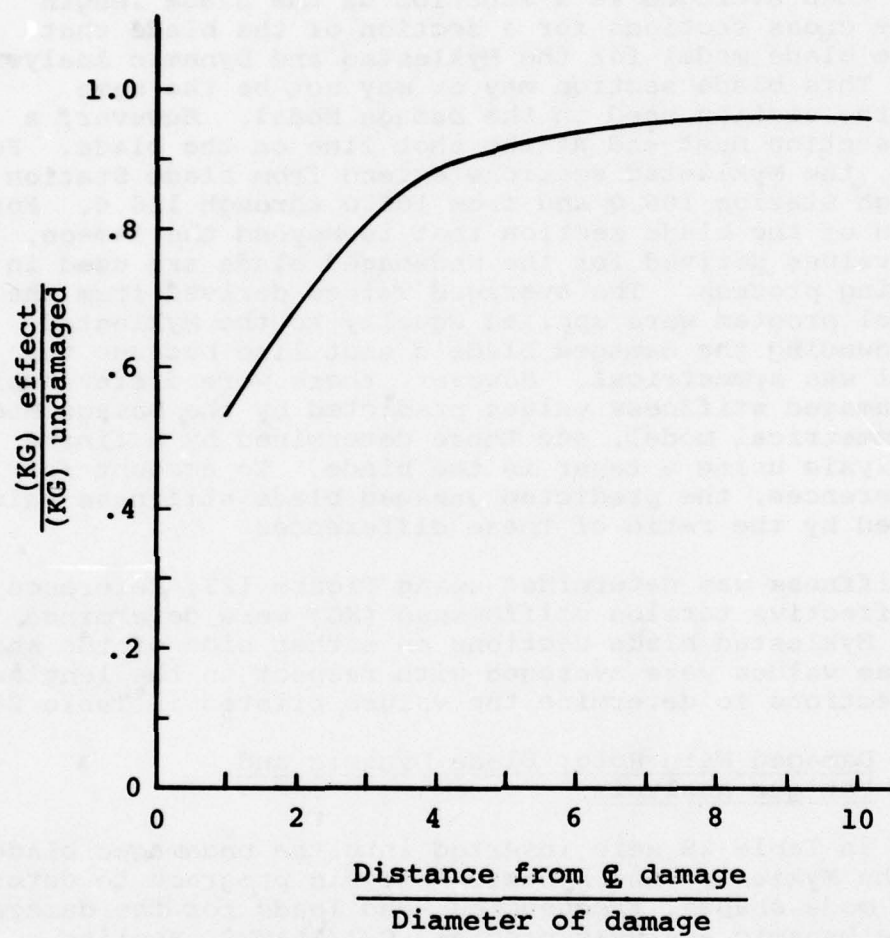


Figure 123. Nondimensional torsional stiffness as a function of distance from the centerline of damage.

TABLE 28. AVERAGE STIFFNESS PROPERTIES OF THE DAMAGED OH-58C
COMPOSITE MAIN ROTOR BLADE

Shot angle (deg)	Projectile (mm API)	Myklestad Section Inboard of Damage Shot Line (Sta. 106.0)				Myklestad Section Outboard of Damage Shot Line (Sta. 106.0)			
		Avg. Beam Stiffness (EI _B x10 ⁻⁶ lb-in. ²)	Avg. Chord Stiffness (EI _C x10 ⁻⁸ lb-in. ²)	Avg. Torsion Stiffness (KGx10 ⁻⁶ lb-in. ²)		Avg. Beam Stiffness (EI _B x10 ⁻⁶ lb-in. ²)	Avg. Chord Stiffness (EI _C x10 ⁻⁸ lb-in. ²)	Avg. Torsion Stiffness (KGx10 ⁻⁶ lb-in. ²)	
45	7.62 (Tumbled)	4.483	2.259	2.88		4.01	1.979	2.43	
45	12.7 (Tumbled)	4.298	2.258	2.72		3.8.45	1.978	2.28	
45	23 (Aligned)	4.419	2.259	2.47		3.952	1.979	2.09	
60	7.62 (Tumbled)	4.488	2.26	2.88		4.014	1.98	2.43	
60	12.7 (Tumbled)	4.286	2.258	2.72		3.834	1.978	2.28	
60	23 (Aligned)	4.407	2.259	2.47		3.943	1.979	2.09	

TABLE 29. RESULTS OF THE DYNAMIC ANALYSIS FOR THE DAMAGED
OH-58C COMPOSITE MAIN ROTOR BLADE*

Projectile (mm API)	Peak Beam Bending Moment (in.-lb)	Corres- ponding Chord Bending Moment (in.-lb)	Peak Chord Bending Moment (in.-lb)	Corres- ponding Beam Bending Moment (in.-lb)	Last Rev Oscillatory Beam Bending Moment (in.-lb)	Last Rev Oscillatory Chord Bending Moment (in.-lb)	Last Rev Steady Beam Bending Moment (in.-lb)	Last Rev Steady Chord Bending Moment (in.-lb)
7.62 (Tumbled)	690	3080	3080	690	690	3080	0	1380
12.7 (Tumbled)	720	2700	3000	700	700	3000	80	1440
23 (Aligned)	710	2880	3050	690	690	3050	218	1560

*Values in this table are applicable for both the 45-degree case and the 60-degree case.

The fatigue analysis program uses these data, along with stiffness properties at the damage shot line, to compute steady state and oscillatory stresses at the damaged section. From this, the blade's residual life is determined.

4.9.2 Ballistic Tests of the OH-58C Composite Main Rotor Blade

In conjunction with the ballistic damage analysis of the OH-58C composite main rotor blade, ballistic tests were performed at BHT on a 24-inch section of this blade having a 13-inch chord. A top view of the undamaged test specimen is shown in Figure 124. Figure 125 shows an end view of this specimen. These tests were not run to demonstrate the survivability of this blade but more to show visual damage that results when API threats impact this blade. This test also demonstrated the penetration capabilities of these types of threats, which aided the analysis of this blade discussed in Section 4.9.1. The test consisted of four shots to the specimen. The first shot was an aligned 23mm API projectile traveling 2000 feet per second. The second shot was a fully tumbled 12.7mm API projectile traveling at 2550 feet per second. The third and fourth shots were an aligned 12.7mm API projectile at 1600 feet per second and a tumbled 7.62mm API projectile at 2550 feet per second, respectively. The conditions for these shots are shown in Table 30.

The shot line for the first round was aligned 38° to the chord line with the bottom of the blade as the entry side. The entry hole was approximately 1.2 inches in diameter and bulged outward, as shown in Figure 126. Edges of the hole are feathered with delaminated fiberglass. Some delamination and cracking of the skin has occurred aft of the entrance hole. Due to the deflection of the projectile by the angle of the blade, the center of the hole was 1.5 inches from the leading edge of the blade. Again, the center of the exit hole is below the shot line, 3.5 inches aft of the leading edge. Fiberglass from the leading-edge spar is delaminated forward to the leading edge and spanwise approximately 3.0 inches on both sides of the hole, as shown in Figures 127 and 128. The fiberglass skin over the afterbody is delaminated and peeled away from the honeycomb for approximately 5.0 inches aft and spanwise approximately 3.0 inches either side of exit hole. The exit area is bulged outward.

The chord of the blade for shot number two was oriented 45° to the shot line with the bottom of the blade facing the weapon. The entrance hole was approximately 2.7 inches long x .5 inch wide as shown on the left in Figure 129. The outer skin wrap is cut out in the shape of the projectile. The uniaxial leading-edge spar underneath the skin has only a chordwise crack line

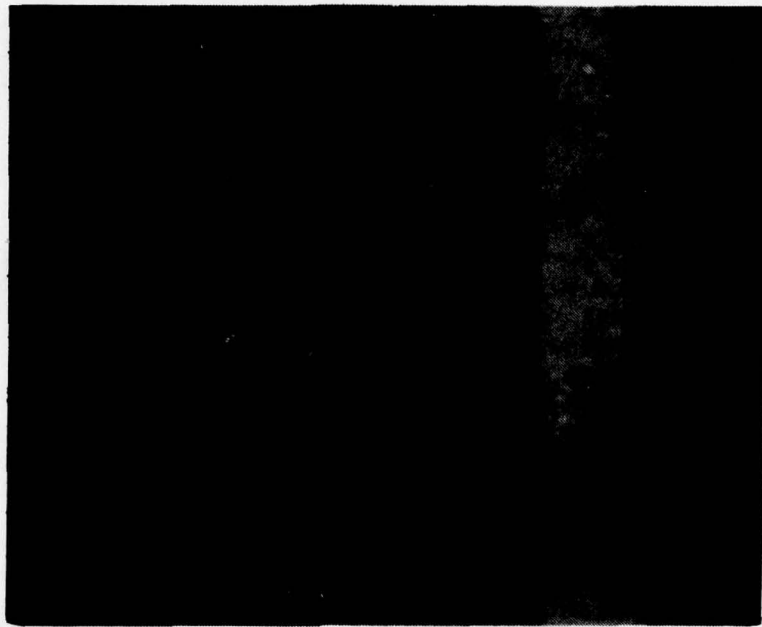


Figure 124. Top view of the undamaged OH-58C composite main rotor blade test specimen.



Figure 125. End view of the undamaged OH-58C composite main rotor blade test specimen.

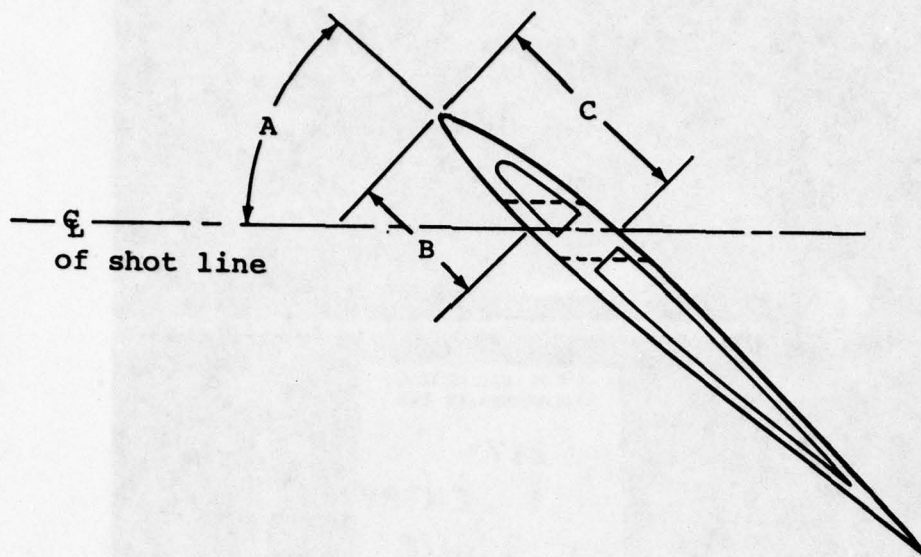


TABLE 30. BALLISTIC TEST CONDITIONS FOR THE OH-58C COMPOSITE MAIN ROTOR BLADE

Shot Number	Velocity (fps)	A (deg)	Orientation	B (in.)	C (in.)	Threat (mm, API)
1	2000	38	Aligned	1.25	3.50	23
2	2550	45	Tumbled	2.37	4.50	12.7
3	1600	90	Aligned	1.00	1.00	12.7
4	2550	90	Tumbled	1.30	-	7.62

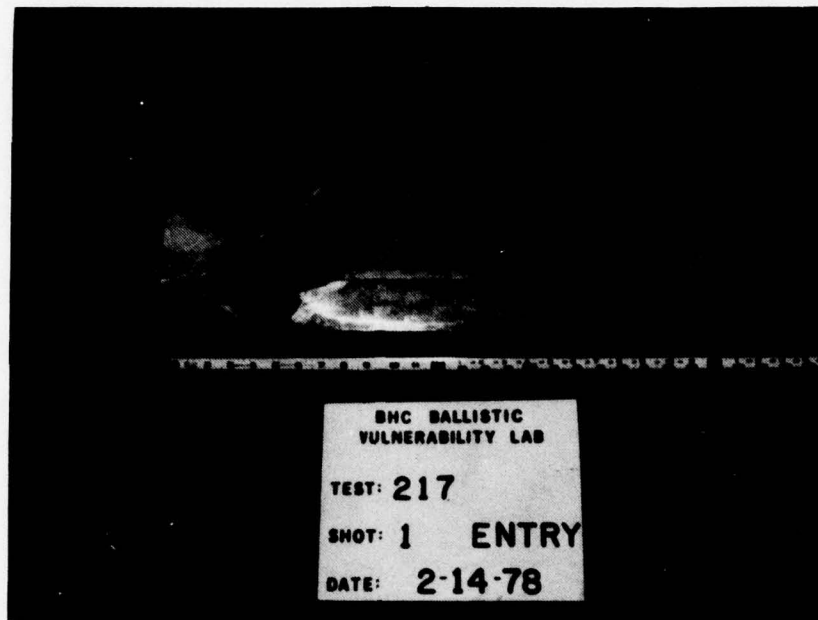


Figure 126. Bottom view of the OH-58C composite main rotor blade test specimen showing projectile entrance.

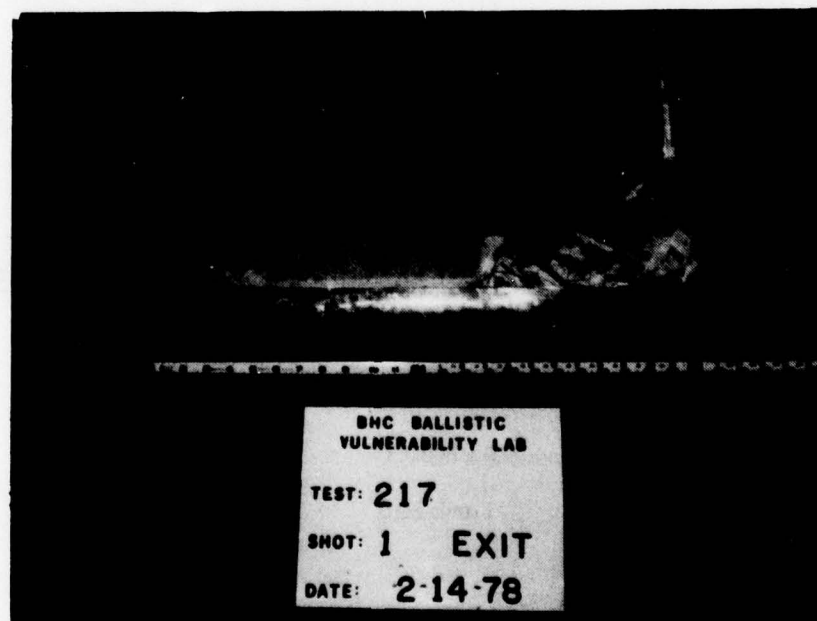


Figure 127. Top view of the OH-58C composite main rotor blade test specimen showing projectile exit.

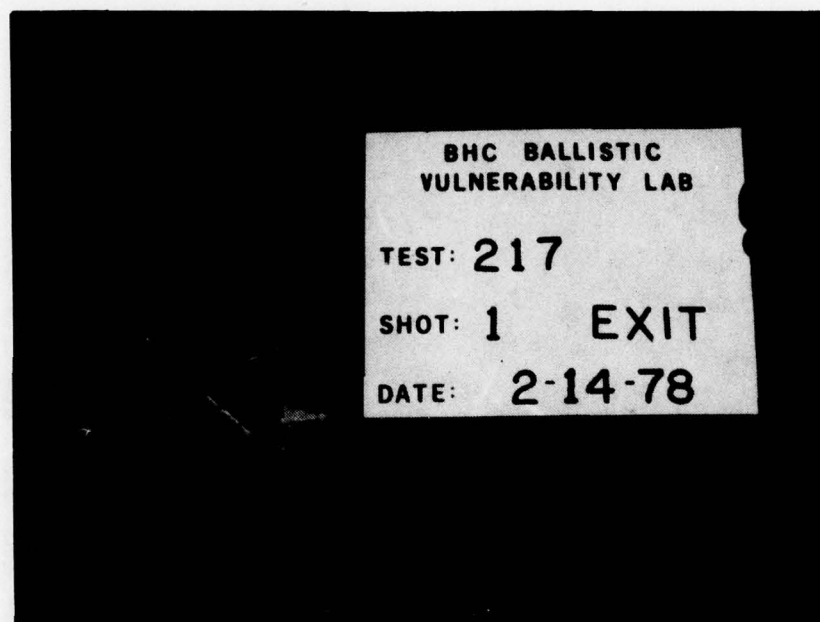


Figure 128. End view of the OH-58C composite main rotor blade test specimen showing 23mm API projectile damage.

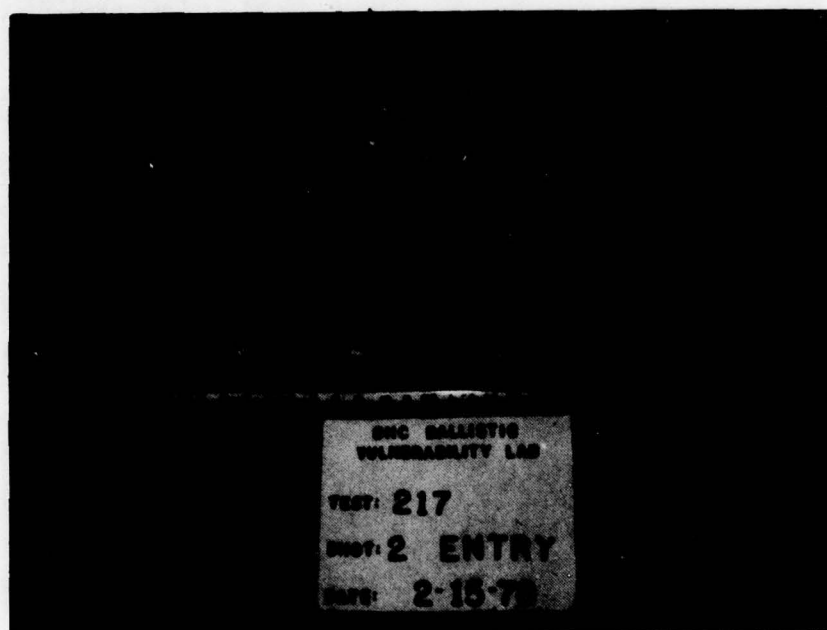


Figure 129. Bottom view of the OH-58C composite main rotor blade test specimen showing entrance of shots one (right) and two (left).

with delaminated edges. Outer skin delaminations and cracking occurred in an approximate 4.0-inch radius from the center of impact extending spanwise and aft. The projectile exited approximately 4.5 inches aft of the leading edge as shown on the left in Figure 130. An area with a 4.5-inch radius from the center of the exit hole is delaminated and severely bulged outward. Delaminations in the leading-edge spar extend to the leading edge as seen in Figure 131.

The shot line for the third shot was aligned 90° to the blade. The entrance hole was approximately .6 inch in diameter located approximately 1.0 inch aft of the leading edge. This shot is shown second from the left in Figure 132. The center of the exit hole was located on the shot line and has a 2.0-inch diameter area that is severely bulged outward. Delaminations radiate from the exit hole spanwise and aftward for an approximate 4.0-inch diameter as seen in Figure 133 near the 22-inch mark on the scale.

The shot line for the fourth shot was also aligned 90° to the chordline of the blade and is located 1.3 inches aft of the leading edge (second from the right in Figure 132). The entrance hole was approximately 1.5 inches long x .3 inch wide and is severely bulged outward. A 30-inch diameter area centered about the entry hole is bulged outward with delaminations around the edges of the entry hole. The projectile did not exit. The exit side is bulged slightly with two 2.0-inch long cracks visible under the leading-edge abrasion strip (Figure 133).

4.9.3 Results

The OH-58C composite main rotor blade was analyzed for ballistic damage survivability using the Helicopter Survivability Model. This blade was analyzed at blade Station 106 (50% R) for a helicopter forward flight speed of 100 knots. This flight condition imposes high stress on the blade at this location.

The threats used in the analysis were the 7.62mm API, 12.7mm API, and the 23mm API projectiles. The 7.62 and 12.7mm projectiles were fully tumbled upon impact with the blade while the 23mm API projectile was 2000 feet per second. Each of the 7.62mm and 12.7mm API projectiles was 2500 feet per second; the 23mm API projectile, 2000 feet per second. Each of the three threats were modeled to enter the blade at blade Station 106.0, approximately 3-1/2 inches aft of the leading edge. The projectiles' directions were toward the trailing edge of the rotor blade at angles of 45° to 60° with respect to the blade's chord. In all, six shots were analyzed, three for each angle.

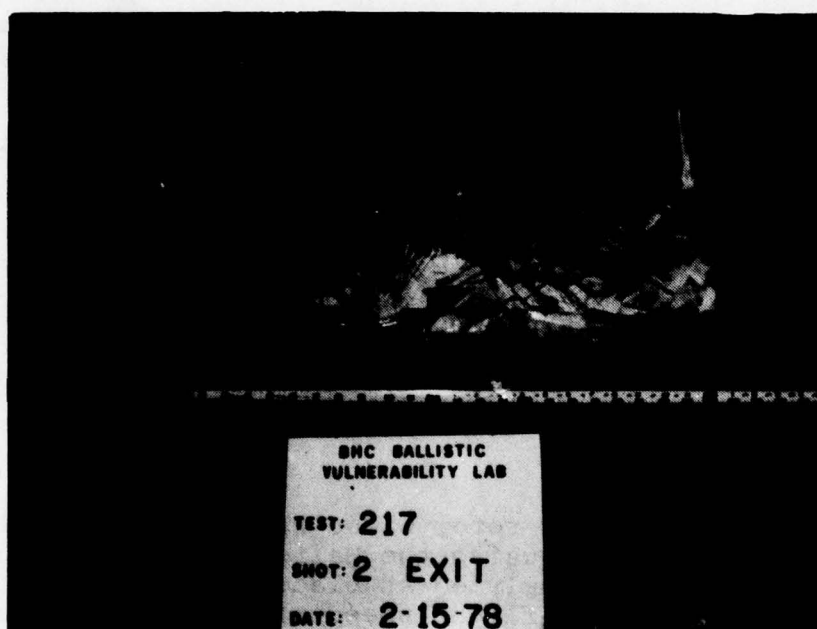


Figure 130. Top view of the OH-58C composite main rotor blade test specimen showing exit of shots one (right) and two (left).

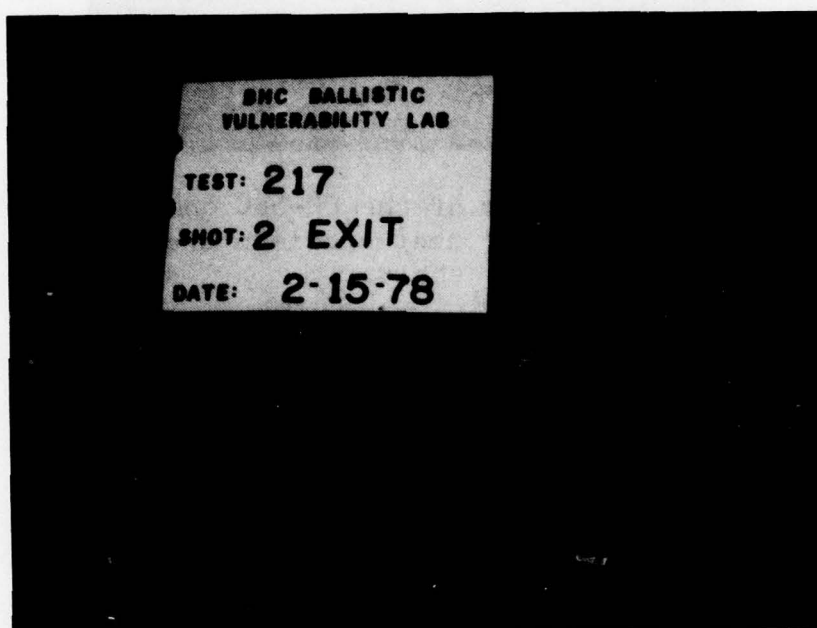


Figure 131. End view of the OH-58C composite main rotor blade test specimen showing 12.7mm API projectile damage.

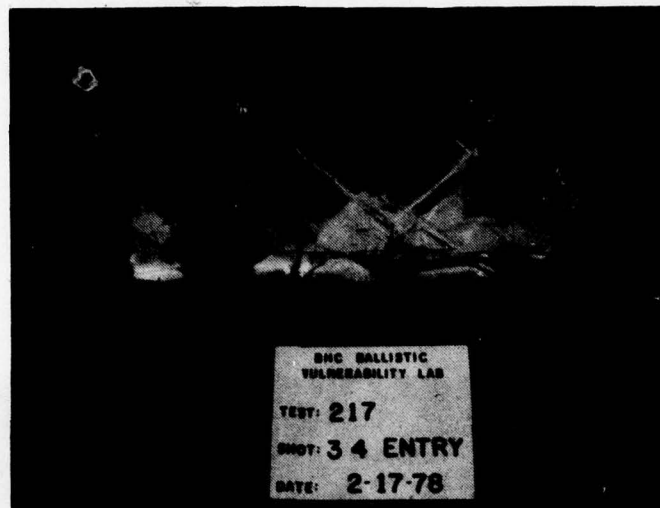


Figure 132. Bottom view of the OH-58C composite main rotor blade test specimen showing entrance of all four shots.

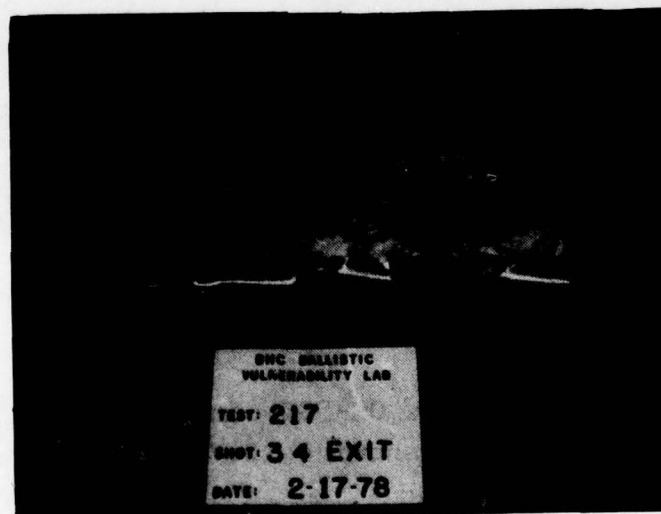


Figure 133. Top view of the OH-58C composite main rotor blade test specimen showing exit of all four shots.

The dynamic analysis program, C81/SLAMUR, predicted no loss of helicopter control and no excessive forces acting on the pilot as a result of main rotor impact with these threats. This was expected because there were no large changes in the oscillatory and steady state bending moments due to projectile damage. This was true for all six shots analyzed.

Table 31 shows damaged blade stiffness values as predicted by the Helicopter Survivability Model at the center of damage, Station 106.0. These values reflect maximum changes from the blade's undamaged stiffness values at this location. Because of low changes in bending moments, the local stiffness value changes governed the blade life as a result of ballistic damage from these projectiles. The greatest change in blade stiffness was in beam bending (EI_B). Values as high as a 66-percent change from the undamaged blade values were predicted. However, the chord stiffness was hardly affected. A maximum change of 2.4 percent was realized from any of the six conditions.

The largest ballistic damage to the rotor blade was from impact with the 12.7mm API projectile fully tumbled. This was followed by damage from the 7.62mm API and the 23mm API projectile, in that order. This pattern held true for all three stiffness values as recorded in Table 31. When considering the projectile cutting lengths, this was expected. The tumbled 12.7mm API projectile had the largest cutting length, 2.7 inches with respect to the blade's chord.

The 7.62mm API showed greater damage in case one (45° shot) than in case two (60° shot). The reverse was true for both the 12.7mm API and 23mm API projectiles. They showed greater damage in case two than in case one. However, for each of these threats, the values between the two cases were too close to predict a definite pattern of damage.

For all six shots, there was no static failure of the rotor blade. A predicted blade life that exceeded the following post-impact goals was demonstrated: 10-hour life after impact by a tumbled 7.62mm API projectile, 5 hours for a tumbled 12.7mm API projectile, and 30 minutes for an aligned 23mm API projectile.

Ballistic test shots on a specimen of the OH-58C composite main rotor blade showed that the tumbled 12.7mm API projectile impacting at 2500 feet per second, and an aligned 23mm API projectile impacting at 2000 feet per second had enough energy to completely penetrate the spar of the rotor blade. The tumbled 7.62mm API at 2500 feet per second, although it did not completely penetrate the blade, did go far enough to effectively do the same damage to the blade as if it had passed

TABLE 31. PREDICTED STIFFNESS VALUES FOR THE DAMAGED OH-58C
COMPOSITE MAIN ROTOR BLADE

Shot Angle (deg)	Projectile (mm API)	Axial Stiffness (EAx10 ⁻⁷ lb)	Percent Reduction *	Beam Stiffness (EI x10 ⁻⁶ lb-in. ²)	Percent Reduction *	Chord Stiffness (EI x10 ⁻⁸ lb-in.)	Percent Reduction *
45	7.62 (Tumbled)	1.402	29.9	2.274	44.4	1.980	1.5
45	12.7 (Tumbled)	1.100	45.0	1.426	65.1	1.962	2.4
45	23 (Aligned)	1.518	24.1	2.680	34.4	1.987	1.2
60	7.62 (Tumbled)	1.408	29.0	2.336	42.8	1.997	0.7
60	12.7 (Tumbled)	1.037	48.2	1.380	66.2	1.963	2.4
60	23 (Aligned)	1.482	25.9	2.601	36.4	2.001	0.5

*Percent reduction is with respect to predicted stiffness values for the undamaged OH-58C fiberglass blade.

completely through. This projectile left the exit surface (top surface of the blade) bulged enough to destroy its structural integrity.

4.9.4 Conclusion

For the six cases analyzed with the Helicopter Survivability Model, the OH-58C composite main rotor blade exceeded the post-impact goals. It is recognized that hits nearer the leading edge of this blade and along the chordline, will, in general, cause more severe damage and, in some cases, result in blade failure. This is largely true because of the tumbled orientation of the 7.62 and 12.7mm API projectiles and the size and kinetic energy of the 23mm API. However, from operational considerations, it is considered highly improbable that the blade would be struck with a fully tumbled 7.62 or 12.7mm projectile. Consequently, it is felt that the conditions for ballistic vulnerability design goals are too stringent to be consistent with the other design priorities set. Although extensive vulnerability analyses were not conducted to compare the present metal blade and the proposed composite blade, it is felt that the new blade will, in general, have smaller vulnerable areas for comparable threats.

4.10 COST AND EFFECTIVENESS

4.10.1 Discussion

Design of the improved blade for the OH-58C was guided by the Army priorities that place life-cycle cost and performance in first and second priority as attributes to be improved relative to the standard blade. Life-cycle cost and effectiveness analyses have been conducted to illustrate the benefits of the improved blade.

Within the ground rules provided by the Army for this study, continued operation of the standard blade has a lower life-cycle cost than operation with the improved blade. However, with changes in assumptions for fleet life, operating rates, and reduction of rate tooling, the improved blade provides a life-cycle cost advantage. The effectiveness benefits of the improved blade include a 24-percent improvement in payload, reduced vulnerability to ballistic damage, and reduced radar cross section.

4.10.2 Life-Cycle Cost

4.10.2.1 Ground Rules and Methods

The life-cycle cost analysis was conducted in accordance with ground rules provided by the Army unless otherwise indicated

herein. These ground rules are shown in Table 32. Reliability and maintainability values derived during the study and reported in Section 4.6 were used in the life-cycle cost analysis. Factors and values used are shown in Table 33. Reliability analysis conducted during this study estimated an MTBR of 422.5 flight hours for the standard blade and this value was used in the cost analysis. Also, the estimated value of 1199 flight hours for the MTBR of the improved blade was used in the study because none of the improved blades reach their life limit of 3600 flight hours in the program life cycle. Field maintenance labor estimates shown in Table 33 were derived in the maintainability study. The basis for the standard blade labor estimates are U. S. Navy 3M data for the TH-57. Unscheduled and scheduled maintenances were adjusted by factors of 2.25 and 1.5 respectively to depict Army operation. For the improved blade, only unscheduled maintenance was applied because none of the blades reach their life limit in the program life cycle. Additional assumptions were necessary and are shown in Table 34.

The cost analysis method consists of identifying the main rotor blade's peculiar life-cycle cost elements and determining the appropriate values for those cost elements. The general cost model used in the study is shown in Table 35. Recurring initial investment is not shown as blade costs are included under the Operation and Support cost element.

For the Baseline Case, i.e., continue to operate with standard blades, there are three main-rotor-blade peculiar life-cycle cost elements, all of which are operation and support cases. These cost elements are as follows:

- Cost of new blades to replace those blades that were scrapped.
- Cost of field maintenance labor.
- Cost of blades repaired at depot.

The life-cycle cost for the Baseline Case is the sum of the above cost elements.

TABLE 32. LIFE-CYCLE COST ANALYSIS GROUND RULES

Fleet Size	- 2432 OH-58 Helicopters
Operating Period	- 1 January 1981 through 1992
Flying Rate	- 12.8 flight hours per month per helicopter
MTBR	- 475 flight hours between removals of standard blades
Standard Blades Disposition	- 30 percent of blades removed from the helicopter are scrapped and the remaining 70 percent are sent to depot for repairs.
Standard Blade Repair Cost	- All costs associated with depot repair come to a cost of \$1080 per blade.
Dollar Purchasing Power	- FY 1976 dollars are to be used.
Blade Production	- Quantity of 3000 blades at a rate of 100 blades per month.

TABLE 33. RELIABILITY AND MAINTAINABILITY VALUES

		<u>Mean Time Between Blade Replacement - Flight Hours</u>	
<u>Blade Replacements</u>		<u>Standard</u>	<u>Improved</u>
Blade Replacement MTBR			
Due to inherent or induced damage		456	1199
Due to all causes including life limit		422.5	932
		<u>Maintenance Manhours Per Flight Hour</u>	
<u>Field Maintenance Labor</u>		<u>Standard</u>	<u>Improved</u>
Unscheduled Maintenance		.011912	.009144
Scheduled Maintenance		<u>.003125</u>	<u>.002084</u>
		.015307	.011228
<u>Improved Blade Disposition</u>		<u>Percent of Removed Blades</u>	
Scrapped		15	
Repaired at AVUM		15	
Repaired at AVIM		68	
Repaired at Depot		2	

TABLE 34. ASSUMPTIONS

1. The OH-58 fleet size is diminished to account for attrition at a rate of 6.5 aircraft lost per 100,000 flight hours. This is in accordance with the Army Force Cost Planning Handbook. It is estimated that the fleet consisted of 2432 aircraft as of 1 January 1977.
2. For the Baseline Case, the OH-58 fleet continues to use the standard blade.
3. For the Alternate Case, improved blades are installed starting in 1981. As the fleet program life cycle proceeds, the portion of the fleet equipped with improved blades continues to increase.
4. The number of improved blade spares can be quite low because of the small fraction repaired at depot. A value of 5 percent of installed blades was used to account for initial spares.
5. Costs of \$20 per manhour and \$1500 per blade were used for field maintenance and depot repair.
6. Spare standard blades at the beginning of the accounting period are 30 percent of installed blades.

TABLE 35. GENERAL COST MODEL

<u>Cost Element</u>	<u>Estimate Basis</u>
1. Research, Development, Test, and Evaluation	BHT Estimating Process
2. Nonrecurring Initial Investment	BHT Estimating Process
3. Operation and Support Cost	Reliability and Maintainability Analysis. BHT standard blade price and improved blade price estimates and ground rules and assumptions.

For the Alternate Case there are additional cost elements to account for development qualification and tooling. Cost elements for the Alternate Case are as follows:

- Research, development, test, and evaluation.
- Nonrecurring initial investment; i.e., tooling.
- Cost of new blades to initially install on aircraft.
- Cost of new blades to stock spares inventory.
- Cost of new blades to replace improved blades that are scrapped.
- Cost of field maintenance labor.
- Cost of blade repair at depot.

The life-cycle cost for the Alternate Case; i.e., start equipping the fleet with improved blades 1 January 1981, is the sum of the above cost elements.

There are additional cost factors that can be used to discriminate between the standard and the improved blade. These include fuel cost savings due to improved performance, improved payload capability, and improved survivability. These factors, while not readily quantifiable in terms of life-cycle cost, all favor the improved blade over the standard blade.

4.10.2.2 Development, Tooling, and Unit Costs

The Bell Helicopter Textron formal cost estimating process was used to derive development, tooling, and unit costs required in the life-cycle cost analysis. The program schedules shown in Figures 134 and 135 are the program basis for the cost estimates. Table 36 contains the results of this cost estimate. Values shown are based upon FY 1976 dollars, accounting policy, and labor rates, and in BHT terminology are prices in that they include fees. Additional cost-related data requested by the Army are shown in Table 37. Dollar values shown in Table 37 are costs.

4.10.2.3 Life-Cycle Cost Comparison

Life-cycle cost accounting is started in 1981, the first year that there is any difference in operation and support cost between the baseline and alternate case, and is continued through 1992. Several policies were considered for phasing the improved blades into the fleet. These policies are as follows:

(For Planning Use Only)

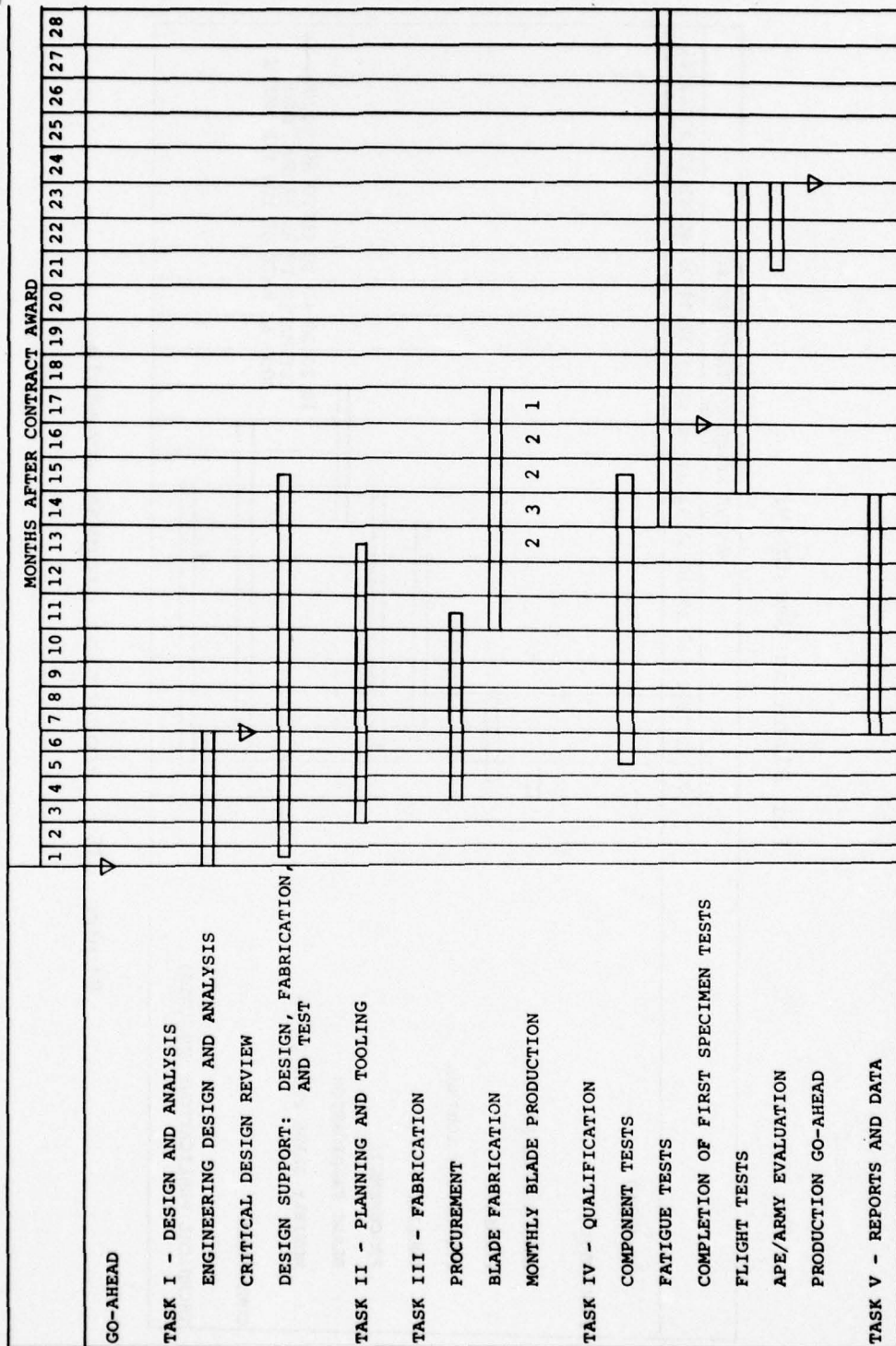


Figure 134. Development program schedule.

(For Planning Use Only)

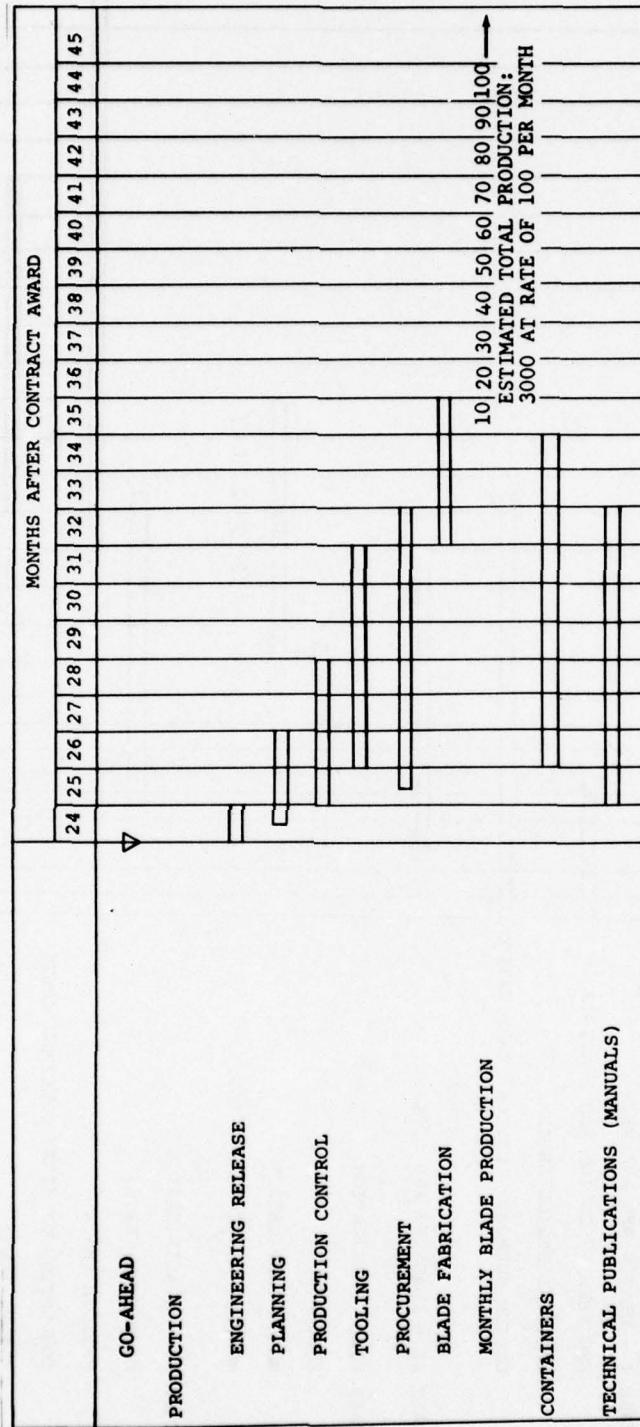


Figure 135. Production program schedule.

TABLE 36. DEVELOPMENT, TOOLING, AND UNIT
COST ESTIMATES (1976 Dollars)

Development Program	\$ 3,258,000
Tooling for 15 Blade per Month	504,611
Tooling for 100 Blades per Month	2,097,675
Improved Blade Unit Price	3,420
Standard Blade Unit Price	2,800

TABLE 37. SUPPORTING DATA

	<u>Per Blade</u>
Manufacturing Direct Labor	54.15 manhours
Spar cap assemblies	6.10 manhours
Spar	10.80 manhours
Lower skin/core	9.00 manhours
Final assembly	21.00 manhours
Miscellaneous labor	4.45 manhours
Material Cost	\$ 1,188
Manufacturing Direct Labor Cost	\$ 1,921

Policy I - Whenever standard blades are removed and scrapped, they are replaced on the aircraft by improved blades. Standard blades not scrapped are either returned to spares or sent to depot for repair.

Policy II - Whenever standard blades are removed and scrapped, they may be replaced on the aircraft by either standard blades or improved blades. This is done in such a manner as to reduce the standard blade total inventory so that the ratio of spare blades to installed blades remains constant.

Policy III - Equip the entire fleet in four years

Policy III does not take advantage of inherited assets and was discarded. Policies I and II take advantage of inherited assets with Policy II having the potential for minimum life-cycle costs. The viability of Policy II is dependent upon the initial conditions of the standard blade inventory as to number of spares and inventory blades' remaining lives. Determination of these factors was beyond the scope of this study. Both Policies I and II were applied and the life-cycle comparison of the baseline case and the Alternate Case are shown in Table 38. The basic comparison refers to Table 32 ground rules excepting blade MTBR, Table 33 reliability and maintainability values, Table 34 assumptions, and Table 36 cost estimates. Policy II provides the lowest life-cycle cost. The cost of Policy III is \$24.6 million which is 21 percent higher than Policy I and 48 percent higher than the baseline case. However, for both policies, the life-cycle cost of the Alternate Case is greater than that of the Baseline Case.

Since other assumptions that would tend to favor the Alternate Case may be acceptable, some of these were identified and evaluated for Policy I. These assumptions are as follows:

- Operate the OH-58 fleet at 20 flight hours per month as indicated in the U. S. Army Force Cost Planning Handbook instead of 12.8 FH/Mo/AC.
- Extend the OH-58 program life through 1995 instead of 1992.
- Procure tooling for a rate of 30 blades per month. This rate is adequate to meet the phase-in policies investigated.

Altering the Basic Comparison only by the above stated assumptions, the life-cycle costs of the Baseline Case and the Alternate Case were derived. Results are shown in Table 39. The Alternate Case provides a lower life-cycle cost.

TABLE 38. LIFE-CYCLE COST BASIC COMPARISON¹
(Millions of Dollars)

COST ELEMENTS	POLICY I		POLICY II	
	Baseline Case	Composite Blade	Baseline Case	Composite Blade
RDT&E	0	3.258	0	3.258
Nonrecurring Initial Investment	0	2.098	0	2.098
Operations and Support				
Initial Installation of Blades	0	7.542	0	5.721
Initial Spares	0	.373	0	.286
Replacement Spares	8.107	.431	6.248	.393
Field Maintenance Labor	1.248	1.124	1.236	1.122
Depot Repair	<u>7.296</u>	<u>5.52</u>	<u>7.222</u>	<u>5.600</u>
LIFE-CYCLE COST TOTAL	16.651	20.346	14.706	18.478

1. The OH-58 fleet flies 4.0 million flight hours. In the Alternate Case 25 and 75 percent of this time are flown with improved and standard blades, respectively.

TABLE 39. LIFE-CYCLE COST COMPARISON VARIANT¹
(Millions of Dollars)

COST ELEMENTS	POLICY I	
	Baseline Case	Alternate Case
RD&E	0	3.258
Nonrecurring Initial Investment	0	0.788
Operations and Support		
Initial Installation of Blades	0	10.602
Initial Spares	0	.534
Replacement Spares	14.678	1.293
Field Maintenance Labor	2.260	1.890
Depot Repair	13.200	7.890
	30.138	26.255

1. The OH-58 fleet flies 7.3 million flight hours. In the Alternate Case, 41 and 59 percent of the time are flown with improved and standard blades, respectively.

4.10.3 Effectiveness Comparison

The improved blade's performance provides several significant effectiveness benefits relative to the standard blade. The reduction in power required can be interpreted in several ways to illustrate the effectiveness benefits. When operating HOGE at 4000 feet, 95°F conditions, there is a net increase of 24 percent in payload. For missions where the payload is divisible and maximum payload is carried, this performance improvement is equivalent to a 24-percent increase in the fleet size. Another important benefit is the increased agility. When operating HOGE in 4000 feet, 95°F conditions at a gross weight of 3200 pounds, the vertical rate of climb (VROC) increases from 100 fpm for the standard blade to 400 fpm for the improved blade. This improved VROC will improve the aircraft's survivability and safety for combat NOE conditions. The improved blade provides survivability benefits by two other important means; i.e., reduced radar cross section and reduced ballistic vulnerability.

5. CONCLUSIONS

The OH-58 main rotor blade designed during this preliminary design investigation will have significant improvements over the production blade. It will have better performance throughout the flight regime. A 5- to 6-percent improvement in hover performance is expected as well as a 4-knot increase in V_H at maximum continuous power. This will enhance the mission capability of the OH-58C/A helicopter.

The composite blade will have improved damage tolerance and higher survivability. This tolerance is inherent in the composite material's fatigue resistance and fracture toughness and is the result of the failsafe blade construction.

The effectiveness of the Interim Scout mission will be improved by the composite blade's reduced detectability. Both radar signature and accurate emission are reduced significantly compared to the present blade.

Electrothermal deicing and low radar reflectivity of the blade are conflicting requirements. However, either the deicing blanket or the radar-absorbent material can be provided during fabrication of the blade spar using the same tooling.

The improved blade will have better dynamic characteristics than the production blade. Airframe vibrations will be reduced, thus lowering induced and inherent failure rates.

The blade will be more easily repaired in the field. Repair procedures have been established to repair punctures in the skin and damage to the spar and trailing edge in noncritical areas of the blade.

The improved composite blade offers a longer fatigue life. Preliminary analysis indicates an unlimited life due to fatigue, making it possible for on-condition replacement or repair.

The life-cycle cost analysis showed no savings for the composite blade for the specified operating period and utilization rate. However, increasing these parameters would result in a life-cycle cost savings for the composite blade.

6. RECOMMENDATIONS

The composite main rotor blade developed during this preliminary design investigation meets or exceeds nearly all of the design goals and objectives of the program. The blade is a major improvement over the existing metal blade, having realistic expectations of increased performance, structural capability, survivability, reliability and maintainability, and reduced life-cycle costs.

It is recommended that the OH-58 composite main rotor blade program continue into the development phase. The program should proceed to detail design, fabrication of prototypes, qualification, and production of the improved blades so that they can be introduced into the Army inventory as soon as possible.

REFERENCES

1. Van Gaasbeek, J. R., C8176 ROTORCRAFT FLIGHT SIMULATION WITH COUPLED ROTOR AEROELASTIC STABILITY ANALYSIS, Report 599-326-900, Bell Helicopter Textron, Fort Worth, Texas, May 1977.
2. Popelka, D., MAIN ROTOR FLAPPING CLEARANCE ANALYSIS, Report 299-099-873, Bell Helicopter Textron, Fort Worth, Texas, February 1977.
3. Schramm, M., DEVELOPMENT, CAPABILITIES, AND LIMITATIONS OF REAL TIME HYBRID C81, Report 299-099-535, Bell Helicopter Textron, Fort Worth, February 1972.
4. Military Specification MIL-H-8501A(1), GENERAL REQUIREMENTS FOR HELICOPTER FLYING AND GROUND HANDLING QUALITIES, Department of Defense, Washington, D. C., 3 April 1963.
5. Jordan, G. L., STRUCTURAL DESIGN CRITERIA FOR 206A-1/OH-58A, Report 206-099-200, Bell Helicopter Company, Fort Worth, Texas, August 1968.
6. Eaton, H., et al., CONTROL SYSTEMS STRUCTURAL ANALYSIS, February 1969.
7. FATIGUE DESIGN HANDBOOK, Report 299-099-076, Bell Helicopter Company, Fort Worth, Texas, April 1972.
8. Boller, K. H., FATIGUE CHARACTERISTICS OF TWO NEW PLASTIC LAMINATES, REINFORCED WITH UNWOVEN S-GLASS FIBERS, UNDER CYCLIC AXIAL OR SHEAR LOADING, AFML Technical Report 66-54, U. S. Air Force Materials Laboratory, Wright-Patterson AFB, Ohio, May 1966.
9. Cutler, M. G. and Pickney, R. L., STATIC AND FATIGUE TEST PROPERTIES FOR WOVEN AND NONWOVEN S-GLASS FIBERS, Boeing Vertol Company; USAAVLABS Technical Report 69-9, U. S. Army Aviation Material Laboratories, Fort Eustis, Virginia, April 1969, AD 688971.
10. Hoffstedt, D. J., ADVANCED GEOMETRY, GLASS-FIBER-REINFORCED PLASTIC ROTOR BLADE TEST PROGRAM, Boeing Vertol Company; USAAMRDL Technical Report 71-42, Eustis Directorate, U. S. Army Air Mobility Research and Development Laboratory, Fort Eustis, Virginia, September 1971.

REFERENCES (Continued)

11. Brogdon, V. H., FATIGUE ALLOWABLES FOR SP-250-SF1 S-GLASS PREPREG LAMINATES USING NORMAL DISTRIBUTION, Memo 81-VHB: gs-8147, Bell Helicopter Textron, Fort Worth, Texas, 9 December 1976.
12. The Army Maintenance Management System (TAMMS), Technical Manual 38-750, Headquarters, Department of the Army, Washington, D. C., 21 November 1972, with Change No. 1, 1 April 1974.
13. MAJOR ITEM REMOVAL FREQUENCY, OH-58A FLEET, A RELIABILITY AND MAINTAINABILITY MANAGEMENT IMPROVEMENT TECHNIQUES REPORT, Period Covered October 1, 1969 through May 31, 1974, Systems Engineering Directorate, U. S. Army Aviation Systems Command, St. Louis, Missouri.
14. Carr, P. V., and Hensley, O. L., UH-1 AND AH-1 HELICOPTERS MAIN ROTOR BLADE FAILURE AND SCRAP RATE DATA ANALYSIS, Bell Helicopter Company; USAAVLABS Technical Report 71-9, Eustis Directorate, U. S. Army Air Mobility Research and Development Laboratory, Fort Eustis, Virginia, January 1971, AD 881132L.
15. Kaplan, E. L. and Meier, P., NONPARAMETRIC ESTIMATION FROM INCOMPLETE OBSERVATIONS, American Statistical Association Journal, June 1958, pp. 456-480.
16. Bazovsky, Igor. RELIABILITY: THEORY AND PRACTICE, Englewood Cliffs, New Jersey, Prentice-Hall, Inc., 1961.
17. Herd, W., ESTIMATION OF RELIABILITY FROM INCOMPLETE DATA, Sixth Symposium on Reliability and Quality Control, page 206, 1960.
18. Head, Robert E., EROSION FOR THE AH-1G LOW RADAR CROSS-SECTION MAIN ROTOR BLADE, VOLUME I - SAND AND RAIN EROSION EVALUATION, Hughes Helicopter, Division of Summa Corporation; USAAMRDL Technical Report 76-40A, Eustis Directorate, U. S. Army Air Mobility Research and Development Laboratory, Fort Eustis, Virginia, January 1977, AD A035961.
19. Military Specification, MIL-E-38453A, ENVIRONMENT CONTROL, ENVIRONMENTAL PROTECTION, AND ENGINE BLEED AIR SYSTEMS, AIRCRAFT AND AIRCRAFT-LAUNCHED MISSILES, GENERAL SPECIFICATION FOR, Department of Defense, Washington, D. C., 2 December 1971.

REFERENCES (Concluded)

20. Zinburg, H., ROTOR BLADE DYNAMIC RESPONSE AND BALLISTIC DAMAGE SURVIVABILITY, TASKS B AND C - DEVELOPMENT AND USE OF HELICOPTER SURVIVABILITY MODEL, Report 699-099-054, Bell Helicopter Textron, Fort Worth, Texas, June 1977.
21. Bain, L. W., Jr., and Reisinger, M. J., THE GIFT CODE USER MANUAL; VOLUME 1. INTRODUCTION AND INPUT REQUIREMENTS, USABRL Report No. 1802, U. S. Army Ballistic Research Laboratories, Aberdeen Proving Ground, Maryland, July 1975.
22. Van Gaasbeek, J. R., ROTORCRAFT FLIGHT SIMULATION WITH COUPLED ROTOR AEROELASTIC STABILITY ANALYSIS - VOLUME II, USER'S MANUAL, Bell Helicopter Textron; USAAMRDL Technical Report 76-41B, U. S. Army Air Mobility Research and Development Laboratory, Fort Eustis, Virginia, May 1977, AD A042908.

APPENDIX A

PERFORMANCE TRADE-OFF ANALYSIS

This section details the methodology and design rationale used for the aerodynamic concept selection of the improved OH-58C/A main rotor blade.

A.1 PERFORMANCE IMPROVEMENT GOALS

A primary objective for the improved main rotor blade is performance enhancement through the use of advanced aerodynamic technology. To guide the selection of configuration parameters for the improved blade, the following goals for hover and forward flight were established:

Hover. A design goal of a 6-percent reduction in shaft horsepower required to hover out of ground effect at 4000 feet, 95°F, at the OH-58C gross weight of 3200 pounds was established. Hover improvement was considered the primary performance goal.

Forward Flight. It was established that forward flight performance could have no degradation.

Improvements to forward flight performance were, therefore, not explicitly pursued. However, the design approach chosen to be used in hover generally complements forward flight. Design compromise between the two flight regimes was thus minimized.

As a further constraint on these goals, it was established that maneuver and autorotational performance could not be degraded. In addition, an important consideration was that control rigging and blade retention interface with the existing aircraft were not to be changed.

A.2 METHODS OF ANALYSIS

A.2.1 Incremental Performance Approach

The state of the art of performance methodology is such that overall performance estimates vary substantially, depending on the analysis used. To arrive at the most accurate predictions possible for the improved blade, and thus minimize risk, calculations of absolute level of performance were not relied upon. Instead, calculated incremental benefits of the improved blade with respect to the current blade configuration were added to the measured baseline performance of the OH-58C/A with standard blades. The potential error in the performance estimates is thus limited to the calculated performance delta.

Also, since performance analyses rely on experimental two-dimensional airfoil data, an additional range of predicted performance is possible because different wind tunnels can produce substantially different characteristics for the same profile. The delta approach minimizes this problem. Estimates of performance benefit deltas from airfoils, based on data from the same wind tunnel test facility, are considered reasonably accurate. Even though the measured two-dimensional airfoil characteristics may not be 100 percent accurate, higher confidence is placed in the relative characteristics of profiles tested in the same facility.

All calculated baseline performance characteristics were established for the OH-58C/A rotor (the baseline rotor is defined in Contract DAAJ02-77-C-0073) using government-furnished NACA 0012 airfoil data. The NACA 0012 data was obtained from the NASA Langley 6-inch by 28-inch transonic tunnel. The data is that of the smooth airfoil reported in NASA TMX-73990. Incremental performance benefits with the improved blade were calculated with respect to this baseline.

A.2.2 Computational Methods

Performance calculations were made in hover with the BHT Lifting Surface Hover Analysis, and in forward flight with the BHT Rotor Aerodynamic Characteristic Program. The BHT Lifting Surface Hover Analysis represents the technology base for evaluation of aerodynamic concepts for advanced configuration rotor blades. The analysis was developed over the past several years at BHT through a balanced approach, with analysis guided by detailed experimental study of scale model rotor performance and wake structure. The major technical features of this analysis now include:

- Lifting surface blade representation.
- Introduction of section aerodynamic characteristics through circulation response tailoring.
- Prescribed wake model extended from an experimental data base through circulation coupling, and thus applicable to advanced rotor geometry.
- Full treatment of compressible flow through a similarity law for hovering rotors.

Figure A-1 demonstrates the BHT analysis' capability to correlate predicted OH-58C/A hover performance to flight test measurements. Two calculations are shown. First is that made using the airfoil data of the internal tables in the Army's

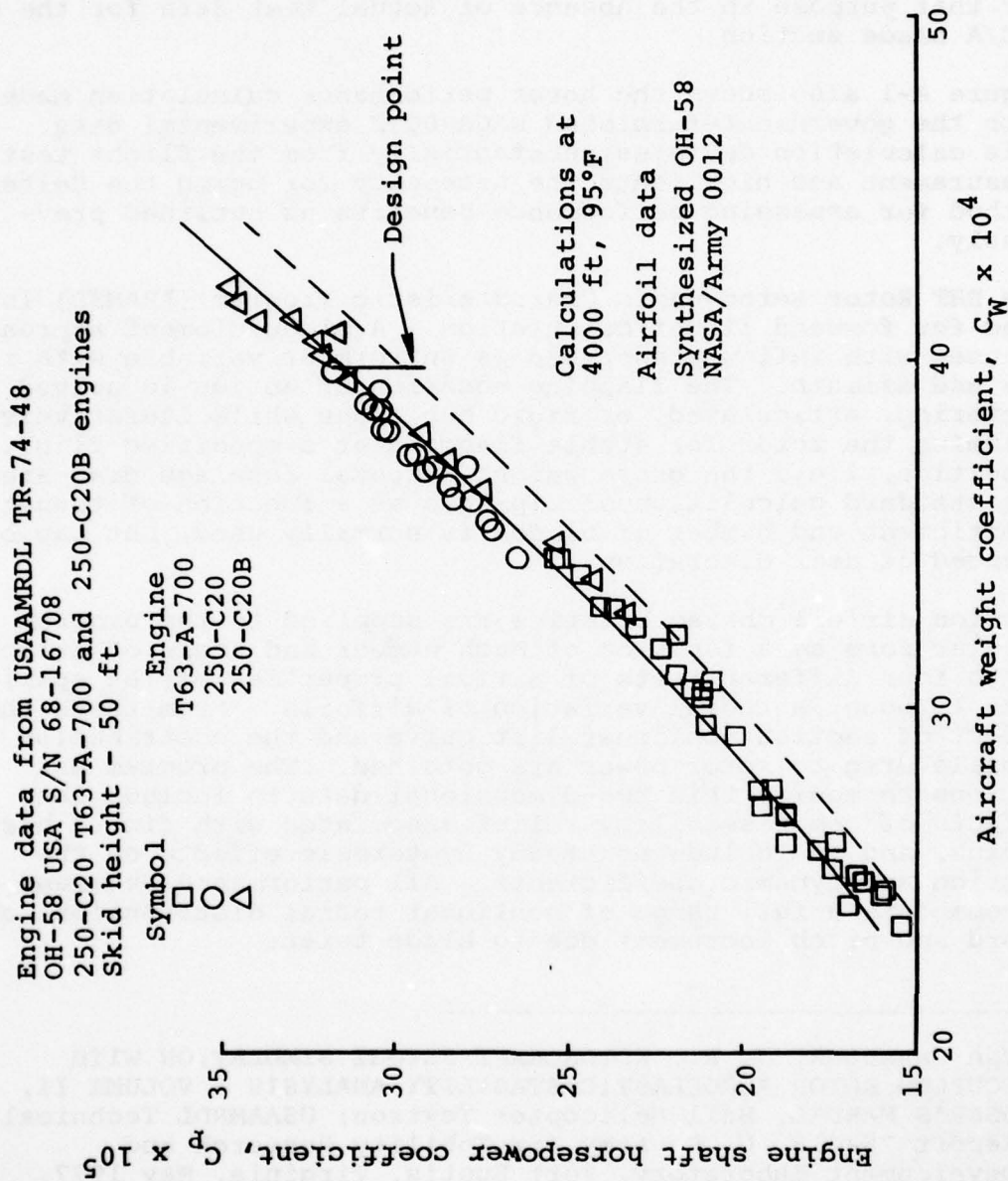


Figure A-1. Hover performance.

Rotorcraft Flight Simulation Program C81 (USAAMRDL TR-76-41B) (Reference 22). These data are synthesized to represent the NACA 0012 airfoil. These data have also been found to represent the characteristics of the OH-58C/A rotor, and have been used at BHT for that purpose in the absence of actual test data for the OH-58C/A blade section.

Figure A-1 also shows the hover performance calculation made with the government-furnished NACA 0012 experimental data. This calculation deviates substantially from the flight test measurement and highlights the necessity for using the delta method for assessing performance benefits as outlined previously.

The BHT Rotor Aerodynamic Characteristic Program (ARAM38) is used for forward flight calculation. A blade element approach is used with inflow prescribed as uniform or variable with radius and azimuth. The flapping equation of motion is solved for teetering, articulated, or rigid hub types while iteratively trimming the rotor for stable flapping at a specified flight condition, i.e., the gross weight, frontal fuselage drag area. The standard calculation of tip loss as a function of thrust coefficient and number of blades is normally used, but can be changed at user discretion.

Section airfoil characteristics are supplied to the program in tabular form as a function of Mach number and angle of attack. Up to four different sets of airfoil properties may be specified to model a radial variation of airfoils. From these the effect of section nonlinear lift curve and the contribution of profile drag to rotor power are obtained. The program has options to modify this two-dimensional data to include the effects of compressibility relief associated with finite blade radius, and to include nonsteady hysteresis effects on the section aerodynamic coefficients. All performance programs can accommodate a full range of nonlinear radial distributions of chord and pitch increment due to blade twist.

²²Van Gaasbeek, J. R., ROTORCRAFT FLIGHT SIMULATION WITH COUPLED ROTOR AEROELASTIC STABILITY ANALYSIS - VOLUME II, USER'S MANUAL, Bell Helicopter Textron; USAAMRDL Technical Report 76-41B, U. S. Army Air Mobility Research and Development Laboratory, Fort Eustis, Virginia, May 1977, AD A042908.

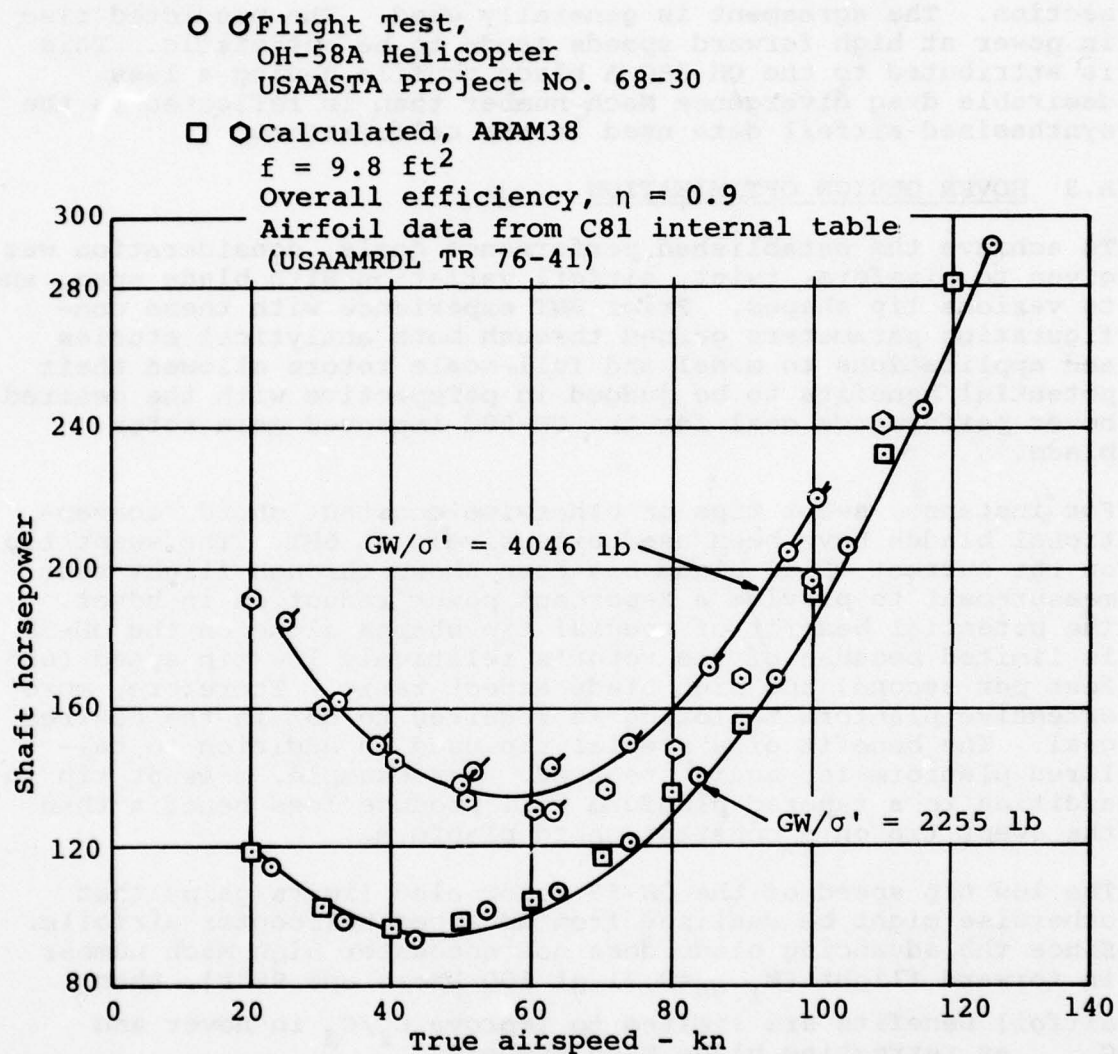


Figure A-2. Comparison of predicted and measured level flight performance of the OH-58A helicopter.

Forward flight performance calculations are compared to flight test measurements in Figure A-2. Cases are illustrated for the current OH-58A at both low weight and a high weight near the design point for the improved blades. These calculations were made with the synthesized airfoil data for the OH-58C/A blade section. The agreement is generally good. The predicted rise in power at high forward speeds tends to be optimistic. This is attributed to the OH-58C/A blade profile having a less desirable drag divergence Mach number than is reflected in the synthesized airfoil data used in the calculations.

A.3 HOVER DESIGN OPTIMIZATION

To achieve the established performance goals, consideration was given to planform, twist, airfoil variation with blade span, and to various tip shapes. Prior BHT experience with these configuration parameters gained through both analytical studies and applications to model and full-scale rotors allowed their potential benefits to be judged in perspective with the desired hover performance goal for the OH-58C improved main rotor blade.

For instance, swept tips on otherwise constant chord, conventional blades have been used extensively at BHT. The swept tip on the current OH-58 blade has been shown through flight test measurement to provide a 2-percent power reduction in hover. The potential benefit of special tip shapes alone on the OH-58 is limited because of the rotor's relatively low tip speed (655 feet per second) and high blade aspect ratio. Therefore, more extensive planform tailoring is required to obtain the desired goal. The benefit of a special tip used in addition to tailored planform is, again, reduced. For example, a swept tip in addition to a tapered planform will produce less benefit than the swept tip on a constant chord planform.

The low tip speed of the OH-58 rotor also limits gains that otherwise might be realized from advanced helicopter airfoils. Since the advancing blade does not encounter high Mach number in forward flight ($M_{1.90} = 0.71$ at 100 knots and 95°F), then airfoil benefits are limited to improve C_l/C_d in hover and $C_{l_{max}}$ at retreating blade Mach numbers.

Thus, rather than perturbing specific blade configuration concepts in search of an optimum, a more generalized approach was taken that systematically reduced hover-induced power, and then optimized the planform for desired airfoil operating range. The key steps of the aerodynamic design procedure in hover were as follows:

- Examine sensitivity of baseline rotor-induced power to systematic changes in circulation distribution, and tailor the circulation to minimize induced power.
- Establish chord distribution from circulation in view of optimum airfoil characteristics.
- Refine twist distribution to complement the planform in maintaining the desired circulation.
- Assess and select specific airfoil.

A.3.1 Baseline Rotor-Induced Power Reduction

Baseline OH-58C induced power sensitivity to circulation distribution was examined using the Lifting Surface Hover Analysis computer program. For this phase of the optimization, linear lift curve slopes varying with Mach number and zero profile drag were assumed for airfoil properties.

The blade twist was used as a "pseudo" independent variable to systematically manipulate the true independent variable of the blade aerodynamics, circulation, until induced power was reduced to the apparent minimum. The resulting circulation distribution is compared to that of the baseline rotor in Figure A-3. An induced power reduction of 7.6 percent was achieved in this step.

A.3.2 Planform Definition

The blade planform was next defined from the desired circulation distribution previously prescribed. This was done through the relationship of bound circulation (Γ), chord (c), lift coefficient (C_l), rotational velocity (Ω), and position along the blade (r), $cC_l = 2\Gamma/\Omega r$.

The first consideration was to establish a criterion for selecting the values of the individual terms of the product cC_l . A choice exists between assuming a constant chord and allowing twist to vary to provide the desired C_l , or setting C_l at a desired level and allowing chord to vary along with twist. In the first approach, twist is the major power reduction factor and in the second, chord distribution is the major factor with twist having a secondary effect. To avoid forward flight degradation with a constant chord/high twist blade, the second was chosen.

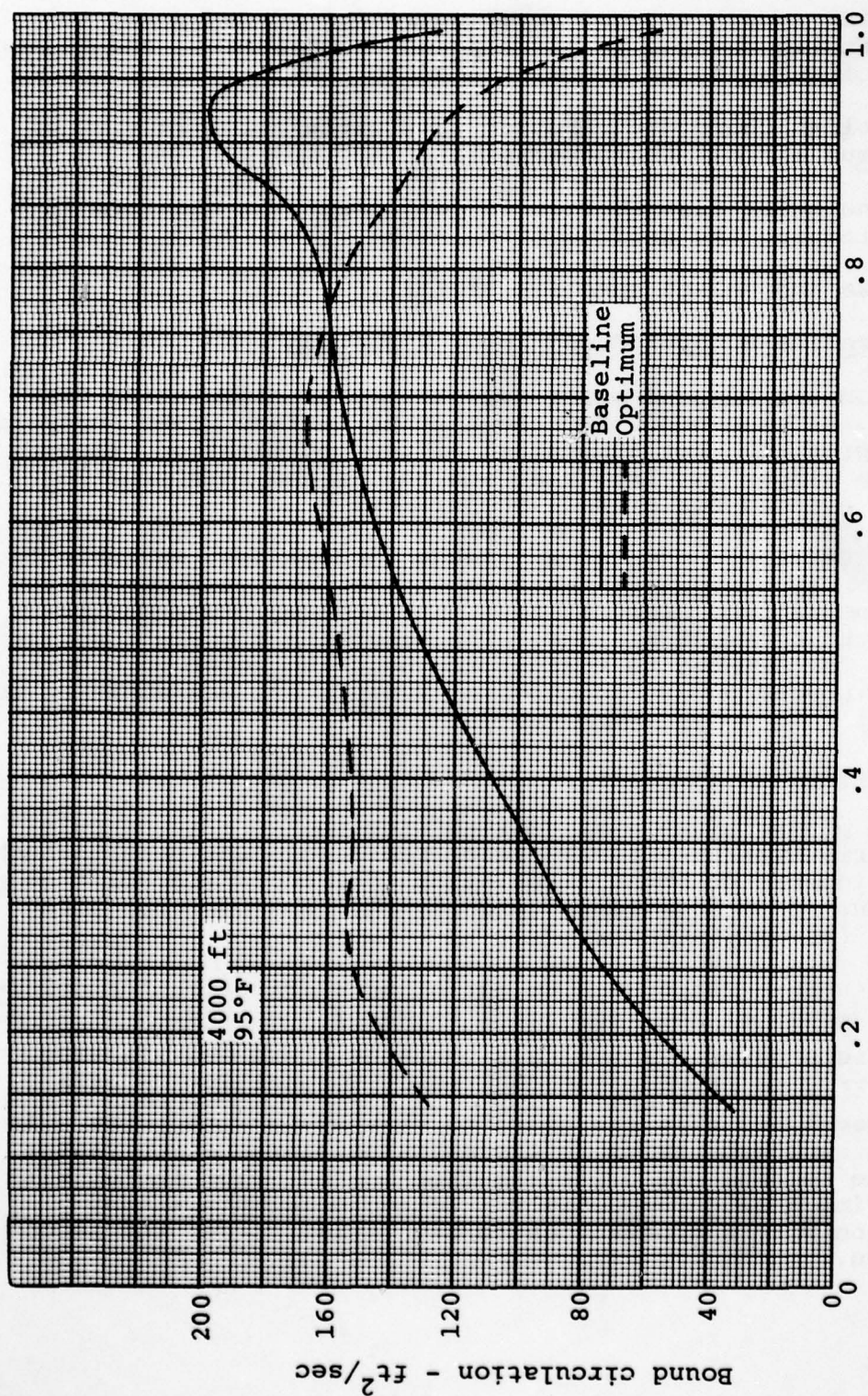


Figure A-3. The optimum circulation distribution for minimum induced power compared to baseline OH-58C circulation distribution.

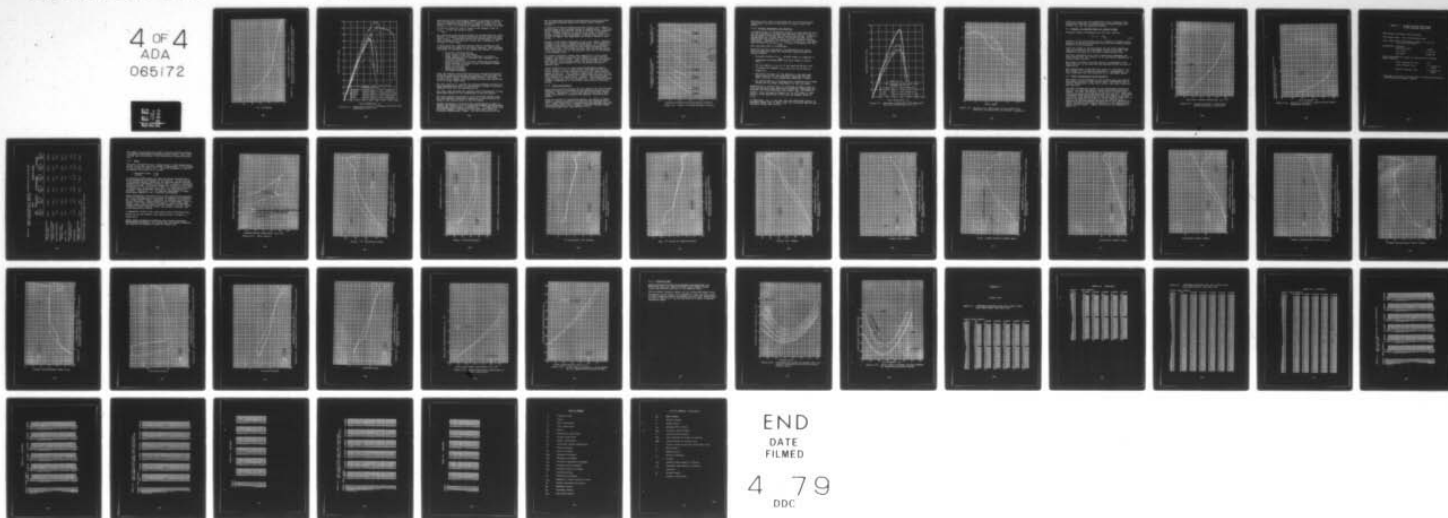
AD-A065 172

BELL HELICOPTER TEXTRON FORT WORTH TEX
OH-58 COMPOSITE MAIN ROTOR BLADE. PRELIMINARY DESIGN INVESTIGAT--ETC(U)
DEC 78 V H BROGDON, J BRASWELL, F FREEMAN DAAJ02-77-C-0073
699-099-086 USARTL-TR-78-38A NL

UNCLASSIFIED

4 OF 4
ADA
065172

1/1



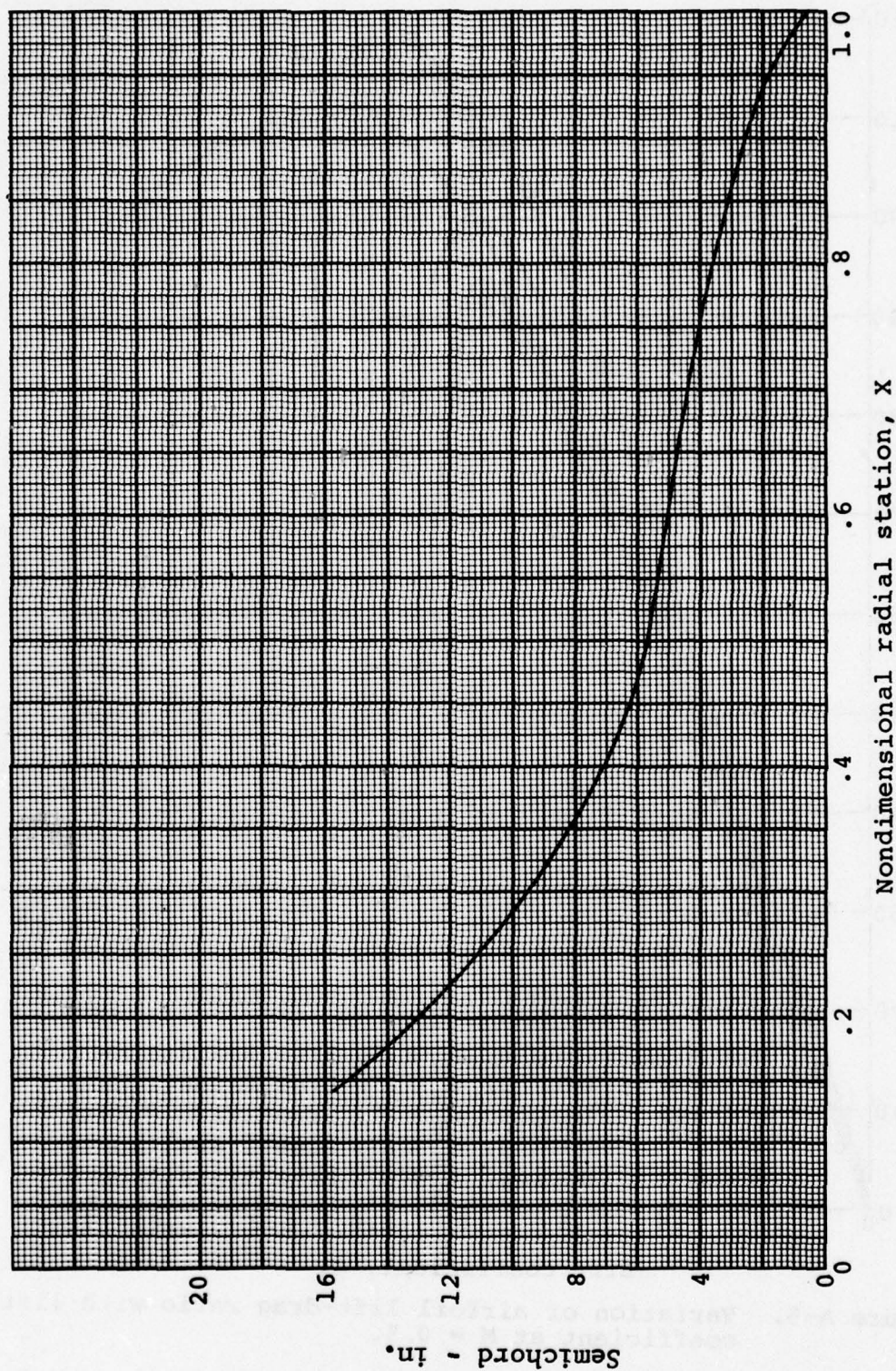


Figure A-4. Chord distribution corresponding to optimum circulation distribution for a design lift coefficient of unity.

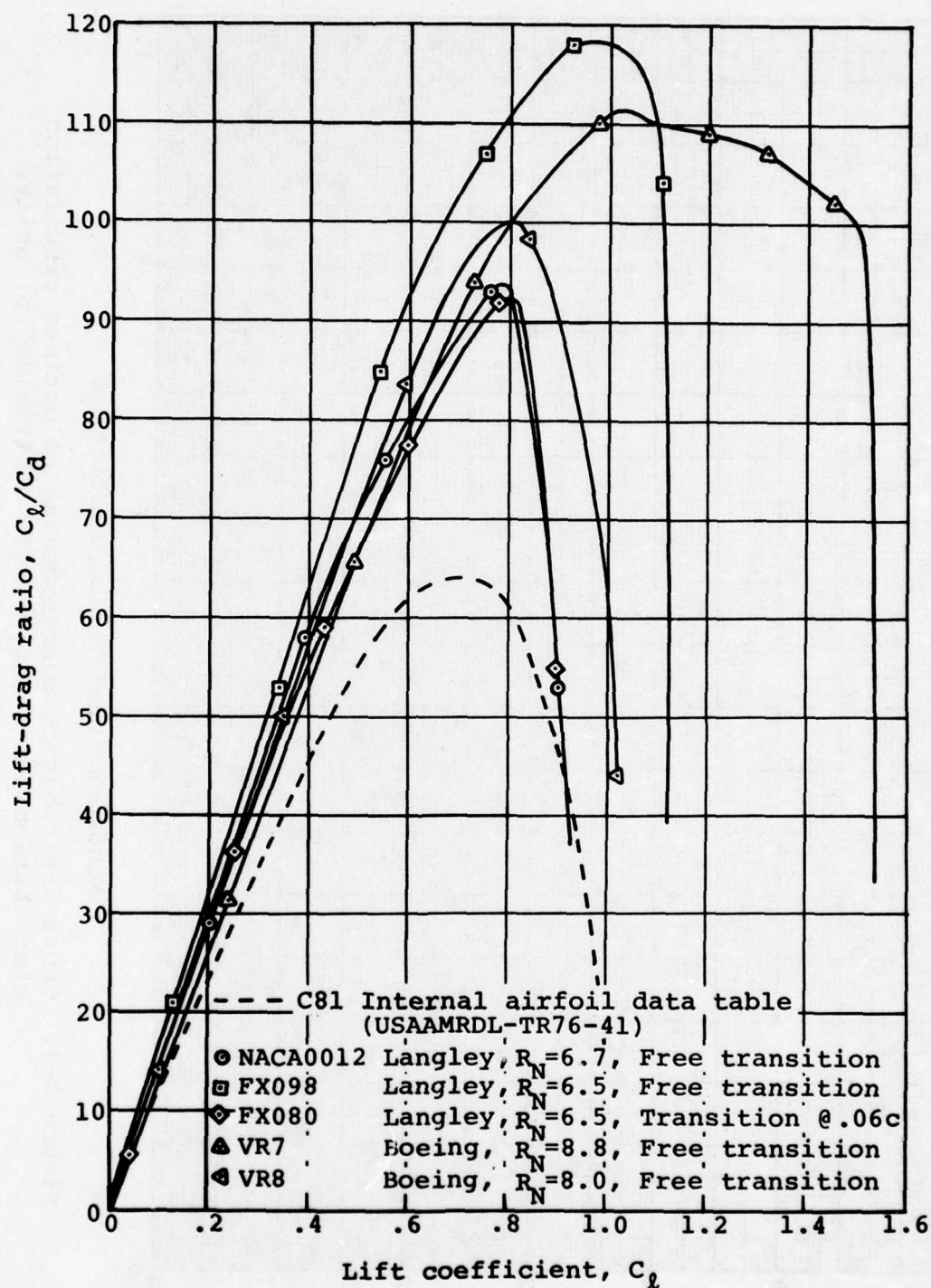


Figure A-5. Variation of airfoil lift-drag ratio with lift coefficient at $M = 0.5$.

With section lift coefficients assumed to be equal to unity, a chord distribution was produced for a planform that could be termed a normalized planform and is shown in Figure A-4. The design C_l of 1.0 is relatively independent of airfoil selection as seen in Figure A-5 and is close to the highest value of $C_l/C_{d_{max}}$ of all the airfoils shown.

The resultant blade design provides the optimum hovering rotor; however, it presents several manufacturing and technical problems as well. A compromise design was established to overcome these problems and to provide a rotor that conformed to the criteria of this study.

In developing the compromise design several constraints and conditions had an impact on the final planform. The following also apply to evaluation of tip shapes and changes in solidity:

- Structural discontinuities
- Fiber volume in the tip region
- Large inboard cuffs could contribute to forward flight degradation in reversed flow, dynamics, and structural problems
- High tip region C_l 's in hover indicating retreating blade problems in forward flight and possible degradation of autorotation
- Radar reflectivity
- Frequency placement
- Tip weight placement

First the inboard chord distribution was reduced and faired to eliminate production problems and possible loads problems due to the "tennis racket" pitching moment effect. This step resulted in an inboard chord distribution nominally equivalent to a 2:1 linear taper ratio.

The next step was to increase the thrust-weighted solidity to a value approximately equal to the baseline in order to maintain adequate blade area for maneuverability.

The final step smoothed the outboard chord distribution to minimize peak values of lift coefficient in the tip region.

The final planform selected not only minimized induced power, but also showed a substantial reduction in profile power because of the reduced chord in the tip region.

Further variations of planform were investigated in order to examine the possibility of a compromise between minimum profile and minimum induced power configurations. In almost every case planform changes to minimize profile power were offset by increased induced power losses. The best hovering rotor was

the one previously defined by manipulating circulation except for the same planform shape with reduced thrust-weighted solidity.

A reduction of thrust-weighted solidity (Figure A-6) reduced profile power with a minimal change in induced power. The final thrust-weighted solidity was set at 95 percent of the baseline value. Further reduction of solidity was shown to begin to degrade forward flight performance, increase peak values of C_l in the tip region, and compromise the OH-58C's maneuver capability.

Because of the design constraint on the rotor radius, geometric solidity could only be changed through chord. The design philosophy of this study eliminated the possibility of choosing a constant chord blade because it would require prohibitively high twist rates. This study did show that the optimum solidity at baseline twist for the baseline rotor was at 95 percent of the present value.

Tip shapes considered showed some reductions in rotor power; however, tip shapes alone were not adequate to meet the performance goal of 6 percent. Tips such as the Ogee also present difficulties such as maintaining a constant volume of fibers near the tip, and placement of the tip weights because of reduced chord.

Severe reductions in tip chord showed performance improvements; however, closer investigation indicated that the vorticity trailed over the inboard portion of the blade-induced upwash at the tip. This caused a significant rise in lift and drag coefficients. A dimensional profile drag increase did not occur because of reduced chord. However, the upwash tended toward forcing the tip into autorotation. This condition would produce a degradation of the OH-58C's autorotation characteristics.

A.3.3 Twist Distribution

Up to this point the planform has been defined and has deviated somewhat from that prescribed by the optimum circulation distribution. Therefore, a twist distribution that best complements the planform in achieving the desired circulation was sought.

Twist was varied in a methodical manner, the result of which, however, showed no benefits in hover with an increased twist rate. Model studies for a tapered blade did highlight the need for increased twist rates in order to prevent forward flight retreating blade stall (see Section 4.2.3).

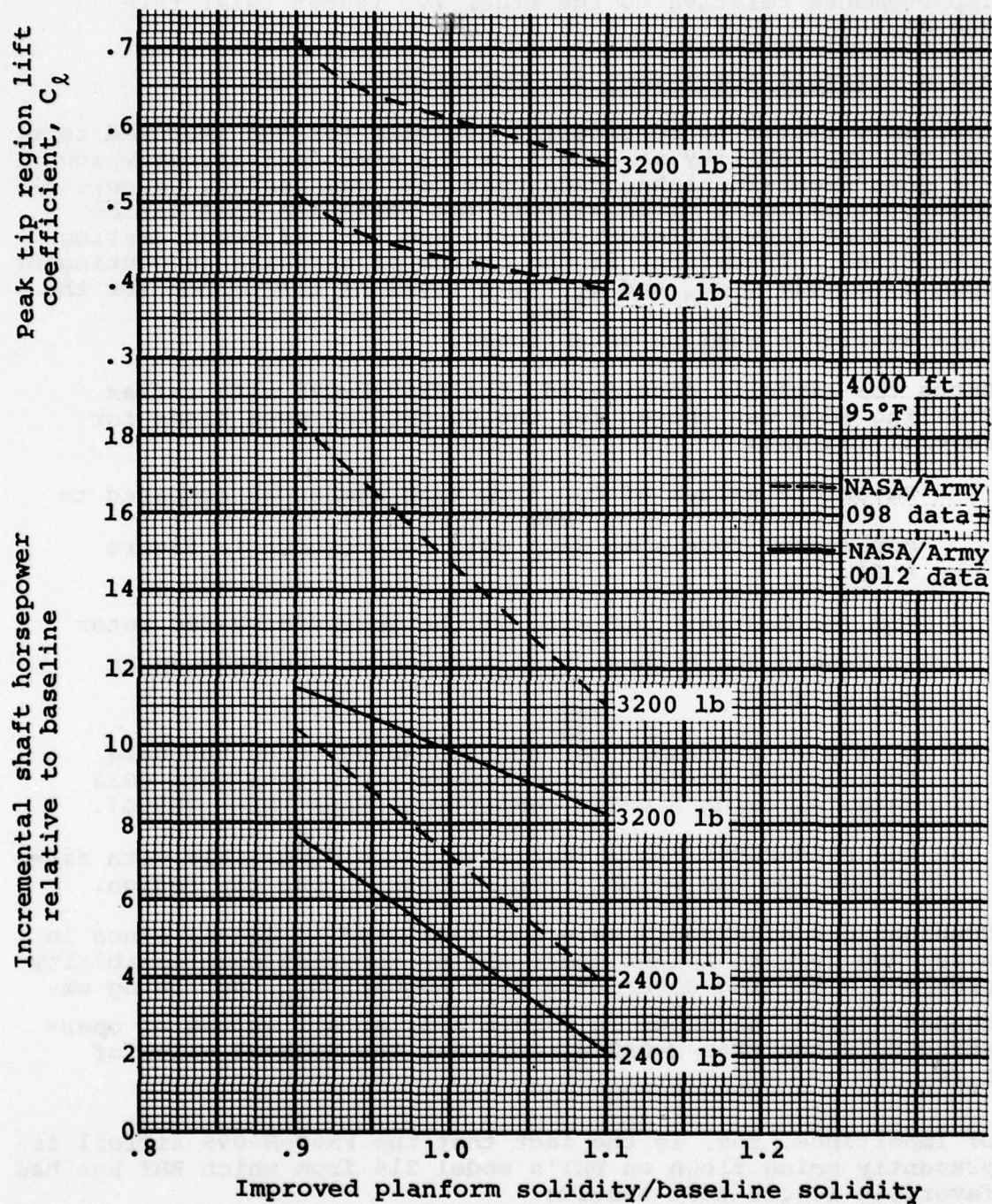


Figure A-6. Effect of thrust weighted solidity.

Nonlinear twist rates investigated did not show performance improvements relative to the final 14° linear twist rate chosen.

A.3.4 Airfoil Assessment and Selection

A primary factor in considering airfoils for the improved rotor was the availability of data from the same facility at which the government-furnished NACA 0012 data was tested. Figure A-7 demonstrates for a given airfoil the variation that can be experienced from different tunnels and for different testing conditions. Therefore, if the choice of airfoils is contingent upon favorable C_l/C_d and $C_{l_{max}}$, a level of confidence for the data available must be established.

Among the airfoils considered, the FX69-H-098 with reflex trailing edge was chosen for the OH-58C improved blade for several reasons:

- Favorable values of $C_{l_{max}}$ vs Mach number as compared to government-furnished NACA 0012 data (shown in Figure A-8).
- For the design C_l ($C_l=.6$) of the improved OH-58C rotor it showed the highest C_l/C_d ratios as can be seen in Figure A-5.
- Data were available for the FX69-H-098 from the same tunnel test as for the government-furnished NACA 0012 data, allowing a valid comparison (NASA TMX - 73990).
- The FX69-H-098 has a thickness ratio compatible with fiber volume and tip weight requirements in the tip region.

Combinations of airfoil were not evaluated in detail since in hover and forward flight there are no apparent compressibility problems with drag divergence Mach number, M_{dd} , not being exceeded. Also, as shown in Figure A-5, at all values of operating C_l 's the FX69-H-098 airfoil has the highest value of C_l/C_d .

Of importance, too, is the fact that the FX69-H-098 airfoil is presently being flown on BHT's model 214 from which BHT has had favorable flight test results.

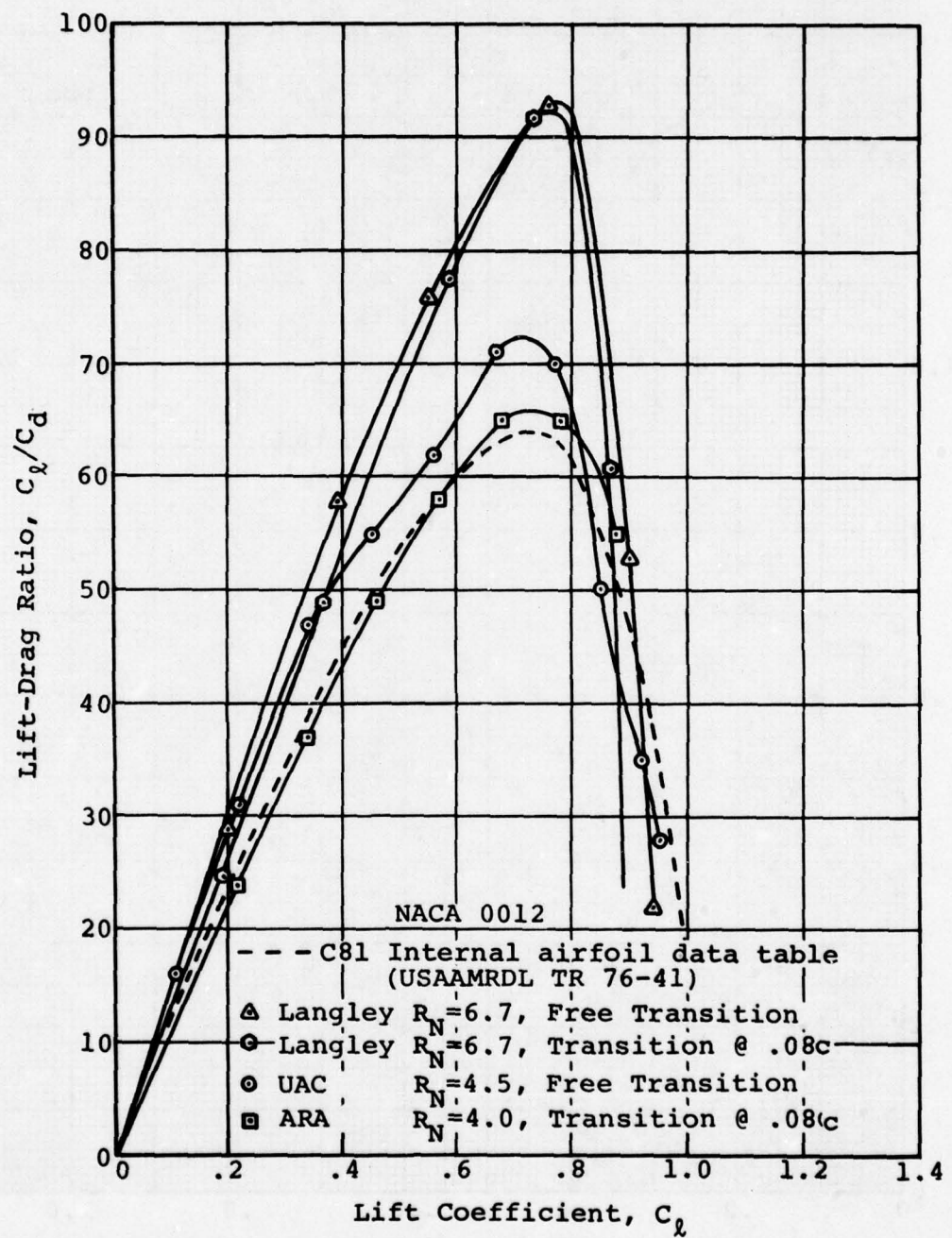


Figure A-7. Variation of NACA 0012 lift-drag ratio with lift coefficient at $M = 0.5$.

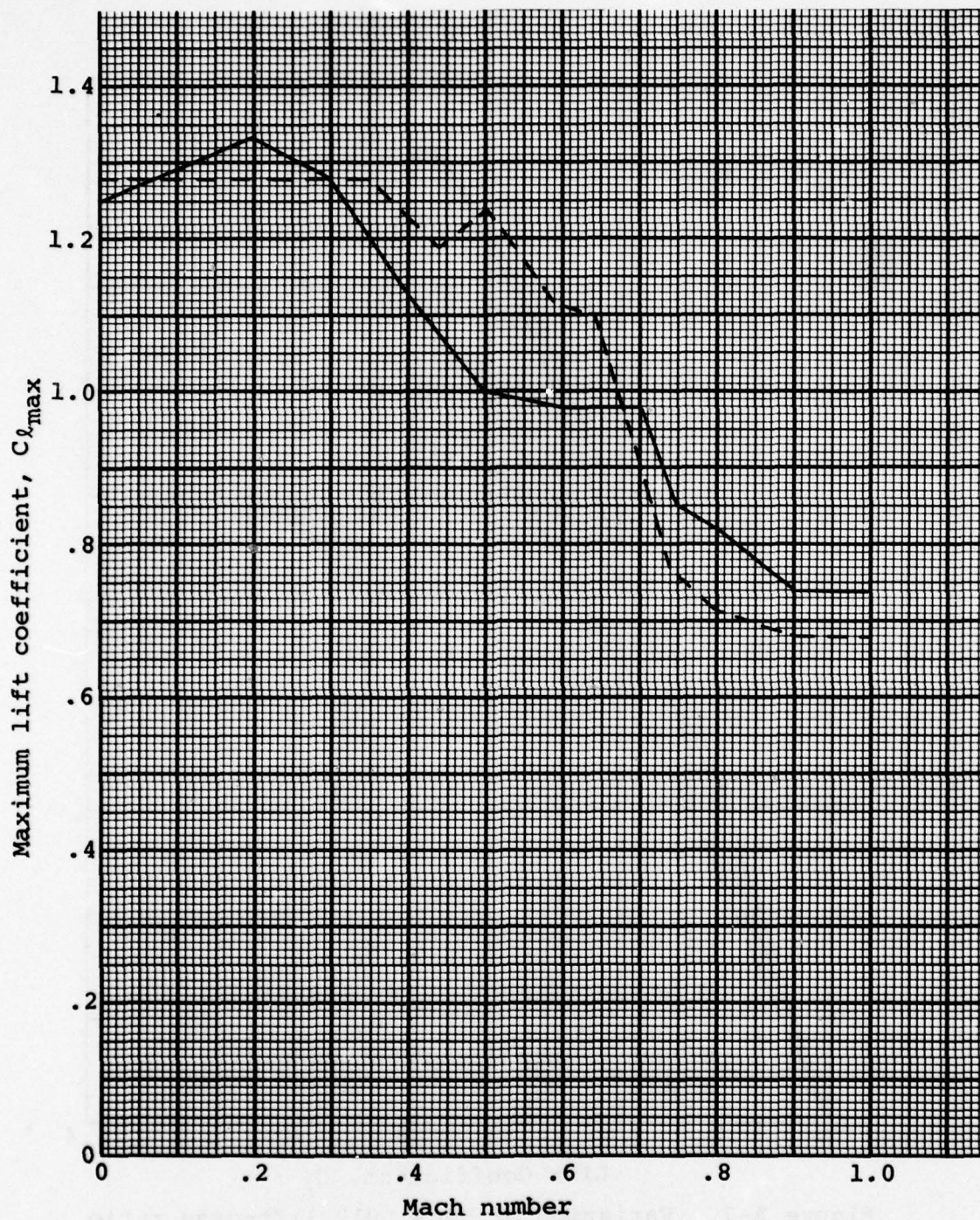


Figure A-8. Maximum lift coefficient vs Mach number from NACA 0012 and FX69-H-098 data tables, Appendix B.

Figure A-9 shows that the FX69-H-098 airfoil improved hover performance relative to the NACA 0012 at design thrust coefficient, C_T , for the improved planform.

A.4 Analysis of Improved Rotor in Forward Flight

Classical means of accounting for tip loss, such as

$$B = 1 - \frac{2C_T}{b} \quad (A-1)$$

(where B is tip loss station and b is number of blades) would penalize the blade with greatest tip area when thrust-weighted solidity is held constant.

Since tip losses in forward flight are not fully understood from the standpoint of a dependable mathematical model, the assumption was made that the entire blade creates lift.

This was considered to be a more conservative approach and would assure that the criteria of no performance degradation in forward flight was met.

The effect of using a tip loss factor as prescribed in the above equation on the baseline and improved OH-58C is shown in Figure A-10.

The configuration established for hover was evaluated in forward flight with no apparent degradation. Consequently, further iterations were not necessary for a compromise design.

A.5 Final Configuration Characteristics

The results to be presented in this section may vary somewhat from those reported in BHT interim report 699-099-084 due to further definization of the cuff, cutout, and twist variation near the grip.

In order to check the results of the performance predictions made for the improved OH-58C, sample calculations were performed. In hover, performance of the baseline rotor alone was calculated using the losses described in Table A-1. Calculated incremental performance benefits were then added to the baseline rotor alone and adjusted for losses (same as Table A-1) to predict the complete helicopter with the improved rotor. Improved OH-58C performance characteristics were developed by adding incremental performance benefits to the complete helicopter without losses. Sample calculations are presented in Table A-2.

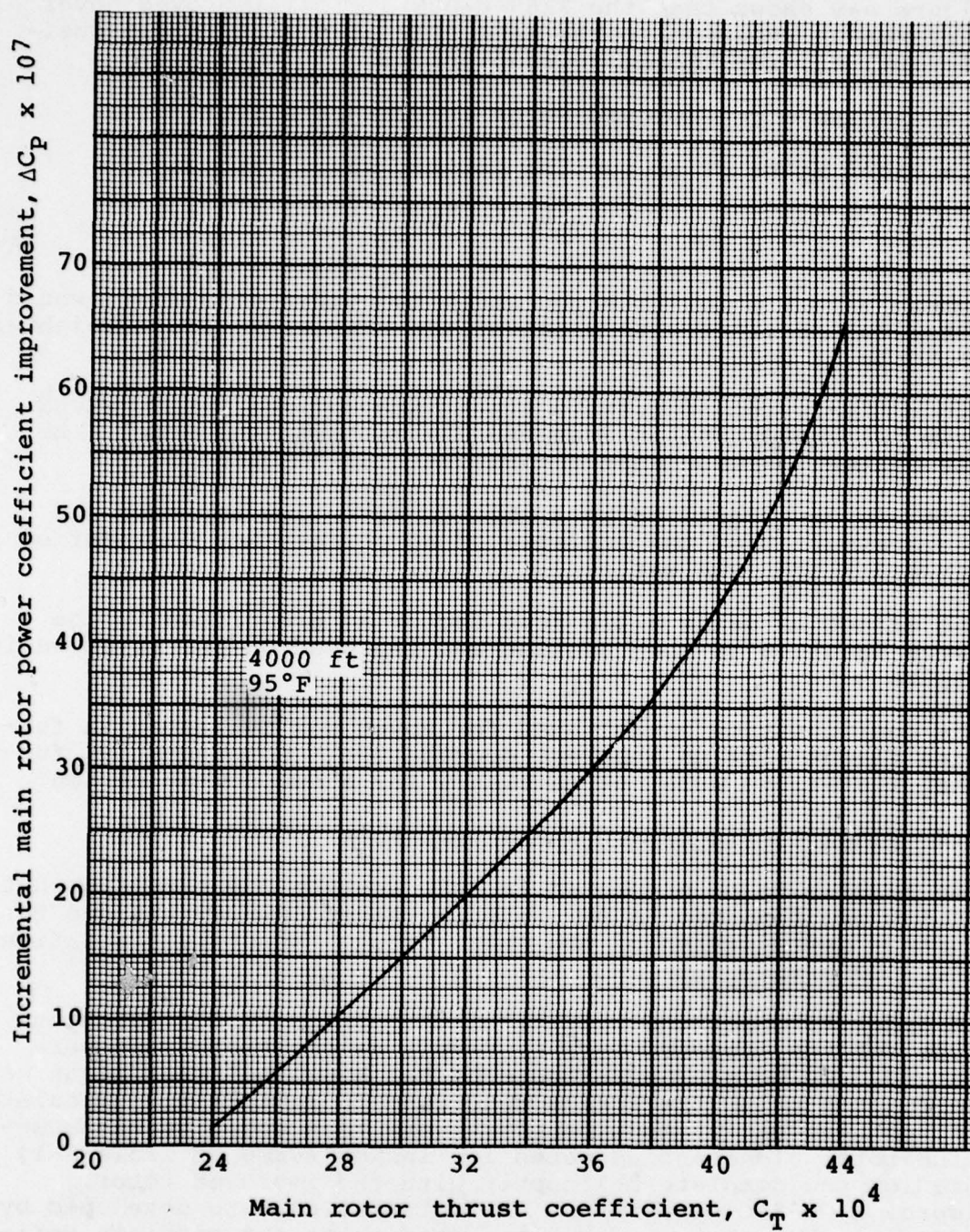


Figure A-9. Calculated effect of FX69-H-098 airfoil relative to NACA 0012.

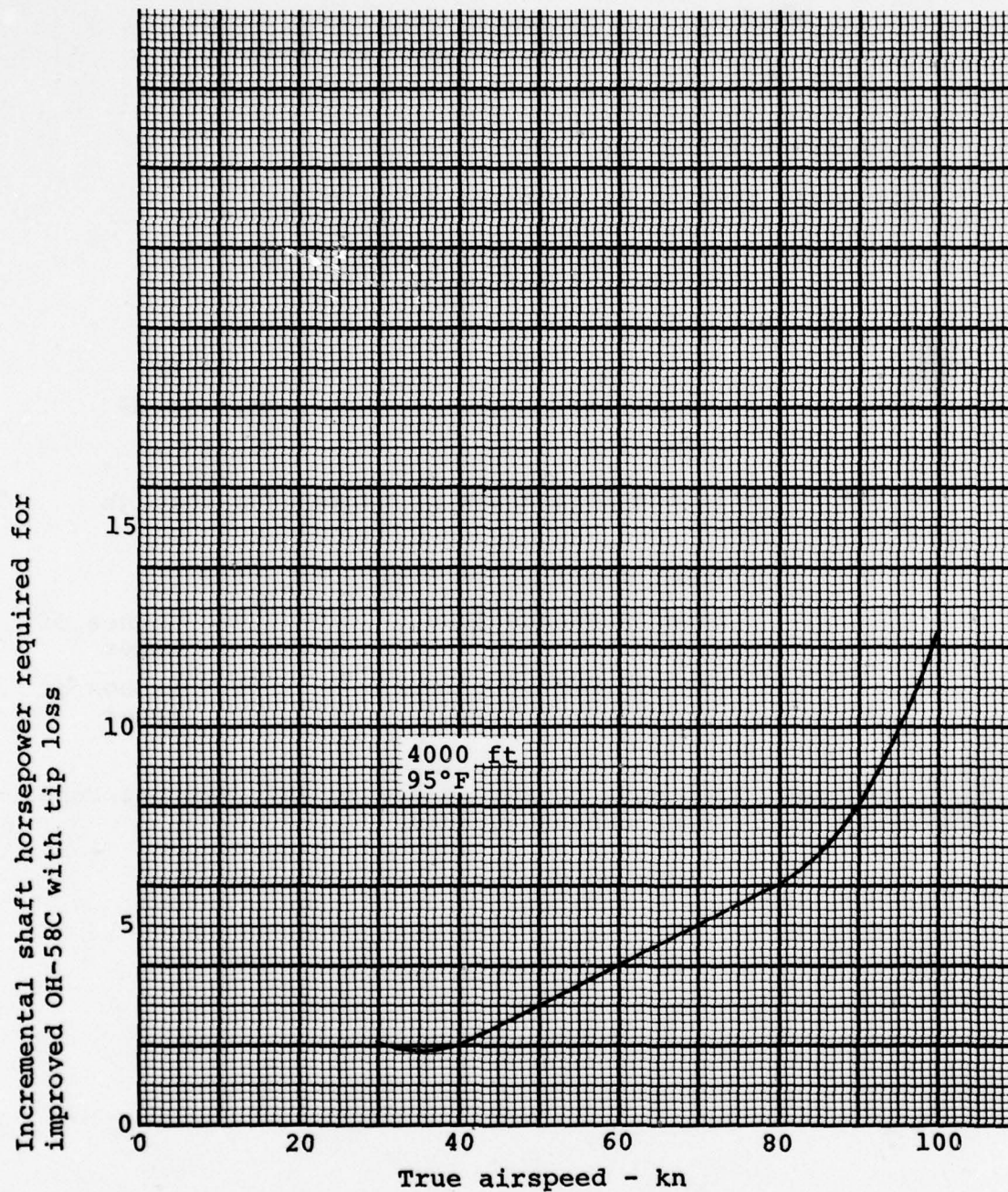


Figure A-10. Effect of tip loss on improved OH-58C shaft horsepower required.

TABLE A-1. CONVERSION FROM ROTOR ALONE
TO THE COMPLETE HELICOPTER

Rotor Alone (includes 2.8%* download)

Tail Rotor Power - 8% of Rotor Alone Power

Tail & Main Rotor Transmission Losses - 3% of tail
and main rotor power

Accessories (Constant)

Hydraulic Pump	- .88 HP
Oil Cooler	-4.9754 HP
Extractor	-6.885 HP

Engine installation losses are accounted for through
power available.

Inlet temperature rise	2°F
Inlet pressure loss	4.3 inches of water
Exhaust pressure loss	1.2 inches of water

* Includes -25 pounds of thrust due to infrared suppression
stack deflecting exhaust upward.

TABLE A-2. SAMPLE CALCULATIONS OF COMPLETE IMPROVED OH-58C HELICOPTER
SHAFT HORSEPOWER (SHP) REQUIRED

	<u>Hover</u>		<u>Forward flight</u>			
	<u>Design point</u>		<u>Minimum power</u>		<u>100 knots</u>	
	<u>OWE*</u> SHP @ 2400 lb (hp)	SHP @ 3200 lb (hp)	SHP @ 2400 lb (hp)	SHP @ 3200 lb (hp)	SHP @ 2400 lb (hp)	SHP @ 3200 lb (hp)
Baseline helicopter, total power	201.0	298.0	108.2	151.0	210.0	266.0
Baseline helicopter without losses	169.3	256.4	85.8	124.3	177.3	227.7
Calculated benefit	8.6	17.0	7.3	9.5	5.9	16.0
Improved rotor without losses	160.7	239.4	78.5	114.8	171.4	211.7
Tail rotor	12.9	19.2	6.3	9.2	13.7	16.9
Main and tail rotor transmissions	5.2	7.8	2.5	3.7	5.6	6.9
Accessories	12.74	12.74	12.74	12.74	12.74	12.74
Improved helicopter, total power	191.5	279.1	100.0	140.4	203.4	248.2

* Operating weight empty (includes two pilots)

The sample calculations are within 1-percent accuracy relative to graphical data points presented in this report. Minor deviations are attributable to the limitations on plotting accuracy.

A.5.1 Hover

The final configuration at a design point of 3200 pounds gross weight, 4000 feet, and 95°F showed an improvement of 6.3 percent as can be seen in Figure A-11. The final breakdown of the improvements calculated is as follows:

- Nonlinear taper 4.1%
- Airfoil 2.2%

At operating weight empty the improved OH-58C demonstrated a hover performance improvement of 4.5 percent. At high values of helicopter weight coefficient the improved design indicates further hover improvements primarily due to airfoil, indicating potential growth. Since wind tunnel data accuracy for the drag coefficient is on the order of ± 0.0005 , a ± 1.9 -percent deviation in engine shaft horsepower required at the design point is possible. Therefore, a 5- to 6-percent improvement in hover performance appears to be a realistic achievement.

Blade performance characteristics of the baseline and improved rotors at the design point are shown in Figures A-12 through A-26. These figures show a comparison of spanwise variation of bound circulation, induced velocity, lift coefficient, angle of attack, lift, drag, and pitching moment; thrust loading and torque loading coefficients; profile, induced and total torque loading to thrust loading ratios; and profile, induced, and total drag-to-lift ratios.

A comparison of main rotor alone hover power coefficient (C_p) versus C_T for the baseline and improved rotors is made in Figure A-27.

Engine shaft horsepower-to-density ratio versus helicopter gross-weight-to-density ratio curves for the complete baseline and improved helicopters is shown in Figure A-28.

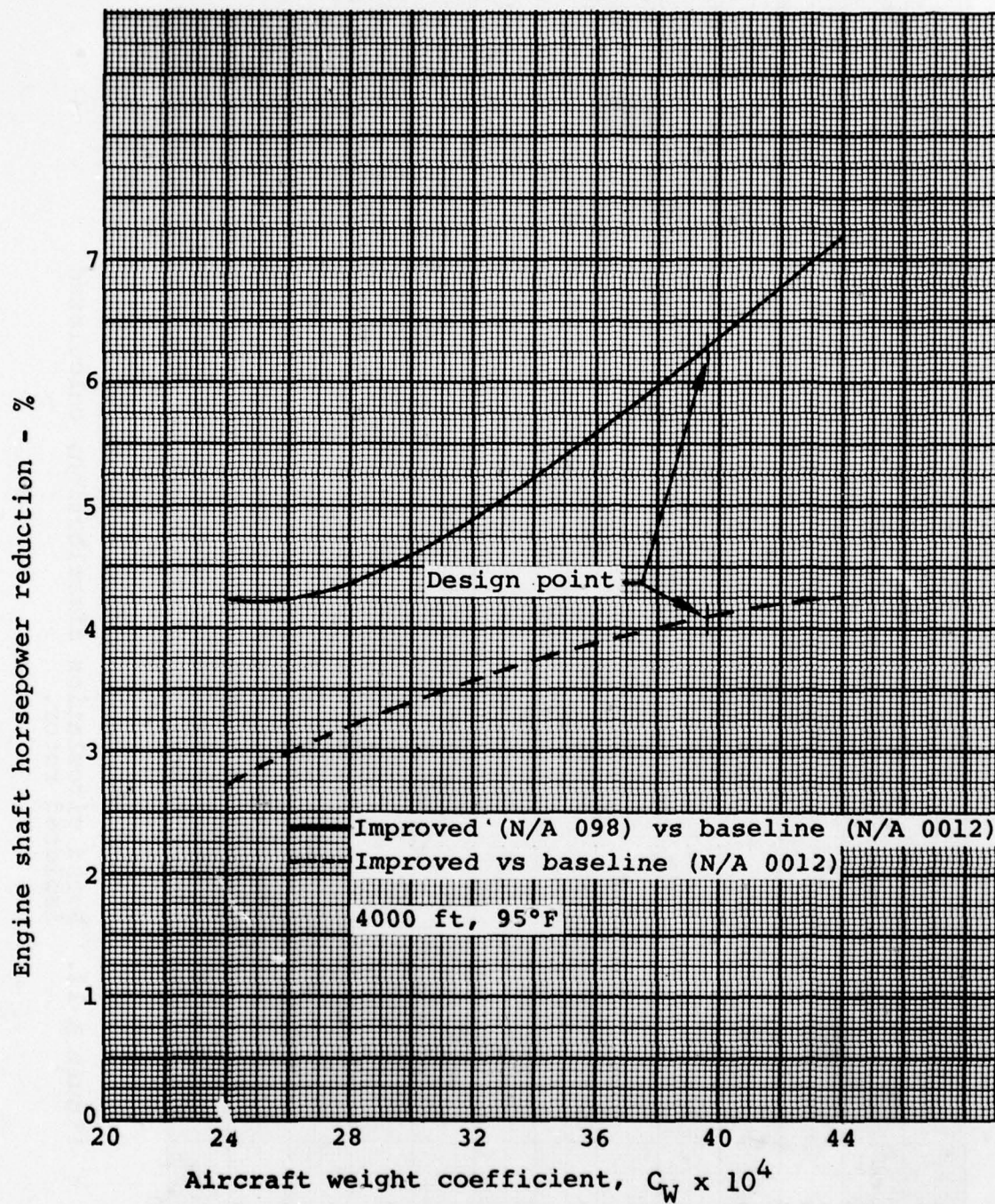


Figure A-11. Hover benefit.

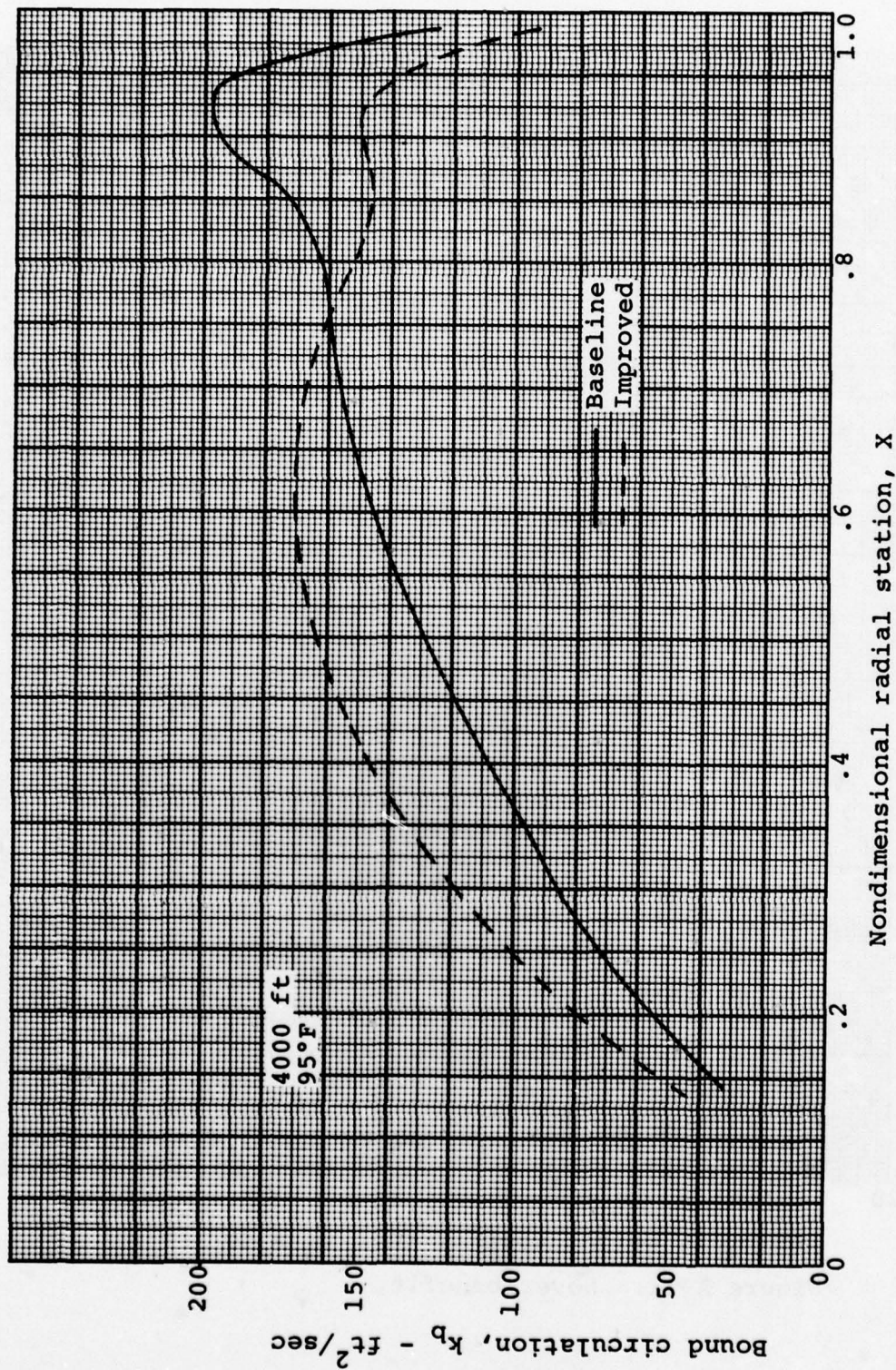


Figure A-12. Bound circulation distribution, calculated isolated rotor.

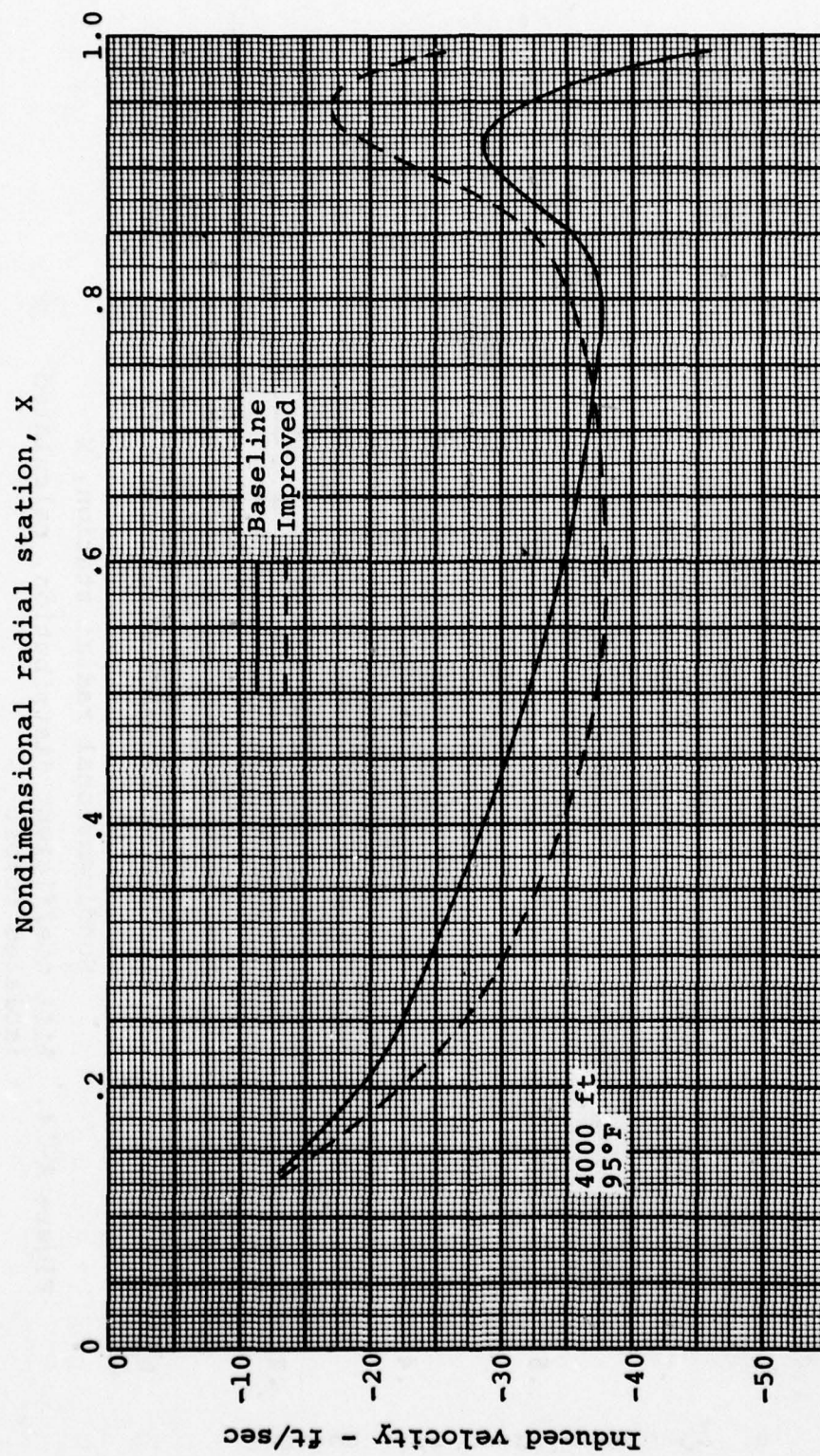


Figure A-13. Induced velocity distribution, calculated isolated rotor.

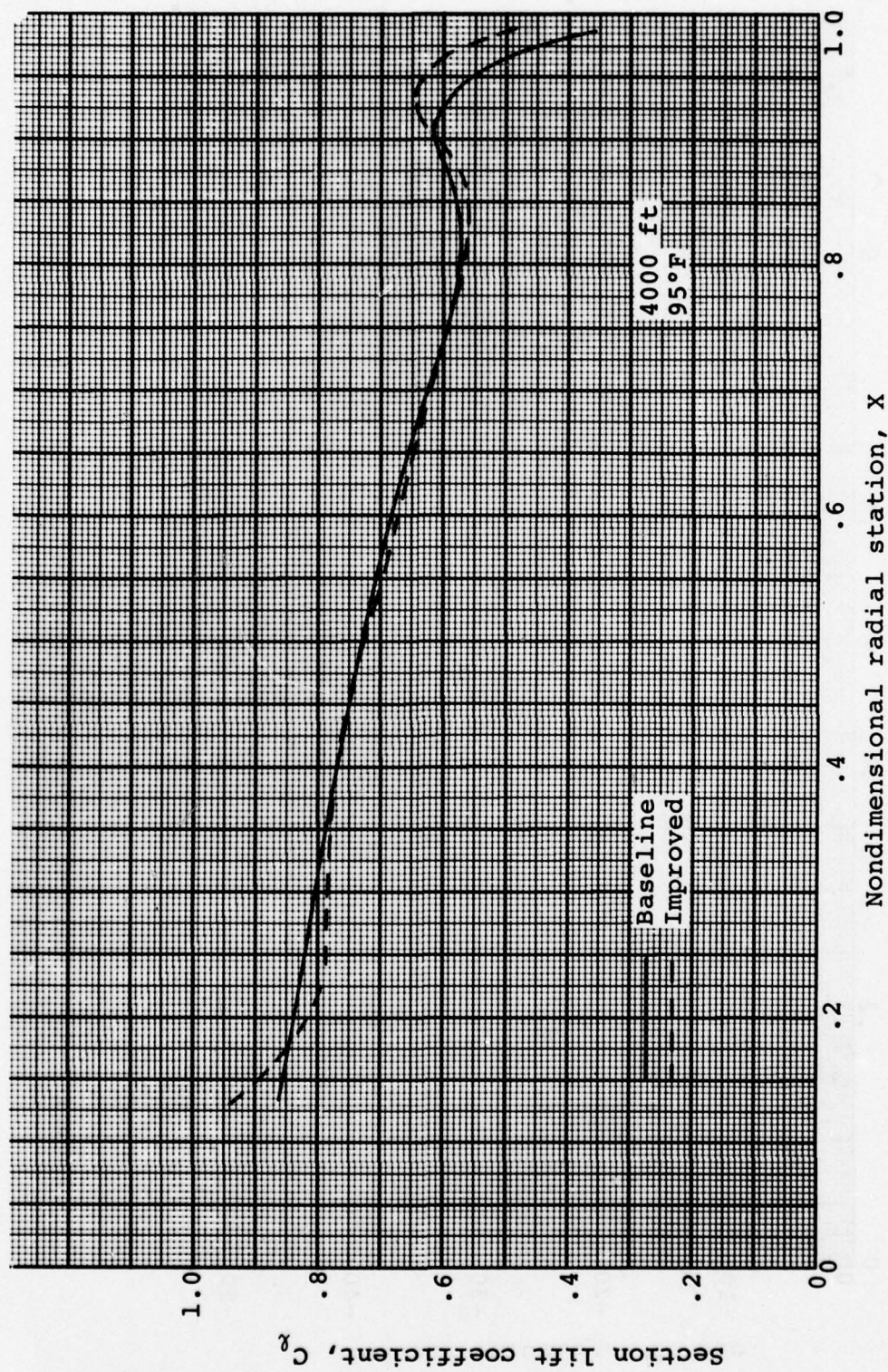


Figure A-14. Lift coefficient distribution, calculated isolated rotor.

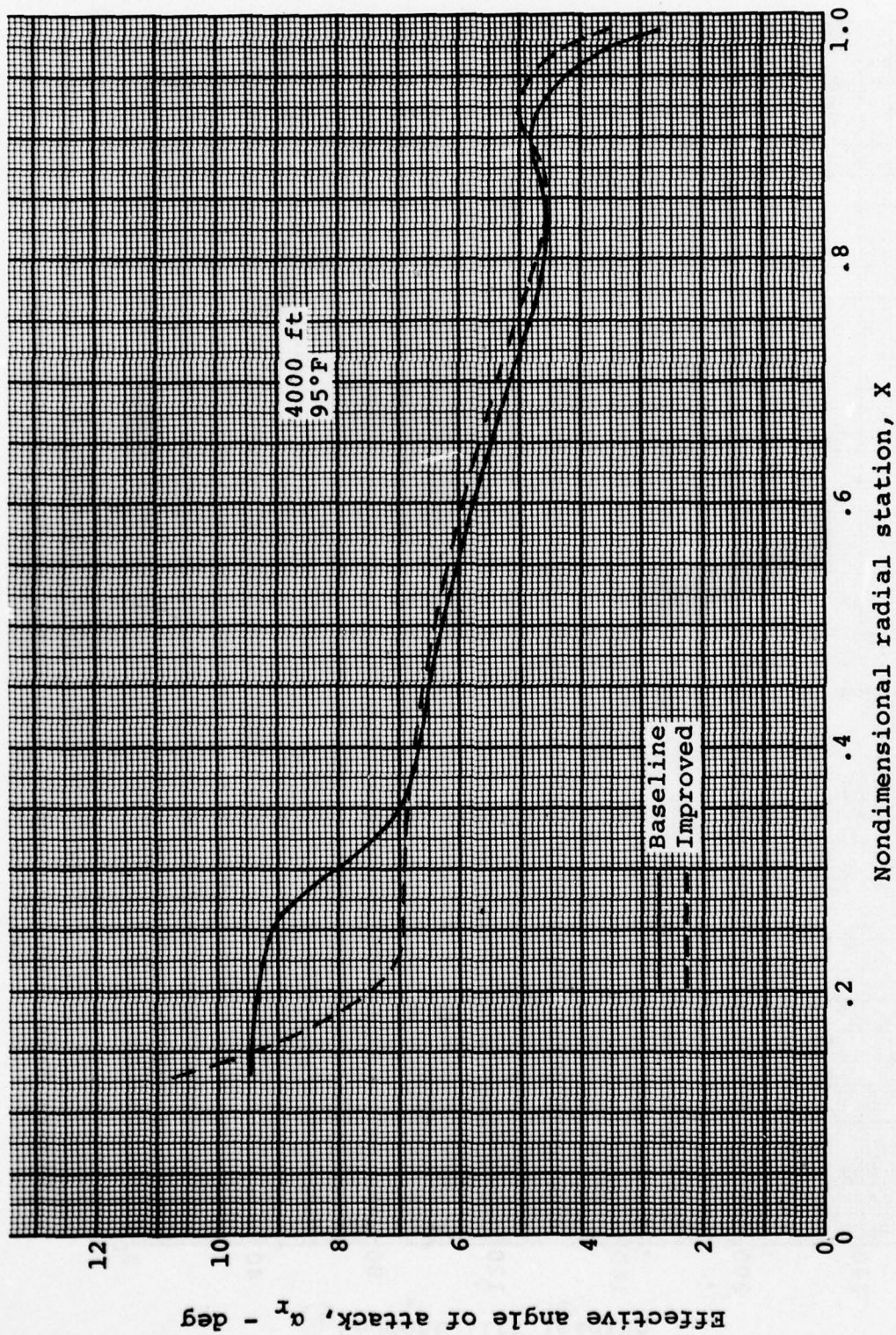


Figure A-15. Effective angle of attack distribution, calculated isolated rotor.

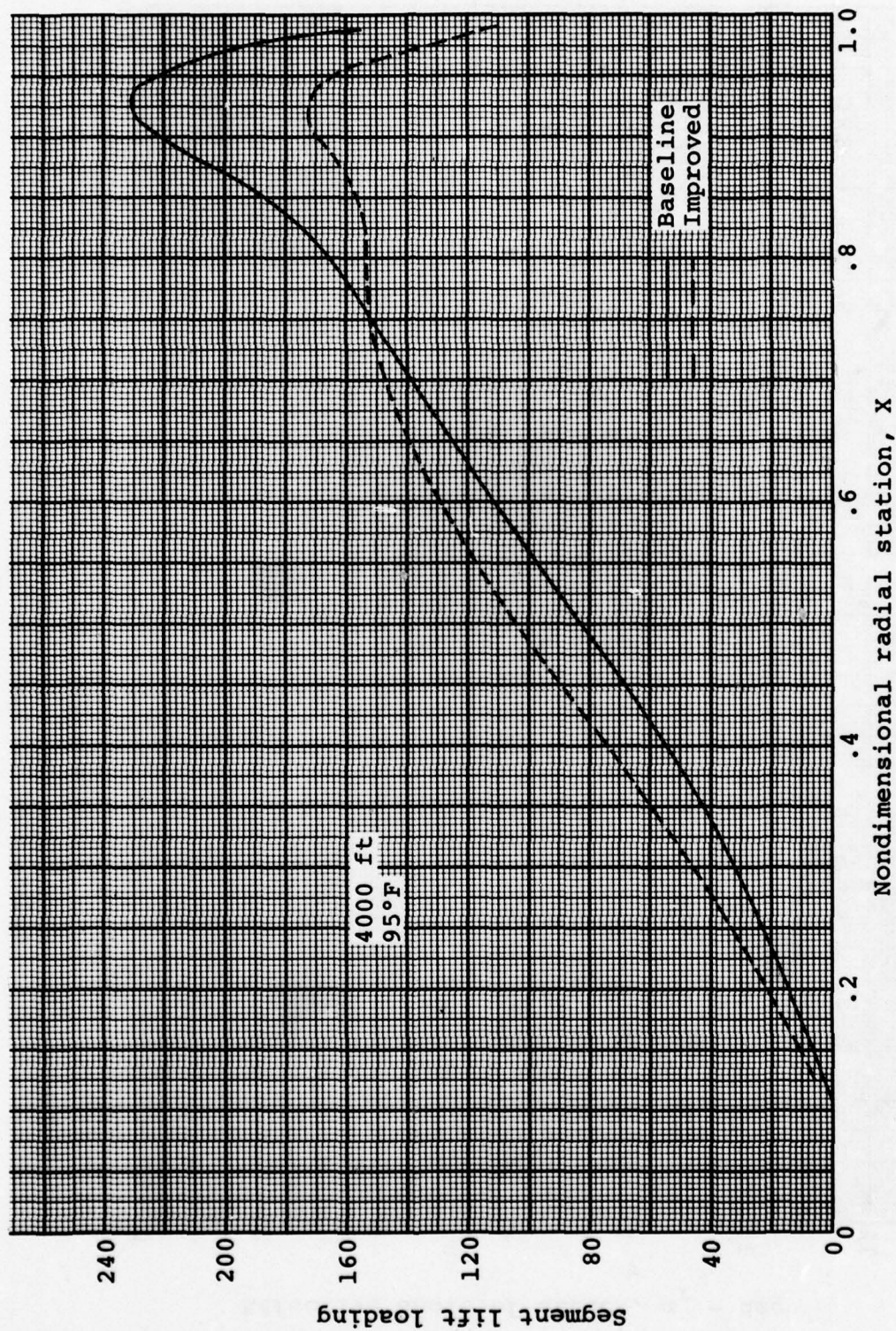


Figure A-16. Blade segment lift distribution, calculated isolated rotor.

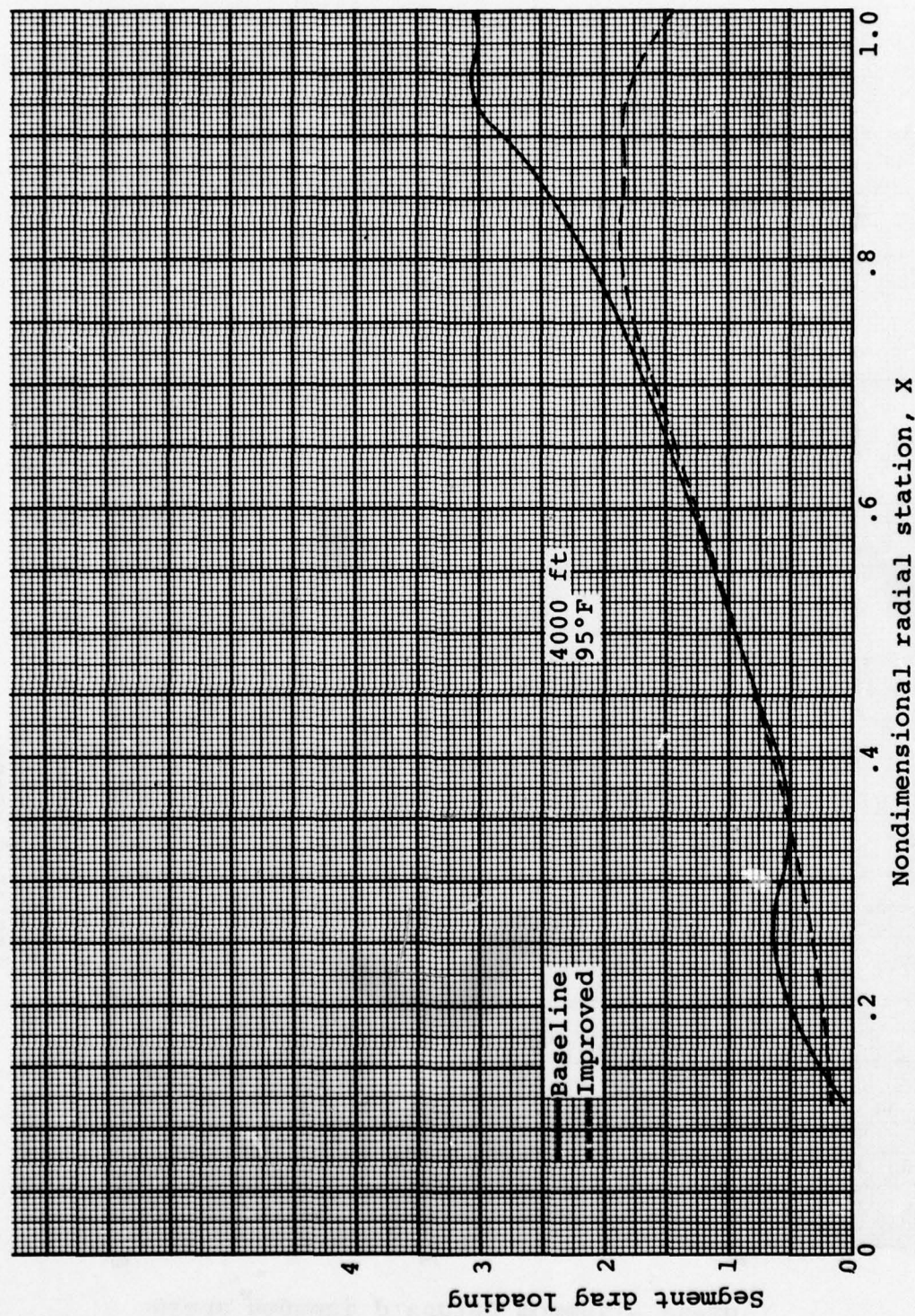


Figure A-17. Blade segment drag distribution, calculated isolated rotor.

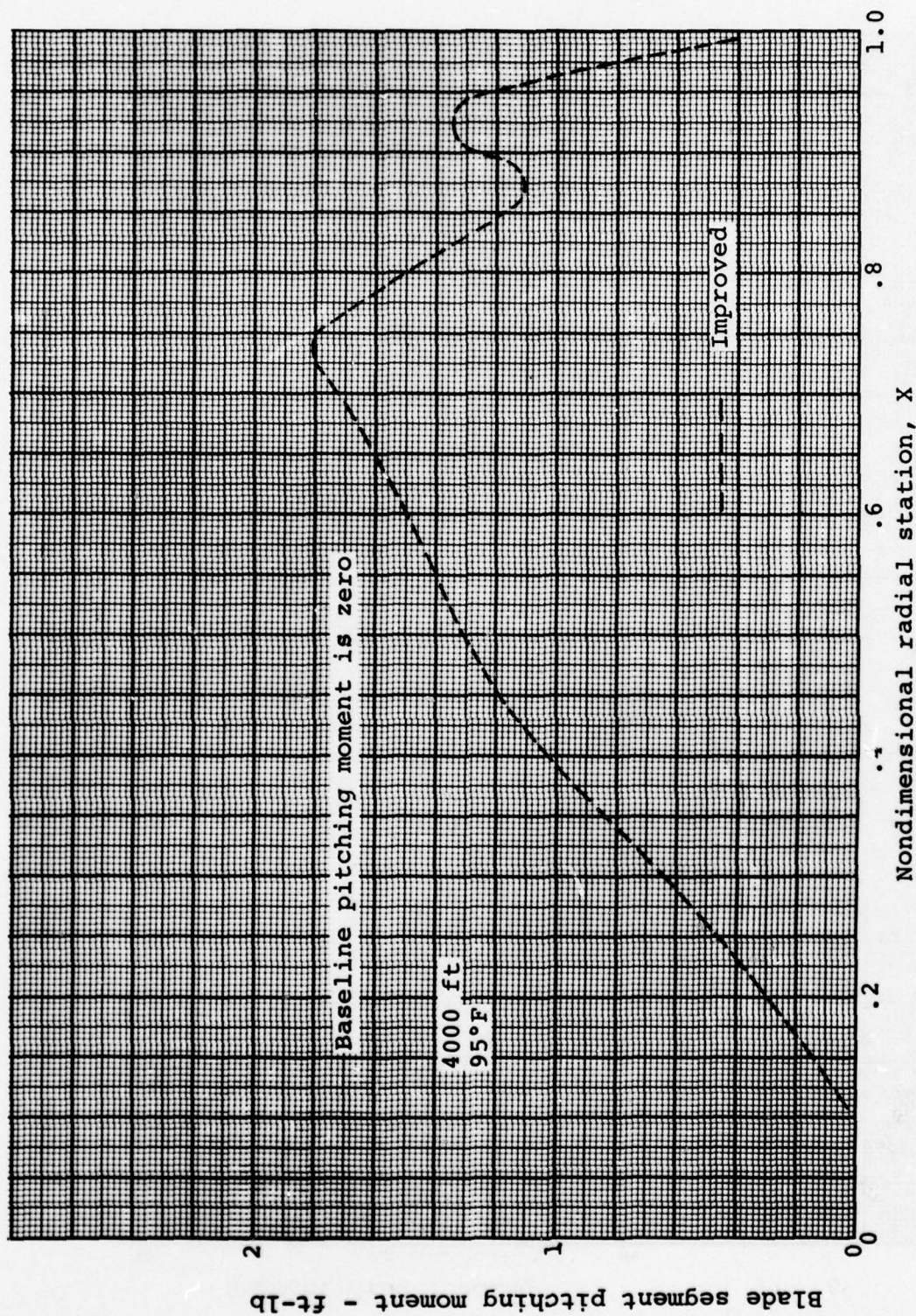


Figure A-13. Blade segment pitching moment distribution, calculated isolated rotor.

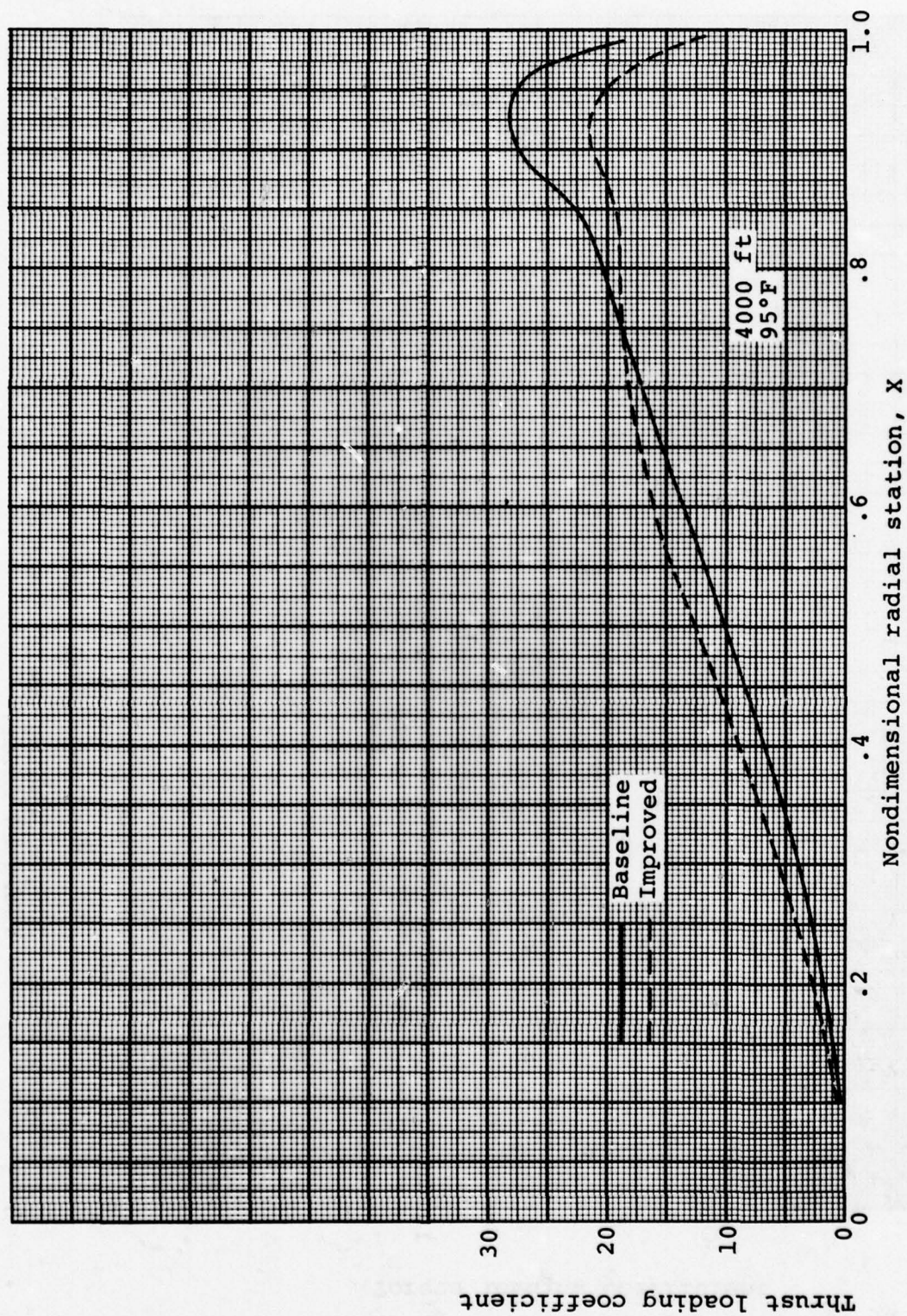


Figure A-19. Thrust loading coefficient distribution, calculated isolated rotor.

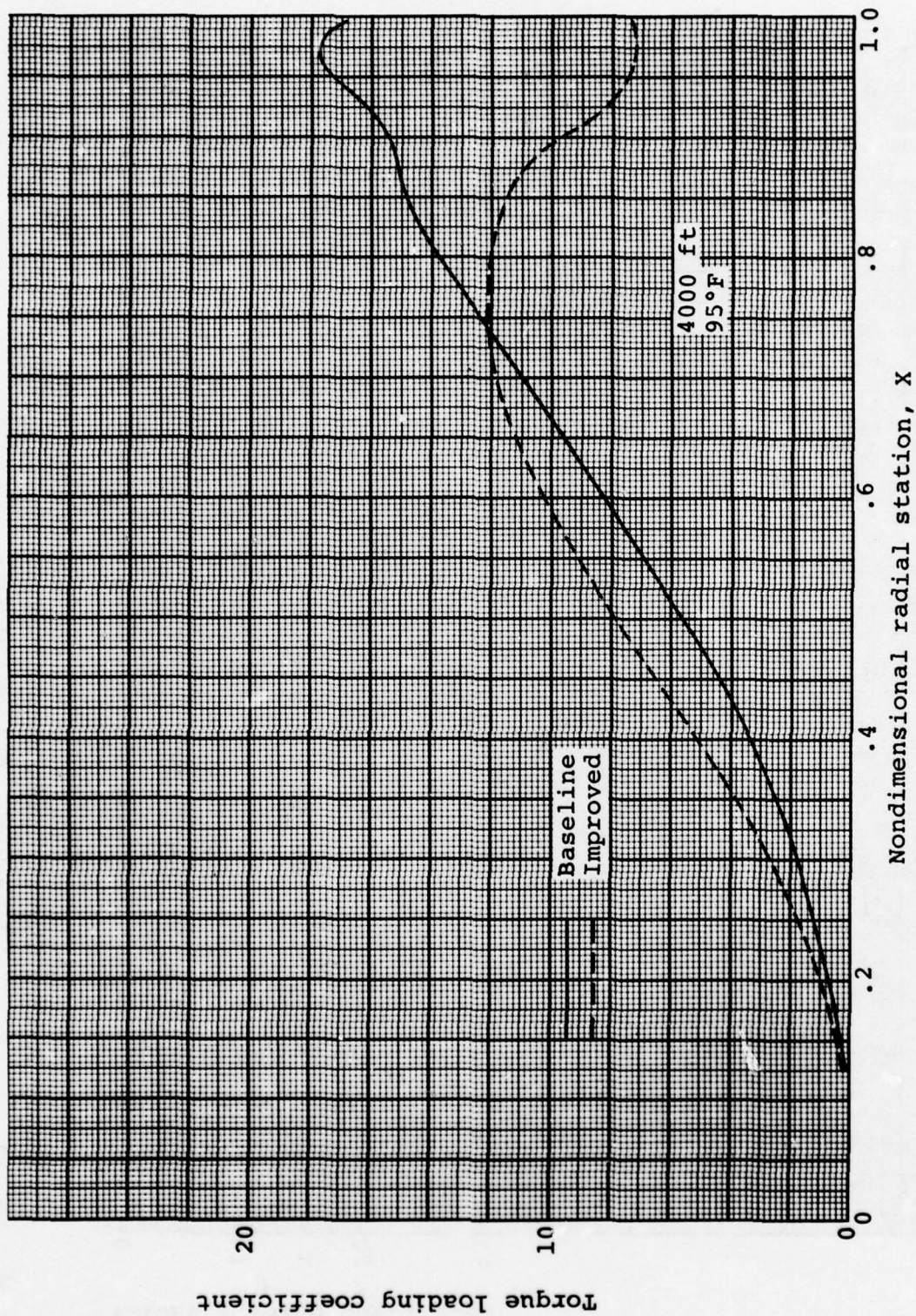


Figure A-20. Torque loading coefficient distribution, calculated isolated rotor.

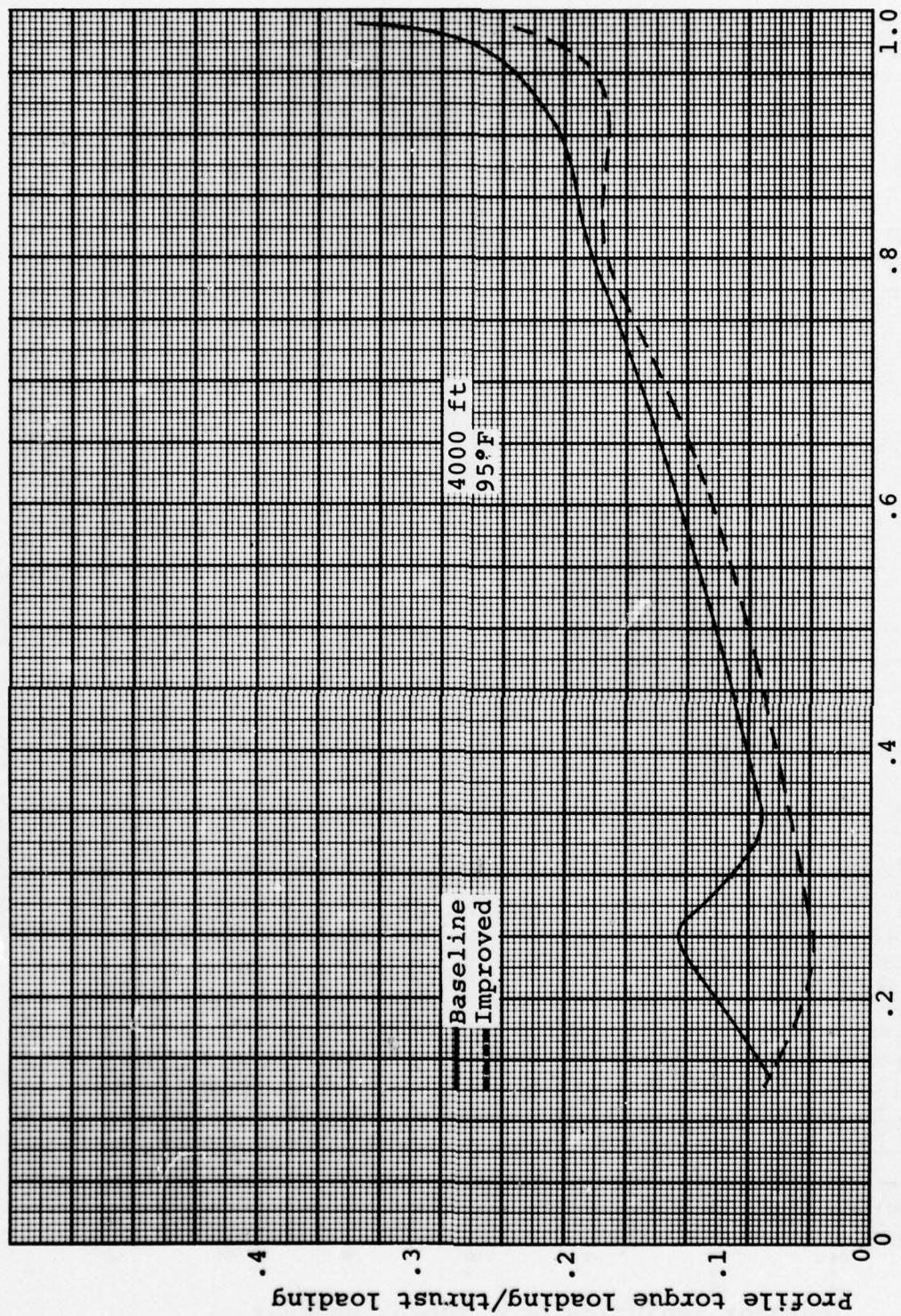


Figure A-21. Profile torque loading/thrust loading distribution, calculated isolated rotor.

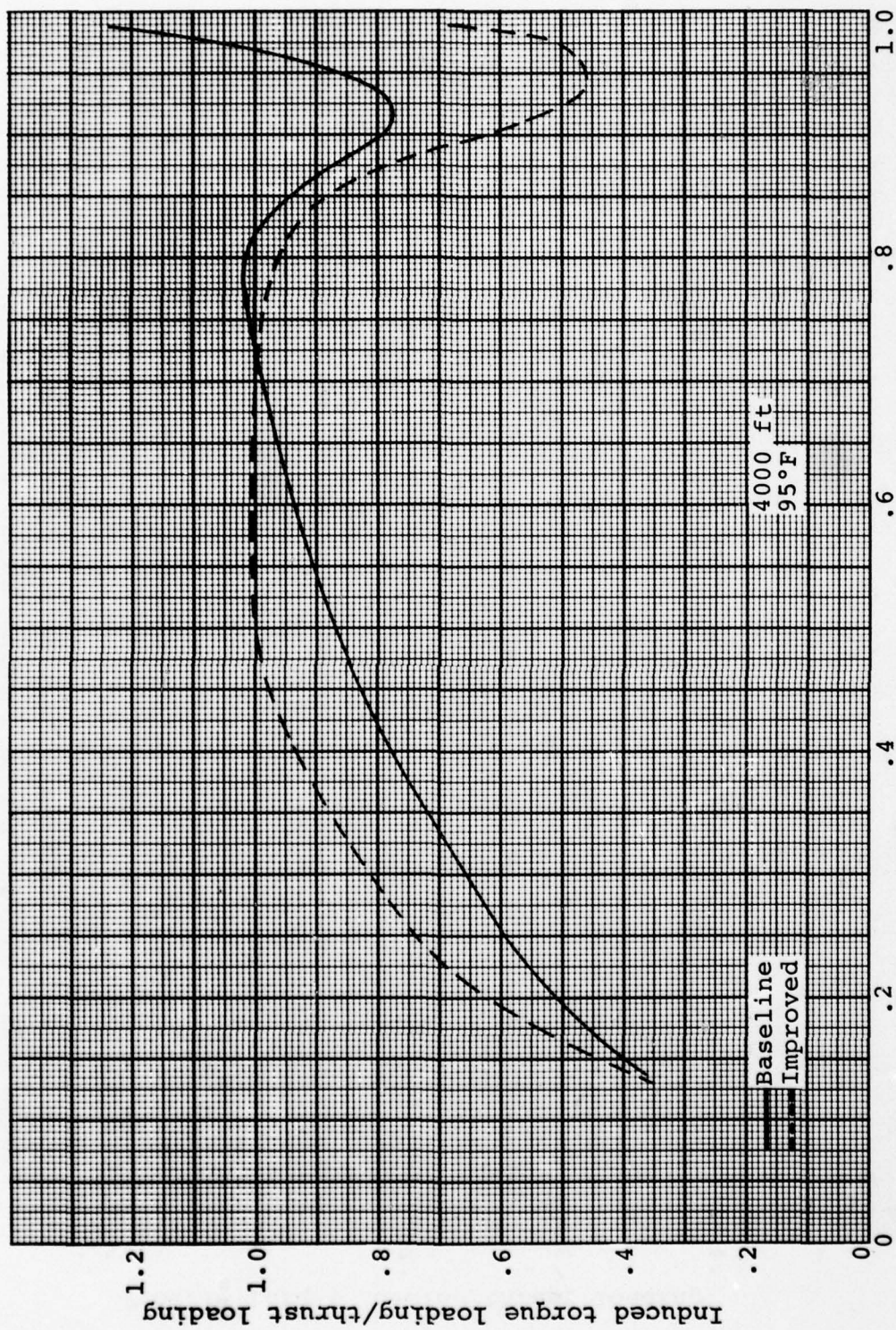


Figure A-22. Induced torque loading/thrust loading distribution, calculated isolated rotor.

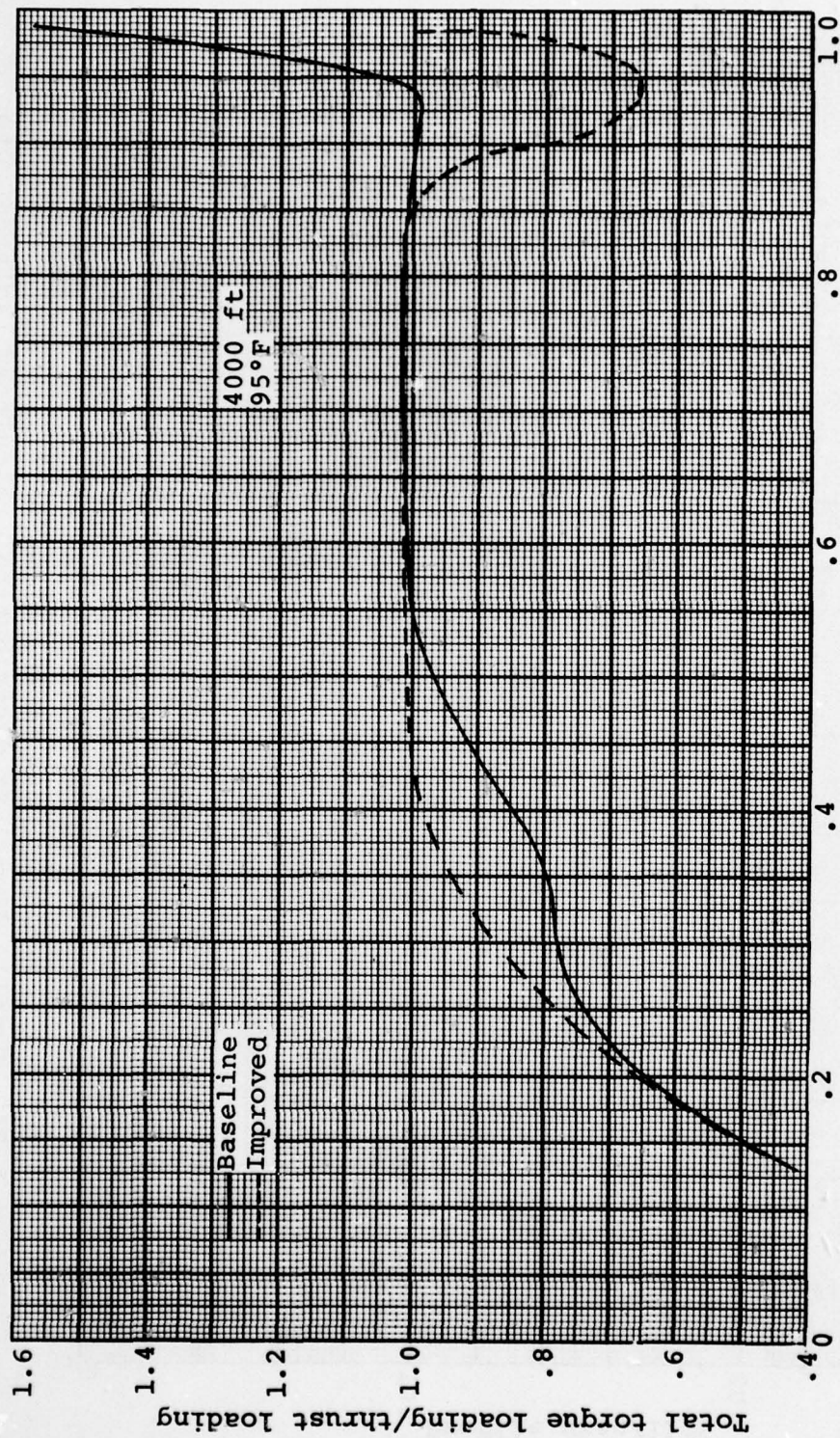


Figure A-23. Total torque loading/thrust loading distribution, calculated isolated rotor.

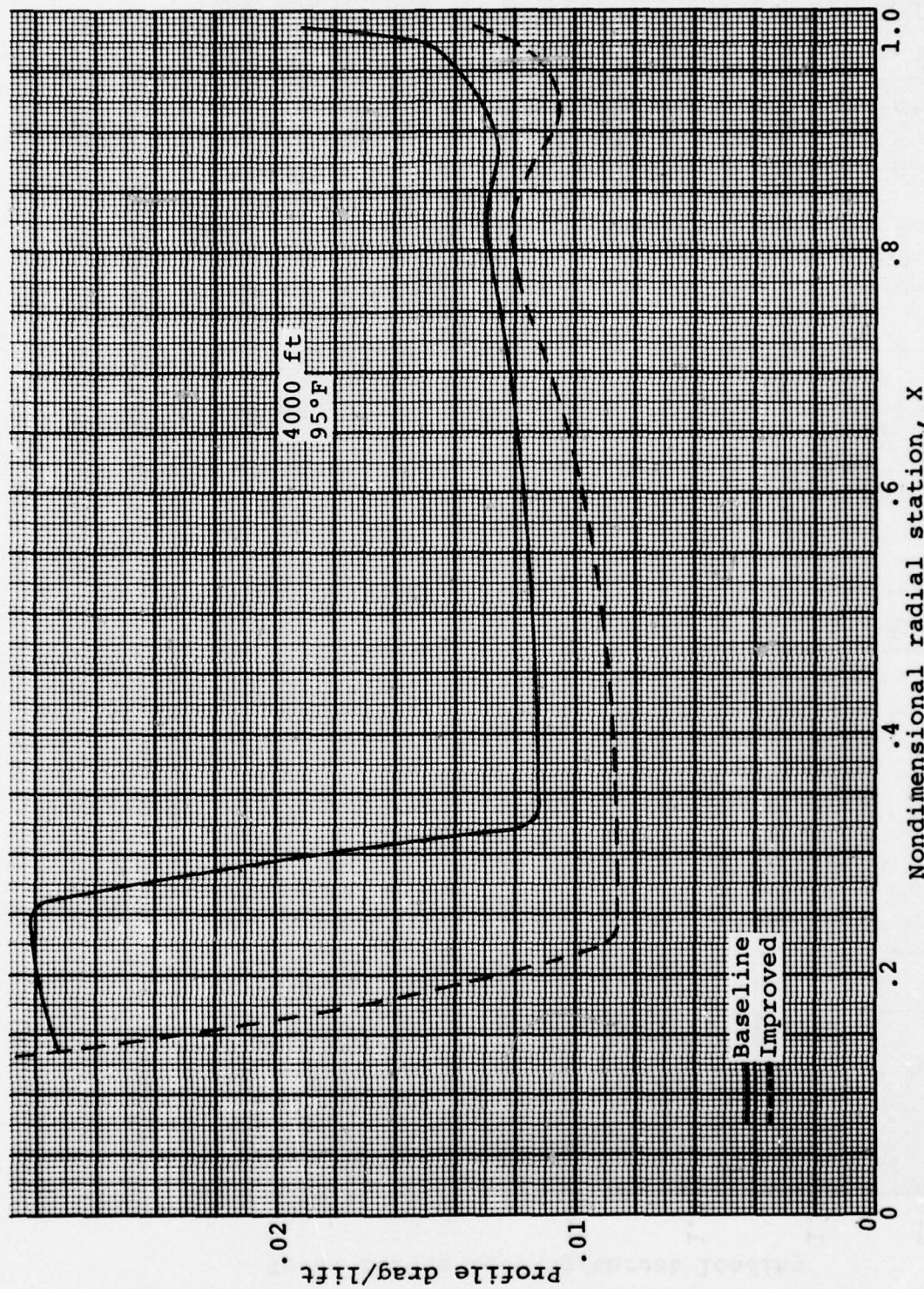


Figure A-24. Profile drag/lift distribution, calculated isolated rotor.

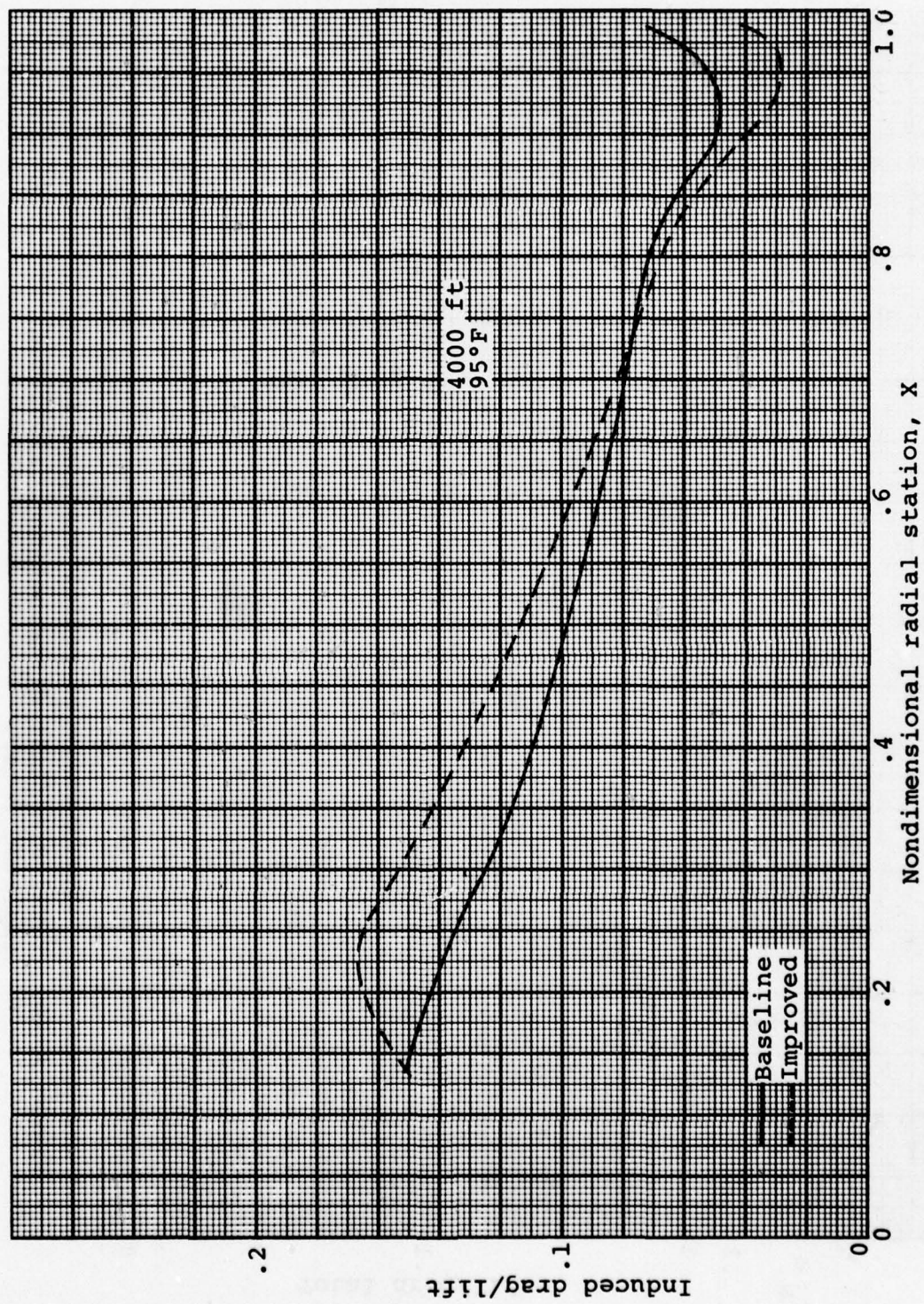


Figure A-25. Induced drag/lift distribution, calculated isolated rotor.

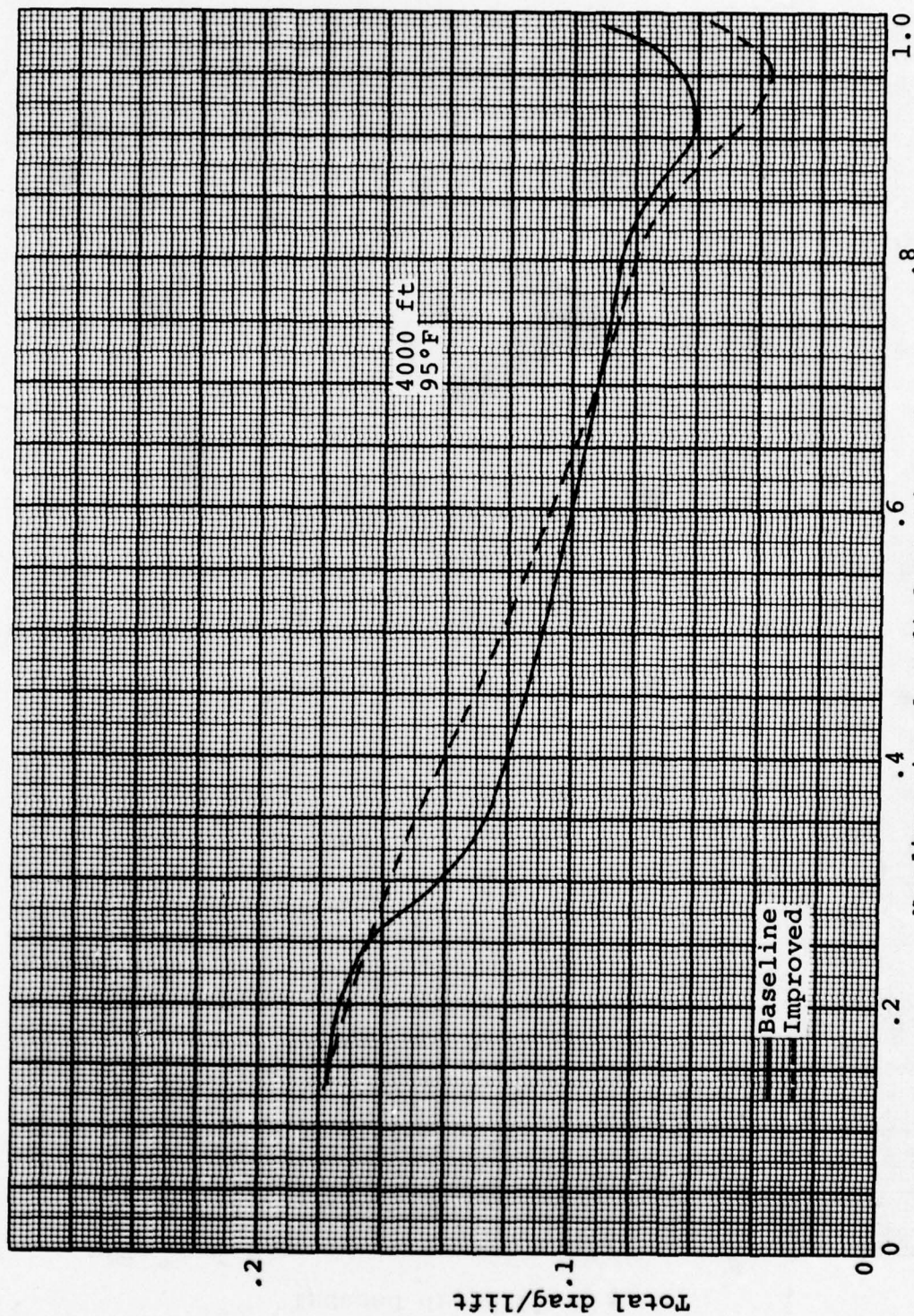


Figure A-26. Total drag/lift distribution, calculated isolated rotor.

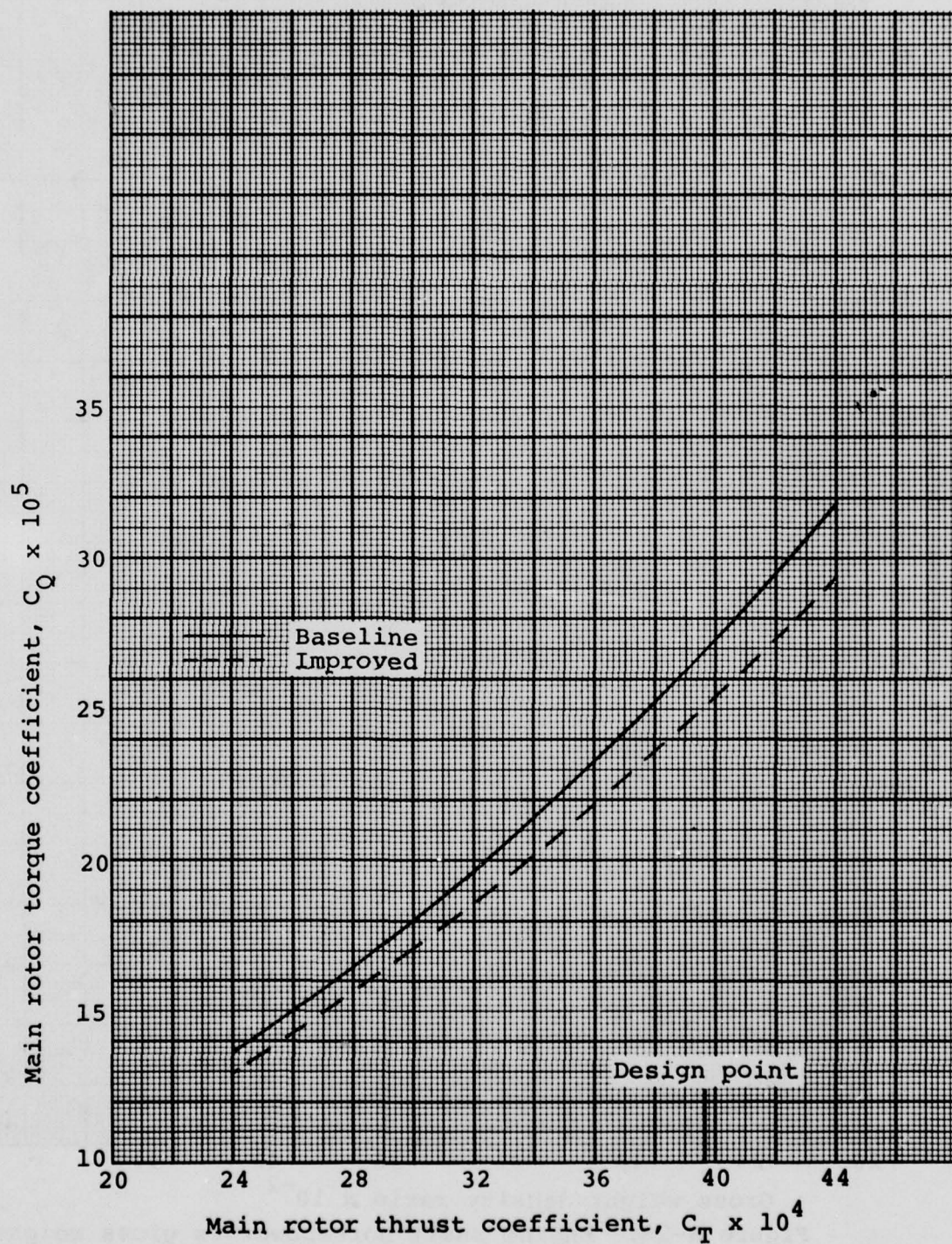


Figure A-27. Rotor alone torque coefficient vs thrust coefficient.

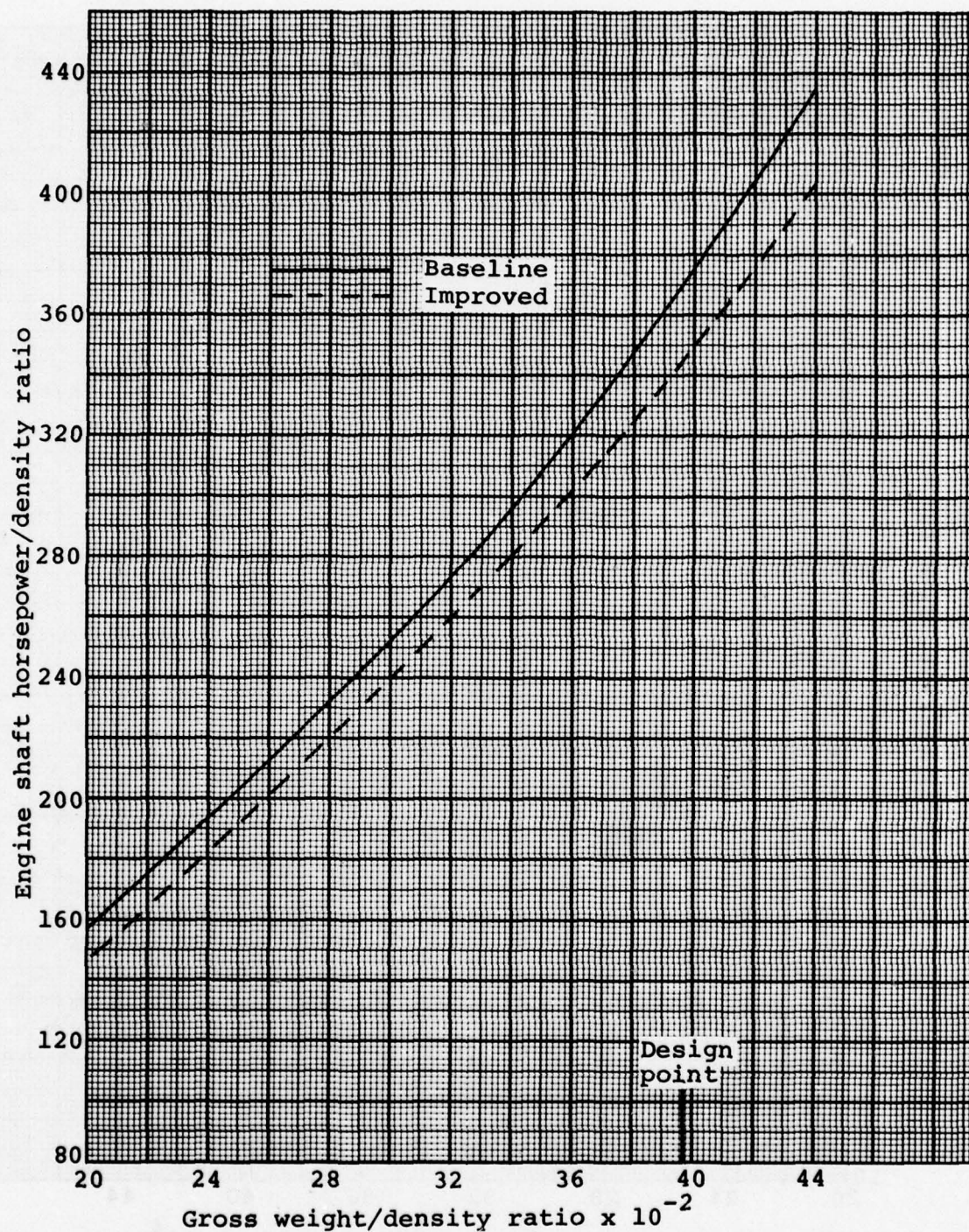


Figure A-28. Engine shaft horsepower vs gross weight for the improved and baseline OH-58C.

A.5.2 Forward Flight

Using calculations based on government-furnished data and FX69-H-098 data, the improved OH-58C blade showed forward flight improvements relative to the baseline rotor.

The helicopter (without losses) C_P - C_T - μ curves and engine shaft horsepower curves versus true airspeed for 3200 and 2400 pounds of gross weight are shown in Figures A-29 and A-30, respectively. As seen in Figure A-30, V_H was increased by 4 knots at maximum continuous power.

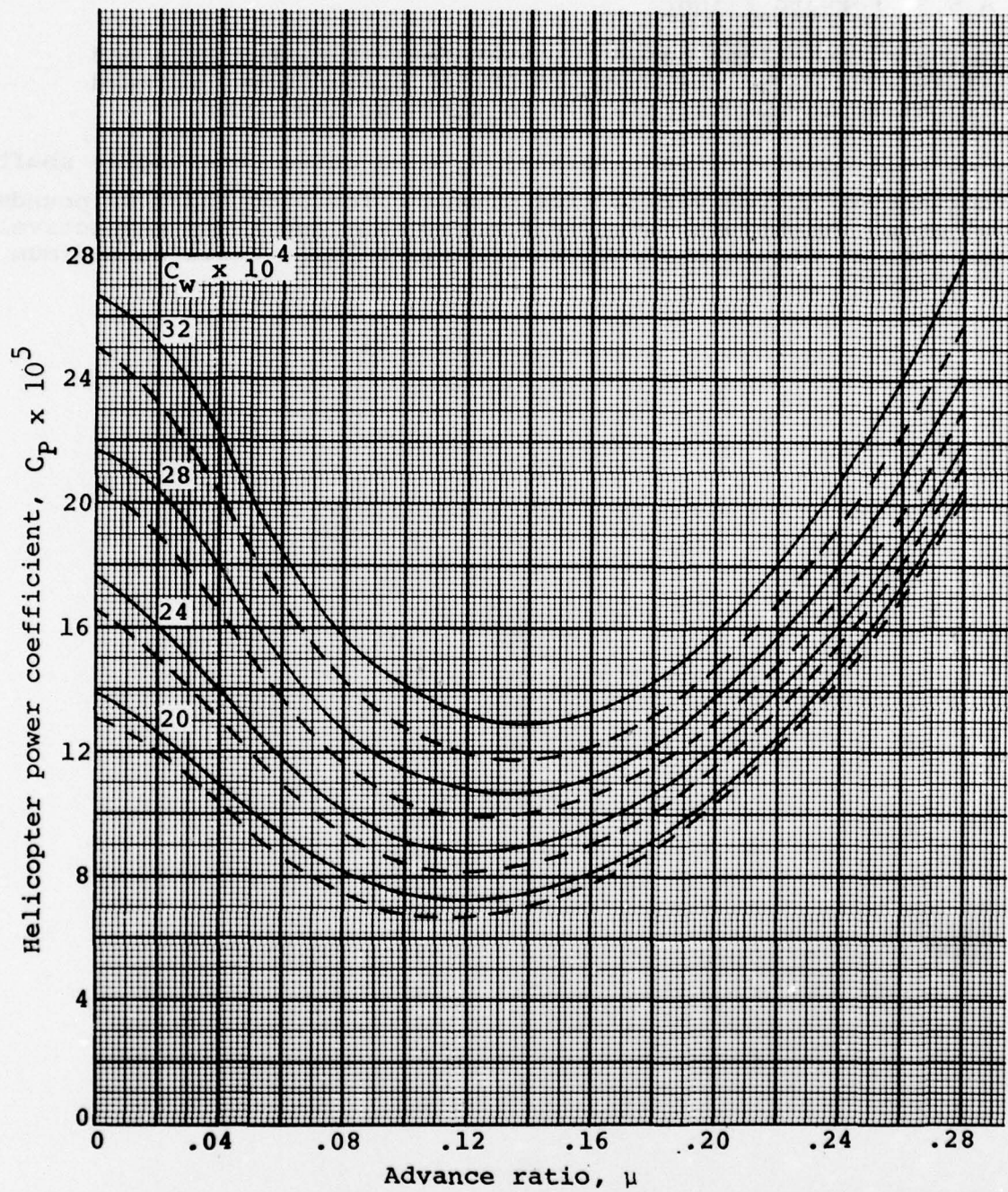


Figure A-29. Nondimensional torque vs advance ratio for improved and baseline OH-58C helicopters without losses.

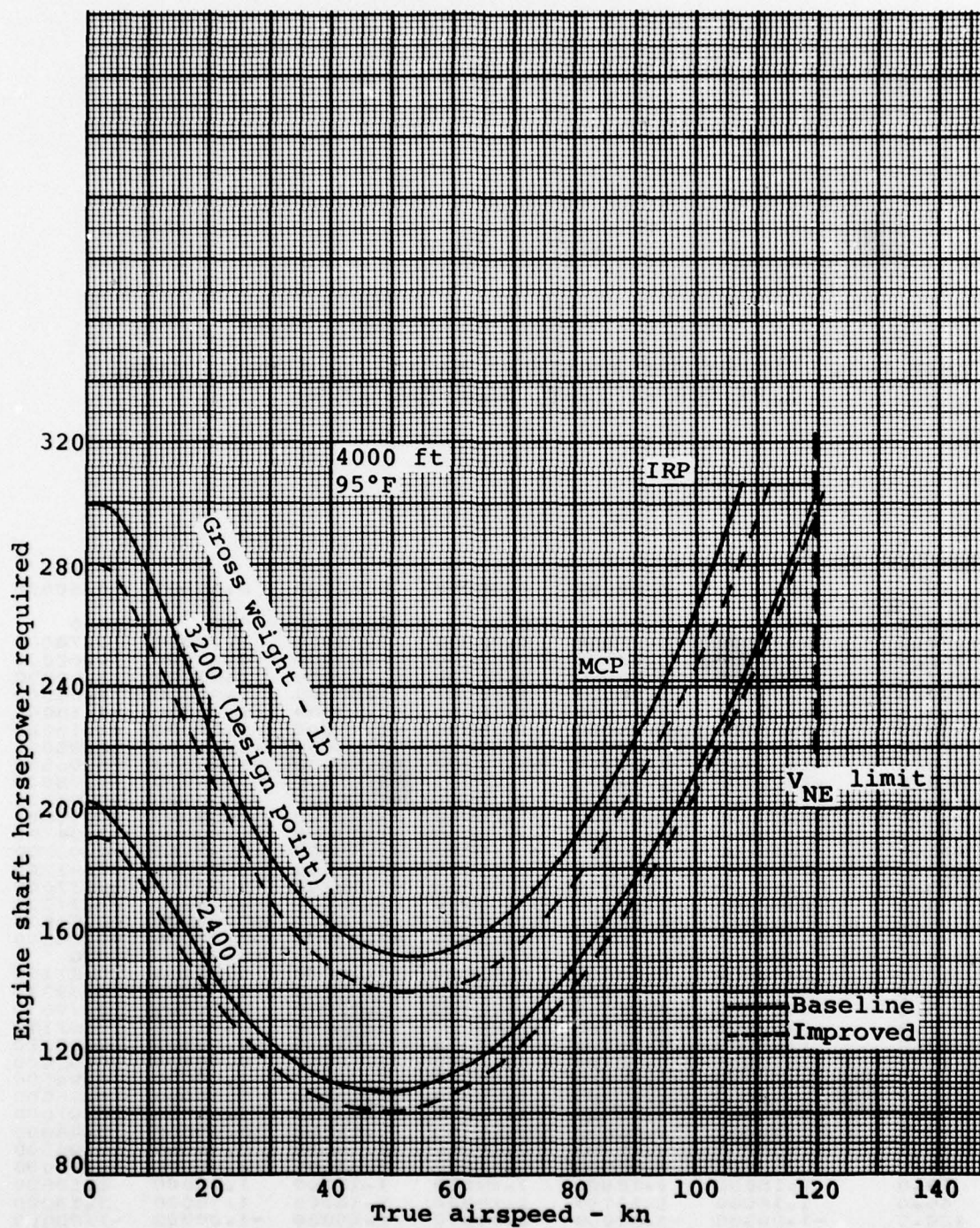


Figure A-30. Engine shaft horsepower vs true airspeed for improved and baseline OH-58C.

APPENDIX B

AIRFOIL DATA

TABLE B-1. GOVERNMENT FURNISHED NACA 0012 AIRFOIL DATA,
LIFT COEFFICIENT, NASA TMX-73990

Angles of Attack	Mach numbers					
	0.0	0.20000	0.30000	0.40000	0.50000	0.60000
-180.0	0.0	0.0	0.0	0.0	0.0	0.0
-172.5	0.78000	0.78000	0.78000	0.78000	0.78000	0.78000
-161.0	0.62000	0.62000	0.62000	0.62000	0.62000	0.62000
-147.0	1.00000	1.00000	1.00000	1.00000	1.00000	1.00000
-129.0	1.00000	1.00000	1.00000	1.00000	1.00000	1.00000
-49.0	-1.18000	-1.18000	-1.18000	-1.18000	-1.18000	-1.18000
-39.0	-1.18000	-1.18000	-1.18000	-1.18000	-1.18000	-1.18000
-21.0	-0.80000	-0.80000	-0.81000	-0.83000	-0.85000	-0.85000
-16.5	-1.00700	-1.00700	-0.94400	-0.96000	-0.96500	-0.96500
-15.0	-1.19000	-1.19000	-1.09000	-1.05500	-0.99000	-0.98000
-14.0	-1.33300	-1.33300	-1.22000	-1.09600	-1.00000	-0.97000
-13.0	-1.33400	-1.33400	-1.28000	-1.12000	-1.00000	-0.96000
-12.0	-1.25500	-1.25500	-1.26000	-1.13000	-1.00000	-0.94700
-11.0	-1.16100	-1.16100	-1.19000	-1.12000	-0.99400	-0.93000
-10.0	-1.05500	-1.05500	-1.01000	-1.08200	-0.98500	-0.91000
-8.0	-0.84400	-0.84400	-0.88000	-0.90700	-0.92200	-0.87000
-6.0	-0.63300	-0.63300	-0.66000	-0.68400	-0.74100	-0.77000
-4.0	-0.46000	-0.46000	-0.46000	-0.48050	-0.52000	-0.56570
-2.0	-0.25000	-0.25000	-0.25000	-0.23990	-0.27000	-0.28200
0.0	0.0	0.0	0.0	0.0	0.0	0.0
2.0	0.23000	0.23000	0.23000	0.24030	0.25000	0.27100
4.0	0.45000	0.45000	0.45000	0.49160	0.51000	0.57310
6.0	0.70000	0.70000	0.70000	0.72240	0.75000	0.79670
8.0	0.89000	0.89000	0.89000	0.94160	0.92200	0.87110
10.0	1.08000	1.08000	1.08000	1.03330	0.98500	0.88020
11.0	1.15000	1.16100	1.19000	1.12000	0.99400	0.93000
12.0	1.21000	1.25500	1.26000	1.13000	1.00000	0.94700
13.0	1.23000	1.33400	1.28000	1.12000	1.00000	0.96000
14.0	1.25000	1.33300	1.22000	0.89750	1.00000	0.97000
15.0	1.14000	1.14000	1.14000	1.01000	0.99000	0.98000
16.5	1.00700	1.00700	0.94400	0.96000	0.96500	0.96500
21.0	0.80000	0.80000	0.81000	0.83000	0.85000	0.85000
39.0	1.18000	1.18000	1.18000	1.18000	1.18000	1.18000
49.0	1.18000	1.18000	1.18000	1.18000	1.18000	1.18000
129.0	-1.00000	-1.00000	-1.00000	-1.00000	-1.00000	-1.00000
147.0	-1.00000	-1.00000	-1.00000	-1.00000	-1.00000	-1.00000
161.0	-0.62000	-0.62000	-0.62000	-0.62000	-0.62000	-0.62000
172.5	-0.78000	-0.78000	-0.78000	-0.78000	-0.78000	-0.78000
180.0	0.0	0.0	0.0	0.0	0.0	0.0

TABLE B-1. CONCLUDED

Angles of Attack	Mach numbers				
	0.70000	0.75000	0.80000	0.90000	1.00000
-180.0	0.0	0.0	0.0	0.0	0.0
-172.5	0.78000	0.78000	0.78000	0.78000	0.78000
-161.0	0.62000	0.62000	0.62000	0.62000	0.62000
-147.0	1.00000	1.00000	1.00000	1.00000	1.00000
-129.0	1.00000	1.00000	1.00000	1.00000	1.00000
-49.0	-1.18000	-1.18000	-1.18000	-1.18000	-1.18000
-39.0	-1.18000	-1.18000	-1.18000	-1.18000	-1.18000
-21.0	-0.85000	-0.71000	-0.68000	-0.64000	-0.64000
-16.5	-0.96500	-0.79500	-0.76000	-0.70000	-0.70000
-15.0	-0.98000	-0.83000	-0.79000	-0.72000	-0.72000
-14.0	-0.97000	-0.84000	-0.80500	-0.73000	-0.73000
-13.0	-0.96000	-0.85000	-0.81500	-0.73500	-0.73500
-12.0	-0.94000	-0.85000	-0.82000	-0.74000	-0.74000
-11.0	-0.92300	-0.85000	-0.81000	-0.74000	-0.74000
-10.0	-0.90000	-0.84500	-0.80500	-0.73000	-0.73000
-8.0	-0.84000	-0.82000	-0.77000	-0.69500	-0.69500
-6.0	-0.75000	-0.77000	-0.72000	-0.59300	-0.59300
-4.0	-0.64010	-0.72440	-0.53000	-0.39600	-0.39600
-2.0	-0.32740	-0.36050	-0.34690	-0.13990	-0.13990
0.0	0.0	0.0	0.0	0.0	0.0
2.0	0.32450	0.34170	0.36760	0.12450	0.12450
4.0	0.62520	0.63680	0.54280	0.46500	0.46500
6.0	0.73670	0.71690	0.64300	0.59300	0.59300
8.0	0.75130	0.70710	0.70000	0.69500	0.69500
10.0	0.86000	0.84500	0.80500	0.73000	0.73000
11.0	0.92300	0.85000	0.81000	0.74000	0.74000
12.0	0.94000	0.85000	0.82000	0.74000	0.74000
13.0	0.96000	0.85000	0.81500	0.73500	0.73500
14.0	0.97000	0.84000	0.80500	0.73000	0.73000
15.0	0.98000	0.83000	0.79000	0.72000	0.72000
16.5	0.96500	0.79500	0.76000	0.70000	0.70000
21.0	0.85000	0.71000	0.68000	0.64000	0.64000
39.0	1.18000	1.18000	1.18000	1.18000	1.18000
49.0	1.18000	1.18000	1.18000	1.18000	1.18000
129.0	-1.00000	-1.00000	-1.00000	-1.00000	-1.00000
147.0	-1.00000	-1.00000	-1.00000	-1.00000	-1.00000
161.0	-0.62000	-0.62000	-0.62000	-0.62000	-0.62000
172.5	-0.78000	-0.78000	-0.78000	-0.78000	-0.78000
180.0	0.0	0.0	0.0	0.0	0.0

TABLE B-2. GOVERNMENT FURNISHED NACA 0012 AIRFOIL DATA,
DRAG COEFFICIENTS, NASA TMX-73990

Angles of Attack	Mach numbers					
	0.0	0.20000	0.30000	0.40000	0.50000	0.60000
-180.0	0.02200	0.02200	0.02200	0.02200	0.02200	0.02200
-175.0	0.06200	0.06200	0.06200	0.06200	0.06200	0.06200
-170.0	0.13200	0.13200	0.13200	0.13200	0.13200	0.13200
-165.0	0.24200	0.24200	0.24200	0.24200	0.24200	0.24200
-160.0	0.30200	0.30200	0.30200	0.30200	0.30200	0.30200
-140.0	1.04200	1.04200	1.04200	1.04200	1.04200	1.04200
-120.0	1.65200	1.65200	1.65200	1.65200	1.65200	1.65200
-110.0	1.85200	1.85200	1.85200	1.85200	1.85200	1.85600
-100.0	2.02200	2.02200	2.02200	2.02200	2.02200	2.02200
-90.0	2.02200	2.02200	2.02200	2.02200	2.02200	2.02200
-80.0	1.96200	1.96200	1.96200	1.96200	1.96200	1.96200
-70.0	1.84200	1.84200	1.84200	1.84200	1.84200	1.84200
-60.0	1.66200	1.66200	1.66200	1.66200	1.66200	1.66200
-50.0	1.39200	1.39200	1.39200	1.39200	1.39200	1.39200
-30.0	0.56200	0.56200	0.56200	0.56200	0.56200	0.56200
-21.0	0.33200	0.33200	0.33200	0.33200	0.33200	0.33200
-16.0	0.15500	0.15500	0.18100	0.20700	0.23500	0.25700
-15.0	0.10200	0.10200	0.14800	0.18100	0.20900	0.23300
-14.0	0.03800	0.03800	0.09900	0.14600	0.18000	0.21200
-13.0	0.02640	0.02640	0.04550	0.09400	0.14800	0.19100
-12.0	0.02200	0.02200	0.03000	0.06000	0.11100	0.16400
-11.0	0.01960	0.01960	0.02320	0.03800	0.07800	0.13500
-10.0	0.01740	0.01740	0.01890	0.02590	0.05300	0.10500
-9.0	0.01540	0.01540	0.01590	0.01870	0.03510	0.07700
-8.0	0.01380	0.01380	0.01380	0.01470	0.02200	0.05300
-7.0	0.01220	0.01220	0.01220	0.01230	0.01410	0.03500
-6.0	0.01100	0.01100	0.01100	0.01100	0.01100	0.02120
-5.0	0.01000	0.01000	0.01000	0.01000	0.01000	0.01320
-4.0	0.00710	0.00710	0.00710	0.00710	0.00710	0.00760
-3.0	0.00670	0.00670	0.00670	0.00670	0.00680	0.00710
-2.0	0.00650	0.00650	0.00650	0.00650	0.00670	0.00670
-1.0	0.00650	0.00650	0.00650	0.00650	0.00660	0.00660
0.0	0.00640	0.00640	0.00640	0.00640	0.00650	0.00660
1.0	0.00650	0.00650	0.00650	0.00650	0.00660	0.00660
2.0	0.00660	0.00660	0.00660	0.00660	0.00670	0.00670
3.0	0.00680	0.00680	0.00680	0.00680	0.00680	0.00710
4.0	0.00710	0.00710	0.00710	0.00710	0.00710	0.00760
5.0	0.00760	0.00760	0.00760	0.00750	0.00760	0.01050
6.0	0.00820	0.00820	0.00820	0.00820	0.00850	0.02050
7.0	0.00880	0.00880	0.00880	0.00880	0.01410	0.03090
8.0	0.00970	0.00970	0.00970	0.01060	0.02200	0.04120
9.0	0.01020	0.01020	0.01020	0.01350	0.03510	0.05610
10.0	0.01500	0.01500	0.01500	0.01750	0.05300	0.07100
11.0	0.01960	0.01960	0.02320	0.03800	0.05550	0.13500
12.0	0.02200	0.02200	0.03000	0.03460	0.06800	0.16400
13.0	0.02640	0.02640	0.04550	0.05600	0.14800	0.19100
14.0	0.03800	0.03800	0.08050	0.08050	0.18000	0.21200
15.0	0.10200	0.10200	0.14800	0.18100	0.20900	0.23300
16.0	0.15500	0.15500	0.18100	0.20700	0.23500	0.25700
21.0	0.33200	0.33200	0.33200	0.33200	0.33200	0.33200
30.0	0.56200	0.56200	0.56200	0.56200	0.56200	0.56200
50.0	1.39200	1.39200	1.39200	1.39200	1.39200	1.39200
60.0	1.66200	1.66200	1.66200	1.66200	1.66200	1.66200
70.0	1.84200	1.84200	1.84200	1.84200	1.84200	1.84200
80.0	1.96200	1.96200	1.96200	1.96200	1.96200	1.96200
90.0	2.02200	2.02200	2.02200	2.02200	2.02200	2.02200
100.0	2.02200	2.02200	2.02200	2.02200	2.02200	2.02200
110.0	1.85200	1.85200	1.85200	1.85200	1.85200	1.85200
120.0	1.65200	1.65200	1.65200	1.65200	1.65200	1.65200
140.0	1.04200	1.04200	1.04200	1.04200	1.04200	1.04200
160.0	0.30200	0.30200	0.30200	0.30200	0.30200	0.30200
165.0	0.24200	0.24200	0.24200	0.24200	0.24200	0.24200
170.0	0.13200	0.13200	0.13200	0.13200	0.13200	0.13200
175.0	0.06200	0.06200	0.06200	0.06200	0.06200	0.06200
180.0	0.02200	0.02200	0.02200	0.02200	0.02200	0.02200

TABLE B-2. CONCLUDED

Angles of Attack	Mach numbers				
	0.70000	0.75000	0.80000	0.90000	1.00000
-180.0	0.02200	0.02200	0.02200	0.02200	0.02200
-175.0	0.06200	0.06200	0.06200	0.06200	0.06200
-170.0	0.13200	0.13200	0.13200	0.13200	0.13200
-165.0	0.24200	0.24200	0.24200	0.24200	0.24200
-160.0	0.30200	0.30200	0.30200	0.30200	0.30200
-140.0	1.04200	1.04200	1.04200	1.04200	1.04200
-120.0	1.65200	1.65200	1.65200	1.65200	1.65200
-110.0	1.85200	1.85200	1.85200	1.85200	1.85200
-100.0	2.02200	2.02200	2.02200	2.02200	2.02200
-90.0	2.02200	2.02200	2.02200	2.02200	2.02200
-80.0	1.96200	1.96200	1.96200	1.96200	1.96200
-70.0	1.84200	1.84200	1.84200	1.84200	1.84200
-60.0	1.66200	1.66200	1.66200	1.66200	1.66200
-50.0	1.39200	1.39200	1.39200	1.39200	1.39200
-30.0	0.56200	0.56200	0.56200	0.56200	0.56200
-21.0	0.33200	0.33200	0.33200	0.33200	0.33200
-16.0	0.27400	0.29200	0.30500	0.34200	0.34200
-15.0	0.25200	0.27100	0.28200	0.29800	0.29800
-14.0	0.23300	0.24900	0.26000	0.29300	0.29300
-13.0	0.21600	0.23100	0.23900	0.27200	0.29200
-12.0	0.19800	0.21100	0.22000	0.25200	0.29100
-11.0	0.17000	0.19200	0.20200	0.23200	0.27500
-10.0	0.14500	0.17600	0.18600	0.21300	0.25400
-9.0	0.12200	0.15900	0.17200	0.19900	0.23200
-8.0	0.10100	0.14000	0.15500	0.18300	0.21400
-7.0	0.08200	0.11100	0.13900	0.16900	0.19200
-6.0	0.06150	0.08200	0.12000	0.14000	0.17000
-5.0	0.03800	0.05400	0.04800	0.11100	0.14000
-4.0	0.02590	0.04810	0.06330	0.09500	0.11200
-3.0	0.01390	0.02990	0.04550	0.08600	0.10200
-2.0	0.00820	0.01210	0.02870	0.08360	0.08360
-1.0	0.00720	0.00800	0.01380	0.06120	0.06120
0.0	0.00710	0.00760	0.00930	0.04420	0.04420
1.0	0.00720	0.00800	0.01380	0.06120	0.06120
2.0	0.00820	0.01210	0.02870	0.08360	0.08360
3.0	0.01410	0.02990	0.04550	0.08600	0.10200
4.0	0.02590	0.04810	0.06330	0.09500	0.11200
5.0	0.05110	0.06560	0.07240	0.11100	0.14000
6.0	0.06460	0.08040	0.08180	0.14000	0.17000
7.0	0.08040	0.10100	0.13900	0.16900	0.19200
8.0	0.10090	0.15330	0.15500	0.18300	0.21400
9.0	0.11520	0.15900	0.17200	0.19900	0.23200
10.0	0.13020	0.17600	0.18600	0.21300	0.25400
11.0	0.17000	0.19200	0.20200	0.23200	0.27500
12.0	0.19800	0.21100	0.22000	0.25200	0.29100
13.0	0.21600	0.23100	0.23900	0.27200	0.29200
14.0	0.23300	0.24900	0.26000	0.29300	0.29300
15.0	0.25200	0.27100	0.28200	0.29800	0.29800
16.0	0.27400	0.29200	0.30500	0.34200	0.34200
21.0	0.33200	0.33200	0.33200	0.33200	0.33200
30.0	0.56200	0.56200	0.56200	0.56200	0.56200
50.0	1.39200	1.39200	1.39200	1.39200	1.39200
60.0	1.66200	1.66200	1.66200	1.66200	1.66200
70.0	1.84200	1.84200	1.84200	1.84200	1.84200
80.0	1.96200	1.96200	1.96200	1.96200	1.96200
90.0	2.02200	2.02200	2.02200	2.02200	2.02200
100.0	2.02200	2.02200	2.02200	2.02200	2.02200
110.0	1.85200	1.85200	1.85200	1.85200	1.85200
120.0	1.65200	1.65200	1.65200	1.65200	1.65200
140.0	1.04200	1.04200	1.04200	1.04200	1.04200
160.0	0.30200	0.30200	0.30200	0.30200	0.30200
165.0	0.24200	0.24200	0.24200	0.24200	0.24200
170.0	0.13200	0.13200	0.13200	0.13200	0.13200
175.0	0.06200	0.06200	0.06200	0.06200	0.06200
180.0	0.02200	0.02200	0.02200	0.02200	0.02200

TABLE B-3. FX69-H-098 AIRFOIL DATA, LIFT COEFFICIENTS,
NASA TMX-73990

Angles Of Attack	Mach numbers	0.0	0.35000	0.44000	0.50000	0.59000	0.64000
-180.0	0.0	0.0	0.0	0.0	0.0	0.0	0.0
-172.0	0.78000	0.78000	0.78000	0.78000	0.78000	0.78000	0.78000
-160.0	0.62000	0.62000	0.62000	0.62000	0.62000	0.62000	0.62000
-146.0	1.00000	1.00000	1.00000	1.00000	1.00000	1.00000	1.00000
-128.0	1.00000	1.00000	1.00000	1.00000	1.00000	1.00000	1.00000
-47.8	-1.18000	-1.18000	-1.18000	-1.18000	-1.18000	-1.18000	-1.18000
-37.8	-1.18000	-1.18000	-1.18000	-1.18000	-1.18000	-1.18000	-1.18000
-19.8	-0.78000	-0.78000	-0.84000	-0.87500	-0.93000	-0.90000	-0.90000
-16.8	-0.86000	-0.86000	-0.92000	-0.94000	-0.96500	-0.96500	-0.96500
-12.8	-0.92000	-0.92000	-0.92000	-0.92000	-0.92500	-0.92500	-0.94500
-10.8	-0.90000	-0.90000	-0.90000	-0.86000	-0.77000	-0.88000	-0.90000
-9.0	-0.77000	-0.77000	-0.77000	-0.80000	-0.73000	-0.84000	-0.85000
-6.2	-0.61600	-0.61600	-0.65000	-0.64000	-0.64000	-0.70000	-0.74000
-4.2	-0.33600	-0.33600	-0.46500	-0.46500	-0.49000	-0.48500	-0.56000
-2.2	-0.15600	-0.15600	-0.21000	-0.23000	-0.24000	-0.24000	-0.24000
-1.2	-0.06200	-0.06200	-0.08000	-0.10000	-0.10500	-0.10500	-0.09000
-0.2	0.03800	0.03800	0.04000	0.03000	0.04000	0.04000	0.04000
1.8	0.26000	0.26000	0.27700	0.29500	0.32000	0.32000	0.34000
2.8	0.38000	0.38000	0.39500	0.41500	0.45500	0.45500	0.48500
3.8	0.49500	0.49500	0.51000	0.53500	0.58500	0.61500	0.61500
4.8	0.60500	0.60500	0.62500	0.65500	0.71500	0.76000	0.76000
6.8	0.84500	0.84500	0.87000	0.88000	0.97000	0.93000	0.93000
8.8	1.07000	1.07000	1.06000	1.09500	1.10500	1.00800	1.00800
9.8	1.16400	1.16400	1.10800	1.20000	1.11000	1.01000	1.01000
10.8	1.23000	1.23000	1.16500	1.23000	1.11500	0.99000	0.99000
11.8	1.26300	1.26300	1.18500	1.24000	1.08000	0.96000	0.96000
12.8	1.28000	1.28000	1.19000	1.22000	1.07000	0.93000	0.93000
14.8	1.24000	1.24000	1.13000	1.15000	1.03000	0.91000	0.91000
17.0	1.01000	1.01000	1.02000	1.03000	0.96000	0.92000	0.92000
22.2	0.81000	0.81000	0.85000	0.90000	0.93000	0.94000	0.94000
40.2	1.18000	1.18000	1.18000	1.18000	1.18000	1.18000	1.18000
50.2	1.18000	1.18000	1.18000	1.18000	1.18000	1.18000	1.18000
130.2	-1.00000	-1.00000	-1.00000	-1.00000	-1.00000	-1.00000	-1.00000
148.2	-1.00000	-1.00000	-1.00000	-1.00000	-1.00000	-1.00000	-1.00000
162.2	-0.62000	-0.62000	-0.62000	-0.62000	-0.62000	-0.62000	-0.62000
173.7	-0.78000	-0.78000	-0.78000	-0.78000	-0.78000	-0.78000	-0.78000
180.0	0.0	0.0	0.0	0.0	0.0	0.0	0.0

TABLE B-3. CONCLUDED

Angles Of Attack	Mach numbers					
	0.69000	0.74000	0.80000	0.84000	0.90000	1.00000
-180.0	0.0	0.0	0.0	0.0	0.0	0.0
-172.0	0.78000	0.78000	0.78000	0.78000	0.78000	0.78000
-160.0	0.62000	0.62000	0.62000	0.62000	0.62000	0.62000
-146.0	1.00000	1.00000	1.00000	1.00000	1.00000	1.00000
-120.0	1.00000	1.00000	1.00000	1.00000	1.00000	1.00000
-47.8	-1.18000	-1.18000	-1.18000	-1.18000	-1.18000	-1.18000
-37.8	-1.18000	-1.18000	-1.18000	-1.18000	-1.18000	-1.18000
-19.8	-0.88000	-0.83000	-0.80000	-0.76000	-0.72000	-0.72000
-15.8	-0.97000	-0.86000	-0.80000	-0.75000	-0.70000	-0.70000
-12.8	-0.96000	-0.85500	-0.80500	-0.74000	-0.68000	-0.68000
-10.8	-0.92500	-0.85000	-0.81000	-0.73000	-0.66000	-0.66000
-9.0	-0.86500	-0.84000	-0.80000	-0.71000	-0.58000	-0.58000
-6.2	-0.75000	-0.77000	-0.73000	-0.62000	-0.43000	-0.43000
-4.2	-0.57500	-0.63500	-0.60000	-0.53000	-0.32000	-0.32000
-2.2	-0.27000	-0.30000	-0.35000	-0.40000	-0.19000	-0.19000
-1.2	-0.11000	-0.11500	-0.16000	-0.20000	-0.13000	-0.13000
-0.2	0.05000	0.05000	0.05000	0.03500	-0.07000	-0.07000
1.8	0.34000	0.39000	0.45000	0.35500	0.13000	0.13000
2.8	0.49000	0.52000	0.49500	0.40000	0.25000	0.25000
3.8	0.64000	0.62500	0.52500	0.44000	0.33000	0.33000
4.8	0.76500	0.67000	0.56000	0.48000	0.41000	0.41000
6.8	0.89300	0.72000	0.61000	0.55000	0.50000	0.50000
8.8	0.94000	0.75000	0.66000	0.60000	0.55000	0.55000
9.8	0.92000	0.75500	0.68000	0.63000	0.57500	0.57500
10.8	0.92000	0.76200	0.70000	0.65000	0.60000	0.60000
11.8	0.91000	0.76600	0.71000	0.66500	0.62000	0.62000
12.8	0.90000	0.77000	0.71500	0.68000	0.64000	0.64000
14.8	0.90000	0.76000	0.71000	0.70000	0.68000	0.68000
17.0	0.91000	0.74000	0.70000	0.70000	0.70000	0.70000
22.2	0.95000	0.72000	0.68000	0.67000	0.65000	0.65000
40.2	1.18000	1.18000	1.18000	1.18000	1.18000	1.18000
60.2	1.18000	1.18000	1.18000	1.18000	1.18000	1.18000
136.2	-1.00000	-1.00000	-1.00000	-1.00000	-1.00000	-1.00000
148.2	-1.00000	-1.00000	-1.00000	-1.00000	-1.00000	-1.00000
162.2	-0.62000	-0.62000	-0.62000	-0.62000	-0.62000	-0.62000
173.7	-0.78000	-0.78000	-0.78000	-0.78000	-0.78000	-0.78000
180.0	0.0	0.0	0.0	0.0	0.0	0.0

TABLE B-4. FX69-H-098 AIRFOIL DATA, DRAG COEFFICIENTS,
MACH NUMBERS 0.0 THROUGH 0.59, NASA TMX-73990

Angles Of Attack	Mach numbers	0.0	0.35000	0.44000	0.50000	0.54000	0.59000
-180.0	0.02200	0.02200	0.02200	0.02200	0.02200	0.02200	0.02200
-174.0	0.06200	0.06200	0.06200	0.06200	0.06200	0.06200	0.06200
-169.0	0.13200	0.13200	0.13200	0.13200	0.13200	0.13200	0.13200
-164.0	0.24200	0.24200	0.24200	0.24200	0.24200	0.24200	0.24200
-159.0	0.30200	0.30200	0.30200	0.30200	0.30200	0.30200	0.30200
-139.0	1.04200	1.04200	1.04200	1.04200	1.04200	1.04200	1.04200
-119.0	1.65200	1.65200	1.65200	1.65200	1.65200	1.65200	1.65200
-109.0	1.85200	1.85200	1.85200	1.85200	1.85200	1.85200	1.85200
-98.8	2.00200	2.00200	2.00200	2.00200	2.00200	2.00200	2.00200
-88.8	2.02200	2.02200	2.02200	2.02200	2.02200	2.02200	2.02200
-78.8	1.96200	1.96200	1.96200	1.96200	1.96200	1.96200	1.96200
-68.8	1.84200	1.84200	1.84200	1.84200	1.84200	1.84200	1.84200
-58.8	1.66200	1.66200	1.66200	1.66200	1.66200	1.66200	1.66200
-48.8	1.39200	1.39200	1.39200	1.39200	1.39200	1.39200	1.39200
-28.8	0.56200	0.56200	0.56200	0.56200	0.56200	0.56200	0.56200
-19.8	0.33200	0.33200	0.33200	0.33200	0.33200	0.33200	0.33200
-14.8	0.21000	0.21000	0.21000	0.21000	0.21000	0.21000	0.21000
-12.8	0.17500	0.17500	0.17500	0.17500	0.17500	0.17500	0.17500
-10.8	0.14500	0.14500	0.14500	0.14500	0.14500	0.14500	0.14500
-9.0	0.12000	0.12000	0.12000	0.12000	0.12000	0.12000	0.12000
-7.0	0.07500	0.07500	0.07500	0.07500	0.07500	0.07500	0.07500
-5.0	0.02500	0.02500	0.02500	0.02500	0.02500	0.02500	0.02500
-3.2	0.00700	0.00700	0.00700	0.00700	0.00700	0.00700	0.00700
-2.2	0.00680	0.00680	0.00680	0.00680	0.00680	0.00680	0.00680
-1.2	0.00660	0.00660	0.00660	0.00660	0.00660	0.00660	0.00660
-0.2	0.00650	0.00650	0.00650	0.00650	0.00650	0.00650	0.00650
1.0	0.00640	0.00640	0.00640	0.00640	0.00640	0.00640	0.00640
1.8	0.00640	0.00640	0.00640	0.00640	0.00640	0.00640	0.00640
2.8	0.00650	0.00650	0.00650	0.00650	0.00650	0.00650	0.00650
3.8	0.00650	0.00650	0.00650	0.00650	0.00650	0.00650	0.00650
4.8	0.00650	0.00650	0.00650	0.00650	0.00650	0.00650	0.00650
5.8	0.00660	0.00660	0.00660	0.00660	0.00660	0.00660	0.00660
6.8	0.00700	0.00700	0.00700	0.00700	0.00700	0.00700	0.00700
7.8	0.00760	0.00760	0.00760	0.00760	0.00760	0.00760	0.00760
8.8	0.00840	0.00840	0.00840	0.00840	0.00840	0.00840	0.00840
9.8	0.00910	0.00910	0.00910	0.00910	0.00910	0.00910	0.00910
10.8	0.00980	0.00980	0.00980	0.00980	0.00980	0.00980	0.00980

TABLE B-4. CONCLUDED

Angles Of Attack	0.01070	0.01070	0.01200	0.01050	0.02650	0.07200
11.8	0.01350	0.01350	0.01400	0.03500	0.03900	0.11000
12.8	0.02400	0.02400	0.03750	0.06500	0.06400	0.14000
13.8	0.06500	0.06500	0.07200	0.09000	0.11500	0.17000
14.8	0.10000	0.10000	0.11000	0.13700	0.15800	0.19500
15.8	0.14000	0.14000	0.15000	0.19500	0.19000	0.21700
17.8	0.17000	0.17000	0.17500	0.21800	0.22000	0.24000
22.2	0.34000	0.34000	0.34000	0.34000	0.34000	0.34000
31.2	0.56000	0.56000	0.56000	0.56000	0.56000	0.56000
51.2	1.38000	1.38000	1.38000	1.38000	1.38000	1.38000
61.2	1.65000	1.65000	1.65000	1.65000	1.65000	1.65000
71.2	1.84000	1.84000	1.84000	1.84000	1.84000	1.84000
81.2	1.96000	1.96000	1.96000	1.96000	1.96000	1.96000
91.2	2.02000	2.02000	2.02000	2.02000	2.02000	2.02000
101.2	2.00000	2.00000	2.00000	2.00000	2.00000	2.00000
111.2	1.85000	1.85000	1.85000	1.85000	1.85000	1.85000
121.2	1.65200	1.65200	1.65200	1.65200	1.65200	1.65200
141.2	1.04200	1.04200	1.04200	1.04200	1.04200	1.04200
161.2	0.30200	0.30200	0.30200	0.30200	0.30200	0.30200
166.2	0.24200	0.24200	0.24200	0.24200	0.24200	0.24200
171.2	0.13200	0.13200	0.13200	0.13200	0.13200	0.13200
176.2	0.06200	0.06200	0.06200	0.06200	0.06200	0.06200
180.0	0.02200	0.02200	0.02200	0.02200	0.02200	0.02200

TABLE B-5. FX69-H-098 AIRFOIL DATA, DRAG COEFFICIENTS,
MA² NUMBERS 0.64 THROUGH 0.90, NASA TMX-73990

Angles Of Attack	Mach numbers					
	0.64000	0.69000	0.74000	0.80000	0.84000	0.90000
-180.0	0.02200	0.02200	0.02200	0.02200	0.02200	0.02200
-174.0	0.06200	0.06200	0.06200	0.06200	0.06200	0.06200
-169.0	0.13200	0.13200	0.13200	0.13200	0.13200	0.13200
-164.0	0.24200	0.24200	0.24200	0.24200	0.24200	0.24200
-159.0	0.30200	0.30200	0.30200	0.30200	0.30200	0.30200
-139.0	1.04200	1.04200	1.04200	1.04200	1.04200	1.04200
-119.0	1.65200	1.65200	1.65200	1.65200	1.65200	1.65200
-109.0	1.85200	1.85200	1.85200	1.85200	1.85200	1.85200
-98.8	2.00200	2.00200	2.00200	2.00200	2.00200	2.00200
-88.8	2.02320	2.02470	2.04500	2.10000	2.09500	2.24000
-78.8	1.96200	1.96200	1.98440	2.03500	2.09500	2.18500
-68.8	1.84320	1.84470	1.87300	1.93000	2.00400	2.11500
-58.8	1.66520	1.66920	1.69400	1.76000	1.84800	1.98000
-48.8	1.39200	1.39200	1.39840	1.45000	1.54600	1.69000
-28.8	0.86200	0.86200	0.89240	0.95000	1.04000	1.16000
-19.8	0.33200	0.33200	0.40000	0.46700	0.50500	0.54500
-14.8	0.21000	0.21000	0.30000	0.36000	0.38600	0.40500
-12.8	0.17500	0.17500	0.25000	0.29000	0.33500	0.34500
-10.8	0.14500	0.14500	0.21000	0.26500	0.28000	0.28000
-9.0	0.12000	0.11800	0.17000	0.22000	0.23500	0.23500
-7.0	0.10000	0.08200	0.12000	0.17000	0.17500	0.18000
-5.0	0.04000	0.04100	0.06000	0.09300	0.09800	0.11100
-3.2	0.01500	0.01800	0.02500	0.04600	0.05000	0.07000
-2.2	0.00930	0.01170	0.01300	0.02630	0.03100	0.04000
-1.2	0.00720	0.00770	0.00840	0.01050	0.01750	0.03000
-0.2	0.00630	0.00600	0.00660	0.00880	0.01520	0.03700
1.0	0.00600	0.00580	0.00750	0.01560	0.02630	0.03800
1.8	0.00610	0.00680	0.01000	0.02000	0.03800	0.04500
2.8	0.00660	0.00970	0.01680	0.04100	0.05100	0.06000
3.8	0.00790	0.01300	0.03400	0.07000	0.07500	0.08000
4.8	0.01080	0.02750	0.04700	0.09000	0.09600	0.10200
5.8	0.01630	0.03800	0.06600	0.12000	0.12600	0.13200
6.8	0.02600	0.06300	0.08800	0.14000	0.15100	0.16200
7.8	0.03900	0.08200	0.10500	0.15500	0.17000	0.18300
8.8	0.05100	0.10000	0.12220	0.17000	0.19000	0.19600
9.8	0.07200	0.11700	0.13700	0.18500	0.20500	0.21500
10.8	0.09200	0.13500	0.16200	0.20000	0.22000	0.22800

TABLE B-5. CONCLUDED

Angles Of Attack	0-12400	0-15200	0-16600	0-21200	0-23300	0-24000
11.0	0.14500	0.17000	0.18100	0.23000	0.25000	0.24000
12.0	0.17400	0.18800	0.19500	0.24700	0.26500	0.25500
13.0	0.19200	0.20500	0.21000	0.26000	0.28000	0.27000
14.0	0.21600	0.22500	0.23000	0.28000	0.29500	0.28000
15.0	0.23100	0.24000	0.24500	0.29500	0.30800	0.29700
16.0	0.25000	0.25700	0.26200	0.31300	0.32400	0.31200
17.0	0.26000	0.34000	0.34000	0.39500	0.40000	0.32500
22.2	0.56000	0.56000	0.56000	0.56000	0.56000	0.40000
31.2	1.38000	1.38000	1.38000	1.38000	1.38000	0.56000
51.2	1.65000	1.65000	1.65000	1.65000	1.65000	1.38000
61.2	1.84000	1.84000	1.84000	1.84000	1.84000	1.65000
71.2	1.96000	1.96000	1.96000	1.96000	1.96000	1.84000
81.2	2.02000	2.02000	2.02000	2.02000	2.02000	1.96000
91.2	2.00000	2.00000	2.00000	2.00000	2.00000	2.02000
101.2	1.85000	1.85000	1.85000	1.85000	1.85000	2.00000
111.2	1.65200	1.65200	1.65200	1.65200	1.65200	1.85000
121.2	1.04200	1.04200	1.04200	1.04200	1.04200	1.65200
141.2	0.30200	0.30200	0.30200	0.30200	0.30200	1.04200
161.2	0.24200	0.24200	0.24200	0.24200	0.24200	0.30200
166.2	0.13200	0.13200	0.13200	0.13200	0.13200	0.24200
171.2	0.06200	0.06200	0.06200	0.06200	0.06200	0.13200
176.2	0.02200	0.02200	0.02200	0.02200	0.02200	0.06200
180.0	0.02200	0.02200	0.02200	0.02200	0.02200	0.02200

LIST OF SYMBOLS

a_1	Flapping angle
c	Chord
C_d	Drag coefficient
C_l	Lift coefficient
C_m	Moment
C_P	Horsepower coefficient
C_Q	Torque coefficient
C_T	Thrust coefficient
C_W	Helicopter weight coefficient
E	Tension modulus
EA	Axial stiffness
EI_B	Beamwise stiffness
EI_C	Chordwise stiffness
F_{cu}	Ultimate compression strength
F_{su}	Ultimate shear strength
F_{tu}	Ultimate tensile strength
G	Torsion modulus
GJ	Torsional stiffness
I_{xx}	Moment of inertia about x-x axis
K_t	Stress concentration factor
M_B	Beamwise moment
M_C	Chordwise moment
M_{co}	Root-chord moment

LIST OF SYMBOLS (Concluded)

M_t	Mast torque
r	Radial station
R	Blade radius
V_H	Maximum level flight
V_{NE}	Velocity, never exceed
X	Airfoil chord station
XCG	Chord station of center of gravity
XNA	Chord station of neutral axis
Y	Airfoil vertical distance from chord line
α_s	Shaft angle
μ	Advance ratio
ω_n	Natural frequency
ρ	Density
ρI_B	Beamwise mass moment of inertia
ρI_C	Chordwise mass moment of inertia
σ	Solidity
ψ_b	Azimuth angle
ζ	Damping coefficient